

STUDY OF HETEROGENEOUS DEFORMATION IN HEXAGONAL TITANIUM USING
HIGH ENERGY X-RAY DIFFRACTION

By

Harsha J. Phukan

A DISSERTATION

Submitted to
Michigan State University
in partial fulfillment of the requirements
for the degree of

Materials Science and Engineering – Doctor of Philosophy

2021

ABSTRACT

STUDY OF HETEROGENEOUS DEFORMATION IN HEXAGONAL TITANIUM USING HIGH ENERGY X-RAY DIFFRACTION

By

Harsha J. Phukan

It is well known that grain boundaries have a beneficial effect on strengthening properties in crystalline materials. There is however, a much lesser degree of understanding on how grain boundaries determine the propensity of a material for damage nucleation. In polycrystalline aggregates the mechanical response of individual grains to loading conditions is highly heterogeneous and dependent upon the morphology and relative orientation of the neighboring grains. Surface characterization methods such as electron backscatter diffraction (EBSD) present only a partial understanding of this heterogeneous deformation behavior. X-ray diffraction using high brilliance beams from synchrotron sources provide a powerful non destructive means to characterize the subsurface mechanical response of grains. Such high energy x-ray diffraction microscopy (HEDM) methods can measure changes in grain orientation, morphology and local strain evolution with high spatial resolution.

The low crystal symmetry of hexagonal metals make them ideal candidates to study individual slip systems and identify specific types of dislocations. Deformation in hexagonal materials is strongly dependent upon the relative orientation between the c-axis and the loading direction. Conditions that lead to the nucleation of deformation twinning in hexagonal metals are not well understood. This makes it challenging for physically based crystal plasticity models to predict twinning events. Another important consideration in polycrystalline deformation is the dependence of the local stress state on the geometrically necessary dislocation (GND) density.

In this work, two different samples of polycrystalline pure titanium having textures were characterized using two different HEDM techniques. The first specimen has a predominantly "hard" texture with respect to the loading direction. In-situ far field high energy diffraction microscopy (FF HEDM) was used to characterize the formation of discrete twinning events during a tensile

test. The propensity for twin nucleation in a grain by slip transfer from neighboring grains for each of the identified twinning events is evaluated using a geometrical parameter along with conditions of spatial proximity. The second specimen has a largely "soft" texture with respect to the loading direction. The evolution of local morphology and local stress state during a four point bending experiment were captured using differential aperture x-ray microscopy (DAXM). The GND density was estimated for each voxel from the orientation gradient.

In contrast to surface measurements on the same material deformed in bending, where prism slip bands nucleated mechanical twins, a greater amount of pyramidal $\langle c + a \rangle$ slip was correlated to twin formation in the interior of the specimen, though it is not clear whether the twin or the $\langle c + a \rangle$ slip initiated the correlated shear. Comparison with similar studies in titanium shows that the type of slip system likely to nucleate a T1 twin is strongly dependent upon the loading direction and initial texture.

In this work a quantitative matching of the FF HEDM data and more recently collected Near Field (NF) HEDM dataset is done using criteria of maximum crystallographic misorientation and Euclidean distance. Additionally, a comparison was made between the kinematic descriptor (lattice reorientation as a function of load) and the grain averaged stress measures in FF HEDM. This was done in order to determine the limits of FF HEDM for assessing complex mesoscopic loading events such as deformation twinning.

A means to visualize the heterogeneity in the local stress state is enabled by DAXM characterization. Moreover, the in-situ DAXM experiment enabled the estimation of the GND density from the lattice rotation gradient. The analysis was able to identify the contributions to the total GND density from individual slip systems. The local agglomeration of GND (pileups) is strongly dependent upon the local stress state and the transmissivity of dislocations across grain boundaries. In contrast, the global stress state does not have a strong correlation with local GND accumulation.

The present work is a step towards developing a better understanding of local mechanical response in polycrystalline materials. It is expected that results from this study can help better inform constitutive relations governing crystal plasticity based models that simulate material deformation.

Copyright by
HARSHA J. PHUKAN
2021

This thesis is dedicated to my parents.

ACKNOWLEDGEMENTS

At the very onset I take this opportunity to express my gratitude towards my advisor, Dr. Thomas Bieler for his guidance, encouragement and patience throughout this work. I would also like to thank the members of my dissertation committee: Drs. Carl Boehlert, Martin Crimp, Philip Eisenlohr and Patrick Kwon, for their valuable insights and constructive criticism.

I would like to acknowledge the support of the Materials World Network (grant NSF-DMR-1108211) and the Department of Energy (DE-FG02-10ER46637) for this work. Use of the Advanced Photon Source facilities was made possible with the support of the Department of Energy, Office of Basic Energy Sciences under DOE/BES DE-FG02-10ER46637.

I would also like to thank Dr. Leyun Wang, faculty of Materials Science at Shanghai Jiao Tong University, for his collaborative help in conducting beamline experiments at APS, and his technical inputs.

I would be remiss if I did not express my heartfelt thanks to Drs. Peter Kenesei, Wenjun Liu, Jun Sang Park, Hemant Sharma and Ruqing Xu for their help in conducting experiments at APS; and subsequent post processing, interpretation and analysis of data.

Gratitude is also due to Professor Dierk Raabe and colleagues at the Max-Planck-Institut für Eisenforschung for facilitating a wonderful learning experience during my visits there.

I also take this opportunity to thank my fellow graduate students (current and former) for their help and encouragement; in particular Drs. Ajith Chakkedath, Markus Downey, Songyang Han, Mingmin Wang, Chen Zhang, Quan Zhou, and Mr. Yang Su.

Finally I want to thank my wife Mollie for her patience and belief in me. I could not have come this far without her support.

TABLE OF CONTENTS

LIST OF TABLES	x
LIST OF FIGURES	xi
KEY TO ABBREVIATIONS	xxix
CHAPTER 1 INTRODUCTION	1
1.1 Motivation for current work	1
1.2 Deformation systems in hexagonal titanium	2
1.3 High energy x-ray diffraction (HEXRD)	3
1.4 Structure of the dissertation	4
CHAPTER 2 LITERATURE REVIEW	6
2.1 Basics of plastic deformation in crystalline materials	6
2.1.1 Crystallographic Slip	6
2.1.2 Schmid's law for slip in a single crystal	7
2.1.3 Multiplication of dislocations	8
2.1.4 Generalized Schmid Factor	9
2.1.5 Deformation twinning	12
2.2 Plastic deformation in hexagonal titanium	13
2.3 An overview of crystal plasticity principles	18
2.4 Slip transfer and dislocation interactions at grain boundaries	23
2.4.1 Implications of slip transfer in polycrystalline materials	25
2.5 Twin formation as a result of slip transfer from a neighboring grain (S+T twinning)	27
2.6 Geometrically necessary dislocations (GND)	29
2.7 Review of HEXRD methods	35
2.7.1 3D XRD	36
2.7.1.1 Indexing data obtained from 3D XRD	39
2.7.1.2 Local strain tensor evaluation from FF HEDM	41
2.7.1.3 Accuracy in determination of grain positions using 3D XRD	42
2.7.2 Differential aperture x-ray microscopy (DAXM)	43
2.7.2.1 Local strain tensor evaluation from DAXM	47
2.7.2.2 Calculation of GND density from DAXM data	48
2.8 Opportunity for research	48
CHAPTER 3 MATERIALS AND METHODS	52
3.1 Titanium specimens	52
3.1.1 Tensile specimen for Far Field Experiment	52
3.1.2 Four point bending specimen for DAXM Experiment	54
3.2 Far Field HEXRD (Chapter 4)	54
3.2.1 Experimental setup	54
3.2.2 Post deformation surface EBSD of the tensile specimen	55

3.3	Experimental setup for in-situ DAXM characterization (Chapter 6)	56
CHAPTER 4 IN-SITU FAR FIELD XRD CHARACTERIZATION OF TENSILE DEFORMATION OF A COMMERCIAL PURITY TITANIUM SPECIMEN . . . 58		
4.1	Analysis of the diffraction patterns	59
4.1.1	Determination of grain centers of mass and grain averaged strain tensors	59
4.1.2	Quantification of error in local strain calculations	61
4.2	3D Reconstructed model of the microstructure prior to loading	62
4.2.1	Model parameters and simulation of tensile test	62
4.2.2	Sensitivity of mechanical response of model to dilatational layer thickness	64
4.3	Effect of local stress state on deformation systems	65
4.4	Identification of twinning events	66
4.5	Results and Discussion	69
4.5.1	Far Field HEDM Characterization	72
4.5.1.1	Assessment of slip transfer from neighboring grains	72
4.5.1.2	Stress evolution in parent grains	78
4.6	Comparison of FF 3D XRD results with surface EBSD mapping	86
4.7	Cross validation of local stress tensor calculations and grain positions between Fable and MIDAS	88
4.8	Evaluation of identified twins using Near Field HEDM	91
CHAPTER 5 A COMPARATIVE STUDY OF THE ACCURACY OF FF HEDM METHOD WITH RESPECT TO NF HEDM 99		
5.1	Classification of errors from the FF and NF HEDM experiments	99
5.2	Estimation of grain volume	100
5.3	NF HEDM: Reduction of data on the basis of Confidence Index	102
5.4	Matching of centroids between NF and FF HEDM datasets	102
5.4.1	Data reduction	102
5.4.2	Algorithms used for matching grains between FF-NF datasets	103
5.4.3	Grain size comparison between matched grains in FF/NF datasets	105
5.4.4	Implementation of matching algorithm	107
5.4.5	Application of translational correction between FF/NF datasets	109
5.4.6	Relationship between NF grain size and matching centroids in FF	110
CHAPTER 6 COMPARISON OF KINEMATICS OF CRYSTAL ROTATION AND GRAIN AVERAGED STRESS MEASUREMENTS OBTAINED FROM FF HEDM 113		
6.1	Calculation of plastic spin axes for active slip systems	113
6.2	Comparison of slip system plastic spin axis and lattice reorientation	114
CHAPTER 7 IN-SITU DAXM CHARACTERIZATION OF A COMMERCIAL PURITY TITANIUM SPECIMEN SUBJECTED TO A FOUR POINT BENDING TEST 121		
7.1	Texture of CP-Ti specimen	121
7.2	White beam diffraction	121

7.2.1	Local deviatoric strain tensor estimation from DAXM data	124
7.3	Geometrically necessary dislocation density calculation from DAXM data	124
7.3.1	Rotation gradient calculation of DAXM dataset	129
7.3.2	Calculation of dislocation density from the rotation gradient	130
7.4	Results and discussion	134
7.4.1	Localized GND concentrations at grain boundaries	134
7.4.2	Assessment of local stress heterogeneity using principal components	134
7.4.2.1	Local stress heterogeneity within and above the purple grain	138
7.4.2.2	Local stress heterogeneity in region 2 triple junction with hard and soft grains	139
7.4.3	Description of parameters used in analysis of slip transfer at the voxel level	142
7.5	Summary assessment of inter-and intra-granular heterogeneous deformation	144
CHAPTER 8 CONCLUSIONS AND SCOPE FOR FUTURE WORK		146
8.1	Far Field HEDM	146
8.1.1	Twin identification and role of slip transfer in twin nucleation	146
8.1.2	Comparison of FF results with Near Field and surface EBSP mapping	147
8.2	DAXM analysis	148
8.2.1	Assessment of heterogeneity in stress state due to local constraints	148
8.3	Scope for future work	149
APPENDICES		150
APPENDIX A	ADDITIONAL FAR FIELD ANALYSIS RESULTS	151
APPENDIX B	PARENT/TWIN/NEIGHBOR SLIP TRANSFER ANALYSIS FROM NF HEDM	153
APPENDIX C	STEREOGRAPHS OF EVOLUTION OF LATTICE PLASTIC SPIN AXIS AS A FUNCTION OF BULK STRAIN	158
APPENDIX D	HYDROSTATIC STRAIN TENSOR MEASUREMENT USING MONOCHROMATIC SETTING OF DAXM	160
APPENDIX E	PRINCIPAL STRESS AND PRINCIPAL DIRECTION MAPS FOR REGIONS 3,4 AND 5	166
APPENDIX F	CORRELATION OF GND CONTENT WITH RESIDUAL BURGERS VECTOR AND SLIP TRANSFER PARAMETER	170
APPENDIX G	SLIP TRANSFER PARAMETER V/S RESIDUAL BURGERS VECTOR PLOTS	197
APPENDIX H	COORDINATE TRANSFORMATIONS	205
APPENDIX I	LIST OF PYTHON AND MATLAB SCRIPTS USED FOR DATA ANALYSIS	208
BIBLIOGRAPHY		249

LIST OF TABLES

Table 2.1: Parameters associated with the four twinning modes in CP-Ti (Wang, 2011)	15
Table 2.2: Enumeration of the three different configurations for 3D XRD, based on sample to detector distance (L). Adapted from Park et al. (Park et al., 2017).	38
Table 3.1: Composition (wt%) of Grade 1 Titanium Plate. Adapted from Bieler et al. (2014)	52
Table 4.1: Parameters used in Crystal Plasticity model	64
Table 4.2: Summary of Twinning Events Observed in 14 Layers in two specimens	80
Table 4.3: Summary of 13 twinning events and their stress history correlation with respect to neighboring grains.	83
Table 7.1: Slip Systems considered for GND density calculation	133
Table 7.2: Combinations of parameters used to assess relationship between residual Burgers vector, m' and GND density	144

LIST OF FIGURES

Figure 2.1: Schematic showing the geometry of edge and screw dislocations in a simple cubic lattice. (a) perfect lattice, (b) an extra half-plane of atoms ABCD inserted into the top half of the crystal. DC is a positive edge dislocation, (c) left handed screw dislocation DC is formed by displacement of the faces ABCD relative to each other in the direction AB, (c) right handed screw dislocation DC,(e) atomic planes with spacing b in a perfect crystal, (f) planes distorted by a right-handed screw dislocation. (Hull and Bacon, 2011)	7
Figure 2.2: Schematic illustrating the concept of critical resolved shear stress for a single crystal (Hull and Bacon, 2011). It is important to note that in general ϕ and λ are not coplanar.	8
Figure 2.3: Schematic showing the process of regenerative multiplication of dislocations by a Frank-Read source [adapted from Read (1953)].	9
Figure 2.4: Illustration of generalized stress state for an arbitrary grain in a polycrystal. The local stress tensor corresponding to this generalized stress state is shown as a function of X, Y and Z. T is the traction vector, while n and m are the slip plane normal and slip direction respectively.	10
Figure 2.5: Schematic showing the four twinning elements (Christian and Mahajan, 1995). κ_1 and κ_2 are twinning and conjugate planes respectively. The corresponding twinning and conjugate directions are η_1 and η_2 . η_1, η_2 , and the normals to κ_1 and κ_2 lie in shear plane P.	13
Figure 2.6: Schematic illustrating the major crystallographic planes and directions (a) , and the slip modes (b) associated with them (adapted from Wang (2011)).	14
Figure 2.7: Schematic illustrating the geometrical relationship between a T1 twin and its parent lattice. Adapted from (Bieler et al., 2014).	17
Figure 2.8: Schematic illustration of the concept of deformation gradient. The total deformation gradient F can be decomposed into the product of the elastic and the plastic components(Roters et al., 2010).	19
Figure 2.9: Illustration of dislocation pileup at a grain boundary between two crystals A and B. Dislocations shown here are edge type; in reality they are a combination of both edge and screw types. Adapted from Livingston and Chalmers [1957]	24

Figure 2.10: Angles used to calculate the Luster-Morris parameter m' . κ is the angle between slip directions; while ψ is the angle between the slip plane normals. θ is the angle between the slip plane traces on the grain boundary plane. Adapted from Bieler et al. (2009).	26
Figure 2.11: Use of m' to determine the propensity of twin nucleation as a result of slip transfer across a grain boundary. Twins can be observed in grain 2, where the activated twin system has a high m' (0.936) with respect to prism $\langle a \rangle$ slip system in grain 1. Adapted from Yang et al. (2011).	28
Figure 2.12: Schematic diagram showing how GNDs of edge type (left) and screw type (right) can accumulate in a plastically deformed crystal. Here b indicated the slip direction and n denotes the slip plane normal. $m = b \times n$. Adapted from Arsenlis and Parks [1999].	30
Figure 2.13: Schematic illustrating a basic 3D XRD experimental setup. Z is the sample rotation axis; ω is the angle of rotation about Z ; L is the sample to detector distance; 2θ is the Bragg angle; η is the azimuthal angle. Adapted from Poulsen (Poulsen, 2012).	37
Figure 2.14: Schematic illustration of Debye-Scherrer patterns for a polycrystalline material with (a) random texture (well annealed);(b) strong texture (Taddei, 2015).	39
Figure 2.15: Schematic diagram illustrating the Laue condition.	44
Figure 2.16: Schematic representation of an Ewald sphere in two dimensions (a) Monochromatic beam, (b) Polychromatic beam containing a range of wavelengths. The parallel set of crystallographic planes (hkl) that form a reciprocal lattice point are shown on the top right inset (Ice and Pang, 2009)	45
Figure 2.17: Schematic of a DAXM experimental setup to interrogate a polycrystalline specimen. An enlarged view of the differential aperture (profiler) Pt wire is shown on the top right (Yang et al., 2004).	47
Figure 2.18: Example illustrating the importance of relative grain positions for viable S+T twin nucleation. The left figure (a) shows two grains with a favorable relative position (along with a high m' value). Figure (b) shows the same grains with relative positions that may not favor S+T twinning.	49
Figure 3.1: Tensile specimen extracted from a larger sample that was previously subjected to a bend test. Because the sample had a prior bending load, a macro residual stress was initially present in the sample (Wang et al., 2014)	53

Figure 3.2: Right: Cross section of the illuminated volume of the tensile specimen (looking down the tensile axis), showing the distribution of the normal component of the strain tensor (ϵ_{zz}), prior to tensile loading. Left: the coordinates of the strain map are shown in context of the tensile specimen. The tensile axis is parallel to the Z direction. 53

Figure 3.3: Evolution of global stress as function of engineering strain for the tensile experiment. Inset figure shows a schematic representation of the experimental setup for FF-HEDM. A schematic representation of the eleven layers examined along the gage section of the tensile is shown on the right. Inset: Schematic illustration of the load relaxation with respect to time is shown for three different strain states—prior to yield (magenta), post yielding (green) and at maximum stress (red). 55

Figure 3.4: Surface tensile direction EBSD IPF map of the far side (facing detector) of the gage section of the unloaded specimen shows several twins and orientation gradients in some grains. The scanned area is highlighted in green. 56

Figure 3.5: CP-Ti sample setup in the four point bending stage and dimensions are shown on the bottom right of the figure. Experimental setup for the in-situ DAXM characterization of four point bending is shown on the top left. The directions of the incoming and diffracted beams are shown schematically. The beamline coordinate system is shown on the top right: Z denotes the direction of the incoming beam; F is anti-parallel to the surface normal (denoted by the green vector) of the specimen; X is directed normal out of the page. Position and displacement direction of the differential aperture (Pt wire) are shown on the bottom left of the figure (Adapted from Larson et al. (Larson et al., 2002)). . . . 57

Figure 4.1: Outline of data analysis strategy that was implemented in a suite of MatLab codes. The .log files (containing orientation and grain index information), and .gve files (containing scattering vector information) are obtained using FABLE. 58

Figure 4.2: Left:Voronoi tessellated model generated from 3D XRD Data set. This microstructure shown here represents the unstrained condition, prior to the tensile test. A dilatational layer of one volume element thickness is used as the surrounding medium along the X and Y directions. The tensile direction is parallel to the Z axis. Right: Evolution of normal component of stress along the tensile direction σ_{zz} in the crystal plasticity simulation of the tensile loading. In the CP model, a uniform compressive strain of 10^{-3} is applied for each of the first three load steps; followed by a uniform tensile strain of 10^{-3} for each of the subsequent load steps. 63

Figure 4.3: Evolution of volume averaged equivalent (von Mises) stress of the far field microstructure model as a function of bulk strain for four different thicknesses of the surrounding free surface layer. It is seen that the mechanical response is not sensitive to dilatational layer thickness. 64

Figure 4.4: Cumulative distribution function (CDF) plots of Schmid Factors corresponding to three load steps for basal $\langle a \rangle$, prism $\langle a \rangle$, pyramidal $\langle a \rangle$, pyramidal $\langle c + a \rangle$ and T1 systems. The global Schmid factor (top row) is calculated using the global uniaxial stress tensor; while the local grain averaged stress tensor is used to obtain generalized Schmid factors (maximum 0.707) (middle and bottom rows). The middle row shows the comparison of the experimentally obtained local Schmid factors with an earlier CP model that imposes only tensile strain without initial compression. The bottom row shows the comparison of local Schmid factors with the results of the CP model with initial compression. The Schmid factors in the CDF plots are the highest per slip system family for each grain. 67

Figure 4.5: Neighborhood of all grains in layer 1 prior to deformation, at the load step just before twinning at 1.3% engineering strain, and after a twin formed at 1.5% engineering strain in orientation space (top row). The spatial map of the 2D slice is shown in the bottom row with grain identification numbers. The bottom right figure shows an enlarged view of the region of interest for the twin formation with grain unit cell orientations based upon geometrical positions in the lower left map of the slice. Tensile direction is along z direction (out of page). 68

Figure 4.6: Evolution of resolved shear stress (RSS) for each of the six T1 twin systems in the parent grains identified in layers 1, 2, 3, 4 and 5. Green arrows indicate the load step where the twin was first identified, and filled red markers indicate the observed twin variant. 70

Figure 4.7: Evolution of resolved shear stress (RSS) for each of the six T1 twin systems in the parent grains identified in layers 6, 7, 8, 9 and 10. Details of symbols and color conventions are given in the caption of figure 4.6. 71

Figure 4.8: Evolution of resolved shear stress (RSS) for each of the six T1 twin systems in the parent grain identified in layer 11. Details of symbols and color conventions are given in the caption of figure 4.6. 72

Figure 4.9: Schematic outlining the criteria used to identify the neighbor grain associated with the highest likelihood of slip transfer, thereby triggering a twin. θ is the angle between the unit vector joining the centers of masses of the parent grain and neighbor; and the unit vector normal to the slip plane in the neighbor. The three parameters (Absolute value of the Schmid Factor, Absolute value of $\sin \theta$ (Spatial alignment factor SAF) and m' can be plotted in a 3-D space. A point at the origin (red) would have the worst possible spatial alignment for slip transfer, while a point at the top right corner (green) would have the highest likelihood for slip transfer. The purple slip planes have lower SAF while the green slip plane has a higher SAF. 73

Figure 4.10: The m' relationship observed between the activated twin system and pyramidal $\langle c + a \rangle$ system of a neighboring grain is shown for six different instances (Layers 1,2, 4, 6, 9 and 10).The orientations of the parent, twin and neighboring grains are viewed along the tensile Z axis, (left column) as well as the beam X direction, (right column). The letters "P", "T" and "N" indicate the parent, twin and neighbor grains respectively. The corresponding Bunge Euler angles and m' values are also indicated for each instance.The blue vector shows the slip direction from the blue dot away from it on the positive surface of the plane, and a half length orange dot and vector indicates a twin system. The plane normal points out of the page for beige slip planes and into the page for gray planes. The dotted red, green and blue lines represent the a_1 , a_2 and a_3 directions, respectively. Colors of the grains correspond to (0001) inverse pole figure representations of the orientations. 74

Figure 4.11: Summary of twinning events in the 11 layers as a function of m' : Size of the markers are proportional to the Schmid factor rank of the twin system. Filled circles (•) indicate geometrically more plausible instances, where slip transfer may have resulted in nucleation of twins. Data from a previous study (1.01,1.02 and 1.03 (Bieler et al., 2014) in table 4.2) are plotted as □. Cases with SAF > 0.6 ($\theta > 37^\circ$) are represented as filled colored markers, where the colors represent different families of slip and twin systems. Among these, the cases with a highest likelihood of S+T twinning with SAF > 0.8 ($\theta > 53^\circ$) are shown in a darker gold color, while the lighter gold symbols represents instances where $37^\circ < \theta < 53^\circ$. Prism $\langle a \rangle$ is represented by red, basal $\langle a \rangle$ by blue, pyramidal $\langle a \rangle$ by green, pyramidal $\langle c + a \rangle$ by golden (transitions from lighter gold to a darker shade for more plausible cases of S+T twinning); and T1 twinning by black. Inset shows the linear regression plot, considering only the highly plausible $\langle c + a \rangle$ (dark gold) points. 78

Figure 4.12: Evolution of normal component of local stress tensor (along the tensile direction) for parent and neighboring grains (layers 1, 2, 3, 4 and 5). Prisms indicate the Bunge Euler angle orientation of the grains. Transition in background shade from gray to white indicates the bulk strain at which the twin was identified. 81

Figure 4.13: Evolution of normal component of local stress tensor (along the tensile direction) for parent and neighboring grains (layers 6, 7, 8, 9 and 10). Details on symbols and color conventions are given in the caption in figure 4.12.	82
Figure 4.14: Evolution of normal component of local stress tensor (along the tensile direction) for parent and neighboring grains (Layer 11). Details on symbols and color conventions are given in the caption in figure 4.12.	83
Figure 4.15: Evolution of local average von Mises stress σ_{vM} in identified parent and selected neighbor grains across the 11 layers. The load steps corresponding to twin identification is indicated by the gradual transition in background color from gray to white. The measure of local stress deviation from ideal uniaxial tension is given by $\cos \theta = \sigma.U$	84
Figure 4.16: The top row shows the tensile sample and the region from which EBSD measurements were made on the surface between the sample and the detector. The top right figure shows the grain reference orientation deviation map where the reference is the average grain orientation in the EBSD data. Two different regions with twins (labeled a and b) are shown. in the second and third rows. The green prisms show the relative positions of grain centers of mass from the far field data (FF) in which twins were detected, and just beneath them, the enlarged corresponding part of the EBSD maps; the green and black prisms are not in good spatial agreement. Beneath the EBSD scans, misorientation maps between the FF COM orientation and the 2-D EBSD grain orientations show agreement within 10°	87
Figure 4.17: Histogram of Euclidean distance for grains consistent with indexation using Fable and MIDAS (top row), and cumulative distribution plot of the same grains (bottom row), for unstrained (prior to loading) and final unloaded states respectively. The top right plot also shows the histogram of Euclidean distance for grains consistent between FF analysis (MIDAS) for the final unloaded state.	89
Figure 4.18: Cumulative distribution function (CDF) plots of grain radii estimated by MIDAS for the undeformed and final unloaded states respectively. Inset shows a magnified view of the tail of the CDF plots. There is a significant change in the slope towards the tail of curve, going from the state prior to deformation to the final unloaded state.	91
Figure 4.19: Cumulative distribution function plots for equivalent strain (top row) and von Mises stress (bottom row) evolution, showing the differences between two indexing methods. Strain and stress evolution are shown for four different load states: unstrained state prior to tensile loading, 75% of bulk strain prior to yield, maximum load and final unloaded state.	92

Figure 4.20: Perspective (left) and XY plane (right) projections for the gage volume interrogated by NF HEDM, shown with IPF colors. The data corresponds to the final unloaded state in the tensile experiment (after dismounting of the specimen from the tensile stage). The tensile direction was along the Z axis. 93

Figure 4.21: Analysis of the first parent, twin and high m' grain from figure 4.10. NF HEDM provides a more precise relative position and information on grain shape. Bottom left: plot of the c-axis disorientation of the neighboring grain as a function of bulk strain, along with the evolution of equivalent stress in both parent and neighboring grains. Top right: Evolution of resolved shear stress for 4 families of slip in the neighboring grain, and bottom right: misorientation of the plastic spin axis for each of the 12 pyramidal $\langle c + a \rangle$ slip systems as function of bulk strain. The color scheme used for the 12 pyramidal $\langle c + a \rangle$ slip systems is the same for the top right and bottom right plots. The symbol and color scheme for the slip systems is indicated in the inset text. 94

Figure 4.22: Revisit of the third parent, twin and high m' grain from figure 4.10. NF HEDM enables a more precise relative position and information on grain shape. Bottom left: plot of c-axis disorientation of the neighboring grain as a function of bulk strain, along with the evolution of equivalent stress in both parent and neighboring grains. Top right: Evolution of resolved shear stress for 4 families of slip in neighboring grain, and bottom right: misorientation of the plastic spin axis for each of the 12 pyramidal $\langle c + a \rangle$ slip systems as function of bulk strain. The color scheme used for the 12 pyramidal $\langle c + a \rangle$ slip systems is the same for the top right and bottom right plots. The symbol and color scheme for the slip systems is indicated in the inset text. 96

Figure 4.23: Resolved shear stress plot as a function of m' for the seven twinning events validated with NF HEDM data plotted in the same manner as figure 4.11. Here, all of the slip systems with a favorable geometric compatibility with respect to the active twin variant in the parent grain are of pyramidal $\langle c + a \rangle$ type. The data points from the FF HEDM analysis that correspond to high m' relationship with respect to the active twin variant are indicated by 'x'. The size of the markers are proportional to the Schmid factor rank of the active twin variant. The NF points that coincide with the FF results are indicated by translucent circles. 98

Figure 5.1: Classification of errors from the FF and NF HEDM experiments. 100

Figure 5.2: Maps showing distribution of the confidence index (CI) in the interrogated microstructure projected on the XY plane (looking down along tensile axis over the entire interrogated volume). Cumulative distribution plots of CI (unfiltered data and with different threshold values) are shown in bottom left. The cumulative distribution curves converge at a CI value ~ 0.95 101

Figure 5.3: Cumulative distribution plot of the disorientation between two different grain averaging techniques for the reduction of the NF data. The same group of orientations are averaged: the first approach being simple quaternion averaging, and the second using the more optimized grain averaging algorithm available in DAMASK. The maximum disorientation between the mean quaternion approach and the DAMASK algorithm is less than 3° . At least 90% of the points have a disorientation of 1.5° or less. The point cloud of the reduced NF data is shown on the right with IPF colors denoting crystal orientation with respect to the Z axis. 104

Figure 5.4: Forward algorithm used for matching grains between the FF and NF datasets, where the misorientation criterion is applied before the ball radius. 105

Figure 5.5: Reverse algorithm used for matching grains between the FF and NF datasets, where the ball radius criterion is applied first and the misorientation threshold is applied in the second step. 106

Figure 5.6: Cumulative distribution function plots for matched grains using forward algorithm (left) and reverse algorithm (right), using a misorientation tolerance of 5° . In both the matching operations, a ball radius of $1500 \mu m$ was used (entire domain of the NF dataset). Both the approaches yield identical results. Inset on the right hand side shows CDF plot for a much smaller subset, i.e. only centroids within a $200 \mu m$ ball radius are considered. 107

Figure 5.7: Arrangement of voxels in a 2D slice of the NF HEDM data, looking down the tensile (Z) axis. 108

Figure 5.8: Cumulative distribution plots for FF and NF grain radius value for the matched grains with a cut-off ball radius of $200 \mu m$. The figure on the left shows the comparison between the two datasets with the as-is FF grain radius values. The figure on the right shows the comparison after the FF grain radius values were multiplied by a factor of 2.9, which gives a closer match with the NF data. 108

Figure 5.9: Comparison of grain centroid positions from FF and ND HEDM results, corresponding to the final unloaded state of the specimen. Only the centroids with NF-FF Euclidean distance $\leq 200 \mu m$ are considered here. The left side of the figure shows the connecting vectors scaled and shaded in proportion to the calculated values of NF grain radius. The same set of plots are repeated on the right side, with the connecting vectors scaled and shaded in proportion to FF grain radius, without a corrective scaling factor. 109

- Figure 5.10: Left: CDF plot of same data from Figure 5.9, with and without the correction vector. From the leftward shift of the CDF curve, using the correction vector results in a better spatial match between the two datasets. Right: projection of the calculated correction vector in the YZ plane. Its magnitude and direction are also indicated. 110
- Figure 5.11: Replotting of the same data as in figure 5.9, except in this case the correction vector is applied to the FF data points. The the FF data appears much better aligned with the corresponding NF data points. 111
- Figure 5.12: Top right: cumulative distribution plots of grain sizes, in terms of number of constituent voxels. For the subset of grains matched with FF dataset, there is a shift to right, indicating a larger average grain size. Left: For matched grains, grain size plotted as a function of the unscaled grain radius. Bottom right: variation of the correlation coefficient as a function of threshold number of voxels. 112
- Figure 6.1: Schematic representation showing the sense of shear and plastic spin effected by crystallographic slip, that results in lattice rotation. n denotes the slip plane normal, while b denotes the slip direction. 114
- Figure 6.2: The upper left prism identifies the initial grain orientation in the sample frame with the three $\langle a \rangle$ axes labeled. The top row shows three (0001) stereographic projections showing the lattice spin axis at each load step from from the beginning of the plastic regime (white) to $\sim 3\%$ (black). The $\langle a \rangle$ axes of the crystal frame are identified at the center of the upper right stereographic projection. Increasing the spacing i between load steps from 1 to 5 (left to right) smooths the fluctuations between load steps. Middle and bottom rows: Stereographic projections show the plastic spin axes for (basal $\langle a \rangle$) (light blue circles on perimeter), prism $\langle a \rangle$ (red circles in the center) and pyramidal $\langle c + a \rangle$ (rainbow colors). The rainbow color scheme for the 12 pyramidal $\langle c + a \rangle$ slip system spin axes are shown in the lower left-hand corner (the two spin axes for different directions on the same plane are close together with dark and light tones of the same color (plane), and more widely spaced adjacent spin axes are for the same slip direction on different planes, which have either a darker or lighter color of the two planes). The symbols for each spin axis are scaled in proportion to their resolved shear stress magnitude. The black point identifies the observed spin axis. A blue arc connects a blend of the two most highly stress slip systems (largest symbols). The observed spin axis has an arrow pointing to the blend of the top two slip systems that is closest (largest dot product), In the middle and bottom rows, the most favored slip systems are different, indicating significant fluctuations in the stress state, but the black arrows indicate that that the observed spin axis is closer to the blend of the highly stressed slip systems. With smoothing, the black arrow gets longer (dot product becomes smaller). 115

- Figure 6.3: Maximum dot product between lattice spin axis and blended slip system plastic spin axes (linear combination of the highest and second highest resolved shear stress slip systems), for the twinned grain in figure 6.2. The effect of smoothing (increasing i) leads to less fluctuation, and suggests alternating sets of active slip systems. The colors of the markers indicate the fraction of the slip system with the second highest resolved shear stress in the blended axis. 117
- Figure 6.4: Maximum dot product between the observed lattice spin axes and blended high resolved stress slip system axes (slip systems with highest and second highest resolved shear stress), plotted as a function of bulk strain for six members of three types of grains; twinned grains, neighbors to the twinned grains, and arbitrarily chosen grains. For each plot, the average value of the dot product is plotted as a dashed horizontal line and annotated in each plot. . . 119
- Figure 6.5: Cumulative distribution plots for the maximum dot product for the three categories of grains shown in 6.4. The effect of spacing between load steps is more significant for the twinned grains than for the other two classes of grains. 120
- Figure 7.1: (a) OIM Map of the undeformed microstructure of the 4 point bending specimen prior to bending. The region interrogated by DAXM is outlined with a dashed rectangle. Prisms indicating orientations of the soft and hard grains are shown. (b) Optical image of the microstructure at the end of the final bending increment ($\sim 3.5\%$ macroscopic strain). The soft and hard oriented grains are outlined in blue and green respectively. 122
- Figure 7.2: Surface global Schmid factor maps for specimen prior to bending. The overall texture is conducive to basal and prism $\langle a \rangle$ slip. 122
- Figure 7.3: Orientation maps from the indexed DAXM results. The undeformed specimen was interrogated before mounting with a step size of $4\mu\text{m}$ (a). For the subsequent bending increments 1, 2, 3 and 4 ((b) through (e)) a coarser step size ($6\mu\text{m}$) was used. The vertical and horizontal lines (colored yellow) overlaid on the coarse dataset in (b) indicate the locations of finer finer $2\mu\text{m}$ step size H and X scans that are shown beneath the coarser map. 123

Figure 7.4: Local equivalent strain distribution map corresponding to the unstrained state and after four subsequent bending increments. The cumulative distribution function compares the equivalent strain corresponding to the unstrained state prior to bending (blue), and the four subsequent bending increments. The inset shows the evolution of the equivalent strain averaged over the entire interrogated volume for five strain states. The lower row shows the spatially resolved equivalent strain maps for the unstrained and four deformation states. The IPF color map for the microstructure corresponding to the unstrained state is shown on the left hand side of the top row. The unstrained scan was done prior to the bending experiment and covered a larger volume with a finer step size. The other scans were taken after each load step during the bending experiment. 125

Figure 7.5: Schematic outlining strategy used to calculate GND density from DAXM dataset. 127

Figure 7.6: Left: The sphere surrounding a kernel for an exemplary voxel within the combined (Coarse scan + Fine scan) DAXM dataset for bend increment 2 is shown for ball radii range of 10-40 microns. Cumulative distribution function (CDF) plots of the residual sum of squares error for each of the three components of the rotation gradient tensor. The error increases with increasing ball radius used for the nearest neighbor search. 128

Figure 7.7: Bend increment 2: Line scan DAXM dataset superposed on coarse serial probed DAXM dataset. The two datasets are combined for purposes of the lattice rotation gradient calculation. 130

Figure 7.8: Bend increment 2: Maps showing the distribution of the nine components of the rotation gradient tensor for the fine scan grid. 131

Figure 7.9: Bend increment 2: GND density maps, showing total GND density (b) and GND densities specific to slip system families. Screw dislocation contributions of $\langle a \rangle$ type are in (g). Comparing the total GND density with the IPF map (a), it can be seen that the GND concentrations coincide with the grain boundaries. 135

Figure 7.10: Bend increment 2: Orientation map of the regions of interest where the scaled slip transfer parameter is plotted as a function of residual Burgers vector. Region 1 comprises a grain boundary and an intragranular region with an orientation gradient; region 2, 3 and 5 are triple junctions; and region 4 is a grain boundary. 137

Figure 7.11: Principal Stress distribution for the intragranular region in the purple grain shows varying local stress states indicated by different "principal stress jacks" that differ from the average stress tensor for the purple grain shown on the left. The color of each line in the stress jack indicates the value of the principal stress component in MPa, which are annotated on the average stress jacks. The tensile direction is parallel to the *Y* axis in the coordinate system shown while *Z* is the surface normal. The stress jacks are oriented according to the XYZ axes, indicating that the largest compressive principal stress is roughly perpendicular to the stress axis. The average principal stress jack corresponding to the entire measured volume is also shown on the light gray sphere. 139

Figure 7.12: Principal Stress map for the high angle grains near the boundaries above the purple grain, including the corresponding grain average "principal stress jacks" for the pink and lavender grains above the purple grain, which have a significantly different stress state than the purple grain. The tensile axis is parallel to the global *Y* direction (shown on the right of figure). The principal stress values are annotated on the grain average and volume average stress jacks. The stress in the pink and lavender grains are much different from the purple grain, and the stress state near the boundaries differ significantly from the grain interiors. 140

Figure 7.13: Bend increment 2: Principal Stress maps for the entire vertical fin containing the LAGB and HAGB of region 1, with each principal component shown separately. 140

Figure 7.14: Principal Stress direction map for the triple junction in region 2, where the viewpoint is identified by the X-Y-Z arrows. The grain boundaries are delineated by black lines. Principal stress jacks corresponding to average stress tensor for each individual grain, along with their magnitudes and sense are also shown for comparison. The tensile axis is parallel to the global *Y* axis shown on the left of the figure. 141

Figure 7.15: Orientation and total GND density maps for region 1. The voxels chosen for slip transfer analysis in the high angle grain boundary (~ 28 °misorientation) and intragranular (low angle grain boundary with misorientation < 1.5°) regions are shown (circled voxels). The Bunge Euler angles denoting the average grain orientations are also noted here. It is important to note here that prisms denoting the crystal orientations are drawn from the perspective of the sample normal direction, with *Y* pointing vertically up and *X* to the right. 143

Figure 7.16: Map showing spatially resolved deviation from the average grain orientation in the lower grain of region 1 (Left). The cumulative distribution of misorientation deviation within this grain is shown on the right. The region with a relatively higher deviation coincides with the high local GND accumulation region 143

Figure A.1: The m' relationship observed between the activated twin system and pyramidal $\langle c + a \rangle$ system of a neighboring grain is shown for layers 3 and 5. The orientations of the parent, twin and neighboring grains are viewed along the tensile Z axis, (left column) as well as the beam X direction, (right column). For description of the symbols, the reader is referred to figure 4.10. 151

Figure A.2: The m' relationship observed between the activated twin system and pyramidal $\langle c + a \rangle$ system of a neighboring grain is shown for layers 6, 7, 8 and 11. The orientations of the parent, twin and neighboring grains are viewed along the tensile Z axis, (left column) as well as the beam X direction, (right column). For description of the symbols, the reader is referred to figure 4.10. 152

Figure B.1: Parent/Twin/High m' neighbor for twin identified in layer 6 in FF HEDM and validated by NF HEDM. 153

Figure B.2: Parent/Twin/High m' neighbor for twin identified in layer 7 in FF HEDM and validated by NF HEDM. 154

Figure B.3: Parent/Twin/High m' neighbor for twin identified in layer 9 in FF HEDM and validated by NF HEDM. 155

Figure B.4: Parent/Twin/High m' neighbor for twin identified in layer 7 in FF HEDM and validated by NF HEDM. 156

Figure B.5: Parent/Twin/High m' neighbor for twin identified in layer 7 in FF HEDM and validated by NF HEDM. 157

Figure C.1: Stereographic projection of the evolution of the lattice plastic spin axis is shown for different values of bulk strain for a twinned grain. 158

Figure C.2: Stereographic projection of the evolution of the lattice plastic spin axis is shown for different values of bulk strain for the neighbor with a high m' relationship with respect to the active twin variant in the grain shown in figure C.1 159

Figure D.1: Laue patterns obtained from energy wire scans of (a) soft grain (unstrained condition through bend increment 3), (b) hard grain (unstrained condition through bend increment 4). The variation of reciprocal lattice vector magnitude with depth is shown for each bend increment. The plots on the third row of (a) and (b) show the intensity profiles as a function of the reciprocal lattice vector magnitude. The approximate locations in the grain interior used for the energy wire scans in the hard and soft grains are shown (marked in red) as insets in the intensity plots. The depths at which the subsurface grain boundary exists is shown by blue vertical lines in the Q v/s depth plots for both the hard and soft orientations. 163

Figure D.2: Local hydrostatic strain maps for the soft (left) and hard (right) grains, shown for bend increments 0 (unstrained state) to 3. The prisms indicating the orientations of the hard and soft grains with respect to the loading direction are also shown. 164

Figure E.1: Principal Stress direction map for the triple junction in region 3. The grain boundaries are delineated by black lines. Principal stress jacks corresponding to average stress tensor for each individual grain, along with their magnitudes and sense are also shown for comparison. 167

Figure E.2: Bend increment 2: Principal Stress distribution for the triple junction in region 5. 168

Figure E.3: Bend increment 2: Principal Stress distribution for the triple junction in region 4. 169

Figure F.1: Orientation and total GND density maps for regions 2, 3, 4 and 5, corresponding to the second bending increment. The voxels on either side of the grain boundary used for slip transfer parameter calculations are shown on the right of each orientation map. The Bunge Euler angles denoting the average grain orientations are also shown. Prisms denoting orientations are drawn from the perspective of the sample normal, with Y pointing up and X pointing to the right (coordinate system shown on the right side of image). The sample coordinate system is shown on the left hand side of image. The tensile direction is parallel to the Y direction. 171

Figure F.2: The Luster-Morris parameter plotted as a function of magnitude of residual Burgers vector for the LAGB (top row) and HAGB (bottom row) in region 1. Legends in the plots show the color/shape convention used to denote the interacting slip system in a voxel pair. This convention is followed for the subsequent plots. The symbol size for each datum point is scaled with the sum of the local Schmid factors for the interacting slip systems. 172

Figure F.3: LAGB in region 1 scaled by GND density: Left column shows $m'' = \frac{m'}{\max(\rho_{s\alpha}, \rho_{s\beta})}$ plotted as a function of $\max(\rho_{s\alpha}, \rho_{s\beta}) \times |b_{Residual}|$; while $m'' = \frac{m'}{\min(\rho_{s\alpha}, \rho_{s\beta})}$ as a function of $\min(\rho_{s\alpha}, \rho_{s\beta}) \times |b_{Residual}|$ plots are shown on the right column. Each plot corresponds to one of four transmitting slip systems considered. Four voxel pairs along the grain boundary are considered here. For each transmitting slip system type in each voxel pair, only the data points with the five highest local Schmid factor sums are plotted (A total of 20 plots per plot). The choice of the transmitting slip system is arbitrarily made as described in section 7.4.3. 178

Figure F.4: For four voxel pairs in the LAGB in region 1, each row of plots corresponds to the initiator slip system families with the *higher local Schmid factor* considered as the transmitting system, leading to more datum points in the pyramidal $\langle a \rangle$ slip system plot as initiators than other systems. For each initiating slip system family member in each voxel pair, only the datum points with the five highest local Schmid factor sums are considered. The number of data points plotted for each initiator slip system type are indicated. The number of datum points per slip system family for the plots scaled by maximum and minimum GND density (left and right columns respectively) are identical. 179

Figure F.5: For four voxel pairs in the LAGB in region 1, each row of plots corresponds to the initiator slip systems with the *lower GND density* is considered as the transmitting system, leading to more datum points in the basal and prism $\langle a \rangle$ slip system plot as initiators than when the Schmid factor is considered in figure F.4. For each voxel pair, only the data points with the five highest local Schmid factor sums are considered. The number of data points plotted for each initiator slip system type are indicated. 180

Figure F.6: LAGB region 1: m'' v/s scaled $|b_{Residual}|$ plots for the same data points shown in figure F.3, filtered using a criterion of $m' \geq 0.8$ 181

Figure F.7: LAGB region 1: m'' v/s scaled $|b_{Residual}|$ plots for the same data points shown in figure F.4, filtered using a criterion of $m' \geq 0.8$ 182

Figure F.8: LAGB region 1: m'' v/s scaled $|b_{Residual}|$ plots for the same data points shown in figure F.5, filtered using a criterion of $m' \geq 0.8$ 183

Figure F.9: Some instances of slip system interactions for basal, prism $\langle a \rangle$, pyramidal $\langle a \rangle$ and pyramidal $\langle c + a \rangle$ initiating systems for the LAGB voxels in region 1 are shown. The LSf values, which were calculated using the local stress tensor, and the Bunge Euler angles and m' values are noted. The size of the prisms is proportional to the sum of the LSf values of the sum of the Schmid factors for the slip system pair. Prisms are drawn from the perspective of the sample normal, with Y pointing upwards and X pointing towards the right. 184

Figure F.10: HAGB region 1: Scaled slip transfer parameter m'' plotted as a function of scaled residual Burgers vector. The methodology used to plot the data is identical to F.3. In this case the initiator in an interacting pair of slip systems is chosen arbitrarily as described in section 7.4.3.	185
Figure F.11: HAGB region 1: Scaled slip transfer parameter m'' plotted as a function of scaled residual Burgers vector, using the maximum of LSf as criterion for choosing the transmitting slip system.	186
Figure F.12: HAGB region 1: Scaled slip transfer parameter m'' plotted as a function of scaled residual Burgers vector, using the minimum of GND density as criterion for choosing the transmitting slip system.	187
Figure F.13: HAGB region 1: Same data as plotted in figure F.10: only points with $m' \geq 0.8$ are plotted here	188
Figure F.14: HAGB region 1: Same data as plotted in figure F.11: only points with $m' \geq 0.8$ are plotted.	189
Figure F.15: HAGB region 1: Same data as plotted in figure F.12: only points with $m' \geq 0.8$ are plotted.	190
Figure F.16: Using the minimum GND density criterion for the transmitting grain, m'' is plotted as a function of scaled residual Burgers vector magnitude for the boundary between the hard (beige) and soft oriented (blue) grains in region 2. Data plotted is for four pairs of voxels situated along the grain boundary. Only the top five points (sorted by descending order of sum of LSf values) per voxel pair are considered here. The locations of the points that correspond to a high likelihood of slip transfer are encircled.	191
Figure F.17: Using the minimum GND density criterion for the transmitting grain, m'' is plotted as a function of scaled residual Burgers vector magnitude; for the boundary formed by the two softer oriented grains (blue and purple) in region 2. This boundary has the lowest likelihood for slip transfer of the three. Data plotted is for four pairs of voxels situated along the grain boundary. Only the top five points (sorted by descending order of sum of LSf values) per voxel pair are considered here.	192
Figure F.18: Using the minimum GND density criterion for the transmitting grain, m'' is plotted as a function of scaled residual Burgers vector magnitude for the boundary between the hard beige and soft oriented purple grain in region 2. Data plotted is for four pairs of voxels situated along the grain boundary. Only the top five points (sorted by descending order of sum of LSf values) per voxel pair are considered here.	193

- Figure F.19: m' plotted as a function of $\max(\rho_{s_\alpha}, \rho_{s_\beta})$ and $\min(\rho_{s_\alpha}, \rho_{s_\beta})$, considering basal slip as the transmitting system. The transmitting slip system is chosen on the basis on minimum slip system specific GND density in voxel pair. The data plotted are from 12 grain boundaries encompassed by regions 1, 2, 3, 4 and 5. The envelope of data points for the $\max(\rho_{s_\alpha}, \rho_{s_\beta})$ case shows an inverse correlation between GND density and slip transmissibility are enclosed within the lines in each plot. The description of the symbol shape and color scheme of the data points is explained in section F.0.1 194
- Figure F.20: m' plotted as a function of $\max(\rho_{s_\alpha}, \rho_{s_\beta})$ and $\min(\rho_{s_\alpha}, \rho_{s_\beta})$, considering prism $\langle a \rangle$ slip as the transmitting system. The transmitting slip system is chosen on the basis on minimum slip system specific GND density in voxel pair. Data plotted from 12 grain boundaries encompassed by regions 1, 2, 3, 4 and 5. The envelope of data points for the $\max(\rho_{s_\alpha}, \rho_{s_\beta})$ case shows an inverse correlation between GND density and slip transmissibility are enclosed within the lines in each plot. 195
- Figure F.21: Bend increment 2: m' plotted as a function of $\max(\rho_{s_\alpha}, \rho_{s_\beta})$ and $\min(\rho_{s_\alpha}, \rho_{s_\beta})$, considering pyramidal $\langle a \rangle$ slip as the transmitting system. The transmitting slip system is chosen on the basis on minimum slip system specific GND density in voxel pair. Data plotted from 12 grain boundaries encompassed by regions 1, 2, 3, 4 and 5. The envelope of data points for the $\max(\rho_{s_\alpha}, \rho_{s_\beta})$ case shows an inverse correlation between GND density and slip transmissibility are enclosed within the lines in each plot. 195
- Figure F.22: Bend increment 2: m' plotted as a function of $\max(\rho_{s_\alpha}, \rho_{s_\beta})$ and $\min(\rho_{s_\alpha}, \rho_{s_\beta})$, considering pyramidal $\langle c + a \rangle$ slip as the transmitting system. The transmitting slip system is chosen on the basis on minimum slip system specific GND density in voxel pair. Data plotted from 12 grain boundaries encompassed by regions 1, 2, 3, 4 and 5. 196
- Figure G.1: Bend increment 2: Scaled slip transfer parameter plotted as a function of scaled residual Burgers vector magnitude for the first grain boundary (shown in the inset) constituting the triple junction in region 3 of microstructure described in 7.4.3. The choice of the transmitting slip system is made on the basis of minimum GND density of the voxel pair. 198
- Figure G.2: Bend increment 2: Scaled slip transfer parameter plotted as a function of scaled residual Burgers vector magnitude for the second grain boundary (shown in the inset) constituting the triple junction in region 3 of microstructure described in 7.4.3. The choice of the transmitting slip system is made on the basis of minimum GND density of the voxel pair. 199

Figure G.3: Bend increment 2: Scaled slip transfer parameter plotted as a function of scaled residual Burgers vector magnitude for the third grain boundary (shown in the inset) constituting the triple junction in region 3 of microstructure described in 7.4.3. The choice of the transmitting slip system is made on the basis of minimum GND density of the voxel pair. 200

Figure G.4: Bend increment 2: Scaled slip transfer parameter plotted as a function of scaled residual Burgers vector magnitude for the grain boundary in region 4 of microstructure described in 7.4.3. 201

Figure G.5: Bend increment 2: Bend increment 2: Scaled slip transfer parameter plotted as a function of scaled residual Burgers vector magnitude for the first grain boundary constituting the triple junction in region 5 of microstructure described in 7.4.3. Each column of plots correspond to slip system interaction at a grain boundary (inset). 202

Figure G.6: Bend increment 2: Bend increment 2: Scaled slip transfer parameter plotted as a function of scaled residual Burgers vector magnitude for the second grain boundary constituting the triple junction in region 5 of microstructure described in 7.4.3. Each column of plots correspond to slip system interaction at a grain boundary (inset). 203

Figure G.7: Bend increment 2: Bend increment 2: Scaled slip transfer parameter plotted as a function of scaled residual Burgers vector magnitude for the third grain boundary constituting the triple junction in region 5 of microstructure described in 7.4.3. Each column of plots correspond to slip system interaction at a grain boundary (inset). 204

Figure H.1: Schematic showing the transformation from the APS Beamline 34 Coordinate system to TSL-OIM coordinate system. The two systems can be brought into coincidence by rotating the APS system clockwise about the X axis by 135° . The transformation matrix (g_{TSL}^{34IDE}) is calculated from the direction cosines between the two coordinate systems. 206

Figure H.2: Schematic showing the transformation from the APS Beamline 1 Coordinate system to TSL-OIM coordinate system. The two systems can be brought into coincidence by rotating the APS system counter clockwise about the X axis by 90° . The transformation matrix (g_{TSL}^{ID1}) is calculated from the direction cosines between the two coordinate systems. 207

KEY TO ABBREVIATIONS

3DXRD three-dimensional X-ray Diffraction

APS Advance Photon Source

CP Crystal Plasticity

CP-Ti Commercial purity titanium

CRSS Critical Resolved Shear Stress

DAXM Differential Aperture X-ray Microscopy

EBS Electron Backscatter Diffraction

FFHEDM Far Field High Energy Diffraction Microscopy

GND Geometrically Necessary Dislocations

hcp hexagonal close packed

HEDM High Energy Diffraction Microscopy

Lsf Local Schmid factor

NFHEDM Near Field High Energy Diffraction Microscopy

OIM Orientation Imaging Microscopy

SAF Spatial Alignment Factor

SSD Statistically Stored Dislocations

XRD X-ray Diffracton

CHAPTER 1

INTRODUCTION

Titanium and its alloys find widespread use as structural materials due to their favorable strength to weight ratio. Bulk deformation behavior of metals can be sufficiently predicted by continuum based models that assume isotropic character. At the meso-scale however, mechanical behavior of crystalline materials is governed by their anisotropic character. Furthermore, in a polycrystal the morphology and stress state within each grain is strongly influenced by the deformation of its neighbors. This has major implications for bulk strength, texture evolution and room temperature formability. It is therefore imperative that material models at the meso scale are able to capture this heterogeneity in strain response.

1.1 Motivation for current work

Mesoscale mechanical response of individual grains in polycrystals is strongly dependent on the strain accommodation provided by the neighboring grains. Furthermore, conditions of local subsurface stress states that could lead to nucleation of mechanical twins are not well understood. Current crystal plasticity (CP) based material models that simulate mechanical behavior do not have a reliable means of predicting twin nucleation. In light of these observations, a true three-dimensional characterization of local stress state and morphology is necessary to reliably map structure property relationships. Development of such a body of knowledge has significant implications in material processing and furthering the understanding of damage nucleation. The electron backscatter electron diffraction (EBSD) method is a well known means to characterize the response of grains to local stress, but it only provides surface information. three-dimensional EBSD (EBSD tomography) can provide 3D characterization at spatial resolution of the order of tens of nanometers (Konijnenberg et al., 2015). This however, requires expensive focused ion beam (sequential serial sectioning); or Laser (sequential layer ablation) infrastructures. Moreover these methods are not non-destructive in nature. In this work, synchrotron based X-ray diffraction

is used to obtain three-dimensional characterization of polycrystals in a nondestructive manner at high spatial resolutions.

In addition to characterization of the three-dimensional morphology of the constituent grains, a second important question arises with regard to the local stress state and its effect on macroscale mechanical response. This necessitates the measurement of local grain orientations and stress states within a polycrystalline aggregate using reliable experimental techniques. Towards this end, the present work quantifies the capability of two different high energy x-ray diffraction methods (HEDM) in measuring grain orientations, positions and local stress states.

This work will help advance the understanding of the local stress state in polycrystalline aggregates. It is expected to help identify conditions where twin nucleation occurs by slip transmission across grain boundaries. Moreover, local grain averaged strain accommodation in the twin neighborhood is also assessed. Furthermore, a correlation is identified between the local stress state and the role of geometrically necessary dislocation (GND) density as an indicator of how strain is accommodated in polycrystalline materials.

1.2 Deformation systems in hexagonal titanium

Plastic deformation in crystalline materials is the result of atomic scale displacements brought about by slip mechanisms. At low homologous temperatures and strain rates, crystallographic slip is the predominant mechanism of deformation, while mechanical twinning is dominant at low temperatures and/or high strain rates. Hexagonal titanium has a c/a ratio of about 1.588, which is less than the ideal value¹. Under conditions where the loading direction is almost perpendicular to the c -axis (soft orientation), prism $\langle a \rangle$ slip is readily activated; whereas when the c -axis is inclined between 20° and 70° to the loading direction, basal $\langle a \rangle$ is favored. On the other hand, if the loading direction is close to being parallel to the c -axis (hard orientation) then pyramidal slip and mechanical twinning become favored –note that being favored does not imply that they occur as they have higher CRSS values, so this leads to complex deformation conditions. There is

¹The ideal c/a ratio for the hexagonal close packed lattice is ~ 1.633 .

some agreement that nucleation of twins is a stochastic event, although slip transfer across grain boundaries has been seen to nucleate twins in certain cases (Bieler et al., 2014; Wang, 2011).

1.3 High energy x-ray diffraction (HEXRD)

X-ray diffraction, specifically using high brilliance beams from synchrotron sources is a highly effective way for three-dimensional characterization of meso scale deformation in polycrystals. HEXRD methods enable non destructive characterization of samples in both in-situ and ex-situ configurations. In the current work, the HEXRD techniques used can be broadly classified into three types listed below.

1. Far field high energy diffraction microscopy (FF HEDM) , that uses a monochromatic beam
2. Near-field high energy diffraction microscopy (NF HEDM) using a monochromatic beam.
3. Differential aperture x-ray microscopy (DAXM), that uses white beam diffraction.

The first method is similar to powder diffraction (Poulsen, 2012), where each diffracting family of crystallographic planes from the polycrystal show up as Debye Scherrer rings. Provided the specimen has a coarse grain size, unique orientations can be identified with a resolution of 0.1° to 0.01° . Spatial resolution is $\sim 10 \mu\text{m}$, and grain averaged strain tensors can be evaluated with a resolution of 10^{-4} (Park et al., 2017). The depth resolution is of the order of a millimeter (Park et al., 2017).

The second method is conceptually similar to FF HEDM—the main difference here is in the sample to detector distance. In the case of NF HEDM this distance is much closer ($\sim 10 \text{ mm}$, compared to $\sim 1 \text{ m}$ for FF HEDM). This method is similar to a non-destructive 3D electron backscatter diffraction characterization of a polycrystalline aggregate using a line focused beam (Shastri et al., 2007; Park et al., 2017). This method is sensitive to orientation gradients—the angular resolution is in the 0.01° - 0.1° range, while the spatial resolution is of the order of units of microns (Park et al., 2017). Strain measurements however, cannot be made using this method.

The third method is based on Laue diffraction (Ice and Pang, 2009) using a highly collimated polychromatic beam. This method enables high spatial resolution and the ability to precisely measure the angles between Laue spots. Comparison of the changes in inter-spot angles with respect to the unstrained unit cell enables measurement of lattice distortion (Ice and Pang, 2009). Thus both lattice orientation and deviatoric strain can be extracted with sub-micron spatial resolution and angular resolution of the order of 0.01° . Furthermore, voxel specific values of local strain can be obtained with a resolution of 10^{-4} (Larson et al., 2008). Since micro Laue diffraction using a polychromatic beam does not yield the magnitude of the reciprocal lattice vectors, lattice dilatation cannot be evaluated using this procedure. An additional procedure enables the use of a monochromatic beam with a calibrated (known) energy that allows the estimation of the scattering vector magnitude that enables identification of the local hydrostatic component of the strain tensor. Therefore it is possible to obtain the full description of the local strain tensor using a combination of the two procedures.

In the present work, two polycrystalline specimens of commercial purity titanium (CP-Ti) were characterized using FF HEDM, NF HEDM and DAXM. The specimen evaluated with FF HEDM/NF HEDM had a hard crystallographic texture and the sample evaluated with DAXM had a predominantly soft texture with respect to the loading direction.

1.4 Structure of the dissertation

This dissertation is structured as follows. The current chapter provides an introduction to the work and the motivation behind the work. Chapter 2 provides a review of the literature and background that forms a basis for the present work. A detailed outline of the materials and methods used is elucidated in chapter 3.

Chapter 4 describes an in-situ far field study of deformation twin evolution in hexagonal titanium during a tensile test. Here, discrete twin-parent grain pairs are identified using geometrical and spatial proximity conditions. Local strain accommodation observed in parent and neighboring grains due to twin formation are discussed. A comparison is made between two different methods

used for post-processing (identification of individual grains) at different loading states of the specimen. A comparison is made between grains identified during the far field experiment and surface EBSD measurements. Additionally, the relative positions and morphology of the twinned and candidate triggering grains are examined in light of the more recently collected near field high energy diffraction microscopy (NF HEDM) data.

Chapter 5 provides a comparative statistical study between the FF HEDM and NF HEDM methods. Two algorithms for matching FF HEDM and corresponding NF HEDM data are discussed here. Furthermore, the relationship between reported grain radius values in FF HEDM and grain size calculated from number of constituent voxels in NF HEDM is explored. A quantitative comparison of the kinematics and grain averaged stress measurements from far field high energy diffraction microscopy (FF HEDM) is presented in chapter 6.

Chapter 7 details an in-situ Differential aperture X-ray microscopy (DAXM) characterization of a hexagonal titanium specimen subjected to a four point bending test. Local strain accommodation and propensity of slip transfer between adjacent grains are discussed. The change in magnitude and direction of local principal stress components are used to characterize the variation in stress state from grain interior to the boundary and surface.

Finally, conclusions and scope for future work are discussed in chapter 8.

CHAPTER 2

LITERATURE REVIEW

2.1 Basics of plastic deformation in crystalline materials

2.1.1 Crystallographic Slip

Plastic deformation by slip in crystalline materials is typically brought about by atomic scale displacements of line defects known as dislocations. These slip mechanisms are comprised of shear displacements and are lattice invariant i.e. despite shape change, the crystal structure remains as it was prior to deformation (Bhadeshia, 1996). Crystallographic slip takes place along specific planes and in specific directions (usually those with the highest atomic density). Dislocations are line defects, that cause local discontinuities in the natural atomic order of a crystal. A dislocation is a line in the plane that separates the slipped and the unslipped parts of the crystal. One way to visualize a dislocation is illustrated in figure 2.1, where an extra half plane of atoms is inserted into the top half of a perfect crystal (b). This would result in a displacement of one atomic spacing of the faces of the slot. The dislocation line DC locates the region where the perturbation of atoms from their normal positions is the most. As one moves away from the dislocation line, the extent of interatomic bond distortion decreases. The dislocation line DC shown in (b) is a positive edge dislocation and is commonly denoted by the \perp symbol. If the extra half plane of atoms was inserted in the bottom half of the crystal, DC would be a negative edge dislocation, denoted by \top .

In the case of screw dislocations, the relative displacement of one side of the crystal occurs parallel to AB. Schematics for left and right handed screw dislocations are shown in figure 2.1 (c) and (d) respectively. Screw dislocations can be represented as a single surface helicoid (Hull and Bacon, 2011) as shown in figure 2.1 (f). In general, dislocations are of mixed character (they can be decomposed into edge and screw components).

The direction and magnitude of shear of a dislocation is denoted by the Burgers vector. One

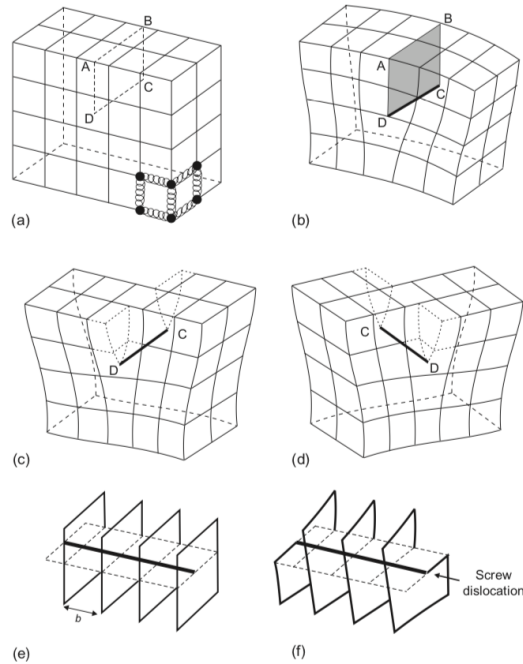


Figure 2.1: Schematic showing the geometry of edge and screw dislocations in a simple cubic lattice. (a) perfect lattice, (b) an extra half-plane of atoms ABCD inserted into the top half of the crystal. DC is a positive edge dislocation, (c) left handed screw dislocation DC is formed by displacement of the faces ABCD relative to each other in the direction AB, (d) right handed screw dislocation DC, (e) atomic planes with spacing b in a perfect crystal, (f) planes distorted by a right-handed screw dislocation. (Hull and Bacon, 2011)

important feature of distinction between edge and screw dislocations is that the direction of the Burgers vector is normal to the edge dislocation line; whereas it is parallel to the screw dislocation line. A combination of a slip plane normal and slip direction (direction of Burgers vector) constitute a slip system.

2.1.2 Schmid's law for slip in a single crystal

The criterion for determining if a slip system will be activated in a single crystal is given by Schmid's law. Schmid proposed that a single crystal subjected to uniaxial load would begin to deform only when the resolved shear stress exceeds a critical value. The concept of resolved shear stress is illustrated in figure 2.2 using a schematic of a cylindrical single crystal of cross sectional area A under a uniaxial tensile load F . The angle between the F and slip plane normal is denoted

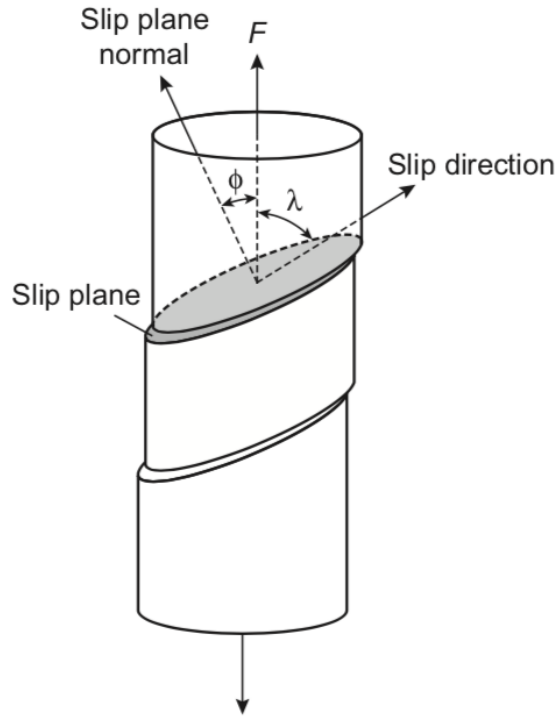


Figure 2.2: Schematic illustrating the concept of critical resolved shear stress for a single crystal (Hull and Bacon, 2011). It is important to note that in general ϕ and λ are not coplanar.

by ϕ , while the angle between F and slip direction is denoted by λ (Hull and Bacon, 2011). The equation for the shear stress resolved in the direction of slip is given as follows.

$$\tau = \frac{F}{A} \cos\phi \cos\lambda \quad (2.1)$$

If in equation 2.1, the force term is substituted by the tensile force necessary to initiate slip F_c , then τ becomes τ_c . This minimum value of shear stress, required to initiate plastic deformation is defined as the critical resolved shear stress (CRSS). The product $\cos\phi \cos\lambda$ is called the Schmid factor (m). For a single crystal subjected to a uniaxial tensile load, the maximum value of Schmid factor is 0.5. Clearly, the most active slip systems will have a higher value of m .

2.1.3 Multiplication of dislocations

Dislocations multiply in the bulk of a crystal by regenerative multiplication mechanisms such as a Frank-Read type source (Hull and Bacon, 2011). A Frank-Read source is activated when a critical

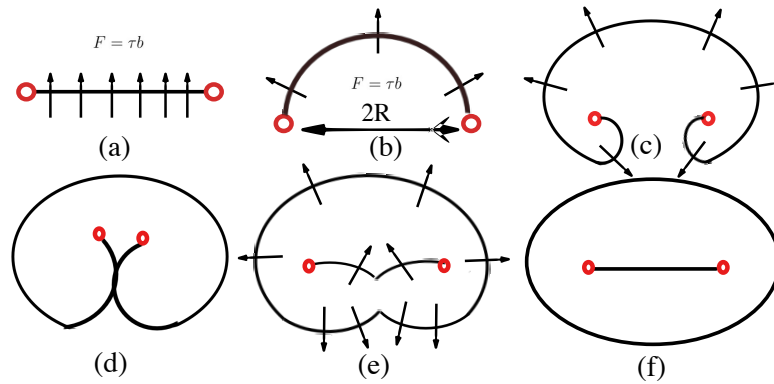


Figure 2.3: Schematic showing the process of regenerative multiplication of dislocations by a Frank-Read source [adapted from Read (1953)].

shear stress is reached that causes a dislocation pinned between two pinning points to bow out into a dislocation loop that can escape from the pinning points. An example of a Frank-Read source is schematically shown for an edge dislocation in figure 2.3. Figure 2.3 (a) shows the segment of dislocation pinned at its two ends by obstacles (which could be dislocation interactions or nodes, jogs, precipitates etc.). The direction of the force acting on the dislocation, $F = b \cdot \tau$ is shown by the arrows, where b is the Burgers vector and τ is the shear stress. As a result of this force the dislocation bows out (figure 2.3 (b)). In order to arrive at the critical configuration of a semi-circle a maximum shear stress $\tau_{max} = Gb/R$, where R is the critical radius of curvature. As the stress exceeds τ_{max} , the radius of curvature becomes smaller and the dislocation becomes unstable and continues to bow out. Figure 2.3 (c) shows the bowing shortly before the curved portions of the segment come in contact with each other. The parts that touch each other annihilate because their Burgers vectors have opposite sign for the same line direction (figure 2.3 (e)). Finally a strain dislocation segment and a loop remain in the stable configuration (figure 2.3 (f)). Under the applied stress the loop will expand and encounter other obstacles. Then the process (a)-(f) repeats.

2.1.4 Generalized Schmid Factor

The Schmid law applies to conditions where the stress tensor has only one non-zero diagonal component and zeroes in off-diagonal components. Because neighboring grains usually deform

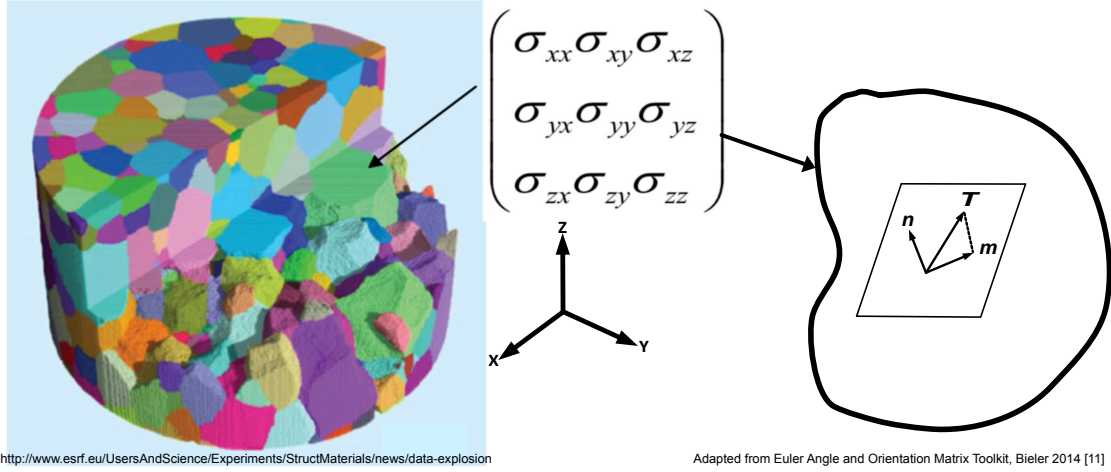


Figure 2.4: Illustration of generalized stress state for an arbitrary grain in a polycrystal. The local stress tensor corresponding to this generalized stress state is shown as a function of X, Y and Z. T is the traction vector, while n and m are the slip plane normal and slip direction respectively.

heterogeneously (Ashby, 1970), the stress state becomes more complicated as shown in figure 2.4. Even though the imposed global load may be uniaxial, the local stress state for an arbitrary grain may have non-zero off diagonal components. The local stress tensor, slip direction and the slip plane normal are used to derive a generalized Schmid factor (Soare, 2014). For a general stress tensor, the maximum possible magnitude of the local Schmid factor is $\frac{\sqrt{2}}{2}$ (~ 0.707) (Bieler, 2014).

As shown in figure 2.4, the local stress tensor σ acts on an arbitrary grain in the polycrystalline aggregate. The traction vector T acting on a unit area on an arbitrary plane is given as follows.

$$T = \sigma n \quad (2.2)$$

where n is the unit plane normal vector. Crystallographic slip is typically expressed in the crystal coordinate system. The first step in this process is to rotate the stress tensor onto the crystal coordinate system as shown below.

$$\sigma' = R^T \sigma R \quad (2.3)$$

where σ' is the rotated stress tensor and $R = g^T$ is the transpose of the orthogonal orientation matrix derived from the crystal orientation.

The shear stress τ acting on the plane defined by n in the direction of slip m is given by:

$$\tau = \mathbf{T} \cdot \mathbf{m} = \boldsymbol{\sigma}' \mathbf{n} \cdot \mathbf{m} = \boldsymbol{\sigma}' : \mathbf{n} \otimes \mathbf{m} = \boldsymbol{\sigma}' : \frac{1}{2}(\mathbf{n} \otimes \mathbf{m} + \mathbf{m} \otimes \mathbf{n}) \quad (2.4)$$

where \mathbf{m} is the slip direction parallel to the Burgers vector.

Now if $\mathbf{P} = \frac{1}{2}(\mathbf{n} \otimes \mathbf{m} + \mathbf{m} \otimes \mathbf{n})$, equation 2.4 can be rewritten as:

$$\tau = \boldsymbol{\sigma}' : \mathbf{P} = \sigma'_{ij} P_{ij} \quad (2.5)$$

If the stress tensor is now normalized i.e. $\|\boldsymbol{\sigma}'\| = 1$, then equation 2.5 gives the generalized Schmid factor that has to be evaluated for every slip system in order to determine which slip systems are most favored for slip.

For polycrystalline materials, Sachs (Sachs, 1928) was the first to suggest a way to estimate a composite Schmid factor by assuming that only one slip system is active per grain and then averaging the Schmid factor values for all individual grains in the specimen. Since no constraint is imposed on the deformation of individual grains by neighboring grains, this approach gives a lower bound for the yield strength in uniaxial tension (Sachs, 1928).

Taylor proposed a model based on the von Mises criterion—which requires that at least five independent slip systems must be active in order to ensure strain compatibility among the constituent grains in a polycrystal (Taylor, 1938). The assumption made here is that these five systems correspond to the least amount of work during the arbitrary shape change of the aggregate. Taylor's assumption can therefore be formalized as follows:

$$\begin{aligned} \sigma d\epsilon &= \tau_c \sum_i d\gamma_i \\ \sigma &= \tau_c \frac{\sum_i d\gamma_i}{d\epsilon} = \frac{1}{m} \tau_c, \end{aligned} \quad (2.6)$$

where, σ and $d\epsilon$ are the macroscopic stress and strain increment in the uniaxial test and $\sum d\gamma$ is the summation of strain increments over all the active slip systems. $\frac{1}{m}$ is the reciprocal of the Schmid factor.

2.1.5 Deformation twinning

Twinning is a secondary deformation mechanism that is common in low symmetry metals and alloys (Christian and Mahajan, 1995). Twinning modes are activated when deformation by slip alone does not provide an adequate number of independent slip systems for shape change. In deformation twinning, reorientation of the parent lattice occurs by coordinated atomic displacements that are equivalent to simple shear, whereby the original volume of the crystal is preserved (Bilby and Crocker, 1965). This requirement of simple shear necessitates that the atomic displacements are an integral fraction of the lattice points¹ (Christian and Mahajan, 1995). This also ensures that the crystal symmetry is retained for twin formation, where the crystal structure of the parent lattice is preserved in the twin. This is in contrast to other shear transformation processes such as martensite formation, where either the crystal structure or the c/a ratio changes in the transformed lattice (Such a transformation does not require the atomic displacements to be a rational fraction of the lattice points).

Figure 2.5 shows the four basic elements of a deformation twin. κ_1 is the invariant plane of shear and the corresponding shear direction is η_1 . The second undistorted plane is κ_2 and the conjugate shear direction η_2 is given by the intersection of κ_2 and the plane of shear P . Fixing κ_1 and η_2 ; or κ_2 and η_1 defines a twinning mode (Christian and Mahajan, 1995).

Twins are classified as type I, type II or compound—depending on which of the four basic elements are rational. For type I twins, κ_1 and η_2 constitute a rational plane and rational direction respectively of the parent lattice. In type II twins, κ_2 and η_1 form the rational plane and direction respectively. For compound twins, all the four crystallographic elements are rational (Christian and Mahajan, 1995).

¹The displacements are multiples of a rational number $\frac{P}{Q}$, where P and Q are integers.

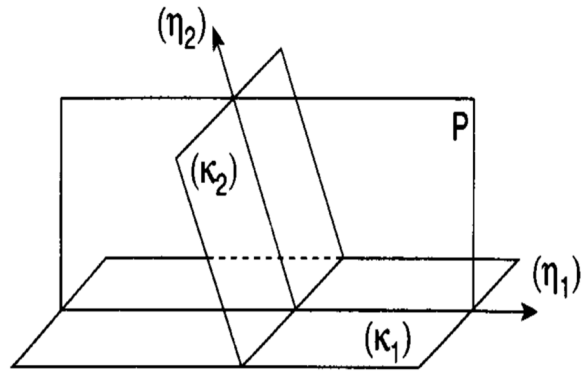


Figure 2.5: Schematic showing the four twinning elements (Christian and Mahajan, 1995). κ_1 and κ_2 are twinning and conjugate planes respectively. The corresponding twinning and conjugate directions are η_1 and η_2 . η_1 , η_2 , and the normals to κ_1 and κ_2 lie in shear plane P .

2.2 Plastic deformation in hexagonal titanium

Hexagonal titanium has a less than the ideal c over a ratio (~ 1.588). The most readily activated slip plane is prism, followed by basal, both having the $\langle a \rangle$ type Burgers vector (Lütjering and Williams, 2007). Due to lower symmetry compared to cubic metals, the slip modes for plastic deformation in hexagonal titanium are strongly dependent upon the orientation of the loading direction with respect to the c -axis. When basal or prism slip systems are active, the grain is in a "soft" orientation, but when they are not easily activated the crystal is in a "hard" orientation (Wang et al., 2010a; Littlewood et al., 2011). Figure 2.6 illustrates the major planes and slip directions (a), and the relevant slip modes (b) that are associated with them (Wang, 2011).

According to Paton et al. (Paton et al., 1973), basal slip ($\{0001\}\langle 11\bar{2}0 \rangle$) and prismatic slip ($\{10\bar{1}0\}\langle 11\bar{2}0 \rangle$) have historically been considered the most important deformation modes in pure alpha titanium. Levine Levine [1966] determined that prism $\langle a \rangle$ slip in the temperature range 0-210 K was activated by overcoming the Peierls barrier. Non-basal $\langle c + a \rangle$ slip was reported as a major deformation mode in Ti-Al alloys by Cass (Cass, 1970). Furthermore Paton, and Backofen (Paton and Backofen, 1970) found that mechanical twinning in pure titanium can occur at any temperature, and is therefore an important mode of plastic deformation.

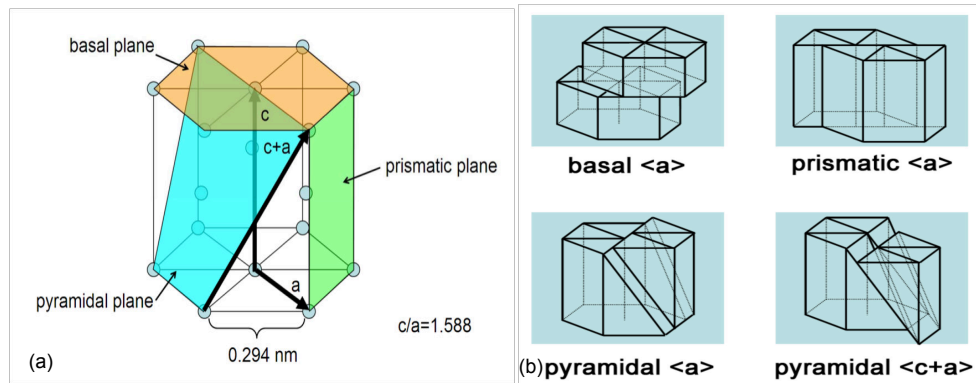


Figure 2.6: Schematic illustrating the major crystallographic planes and directions (a) , and the slip modes (b) associated with them (adapted from Wang (2011)).

More recently, micropillar compression tests conducted on commercial purity titanium (CP-Ti) specimens oriented in the $[2\bar{1}\bar{1}0]$ direction confirm prism $\langle a \rangle$ slip to be the primary slip mode (Kishida et al., 2020). For specimens oriented along the $[0001]$ direction first order pyramidal $\langle c + a \rangle$ slip is observed. Calculations using inverse-power law relationship show that the CRSS values for first order pyramidal $\langle c + a \rangle$ slip is higher than those of any other active slip modes at room temperature (Kishida et al., 2020).

The primary slip directions in hexagonal titanium are the three $\langle 11\bar{2}0 \rangle$ ($\langle a \rangle$) vectors. These lie on three families of crystallographic planes– $\{0001\}$ planes; three $\{10\bar{1}0\}$ and six $\{10\bar{1}1\}$ planes. Out of the twelve slip systems, only eight are independent. Furthermore, the shape changes effected by slip systems $\{0001\}\langle 11\bar{2}0 \rangle$ and $\{10\bar{1}0\}\langle 11\bar{2}0 \rangle$ combined are equivalent to the $\{10\bar{1}1\}\langle 11\bar{2}0 \rangle$ slip system, only four of which are independent. (Lütjering and Williams, 2007).

Even when basal and prism slip are active, they do not satisfy the von Mises criterion, where a minimum of five independent slip systems are needed to effect an arbitrary shape change by plastic deformation (prism and basal slip do not enable a shape change along the the $\langle c \rangle$ axis direction) (Lütjering and Williams, 2007). Therefore, pyramidal $\langle c + a \rangle$ slip and deformation twinning are often observed (Yu et al., 2013). These systems allow changes in the crystal dimension along the

Table 2.1: Parameters associated with the four twinning modes in CP-Ti (Wang, 2011)

Mode	κ_1	η_1	κ_2	η_2	s	Misorientation ²
T1 ³	$\{10\bar{1}2\}$	$\langle\bar{1}011\rangle$	$\{\bar{1}012\}$	$\langle10\bar{1}1\rangle$	$\frac{(\gamma^2-3)}{\sqrt{3}\gamma}=0.174$	85°
T2	$\{11\bar{2}1\}$	$\langle\bar{1}\bar{1}26\rangle$	$\{0001\}$	$\langle11\bar{2}0\rangle$	$\frac{1}{\gamma}=0.630$	35°
C1 ⁴	$\{11\bar{2}2\}$	$\langle11\bar{2}3\rangle$	$\{11\bar{2}4\}$	$\langle22\bar{4}3\rangle$	$\frac{2(\gamma^2-2)}{3\gamma}=0.219$	65°
C2	$\{10\bar{1}1\}$	$\langle10\bar{1}\bar{2}\rangle$	$\{10\bar{1}\bar{3}\}$	$\langle30\bar{3}2\rangle$	$\frac{(4\gamma^2-9)}{4\sqrt{(3)\gamma}}=0.099$	54°

$\langle c \rangle$ axis, though they are less readily activated. It has been observed that the density of twins in commercial purity titanium (CP-Ti) increased significantly with increasing strain rates, strain and decreasing temperature (Christian and Mahajan, 1995; Nemat-Nasser et al., 1999).

Four twinning modes have been observed in hexagonal titanium. T1 and T2 accommodate extension along the c-axis (extension twins), and C1 and C2 accommodate contraction along the c-axis (compression twins). The c/a ratio (referred to as γ in table 2.1) is used to calculate the shear s evolved due to a twinning mode. Table 2.1 summarizes the important parameters associated with the four twin modes. Because the CRSS for $\langle c + a \rangle$ pyramidal slip is higher than twins, twins can be activated when the crystal is in a hard orientation (Littlewood et al., 2011; Britton et al., 2015).

Akhtar and Teghtsoonian (1975) observed a three-stage hardening behaviour during plastic deformation of single crystal titanium. More recently, Chichili et al. (1999) showed that for hexagonal titanium, although dislocation motion accounted for most of the plastic deformation, twin-dislocation interactions play an important role during strain hardening at room temperature. Therefore mechanical twinning can have a strong influence on macroscopic properties like ductility in hexagonal titanium

T1 twins ($\{10\bar{1}2\}\langle\bar{1}011\rangle$) in titanium are also activated when extension along the c-axis is required. The geometrical orientation relationship between a T1 twin and its parent lattice are shown in figure 2.7, where the c-axis misorientation is 85° about the $[11\bar{2}0]$ axis. Moreover, the

²c-axis misorientation between twin and parent lattice

³T: Extension twin

⁴C: Compression twin

parent and the twin lattices share a common $\langle a \rangle$ axis. Twinning provides a necessary response to strain compatibility and has been shown to enable higher ductility in hexagonal metals (Christian and Mahajan, 1995). The exact mechanism behind twin nucleation is complex and is not clearly understood. Prior work (Capolungo et al., 2009; Beyerlein and Tomé, 2010; Bieler et al., 2014) has shown that twinning does not necessarily obey the Schmid law. It is also observed, that in hexagonal titanium, the twin variant activated does not always correspond to the highest resolved shear stress. In their study on deformation twinning in hexagonal titanium, Richeton et al. (2012) observed that although all active variants had relatively high Schmid factors (>0.38), the active twins did not necessarily correspond to the highest Schmid factor among the possible variants. Schuman et al. (2011, 2012) proposed a variant selection criterion for T1 and C1 twins in T40 titanium, based on deformation energy required for nucleation. This criterion was found to account for 85% of the observed variants. It has been observed that deformation twinning plays an important role in enhancing ductility in hexagonal metals. Dislocations at twin boundaries result in strain relaxation and lowering of energy of the crystal (Kochmann and Le, 2009). From the standpoint of material processing, room temperature formability of hexagonal metals is still a significant challenge. Therefore, it is important to understand the relationship between energy dissipation from twin formation and strain relaxation in the parent and neighboring grains. Moreover, several previous studies have confirmed that deformation twins in hexagonal metals nucleate at grain boundaries (Wang et al., 2009a; Beyerlein and Tomé, 2010; Christian and Mahajan, 1995). Therefore, their role in strain accommodation is of particular interest in further developing the understanding of intergranular crack nucleation.

Nucleation and growth of deformation twins in titanium is strongly dependent upon the loading conditions; which can be more complex than simple monotonic loading when practical structural applications or material processing operations are considered. Such complexity in loading conditions can effect further changes within an already formed twin (Wang et al., 2014; Guan et al., 2021). For example, removal or reversal of the direction of a monotonic load can result in detwinning, thereby reducing the twinned volume. Moreover, under conditions where the loading is not

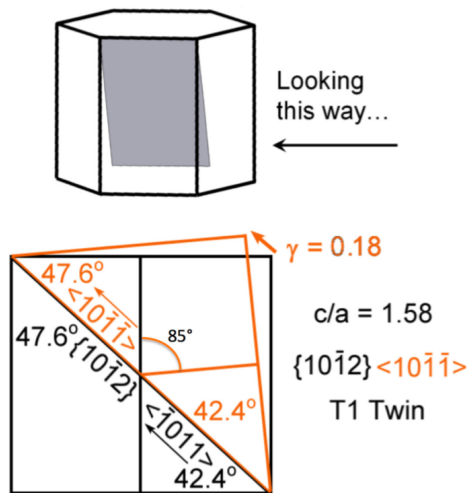


Figure 2.7: Schematic illustrating the geometrical relationship between a T1 twin and its parent lattice. Adapted from (Bieler et al., 2014).

monotonic, new twins can form inside an existing twin (a phenomenon known as double twinning) (Xu et al., 2018; Huang et al., 2019). More recently the kinematics and local stress evolution in parent and twin grains in polycrystalline magnesium during a compression tension experiment were studied in detail by Louca et al. (2021), using 3D Xray diffraction. It was observed that detwinning was typically associated with reversal of sign in the resolved shear stress associated with the active variant.

As mentioned earlier, the interactions of twins and dislocations play an important role in strain hardening of hexagonal titanium. In terms of physics based modeling of deformation behavior, commonly used crystal plasticity (CP) based schemes consider twinning as directionally constrained slip systems (Kalidindi, 1998). Detailed studies of the stress and strain rates associated with a nucleating twin are a subject of current investigations. Spatially resolved models for twin nucleation and propagation have been developed recently for hexagonal and orthorhombic crystal structures (Ardeljan et al., 2015; Guo et al., 2017; Cheng and Ghosh, 2017). Furthermore, numerical studies of the stress field around deformation twins in magnesium have also been conducted (Arul Kumar et al., 2015). Most of these mesoscale models are based on crystal plasticity (CP) principles that use finite element or spectral based solvers. In most of these models, the underlying physics of plastic

deformation is typically captured by the phenomenological power law. In its basic formulation the phenomenological model takes into account the kinematics of elasto-plastic deformation with the evolving critical resolved shear stress as a state variable. Moreover, interactions between slip and twin systems can also be considered. A more sophisticated physical basis is to use the dislocation density as the state variable, which is implemented in the microstructure based formulation. More recently, Wronski et al. used a visco-plastic self-consistent (VPSC) model to simulate the evolution of $\{10\bar{1}2\}$ tensile and $\{11\bar{2}2\}$ compression twinning in hexagonal titanium. Additionally this model also incorporated a simple Monte Carlo scheme to predict variant selection (Wronski et al., 2018).

2.3 An overview of crystal plasticity principles

In this section the basics of deformation kinematics and its application to constitutive relations governing crystal plasticity (CP) are reviewed. A fundamental quantity in the CP formulation is the deformation gradient. The concept of the deformation gradient is illustrated in figure 2.8. The position vector of a material point in a body in the reference configuration is represented by dx . The vector can be mapped in the deformed (current) configuration by $dy = dx + du$, where du is the differential total displacement vector (Roters et al., 2010). The current and reference configuration vectors are related by the deformation gradient as follows.

$$dy = \left(\frac{\partial y}{\partial x} \right) dx = \left(\mathbf{I} + \frac{\partial u}{\partial x} \right) dx = \mathbf{F} dx \quad (2.7)$$

Where \mathbf{I} denotes the identity tensor of rank 2. Therefore the deformation gradient \mathbf{F} can be defined as a second order tensor that maps the displacement of a material point from the undeformed (reference) state to the deformed (current) state. Since the deformation gradient is an indicator of shape change, \mathbf{F} can be expressed as the product of pure rotation \mathbf{R} and a symmetric tensor that captures pure stretching. This can be represented in two ways ,depending on the order of operation.

$$\mathbf{F} = \mathbf{R}\mathbf{U} = \mathbf{V}\mathbf{R} \quad (2.8)$$

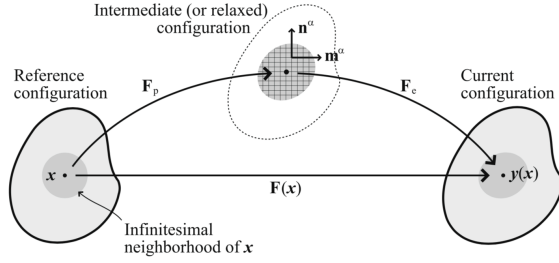


Figure 2.8: Schematic illustration of the concept of deformation gradient. The total deformation gradient F can be decomposed into the product of the elastic and the plastic components (Roters et al., 2010).

Where U and V are the symmetric right and left stretch tensors respectively. A fundamental constitutive premise in crystal plasticity is the multiplicative decomposition of the total deformation gradient into elastic and plastic components as follows.

$$\mathbf{F} = \mathbf{F}_e \mathbf{F}_p \quad (2.9)$$

where \mathbf{F}_e and \mathbf{F}_p are respectively the elastic and plastic components of the deformation gradient. As shown in figure 2.8, the elastoplastic deformation from the reference configuration can be considered to occur in two stages. The first stage is the intermediate (relaxed) configuration, that corresponds to the irreversible (plastic) response. This deformation, captured by \mathbf{F}_p remains even after all external forces and displacements causing it are removed. From this configuration, the elastic deformation corresponding to \mathbf{F}_e is imposed to arrive at the current (deformed) configuration. This two stage breakdown is a theoretical construct; as in reality the intermediate configuration would require that the dislocations causing shape change would not reside within the material point neighborhood (Roters et al., 2010).

The rate of evolution of plastic deformation can be expressed as follows.

$$\dot{\mathbf{F}}_p = \mathbf{L}_p \mathbf{F}_p \quad (2.10)$$

If dislocation slip is the only mode of plastic deformation, the velocity gradient L_p may be expressed as the sum of the shear rates on all active slip systems (Roters et al., 2010).

$$L_p = \sum_{\alpha=1}^n \dot{\gamma}^{\alpha} \mathbf{m}^{\alpha} \otimes \mathbf{n}^{\alpha} \quad (2.11)$$

where \mathbf{m}^{α} and \mathbf{n}^{α} are respectively the unit slip direction and slip plane normal vectors corresponding to slip system α ; $\dot{\gamma}^{\alpha}$ is the shear rate corresponding to slip system α . The summation is made over the total number of active slip systems n .

A constitutive model for deformation typically relates the shear rate to the external stress and microstructural states of the material. There are two distinct approaches to developing constitutive models—phenomenological and microstructure based. The former approach considers critical resolved shear stress (CRSS) as a state variable for each slip system. The latter approach uses the dislocation density as state variable to calculate flow rate.

In the phenomenological treatment, the shear rate is formulated as a function of the resolved shear stress (RSS) and the evolution of material state is related to the total shear and the shear rate (Roters et al., 2010). Rice (Rice, 1971) proposed a formulation on this basis for face centered cubic materials, where the kinetic law on a slip system, relating the shear rate to the RSS τ^{α} and slip resistance τ_c^{α} is given as follows.

$$\dot{\gamma}^{\alpha} = \dot{\gamma}_0 \left| \frac{\tau^{\alpha}}{\tau_c^{\alpha}} \right|^{\frac{1}{m}} \text{sgn}(\tau^{\alpha}) \quad (2.12)$$

In equation 2.12, $\dot{\gamma}_0$ and τ_c^{α} are material parameters.

The phenomenological model also accounts for the hardening caused by the interaction of a fixed slip system α with other slip systems (β) (Roters et al., 2010).

$$\begin{aligned} \tau_c^{\alpha} &= \sum_{\beta=1}^n h_{\alpha\beta} |\dot{\gamma}^{\beta}| \\ h_{\alpha\beta} &= q_{\alpha\beta} \left[h_0 \left(1 - \frac{\tau_c^{\beta}}{\tau_s} \right)^a \right] \end{aligned} \quad (2.13)$$

Here $h_{\alpha\beta}$ is known as the hardening matrix and it relates the influence of slip system β to system α . $q_{\alpha\beta}$ is called the latent hardening parameter, commonly taken to be 1.0 for co-planar slip systems and 1.4 otherwise.

The formulations in equations 2.11, 2.12 and 2.13 can be adapted to account for mechanical twinning as shown by Kalidindi [1998]. In this case, the twinned region is identified by its volume fraction and appropriate boundary conditions are used. The effect of twinning is added as an additional component by taking advantage of the analogy between slip and twin systems (Roters et al., 2010).

A more physically realistic constitutive model for plastic deformation would use dislocation density as the critical internal variable. Furthermore, a full characterization of the microstructure requires specification of other variables such as grain size and shape, second phase fractions and precipitate morphology (Roters et al., 2010). Naturally the complexity of the model increases with the addition of more parameters; currently used models have incorporated only a few of them. Ma and Roters [2004] proposed a model based on the density of mobile dislocation ρ_m^α that glide among the slip system α in order to accommodate plastic deformation. In order to accomplish this they have to overcome the stress fields due to parallel dislocations (that cause the passing stress) and forest dislocations that inhibit their motion, for each slip system α . Accordingly, for face centered cubic crystals the total dislocation density can be decomposed into the parallel (glide, ρ_p^α) and forest components (ρ_F^α). This is related to the density of immobile (statistically stored) dislocations (ρ_{SSD}^β) by an interaction term $\chi_{\alpha\beta}$ (Roters et al., 2010) as follows.

$$\rho_F^\alpha = \sum_{\beta=1}^N \chi_{\alpha\beta} \rho_{SSD}^\beta |\cos(n^\alpha, t^\beta)| \quad (2.14)$$

$$\rho_P^\alpha = \sum_{\beta=1}^N \chi_{\alpha\beta} \rho_{SSD}^\beta |\sin(n^\alpha, t^\beta)| \quad (2.15)$$

Where β is the slip system interacting with α , n^α is the plane normal of slip system α , and t^β is the line direction corresponding to slip system β . It is important to mention that only edge

dislocations are considered in the formulations shown in equations 2.14 and 2.15, due to their limited out of plane mobility (Roters et al., 2010).

The relationship between the shear rate and density of mobile dislocations can be expressed by the Orowan equation.

$$\dot{\gamma}^\alpha = \rho_m^\alpha b v^\alpha \quad (2.16)$$

Here, b is the magnitude of the Burgers vector and v is the average velocity of the mobile dislocations. The interaction strength term accounts for mutual interactions between slip systems α and β i.e. self interaction, co-planar interaction, cross-slip and Lomer Cottrell lock (Roters et al., 2010).

An important distinction can be made between local and non-local constitutive models. In local models, the state variables of a material point are not related to its neighboring points. Such a scheme is adequate for prediction of stress-strain curves for texture in polycrystalline materials. They are however, not as effective in predicting deformation behavior when the simulation scale becomes considerably smaller, as in nanoindentation or micropillar compression (Roters et al., 2010). In this situation, it is important to account for the relationship between grain size and plastic deformation. Non-local models that relate state variables between a material point to its neighbors are more suitable in these instances. The grain size dependence on flow stress is empirically given by the well known Hall-Petch relation (Petch, 1953; Dieter, 2011).

An increase in flow stress with decreasing grain size is often attributed to an increase in pile up of mobile dislocations, which in turn act as pinning sources for dislocations moving on other planes. The average pinning distance of dislocations is inversely proportional to the square root of dislocation density. Therefore, as the pinning distance decreases, the high dislocation density in turn increases the stress required to operate a Frank-Read source and induce further plastic deformation. Therefore pileups of dislocations act as barriers to plastic deformation. It is typically observed that such pileups accumulate at grain boundaries, suggesting that they are strongly correlated with local orientation gradients and contribute towards lattice curvature. In this context the dislocations

associated with these pileups are deemed as geometrically necessary. The analysis of geometrically necessary dislocations (GND) is a focus of the present work; their presence is predicated on the hypothesis that impeded dislocation systems contribute towards pileups. In this analysis, the primary focus is on local accumulation of GNDs, and their long range effect on strain fields (non-local effects) are not considered. Details of the mathematical basis for the GND density calculation methodology used in this work are discussed in section 2.6.

2.4 Slip transfer and dislocation interactions at grain boundaries

At the microscopic level, a flaw can nucleate in a material when the local strain is unable to accommodate changes in geometry (Bieler et al., 2009). In polycrystalline materials, these local accommodations to shape change often occur at and near grain boundaries. This response to mechanical loading is strongly dependent upon the deformation mechanism (crystallographic slip, twinning etc); and the local strain accommodation by the neighborhood of an individual crystallite. Strain transfer across interfaces can occur by the transmission of dislocations. Livingston and Chalmers [1957] studied heterogeneous strain evolution in aluminum bicrystals and observed that on most of the slip systems, dislocations accumulate at the grain boundary. If a grain boundary hinders the movement of a dislocation associated with a particular slip system, the dislocations pile up against the boundary. A schematic representation of this phenomenon for a bicrystal (following Livingston and Chalmers) is shown in figure 2.9. Such pileups are associated with large stress concentrations at the grain boundaries. Furthermore, slip activation in the neighbor occurs when these stress concentrations activate dislocation sources in the adjacent crystal. Bieler et al. [2009] categorized three distinct types of deformation transfer that can occur across a grain boundary.

1. the grain boundary behaves as an opaque barrier that hinders transmission of slip systems. As a result of this additional intragranular slip systems activate in order to facilitate strain accommodation (Zaefferer et al., 2003).
2. the grain boundary is an imperfect barrier to dislocation. It allows partial transmission of slip across it and residual dislocations are left behind.

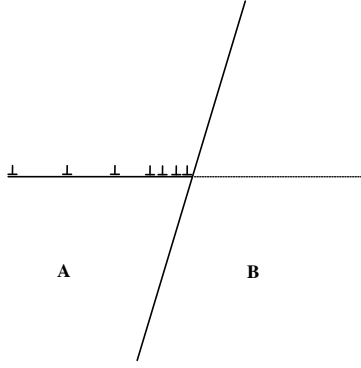


Figure 2.9: Illustration of dislocation pileup at a grain boundary between two crystals *A* and *B*. Dislocations shown here are edge type; in reality they are a combination of both edge and screw types. Adapted from Livingston and Chalmers [1957]

3. the grain boundary allows slip transmission without (nearly) any hindrance. Such boundaries provide little or no resistance to deformation.

From the above observations it is clear that slip transmission is most efficient for low angle grain boundaries (LAGB) and high coincident site lattice (low Σ) boundaries. More recently, Di Gioacchino et al. [2020] showed that strain transfer can also occur in high angle grain boundaries (HAGB) by local lattice rotations.

Several metrics have been used in order to assess the degree of slip transmissibility across grain boundaries. Most of these metrics use the geometry of the interacting slip systems to quantitatively determine the propensity for slip transfer. Livingston and Chalmers developed the following parameter that can be used to quantify slip transmissibility.

$$N = (e_{in} \cdot e_{out}) * (g_{in} \cdot g_{out}) + (e_{in} \cdot g_{out}) * (e_{out} \cdot g_{in}) \quad (2.17)$$

In equation 2.17, e and g refer to the slip plane normal and slip direction respectively. The subscripts "in" and "out" refer to the grains corresponding to the incoming and outgoing slip systems respectively. The second term on the right hand side of the equation 2.17 must be minimized for ease of slip transfer (Livingston and Chalmers, 1957; Kacher et al., 2014). For example, in the ideal case, where the geometry is perfectly aligned for slip transfer, the second term in equation 2.17 vanishes. The parameter proposed by Livingston and Chalmers (equation 2.17) is poorly correlated with experimental observations (Di Gioacchino et al., 2020).

The magnitude of the Burgers vector of the residual dislocation is another commonly used measure of slip transfer.

$$b_r^{gb} = b_{in} - b_{out} \quad (2.18)$$

Here b_r^{gb} denotes the Burgers vector of the residual dislocation at the grain boundary, while b_{in} and b_{out} refer to the Burgers vectors of the incoming and outgoing dislocations. This parameter is associated with the strain energy density increase in the grain boundary. Therefore for ease of slip transmission the strain energy density increase $|b_r^{gb}|$ should be minimized (Kacher et al., 2014).

A third metric is the geometric criterion M_{LRB} proposed by Lee et al. [1989], which is defined as follows.

$$M_{LRB} = (l_{in} \cdot l_{out}) * (g_{in} \cdot g_{out}) = \cos\theta \cos\kappa \quad (2.19)$$

In equation 2.19, l denotes the line of intersection of the slip plane and the grain boundary, and θ is the angle between l_{in} and l_{out} . A schematic representation of the angles ψ , κ and θ that describe the slip transfer geometry is shown in figure 2.10. The first dot product term $(l_{in} \cdot l_{out})$ can be replaced with $(e_{in} \cdot e_{out})$ for an alternative form that does not require knowing the inclination of the grain boundary, which is written as follows (Luster and Morris, 1995).

$$m' = \cos\psi \cos\kappa \quad (2.20)$$

m' is called the slip transfer parameter (or Luster-Morris parameter). ψ is the angle between the normals to the incoming and outgoing slip planes; while κ is the angle between the respective slip directions.

2.4.1 Implications of slip transfer in polycrystalline materials

Slip transfer has major implications for fatigue behaviour and damage nucleation in metals. An impediment to slip transfer can lead to stress concentrations from dislocation pileups that may nucleate cracks at grain boundaries (Hémery et al., 2018). In contrast, conditions where impediment to slip transfer is low result in more homogeneous plastic deformation. Consequently slip transfer

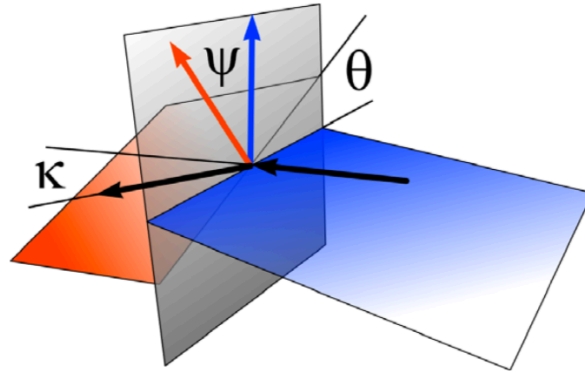


Figure 2.10: Angles used to calculate the Luster-Morris parameter m' . κ is the angle between slip directions; while ψ is the angle between the slip plane normals. θ is the angle between the slip plane traces on the grain boundary plane. Adapted from Bieler et al. (2009).

is an important consideration for materials processing as well as structural health of in-service components.

Some recent studies conducted on polycrystalline Al have shown that slip transfer is rare for grains with near cubic orientation, where it was only observed for $m' > 0.97$ and low angle boundaries (Bieler et al., 2019).

In two phase titanium alloys, it has been found that the propensity for slip transmission is affected by the volume fraction of alpha phase in addition to the relative orientations of interacting grains. Characterization of near alpha titanium (Ti-6242Si) subjected to low cycle fatigue using EBSD and transmission electron microscopy (TEM) (Joseph et al., 2018) has shown that plastic deformation occurs mainly by slip (basal $\langle a \rangle$, prism $\langle a \rangle$ and pyramidal $\langle a \rangle$) in the primary α grains. Furthermore, most of the slip transfer occurred between grains of similar orientation. At the boundaries of soft and hard grains, slip transfer does not readily take place. The stress concentrations at the grain boundary from the dislocation pileup result in activation of dislocation sources within the hard oriented grain. Once nucleated, the dislocations in the hard grain propagate via cross slip (Joseph et al., 2018).

Studies on in-situ scanning electron microscopy (SEM) characterization of Ti-6Al-4V have identified both high values of m' and resolved shear stress in the outgoing slip system to be

important for effective slip transfer (Hémery et al., 2018).

More recently, slip interactions at grain boundaries in commercial purity titanium were characterized using electron channeling contrast imaging (ECCI) by Han and Crimp [2020]. Favorable conditions for transfer of primary slip systems require high global Schmid factors, coupled with small misalignment between slip planes and grain boundary intersection lines.

2.5 Twin formation as a result of slip transfer from a neighboring grain (S+T twinning)

Slip transfer has been identified as a possible mechanism for strain accommodation in both single phase (α) (Guo et al., 2014; Wang et al., 2010a) and two-phase ($\alpha + \beta$) titanium (Seal et al., 2012). In polycrystalline materials there are additional constraints arising from the morphology of the neighborhood of a grain under consideration. In hexagonal metals, it is important to take into account the relative orientation between the c-axis and the loading direction. Deformation twinning is an important mechanism that facilitates strain accommodation in hexagonal metals and its relationship to slip transfer continues to be a topic of interest. Following Wang et al. [2010], twins nucleated as a result of slip transfer across a grain boundary are defined as S+T twinning.

In hexagonal titanium, the likelihood of S+T twinning increases when the value of m' approaches one (Yang et al., 2011). An example is shown in figure 2.11, transfer of prism $\langle a \rangle$ slip takes place more readily across the boundary between grains 1 and 2 than across the boundary between grains 2 and 3. Boundary 1-2 has a higher value of m' (0.936). Fewer geometrically necessary dislocations were found in grain 1 than in grain 3, because of the lack of pileups in grain 1.

Richeton et al. [2012] studied the kinematic compatibility between crystallographic slip and activated twin systems in hexagonal titanium. Based on imposing tangential continuity conditions on plastic distortion at the twin-parent interface, they found that the twin modes observed had compatibility with either prism $\langle a \rangle$ or pyramidal $\langle c + a \rangle$ slip. Bieler et al. [2014] used HEXRD to assess whether twin nucleation in subsurface grains in hexagonal titanium was caused by slip transfer from a neighboring grain onto the parent grain. It was observed that at least some of

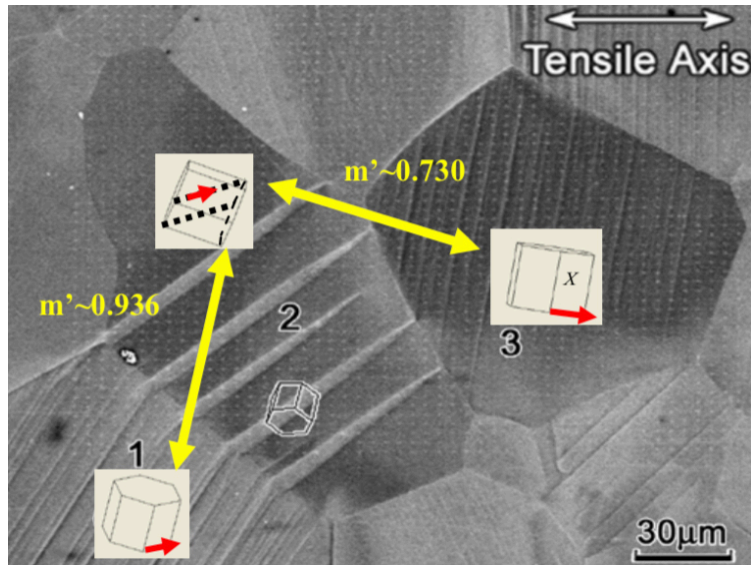


Figure 2.11: Use of m' to determine the propensity of twin nucleation as a result of slip transfer across a grain boundary. Twins can be observed in grain 2, where the activated twin system has a high m' (0.936) with respect to prism $\langle a \rangle$ slip system in grain 1. Adapted from Yang et al. (2011).

the twins may have nucleated as a result of transmission of prism $\langle a \rangle$ slip from a neighboring grain. Nervo et al., [2016] studied twin evolution in Ti-4Al during a compression experiment along a direction normal to the c-axis; and observed high compatibility between subsurface T1 twins and prism $\langle a \rangle$ slip in neighboring grains. Wang et al. [2010] observed slip induced twin nucleation (S+T) in about 25% of the twinned grains in a study with a pre-polished surface of CP-Ti. Abdolvand et al. (Abdolvand et al., 2015a,b) conducted in-situ 3D XRD characterization of tensile behaviour in polycrystalline zirconium. Using the local grain averaged stress tensor, the generalized Schmid factor was calculated in this study. It was observed that in hard oriented grains where twinning is favored, the local (generalized) Schmid factors of the six twinning variants have comparable values. Furthermore, the activated system among the six twin variants did not always have the highest local Schmid factor. It is therefore apparent that details of the loading history and local stress state between parent and adjacent grains influence the likelihood of twin nucleation.

2.6 Geometrically necessary dislocations (GND)

The concept of geometrically necessary dislocations was first proposed by Nye in his seminal work (Nye, 1953) and further developed by Ashby (Ashby, 1970). Work hardening in crystals occurs when dislocation motion is inhibited. Dislocations that accumulate as a result of this inhibition can be categorized into two types—geometrically necessary dislocations (GNDs), and statistically stored dislocations (SSDs) in order to maintain strain compatibility. A schematic illustrating how GNDs of both edge and screw type accumulate is shown in figure 2.12. In both cases a crystal undergoing single slip is shown. If the crystal can be divided into three sections, whereby each section is deformed independently of the others, each section undergoes plastic deformation by expansion of dislocation loops. There is a linear increase of plastic strain (along the slip direction for the edge case; and along direction m for the screw case). For the edge dislocation case, the screw components leave the material once they reach the boundaries of each section. Dipoles of the edge components, however remain; and when the sections are assembled back together, there are remnant negative edge dislocations that do not annihilate. A similar result can be drawn for the case of screw dislocations: the edge components exit the material at the free boundaries for each section and dipoles of positive screw dislocations remain. In both cases the non-annihilating dislocations contribute to lattice curvature.

In contrast to GNDs, statistically stored dislocations (SSDs) are randomly trapped during plastic deformation. Ashby [1970] defines this class of dislocations as "not geometrically necessary in the uniform deformation of a pure single crystal". Rather, the accumulation of such dislocations can be attributed to random interactions and trapping. Although SSDs contribute to the work hardening of a crystal, they do not contribute to lattice curvature.

Nye (1953) introduced a non-symmetrical second order tensor to quantify the GND content in a lattice. In this formulation only the lattice rotation gradient is considered and long range elastic strain fields are neglected as shown in equation 2.21. Here, V is the reference volume, ds is an element of arc length along the dislocation line, and L is the total dislocation line length contained within V . A component of the Nye tensor α_{ij} represents a dislocation with Burgers vector i and line

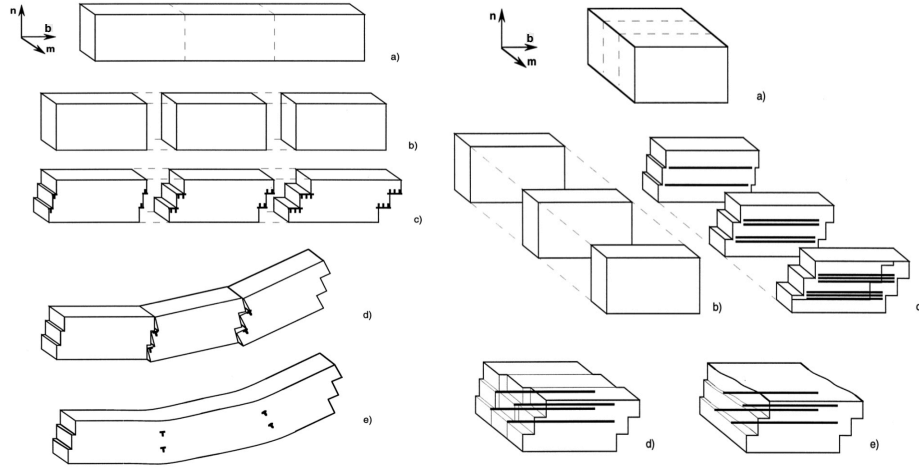


Figure 2.12: Schematic diagram showing how GNDs of edge type (left) and screw type (right) can accumulate in a plastically deformed crystal. Here b indicated the slip direction and n denotes the slip plane normal. $m = b \times n$. Adapted from Arsenlis and Parks [1999].

direction j . Kröner and Ashby extended this formulation by considering the elastic strain gradients (Arsenlis and Parks, 1999). It is important to note here that SSDs do not contribute to the Nye tensor.

$$\alpha_{ij} = \frac{1}{V} \int_L b_i t_j ds \quad (2.21)$$

A continuum based description of the Nye tensor and its use in calculation of the GND density is based on the deformation gradient. In their formulation of deformation theory of plasticity, Fleck and Hutchinson (Fleck et al., 1994) showed that the density of geometrically necessary dislocations is proportional to the plastic strain gradient. Moreover lattice rotation and stretch occurs during elastic deformation. Therefore the relative displacement du of two material points can be resolved into three components (equation 2.22).

$$du = du^p + du^R + du^e \quad (2.22)$$

$$\begin{aligned}
du^p &= \beta_{kj}^p dX_j \\
du^R &= \omega_{kj} dX_j \\
du^e &= \epsilon_{kj}^e f X_j
\end{aligned} \tag{2.23}$$

where du^p is the relative displacement due to slip, β^p is the slip tensor, du^R is the relative displacement due to lattice rotation ω , and du^e is the relative displacement due to elastic strain ϵ^e .

The specific slip tensor β^{p^λ} , is defined for a slip system λ , defined by slip direction s^λ and slip plane normal n^λ . The total slip tensor β^p takes into account the contribution from all of the active slip systems (Das et al., 2018).

$$\beta^p = \sum_{\lambda} \beta^{p^\lambda} s^\lambda \otimes n^\lambda \tag{2.24}$$

Furthermore, following Nye (Nye, 1953), crystallographic slip can be related to the resultant Burgers vector, as a closure failure of the Burgers circuit c , on surface S with plane normal N .

$$\langle B \rangle_k = \oint_c du_k^p = \oint_c \beta_{kj}^p dX_j \tag{2.25}$$

The line integral in equation 2.25 can be converted into a integral over the surface S by using Stoke's theorem as follows.

$$\langle B \rangle_k = \iint_S \left(\epsilon_{ijm} \beta_{kj,i}^p \right) N_m dS = \iint_S \alpha_{km}^{Nye} N_m dS, \tag{2.26}$$

where ϵ_{ijm} is the permutation tensor, α is the dislocation tensor (Nye, 1953). From Fleck and Hutchinson (Fleck et al., 1994) the Nye tensor can be expressed as the curl of the slip tensor as follows:

$$\alpha_{km}^{Nye} = \epsilon_{ijm} \beta_{kj,l}^p \tag{2.27}$$

The Nye tensor can now be related to the dislocation distribution inside the crystal. If the flux of dislocations is defined as q , with Burgers vector b and unit line direction l cutting through the plane with surface normal N , α^{Nye} can be written as follows (Das et al., 2018):

$$\alpha_{km}^{Nye} = q b_k l_m \tag{2.28}$$

It can be defined that $\rho_m = ql_m$ so that $\alpha_{km}^{Nye} = b_k \rho_m$. Therefore, for a general slip system λ the dislocation tensor may be rewritten as follows.

$$\alpha^{Nye} = \sum_{\lambda} (b^{\lambda} \otimes \rho^{\lambda}) \quad (2.29)$$

Since the total relative displacement du along a closed circuit is zero, the closure failure of the Burgers circuit $\langle B \rangle_k = \oint_C dy_k^p$ must be balanced by the net sum of the displacements due to lattice rotation and elastic strain $\oint_C (du_k^R + du_k^e)$.

The deformation gradient (2.8) can be written as follows.

$$F = \frac{\partial x}{\partial X} = I + \frac{\partial u}{\partial X} = I + \beta, \quad (2.30)$$

where u is the displacement, I is the identity matrix and β is the displacement gradient. As seen in section 2.3, F can be decomposed into the elastic (F^e and plastic (F^p) components. Crystallographic slip is captured by the plastic component of F , which is equivalent to the information included in the the slip tensor (equation 2.23). Since $F^p = I + \beta^p$, the Nye tensor can be written as the curl of the plastic deformation gradient.

$$\alpha_{mk}^{Nye} = \epsilon_{ijm} F_{kj,i}^p \quad (2.31)$$

If small strains are considered, the dislocation tensor can be written in terms of elastic (β^e) or plastic (β^p) displacement gradients.

$$\alpha \cong \begin{bmatrix} \frac{\partial \beta_{13}^p}{\partial x_2} - \frac{\partial \beta_{12}^p}{\partial x_3} & \frac{\partial \beta_{11}^p}{\partial x_3} - \frac{\partial \beta_{13}^p}{\partial x_1} & \frac{\partial \beta_{12}^p}{\partial x_1} - \frac{\partial \beta_{11}^p}{\partial x_2} \\ \frac{\partial \beta_{23}^p}{\partial x_2} - \frac{\partial \beta_{22}^p}{\partial x_3} & \frac{\partial \beta_{21}^p}{\partial x_3} - \frac{\partial \beta_{23}^p}{\partial x_1} & \frac{\partial \beta_{22}^p}{\partial x_1} - \frac{\partial \beta_{21}^p}{\partial x_2} \\ \frac{\partial \beta_{33}^p}{\partial x_2} - \frac{\partial \beta_{32}^p}{\partial x_3} & \frac{\partial \beta_{31}^p}{\partial x_3} - \frac{\partial \beta_{33}^p}{\partial x_1} & \frac{\partial \beta_{32}^p}{\partial x_1} - \frac{\partial \beta_{31}^p}{\partial x_2} \end{bmatrix} \quad (2.32)$$

$$\alpha \cong \begin{bmatrix} \frac{\partial \beta_{12}^e}{\partial x_3} - \frac{\partial \beta_{13}^e}{\partial x_2} & \frac{\partial \beta_{13}^e}{\partial x_1} - \frac{\partial \beta_{11}^e}{\partial x_3} & \frac{\partial \beta_{11}^e}{\partial x_2} - \frac{\partial \beta_{12}^e}{\partial x_1} \\ \frac{\partial \beta_{22}^e}{\partial x_3} - \frac{\partial \beta_{23}^e}{\partial x_2} & \frac{\partial \beta_{23}^e}{\partial x_1} - \frac{\partial \beta_{21}^e}{\partial x_3} & \frac{\partial \beta_{21}^e}{\partial x_2} - \frac{\partial \beta_{22}^e}{\partial x_1} \\ \frac{\partial \beta_{32}^e}{\partial x_3} - \frac{\partial \beta_{33}^e}{\partial x_2} & \frac{\partial \beta_{33}^e}{\partial x_1} - \frac{\partial \beta_{31}^e}{\partial x_3} & \frac{\partial \beta_{31}^e}{\partial x_2} - \frac{\partial \beta_{32}^e}{\partial x_1} \end{bmatrix} \quad (2.33)$$

Furthermore, the displacement gradient can be resolved into the lattice rotation and lattice strain components as

$$\beta^e = \omega^e + \epsilon^e \quad (2.34)$$

Then equation 2.33 can be written in the following form:

$$\alpha \cong \begin{bmatrix} \frac{\partial \omega_{12}^e}{\partial x_3} - \frac{\partial \omega_{13}^e}{\partial x_2} & \frac{\partial \omega_{13}^e}{\partial x_1} & \frac{\partial \omega_{21}^e}{\partial x_1} \\ \frac{\partial \omega_{32}^e}{\partial x_2} & \frac{\partial \omega_{23}^e}{\partial x_1} - \frac{\partial \omega_{21}^e}{\partial x_3} & \frac{\partial \omega_{21}^e}{\partial x_2} \\ \frac{\partial \omega_{32}^e}{\partial x_3} & \frac{\partial \omega_{13}^e}{\partial x_3} & \frac{\partial \omega_{31}^e}{\partial x_2} - \frac{\partial \omega_{32}^e}{\partial x_1} \end{bmatrix} + \begin{bmatrix} \frac{\partial \epsilon_{12}^e}{\partial x_3} - \frac{\partial \epsilon_{13}^e}{\partial x_2} & \frac{\partial \epsilon_{13}^e}{\partial x_1} - \frac{\partial \epsilon_{11}^e}{\partial x_3} & \frac{\partial \epsilon_{11}^e}{\partial x_2} - \frac{\partial \epsilon_{12}^e}{\partial x_1} \\ \frac{\partial \epsilon_{22}^e}{\partial x_3} - \frac{\partial \epsilon_{23}^e}{\partial x_2} & \frac{\partial \epsilon_{23}^e}{\partial x_1} - \frac{\partial \epsilon_{21}^e}{\partial x_3} & \frac{\partial \epsilon_{21}^e}{\partial x_2} - \frac{\partial \epsilon_{22}^e}{\partial x_1} \\ \frac{\partial \epsilon_{32}^e}{\partial x_3} - \frac{\partial \epsilon_{33}^e}{\partial x_2} & \frac{\partial \epsilon_{33}^e}{\partial x_1} - \frac{\partial \epsilon_{31}^e}{\partial x_3} & \frac{\partial \epsilon_{31}^e}{\partial x_2} - \frac{\partial \epsilon_{32}^e}{\partial x_1} \end{bmatrix} \quad (2.35)$$

In equation 2.35, the contribution to α from lattice rotation is much larger than from elastic strain gradients (Das et al., 2018). The relationship between the Nye tensor and dislocation density was established in equation 2.29. It is possible to rewrite the 3×3 tensor as a 9×1 column vector. Following Arsenlis et al. (Arsenlis and Parks, 1999), a linear operator A (An $9 \times k$ matrix for k types of dislocations) can now be defined. The k th column of A contains the dyadic product of the Burgers vectors and line direction of the k th dislocation type. The scalar values of dislocation density for k types of dislocations can be arranged in the form of a $k \times 1$ column vector ρ .

$$\alpha = A\rho \quad (2.36)$$

In explicit form, equation 2.36 can be written as follows (Das et al., 2018).

$$\sum_j (b^k \otimes \rho^k) = \begin{bmatrix} b_1^1 l_1^1 & b_1^2 l_1^2 & b_1^3 l_1^3 & \dots & b_1^k l_1^k \\ b_1^1 l_2^1 & b_1^2 l_2^2 & b_1^3 l_2^3 & \dots & b_1^k l_2^k \\ b_1^1 l_3^1 & b_1^2 l_3^2 & b_1^3 l_3^3 & \dots & b_1^k l_3^k \\ b_2^1 l_1^1 & b_2^2 l_1^2 & b_2^3 l_1^3 & \dots & b_2^k l_1^k \\ b_2^1 l_2^1 & b_2^2 l_2^2 & b_2^3 l_2^3 & \dots & b_2^k l_2^k \\ b_2^1 l_3^1 & b_2^2 l_3^2 & b_2^3 l_3^3 & \dots & b_2^k l_3^k \\ b_3^1 l_1^1 & b_3^2 l_1^2 & b_3^3 l_1^3 & \dots & b_3^k l_1^k \\ b_3^1 l_2^1 & b_3^2 l_2^2 & b_3^3 l_2^3 & \dots & b_3^k l_2^k \\ b_3^1 l_3^1 & b_3^2 l_3^2 & b_3^3 l_3^3 & \dots & b_3^k l_3^k \end{bmatrix} \begin{bmatrix} \rho_1 \\ \rho_2 \\ \rho_3 \\ \vdots \\ \vdots \\ \rho_k \end{bmatrix} = \begin{bmatrix} \alpha_{11} \\ \alpha_{12} \\ \alpha_{13} \\ \alpha_{21} \\ \alpha_{22} \\ \alpha_{23} \\ \alpha_{31} \\ \alpha_{32} \\ \alpha_{33} \end{bmatrix} \quad (2.37)$$

In general, $k > 9$, so there exists no unique solution for ρ . If α and A are known, optimization schemes can be used to solve for ρ . Arsenlis and Parks [1999] have outlined two possible optimization methods for this purpose. The first method is the L^2 optimization scheme that minimizes the squares of dislocation densities. In this approach it is necessary to include all possible slip systems

(including the ones least likely to activate), since the calculation is independent of the resolved shear stress. One drawback of this method is the lack of any physical basis, in the sense that the energetics of dislocations are not considered.

A more physically meaningful scheme is the L^1 approach that minimizes the total dislocation elastic energy: $(1 - \nu)^{-1} \sum_k \rho_k^{edge} + \sum_k \rho_k^{screw}$. Here ν is the Poisson's ratio, and both screw and edge contributions from the different k types of dislocations are taken into account. If it is assumed that the magnitude of the Burgers vectors for all dislocations are the same; and the lattice is elastically isotropic, the following relation holds true. Moreover, it is also assumed that the dislocations are either pure edge or pure screw, where

$$\frac{E_{edge}}{E_{screw}} = \frac{1}{1 - \nu} \quad (2.38)$$

Several surface and subsurface techniques have been used for experimental estimation of GND density in polycrystalline materials. A popular surface method is EBSD, which enables the estimation of lattice distortion from local crystal orientation. Ruggles and Fullwood [2013] used high resolution EBSD (HR EBSD) to estimate bulk GND content in face centered cubic material (nickel). This approach only allows for the estimation of the lattice distortion components of the Nye tensor. Konijnenberg et al. [2015] have shown that this drawback can be overcome by using three-dimensional electron backscatter diffraction (3D EBSD). Using serial sectioning to perform 3D EBSD, they were able to calculate GND density in a copper bicrystal during a micro cantilever bending experiment.

DAXM methods have been used by Larson et al. [2008] to experimentally measure lattice curvature and elastic strain in plastically deformed silicon. More recently, Guo et al. [2020] used DAXM to determine spatially resolved values of the rotation gradient in order to estimate the GND density in hexagonal titanium. The approach used by them is based on the methodologies outlined by Arsenlis and Parks [1999] and Das et al. [2018]. Here the L^1 approach is used as the optimization scheme to solve for dislocation density.

2.7 Review of HEXRD methods

X-ray beams from synchrotron sources are typically about fourteen orders of magnitude more brilliant (photons/s/mm²/mrad²/eV) compared to conventional sources (Ice and Pang, 2009). This provides the means to obtain narrow micron or sub-micron beams. Two important advantages of synchrotron based x-ray diffraction techniques are the ability to conduct subsurface characterization non-destructively and minimal sample preparation requirements compared to surface methods such as EBSD. Based on the type of beam used (monochromatic or polychromatic), beam energy and the algorithms used for three-dimensional reconstruction, they can be broadly classified into the following three categories.

1. three-dimensional x-ray diffraction (3D XRD) microscopy (also known as high energy diffraction microscopy (HEDM)): In this approach, a high energy (~ 50 keV or higher) monochromatic beam is used to generate Debye-Scherrer diffraction patterns from a sample that is rotated incrementally about a stationary axis. Thereafter, a 3D reconstruction is done using tomography algorithms (Poulsen, 2012). Here, the primary focus is on a specific setting of 3D XRD, known as far-field HEDM (FF HEDM).
2. A second setting of 3D XRD used in this study is near field HEDM (NF HEDM). The basic principle is the same as FF HEDM, except for the fact that the sample to detector distance used here is much smaller (typically ~ 10 mm). It is possible to obtain finer spatial resolution (2.2) using this setting compared to FF HEDM.
3. Micro-Laue diffraction: Here, a strong polychromatic (white) beam is used to generate Laue diffraction patterns. The reconstruction is typically done using triangulation algorithms with the help of a differential aperture. The beam energy used in this method is generally lower (7-30 keV) than for 3D XRD. The emphasis here is on a special case of micro-Laue diffraction, known as differential aperture x-ray microscopy (DAXM).

In this section, the fundamental aspects of these techniques are discussed, along with their applications in three-dimensional characterization of polycrystalline materials.

A basic underlying principle of x-ray diffraction is the Bragg condition. For a monochromatic x-ray beam of wavelength λ incident on a set of parallel crystal planes, constructive interference of the reflecting waves occurs when the path difference is an integer (n) multiple of λ .

$$2d \sin \theta = n\lambda \quad (2.39)$$

Where d is the interplanar spacing and θ is the angle between the incident beam and the real space set of atomic planes.

2.7.1 3D XRD

The first demonstrations of 3D XRD experiments were done in 1997 by Poulsen et al. (1997). In general, four standard modes of operation have been defined by Poulsen (2012). Mode I is used for quick statistical information of properties of individual crystallites e.g. grain volume, grain averaged strain tensor, orientation, and phase. Mode II can be used to determine the three-dimensional center of mass positions of individual grains, in addition to properties determined by Mode I. Modes III and IV enable a complete volumetric mapping of grains and orientations for undeformed and deformed specimens respectively (Poulsen, 2012).

The schematic representation of a typical 3D XRD experimental setup is shown in figure 2.13. An almost parallel monochromatic x-ray is incident on the specimen. The specimen is mounted on a stage that enables it to rotate about the Z-axis by the angle ω (normal to the beam direction). It is possible to mount a deformation frame on a stage to enable translations in the X, Y and Z directions, as well as additional rotation axes.

As the specimen rotates, there are parts of the illuminated material that satisfy the Bragg condition and generate a diffracted beam. The diffraction patterns are recorded on a series of two dimensional detectors. The rotation is typically done using a constant increment ($\Delta\omega$), for each exposure. This provides a uniform sampling for the specimen and allows for the Bragg condition

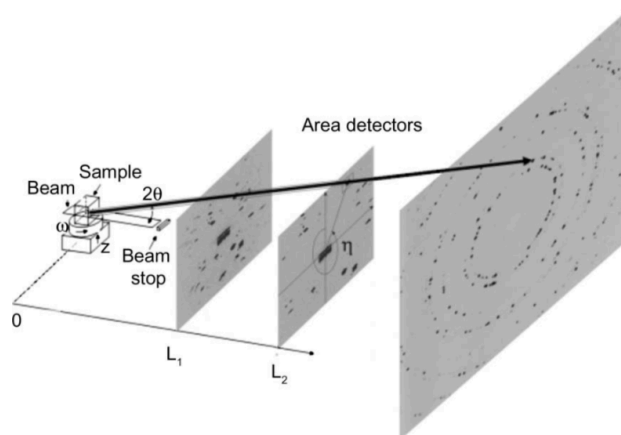


Figure 2.13: Schematic illustrating a basic 3D XRD experimental setup. Z is the sample rotation axis; ω is the angle of rotation about Z ; L is the sample to detector distance; 2θ is the Bragg angle; η is the azimuthal angle. Adapted from Poulsen (Poulsen, 2012).

to be satisfied for a multitude of crystallographic planes for any crystal orientation. Use of multiple two dimensional detectors positioned at different distances (L) from the center of rotation allows for three-dimensional characterization. Depending upon the range of sample to detector distance (L) used, the detector settings can be either near field ($L \sim 10$ mm); far-field ($L \sim 1$ m); or very-far-field ($L \sim 5$ m). For the three aforementioned configurations, there are differences in the resolution and size of the detectors used. Detailed information about the configurations along with information about their spatial, orientation and strain resolutions are enumerated in table 2.2. This configuration is available at 1-ID beamline at the Advanced Photon Source (APS) at the Argonne National Laboratory.

An important advantage of 3D XRD is the ability to perform in-situ analysis. This enables the characterization of lattice rotation and strain evolution during mechanical deformation (e.g. a tensile test). It is also possible to characterize phase transformations, nucleation and grain growth during thermo-mechanical experiments (Poulsen, 2012).

Hereafter, the focus is on the Mode II type of experiment using FF HEDM as applied to polycrystalline materials. In this approach it is possible to obtain information on phase, grain center-of-mass position and volume, and the local grain average strain tensor. For coarse grained specimens the far field setup is quite efficient, although the spatial resolution offered in this

Table 2.2: Enumeration of the three different configurations for 3D XRD, based on sample to detector distance (L). Adapted from Park et al. (Park et al., 2017).

Experimental Technique	Resolution	Remarks
Near-field high energy diffraction microscopy (NF HEDM)	Spatial resolution $\sim 1\mu\text{m}$; 0.1° - 0.01° angular resolution	Area detector ($1.5\mu\text{m}$ square pixels covering $\sim 3.1 \times 3.1\text{mm}^2$. Sample to detector distance ~ 10 mm. Enables 3D reconstruction of polycrystalline structure. Not capable of providing local strain information
Far-field high energy diffraction microscopy (FF HEDM)	Spatial resolution $\sim 10\mu\text{m}$; 0.1° - 0.01° crystallographic orientation resolution; 10^{-4} strain resolution	Area detector resolution: $200\mu\text{m}$ square pixels, covering $\sim 410\text{mm} \times 410\text{mm}$. Sample to detector distance ~ 1 m. Capability of 3D reconstruction, determining centers of masses of crystallites, crystallographic orientations and local elastic strain tensor.
Very-far-field high energy diffraction microscopy (VFF HEDM)	Angular resolution: $\sim 0.01^\circ$	Area detector resolution: $\sim 60\mu\text{m}$ pixels, covering $\sim 50\text{mm} \times 30\text{mm}$ area. Capable of non destructive mapping of individual grains in a polycrystal.

configuration is relatively low. On the other hand, the angular resolution is high, which makes the method sensitive to elastic strain and crystal orientation (Park et al., 2017). This setup is less sensitive to the grain shape, therefore only the average position of the grain center of mass (COM) can be estimated.

In the present study, near field HEDM (NF HEDM) is also used to determine grain positions, morphology and orientations in the illuminated microstructure. Since this technique enables finer spatial resolution compared to FF HEDM, it is possible to capture grain morphology and orientation gradients within an individual grain. In their work on characterization of gold oligocrystals, Menasche et al. [2020] found the resolution in orientation measurement using NF HEDM is about an order of magnitude better than surface electron backscatter diffraction (EBSD) measurements

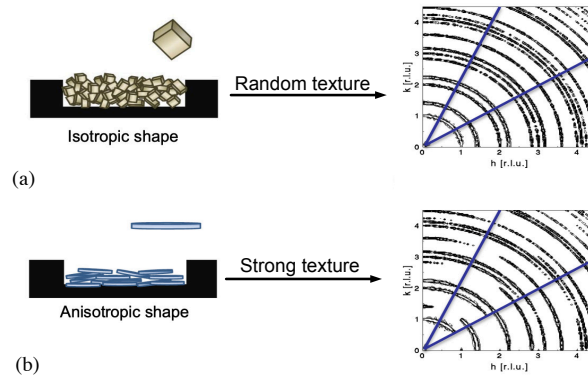


Figure 2.14: Schematic illustration of Debye-Scherrer patterns for a polycrystalline material with (a) random texture (well annealed);(b) strong texture (Taddei, 2015).

that use a standard Hough transform based indexing method.

As mentioned earlier, in a far field experiment, when a particular crystallographic plane satisfies the Bragg condition, the diffracted X-ray is recorded on an area detector as a Debye-Scherrer pattern (Park et al., 2017). For a polycrystalline specimen, the patterns can be distinguished for two different kinds of specimens. If the specimen is well annealed with a random texture, the Debye-Scherrer patterns manifest as a set of concentric circles with peaks randomly located around the circle, where each circle corresponds to a family of crystallographic planes. On the other hand, for a specimen with a strong texture, the concentric circles have portions with no diffraction peaks because certain ranges of crystal orientations are not present in the specimen, relative to the incident beam. Figure 2.14 illustrates the difference in the diffraction patterns for the two cases.

2.7.1.1 Indexing data obtained from 3D XRD

Indexing is the process of assigning unique grain identities to groups of diffraction peaks. Indexing starts with the identification of diffraction peaks for each ω in detector space. The first step in the peak searching process is to uniquely identify diffraction spots in detector space (segmentation). This requires a sufficient number of distinct diffraction spots to ensure that there is minimal overlapping of peak intensity from different grain orientations. Peaks are then filtered by specifying a threshold (lower bound) of intensity. For deformed crystals that exhibit significant

peak broadening, multiple thresholds can be used in the segmentation process. The second step in this process is to determine the directions of the diffracted X-rays corresponding to the peaks (Poulsen, 2012). For FF HEDM, it is initially assumed that all of the grains are positioned at the center of rotation. Broadly speaking, there are two basic approaches to indexing.

1. Forward projection: In this approach, the entire orientation space is traversed in increments. At any given orientation, the theoretical scattering vectors (G) are calculated. Then the theoretical values are matched to the experimental G vectors in the neighborhood. The efficiency of matching is measured by a completeness criterion; which is the ratio of the observed number of G vectors to the expected number.

This approach works well for a smaller number of grains; however the likelihood of false indices increases if the number of grains in the illuminated volume is large (Sharma et al., 2012b). One way to overcome this drawback is to combine the orientation-space scan with a spatial grid in the illuminated volume. At each point in the grid, all orientations are simulated; which narrows the margins used for matching the observed and simulated peaks. This method has been implemented in the Grainspotter program available under the *FABLE* package developed by the Risø National Laboratory (Schmidt, 2014).

2. Backward projection: The basic idea of this approach is to group diffraction spots belonging to the same orientation together. If the diffracting grain is located at the origin of the laboratory coordinate frame, it is possible to assign a straight line for each corresponding diffraction peak in Rodrigues-Frank (RF) orientation space. A unique orientation would be identified from a point where several of these lines intersect. On the other hand if the diffracting grain is not located at the origin of the laboratory frame, each of the diffraction lines in RF space no longer intersect at a point. Rather they form an intersection volume that can be identified as a unique orientation as long as the number of grains is small (Sharma et al., 2012a,b).

One drawback of the methods enumerated above is the increase in the number of false iden-

tifications with increasing number of grains. This is a result of the higher possibility of overlap of diffraction spots on the detector. This is more pronounced when individual grains have large orientation spreads. Other factors that can lead to high overlap are differences in unit cell size in different phases and strongly preferred orientations (sample texture) (Poulsen, 2012).

A second problem that arises during the indexing process is from the difficulty of identifying smaller grains. It is typical for grain sizes to be lognormally distributed in a specimen. Moreover, there is a sharp drop in integrated intensity of peaks with increasing value of the Bragg angle 2θ . For grains that are coarse enough, all or most of the diffraction spots get correctly identified during peak searching. Grains that are very small in size have peaks with lower intensities and do not meet the minimum assigned threshold during peak search are not identified. Grains that have sizes that fall between the two aforementioned categories can be identified if the Bragg angle is low. This however, may require multiple thresholds to be imposed at different 2θ values in an iterative manner (Poulsen, 2012).

More recently, efforts have been made to overcome the drawbacks of forward and backward projections by using a mapping mode that uses a reduced orientation space. This has been incorporated in the MIDAS package developed at Argonne National Laboratory (Sharma et al., 2012a,b; Wozniak et al., 2015). This method has been observed to yield better results for centers of mass and orientation when the number of grains considered is higher. MIDAS has been used for indexing data from a FF HEDM experiment for characterizing irradiated Fe alloys (Park et al., 2015).

2.7.1.2 Local strain tensor evaluation from FF HEDM

The capability to extract local grain averaged strain tensor is an important feature of FF HEDM. One approach is the methodology used by Margulies et al. to calculate lattice strain in a copper polycrystal (Margulies et al., 2002). Here, the fundamental equation for strain calculation is based on measurement of the relative change in interplanar spacing of selected crystallographic planes. A

given strain tensor component can be obtained by differentiation of the Bragg equation as follows.

$$\epsilon = \frac{d - d_0}{d_0} = -\cot \theta \Delta \theta \quad (2.40)$$

where d_0 and d are the interplanar spacings for unstrained and strained lattice respectively.

A specific strain tensor component ϵ_i resolved in the direction of the scattering vector identified by the direction cosines l_i , m_i and n_i can be written as follows.

$$\epsilon_i = (l_i \ m_i \ n_i) \begin{pmatrix} \epsilon_{11} & \epsilon_{12} & \epsilon_{13} \\ \epsilon_{21} & \epsilon_{22} & \epsilon_{23} \\ \epsilon_{31} & \epsilon_{32} & \epsilon_{33} \end{pmatrix} \begin{pmatrix} l_i \\ m_i \\ n_i \end{pmatrix} \quad (2.41)$$

Combining equations 2.40 and 2.41, the six independent strain tensor components resolved in any direction given by direction cosines l , m and n can be evaluated as follows.

$$\epsilon = \epsilon_{11}l^2 + \epsilon_{22}m^2 + \epsilon_{33}n^2 + \epsilon_{12}lm + \epsilon_{13}ln + \epsilon_{23}mn \quad (2.42)$$

In order to solve for the six unknown strain tensor components a minimum of six independent diffraction spots are necessary. In reality, the number of such measurements are greater than six, so an overdetermined system of linear equations is obtained. This can be easily solved using singular value decomposition (SVD) or a least squares scheme. Details of the algorithm used for grain averaged strain tensor calculation are given in section 4.1.1.

2.7.1.3 Accuracy in determination of grain positions using 3D XRD

As enumerated in table 2.2, FF HEDM enables determination of grain positions (centers of mass) with a resolution of $10\mu\text{m}$ or better. On the other hand, NF HEDM enables a finer resolution ($1\mu\text{m}$ or better), and provides information on grain morphology in three-dimensional space. The accuracy in the determination of grain center of mass (COM) using FF HEDM is strongly dependent on the experimental setup and the state of the illuminated volume in the specimen (Park et al., 2017). For example, if there is a large amount of deformation or orientation gradients present in

the microstructure, smearing of the diffraction spots can occur, resulting in higher uncertainty in determination of the grain position.

Based on the combined far field and near field HEDM characterization of an in-situ tensile test in alpha titanium (Ti-7Al alloy), Turner et al. [2016] reported that the average difference in grain positions between the two datasets is $\sim 16\mu m$. In this experiment, the average grain size of the interrogated microstructure was $\sim 100\mu m$.

2.7.2 Differential aperture x-ray microscopy (DAXM)

DAXM is a special application of micro-Laue diffraction that enables depth resolved characterization along the beam direction. This technique was developed by Larson et al. [2002]. A fundamental difference from HEDM is that in this case, a white (polychromatic) beam is typically used to interrogate the specimen. This technique enables characterization at submicron resolution. A notable advantage of this technique is the high level of depth resolution; which is of the order of hundreds of microns for low Z materials and tens of microns for high Z materials. Moreover, orientation measurements can be made with high angular precision (Yang et al., 2004).

The von Laue formulation describes the conditions for constructive interference from a set of parallel crystallographic planes in terms of the scattering vector. Let K_i and K_o denote the wave vectors of the incoming and outgoing (reflected) x-ray beams respectively. If a monochromatic (single wavelength) beam undergoing elastic scattering is considered, then $|K_i| = |K_o| = \frac{1}{\lambda}$, where λ is the wavelength of the beam. The scattering vector is then given as follows.

$$\Delta K = K_i - K_o \quad (2.43)$$

For a crystal plane with Miller indices $(h k l)$, the Laue condition can be written as follows.

$$\Delta K = ha^* + kb^* + lc^*, \quad (2.44)$$

where a^* , b^* and c^* are the basis vectors for the reciprocal lattice; and the term on the right hand side of equation 2.44 is the reciprocal lattice vector corresponding to plane $(h k l)$. It can

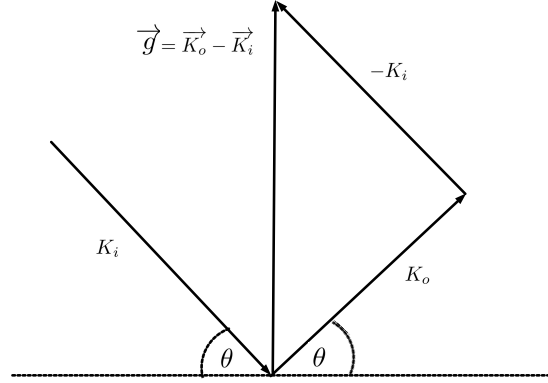


Figure 2.15: Schematic diagram illustrating the Laue condition.

be shown that equation 2.44 is equivalent to the Bragg condition. Figure 2.15 shows a beam with incoming wave vector K_i impinging on a crystal plane at an angle θ . K_o denotes the outgoing wave vector.

According to the Laue condition, the scattering vector $\vec{g} = \vec{K}_i - \vec{K}_o = \Delta K$ is equal to the reciprocal lattice vector corresponding to $(h k l)$. Since the scattering is elastic $|\vec{K}_i| = |\vec{K}_o|$. K_i and K_o make the same angle with the plane normal to \vec{g} . Therefore, scattering is equivalent to a Bragg reflection at an angle θ from a plane with reciprocal lattice vector $ha^* + kb^* + lc^*$.

If d_{hkl} is the interplanar spacing for planes parallel to $(h k l)$ and \vec{g}_0 is the shortest wave vector parallel to \vec{g} , then

$$\vec{g}_0 = \frac{1}{d_{hkl}} \quad (2.45)$$

From equation 2.45 it follows that:

$$\begin{aligned} \vec{g} &= n\vec{g}_0 \\ |\vec{g}| &= \frac{n}{d_{hkl}} \\ |\vec{g}| &= 2|\vec{K}_{in}| \sin \theta \end{aligned} \quad (2.46)$$

From figure 2.15,

$$|\vec{g}| = 2|\vec{K}_{in}| \sin \theta \quad (2.47)$$

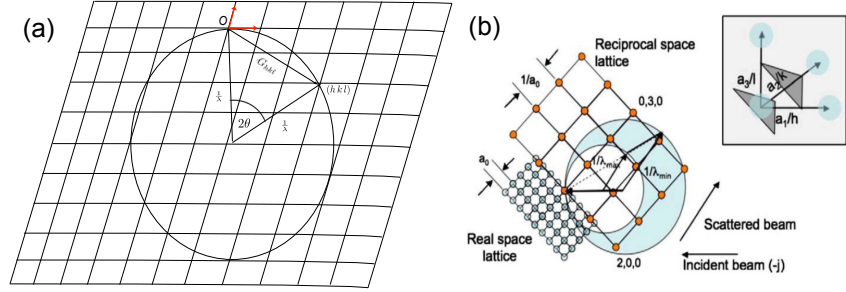


Figure 2.16: Schematic representation of an Ewald sphere in two dimensions (a) Monochromatic beam, (b) Polychromatic beam containing a range of wavelengths. The parallel set of crystallographic planes (hkl) that form a reciprocal lattice point are shown on the top right inset (Ice and Pang, 2009)

From equations 2.46 and 2.47,

$$\frac{2}{\lambda} \sin \theta = \frac{n}{d_{hkl}} \quad (2.48)$$

$$n\lambda = 2d_{hkl} \sin \theta$$

Equation 2.48 is the Bragg condition. If now a polychromatic beam containing wavelengths in the range $[\lambda_{min}, \lambda_{max}]$ is considered; the sets of crystal planes satisfying the Bragg condition can be illustrated by the Ewald sphere in figure 2.16. Figure 2.16 (a) shows the case for a monochromatic beam of wavelength λ . The incident wave vector terminates at the origin O of the reciprocal lattice. A sphere can be drawn with center at the tail of the incident vector having a radius of $\frac{1}{\lambda}$. The sphere passes through the reciprocal lattice origin and any point hkl that it also intersects indicate a set of planes (hkl) that satisfy the Bragg condition. Figure 2.16(b) shows the Ewald spheres for a polychromatic (white) beam containing wavelengths in the range $[\lambda_{min}, \lambda_{max}]$. In the limiting cases, the wave vectors correspond to the minimum and maximum wavelengths λ_{min} (outer sphere) and λ_{max} (inner sphere) respectively. The volume of reciprocal lattice in between these two extreme values (region shaded in blue) will have multiple Ewald spheres intersecting the reciprocal lattice at different points. Therefore, there will be several crystal planes for which the Bragg condition will be satisfied, noting that there are many more points within the sphere than the circular cross section depicted. This illustrates the basic principle behind micro-Laue diffraction.

The schematic illustration of the experimental setup for DAXM at ID-34E beamline at APS is

shown in figure 2.17. A polychromatic x-ray beam from the synchrotron source passes through a removable micro-monochromator setting. The monochromator allows the passage of either a white beam or reflects a monochromatic beam from the lower part of the undulator onto the Kirkpatrick-Baez (K-B) mirrors; which collimate the beam to $1\mu m^2$ cross section. The specimen is typically positioned at 45° with respect to the incident beam direction (Yang et al., 2004).

The Laue diffraction patterns have a high range of angular divergence. In order to profile them, a $50\mu m$ Pt wire is used as a differential aperture (figure 2.17, top right). This wire translates in submicron steps parallel to the specimen surface. Diffracted beams from the specimen pass through the submicron sized opening formed between two successive positions of the profiler wire. By subtracting the Laue patterns before and after each profiler step, the differential intensity distribution of the diffracted beams passing through the aperture can be obtained. Reconstruction of the complete diffraction patterns for voxels along the beam direction is done using algorithms that triangulate from the position of the patterns on the detector to its source along the beam direction. In order to achieve submicron depth resolution, it is important that the distance from the wire to detector D_{Det} is ~ 200 times greater than that from wire to incident beam D_{X-R} (Yang et al., 2004; Ice and Pang, 2009).

Using DAXM it is possible to obtain structural information, orientation, and the strain tensor for each material location along the direction of the incident beam with a positional accuracy of $\sim 0.1\mu m$. Scans can be conducted as line scans where one surface coordinate is varied while keeping the other constant; as well as in a raster mode. Scans with finer step sizes take longer and synchrotron beam time becomes a constraining factor in the experiment.

For coarse grained microstructures, a serial probing method developed by Eisenlohr et al. (Eisenlohr et al., 2017) is effective for depth resolved characterization. In this approach a regular array of DAXM probes is constructed. Each probe in this grid scans the specimen to the desired depth. The second step identifies individual grains based on their similarity of orientation in physical space (Eisenlohr et al., 2017).

A more recent development in this area is dark field DAXM, which was first reported in a study

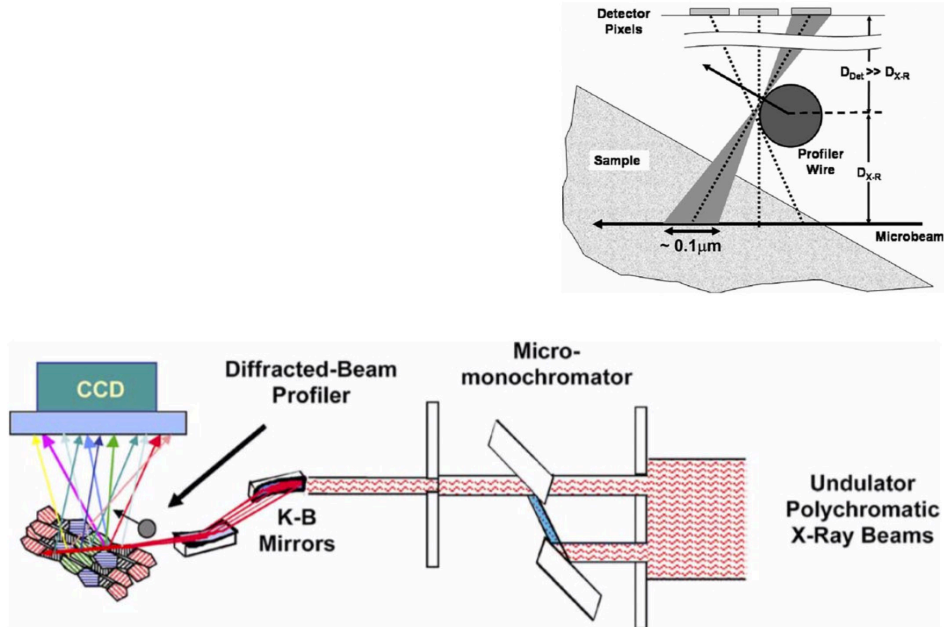


Figure 2.17: Schematic of a DAXM experimental setup to interrogate a polycrystalline specimen. An enlarged view of the differential aperture (profiler) Pt wire is shown on the top right (Yang et al., 2004).

conducted of recovery in tensile deformed aluminum (Simons et al., 2015). This technique uses the monochromatic beam setting and diffraction angles (2θ) in the range of $10\text{-}30^\circ$, enabling spatial resolution of the order of 100 nm .

2.7.2.1 Local strain tensor evaluation from DAXM

In contrast to HEDM that can yield only the grain average strain tensors, the local elastic strain can be obtained with submicron resolution using DAXM. Depending on whether the deviatoric or the full strain tensor is to be obtained, two settings of DAXM can be employed. With the polychromatic beam setting the (deviatoric) shape change of the unit cell can be measured via the change in lattice parameters. In addition, the hydrostatic component can be obtained using the energy scan setting. Here, a monochromatic beam of known energy is used to obtain interplanar spacing for a specific $\{h\ k\ l\}$. This in turn can be compared to the lattice parameters of the unstrained crystal to measure lattice dilatation (Yang et al., 2004).

Yang et al. [2004] have conducted full strain tensor measurements from DAXM analysis of a bent cylindrical specimen of Si. Typically, spatially resolved elastic strains can be measured with an accuracy of 10^{-4} . More recently, Zhang et al. [2018] have shown for a synthetic DAXM dataset that the deviatoric or full deformation gradient can be obtained with an accuracy of 10^{-9} or better.

2.7.2.2 Calculation of GND density from DAXM data

Because lattice orientations can be measured with submicron spatial resolution using DAXM, it enables the evaluation of local lattice curvature in three dimensions. Therefore the GND density can be calculated in plastically deformed regions (Yang et al., 2004).

Larson et al. [2008] calculated the spatially resolved Nye tensor from lattice curvature measurements using DAXM in thin deformed Si plates. More recently Guo et al. [2020] have used the modified Nye-Kröner-Bilby equation to calculate GND density in plastically deformed hexagonal titanium based on lattice rotation gradient measurement using DAXM.

2.8 Opportunity for research

Accommodation of strain during heterogeneous deformation in polycrystalline materials has a strong influence on properties like strength and ductility. This in turn has critical implications in microstructure design for room temperature formability and fatigue resistance. For example, poor formability in low symmetry metals like magnesium is an impediment towards their widespread use in structural applications. It is also crucial to understand the interaction of slip systems with dislocation pileups at grain boundaries for improved design to withstand low cycle fatigue (Joseph et al., 2018). One approach to assess the strain accommodation at the microstructure level in polycrystalline materials is to use the slip transfer parameter as a quantitative marker. To this end, it is important to be able to determine positions and shape information of constituent grains in a polycrystal, along with the local stress state.

Geometrically compatible slip systems in neighboring grains can generate twinning partials at the grain boundary, resulting in a stable twin nucleus (Wang et al., 2009a). The slip transfer

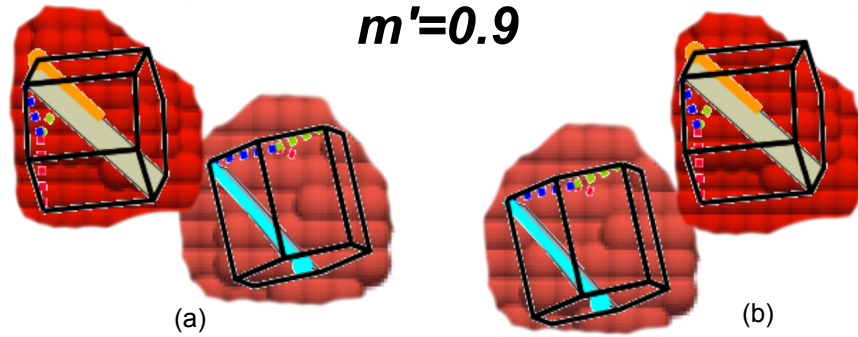


Figure 2.18: Example illustrating the importance of relative grain positions for viable S+T twin nucleation. The left figure (a) shows two grains with a favorable relative position (along with a high m' value). Figure (b) shows the same grains with relative positions that may not favor S+T twinning.

parameter m' can be used as a criterion to assess the possibility of S+T twinning. A high value of m' , however is not a sufficient condition to guarantee twin nucleation by slip transfer because it is also important to also consider the relative positions of the grains and slip planes with respect to each other in three-dimensional space. An illustrative example is shown in figure 2.18, where the slip system in a grain has a favorable m' value with respect to the activated twin variant in its neighbor. Theoretically, shear transfer from the slip system in the adjacent grain is possible across the grain boundary in both cases (figures 2.18(a) and (b)). It is however, the arrangement in figure 2.18(a) that has a more favorable relative position for shear transfer, and thereby S+T twin nucleation, as impingement of the slip system is more likely in this case. Therefore, based upon the geometry, an attempt can be made to answer whether slip transfer plays a significant role in twin formation.

FF HEDM characterization enables the determination of grain orientations and positions, along with quantification of grain averaged stress tensors. It should be noted however, that the uncertainty associated with the determination of the grain centers of mass using FF HEDM is relatively high (most available literature puts it in the order of $10 \mu m$ (Turner et al., 2016)). Moreover, it is not possible to obtain information about grain morphology using FF HEDM, since only the grain centroids are calculated. It is in this context that NF HEDM can be used to assess grain positions determined using FF HEDM, since the positional error using the former method is at least an order

of magnitude smaller. Moreover, with the finer resolution data obtained from NF HEDM it is possible to determine the morphology of individual grains within the interrogated volume.

An important goal of this work is to determine the limits of usability of FF HEDM data, mainly in terms of the error associated with grain position. Using FF data in conjunction with NF analysis, the relative difference in grain positions and orientations can be determined. This information, combined with the grain averaged stress tensors can be invaluable in understanding local deformation behavior—for example mechanical twinning and the role of local strain accommodation in its nucleation.

Using FF HEDM, a measure of the average local stress state, in the form of grain averaged local Schmid factors can be obtained, along with average grain orientation. In order to make an assessment of obstacles in the path of slip however, it is important to take into account the lattice rotation gradients and spatially resolved local stress tensor. In this respect, DAXM proves to be a very useful characterization tool. This would enable a better understanding of the interplay between slip transmissibility and its correlation to slip system specific GND density. It is of particular interest to understand the character of geometrically necessary dislocations piling up at grain boundaries, and their effect on slip transfer. The broad underlying hypothesis here is that regions of local high GND concentrations would act as or reflect impediments to efficient slip transfer. Conversely, low local GND concentration regions near grain boundaries may reflect efficient slip transfer through the boundary, or, a general lack of dislocation activity in the region. As DAXM can also be used to obtain spatially resolved stress tensor information, lattice rotation gradient and grain morphology, it should be possible to correctly interpret the significance of a low GND density near a grain boundary.

The broader goal of this work is to develop a three-dimensional understanding of local deformation behavior near grain boundaries. The ability to predict twin nucleation can help in optimizing microstructure design for room temperature formability. Additionally, prediction of crack initiation sites due to cyclical loading conditions are a challenge in material and component design – local heterogeneity in stress states is an important consideration here. It is well-known that realistic

information on the grain morphology is critical to developing reliable CP models (Zhang et al., 2015). It is expected that a more detailed understanding of the local processes of deformation will reveal relationships that can be introduced into models in order to develop better constitutive formulations that can successfully predict the details of deformation processes near grain boundaries. Such information will improve the ability to bridge the gap between modeling in the microstructural and bulk (continuum) scales. This is important for optimal microstructure design via material processing, as well as going beyond a statistical damage model for prediction of catastrophic failure of in-service structural components.

CHAPTER 3

MATERIALS AND METHODS

3.1 Titanium specimens

Commercial purity titanium specimens were used for both the far field HEDM and DAXM experiments. The chemical composition of the specimens is given in table 3.1 (Bieler et al., 2014). The source material had been annealed to obtain an average grain size of 100 μm .

3.1.1 Tensile specimen for Far Field Experiment

The tensile specimen used for the HEDM in-situ deformation experiment was cut out of a larger sample that was previously subjected to a four point bending test, as shown in figure 3.1. Results of the characterization of this bend specimen has been discussed in a prior work (Wang et al., 2009b). Figure 3.2 shows the distribution of the normal component of the strain tensor (ϵ_{zz}) within a cross section of the gage volume interrogated using FF HEDM. The top half of the cross section shows a compressive residual character, while the bottom half shows a tensile character. This strain state is typical of a cross section of a bent beam, where the neutral axis passes through the center and has a strain approaching zero. The tensile specimen had a 1 mm square cross section with a nominal gage length of 5 mm. Texture analysis of the source specimen revealed that a high density of $\{0001\}$ poles were concentrated around a 30° cone centered about the tensile axis of the bending test as described in previous work (Wang et al., 2010b). This preferred $\{c\}$ texture is about 8 times random parallel to the tensile axis. Therefore, a majority of the grains had a hard orientation with respect to the tensile direction.

Table 3.1: Composition (wt%) of Grade 1 Titanium Plate. Adapted from Bieler et al. (2014)

Element	O	Fe	Al	Cu	C	Ni	S	Cr	N	Ti
Fraction	0.169	0.049	0.017	0.017	0.015	0.013	0.011	0.011	0.004	bal.

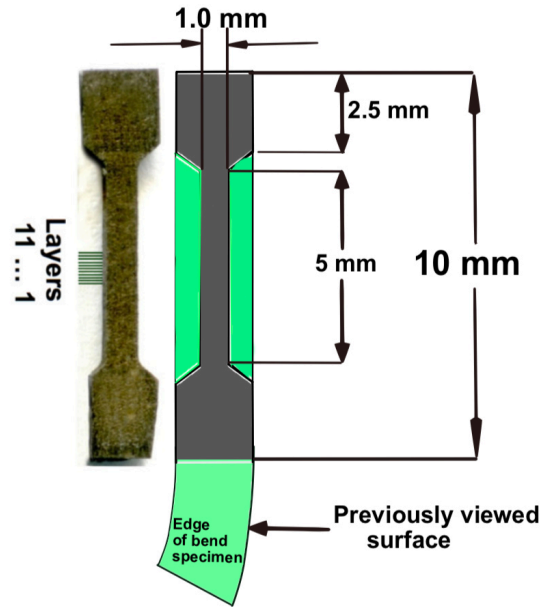


Figure 3.1: Tensile specimen extracted from a larger sample that was previously subjected to a bend test. Because the sample had a prior bending load, a macro residual stress was initially present in the sample (Wang et al., 2014)

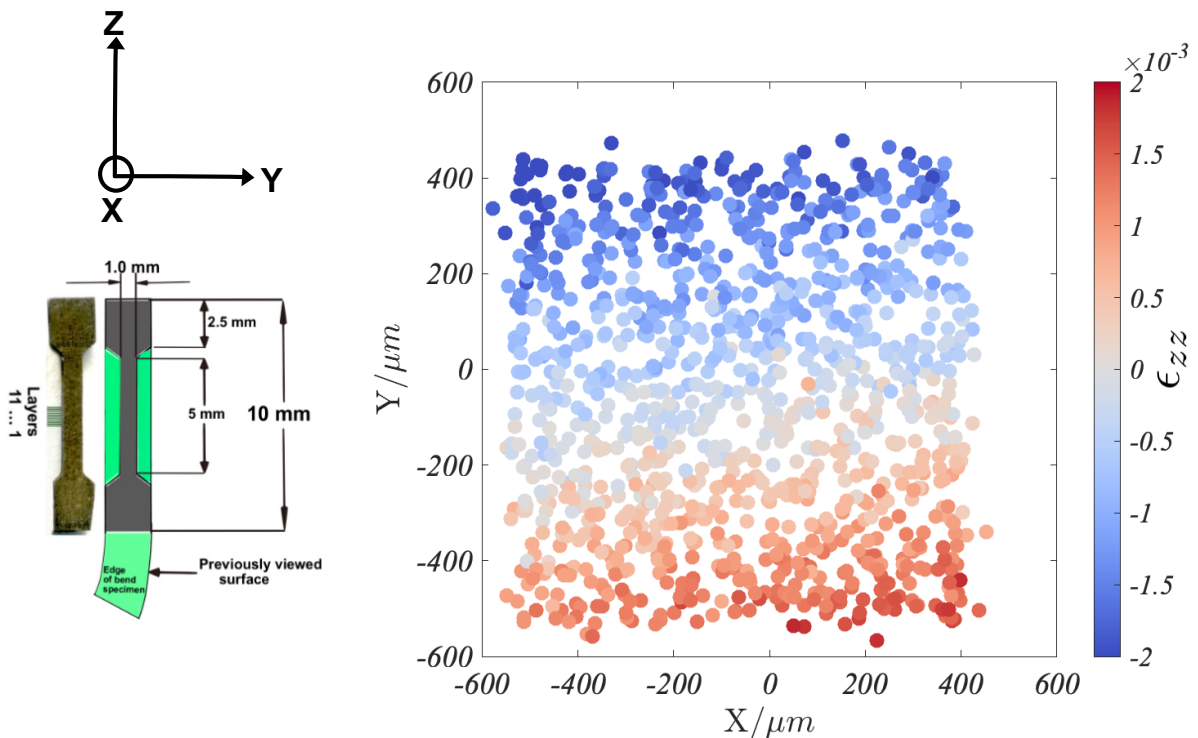


Figure 3.2: Right: Cross section of the illuminated volume of the tensile specimen (looking down the tensile axis), showing the distribution of the normal component of the strain tensor (ϵ_{zz}), prior to tensile loading. Left: the coordinates of the strain map are shown in context of the tensile specimen. The tensile axis is parallel to the Z direction.

3.1.2 Four point bending specimen for DAXM Experiment

The texture of the four point bend specimen had a predominantly soft orientation with respect to the loading direction. A schematic showing the dimensions of the specimen is shown in figure 3.5.

3.2 Far Field HEXRD (Chapter 4)

3.2.1 Experimental setup

The FF-HEXRD experiment was conducted at the beamline 1-ID of the Advanced Photon Source (APS), Argonne National Laboratory. The specimen was mounted on a custom designed load frame and deformed in 37 load steps. Figure 3.3 shows the experimental setup of the FF-HEDM; along with the sequence of tensile loading to $\sim 3\%$ engineering strain and subsequent unloading. Elastic loading took place in the first seven steps, followed by plastic deformation during the succeeding 23 steps. The last seven steps correspond to the unloading of the specimen. It was anticipated that the initial texture, loading state and the relatively high resolved shear stress on twin planes were conducive to the nucleation of $\{10\bar{1}2\}\langle\bar{1}011\rangle$ deformation twins.

Following each load step, the central gage section was illuminated by a high energy (~ 65.4 keV) monochromatic X-ray beam. An area detector with resolution of 2048×2048 pixels, spanning an area of $0.4 \times 0.4m^2$ was placed about 1 m away from the specimen. After each load step, the specimen was held at constant displacement and rotated about the tensile axis through an ω range of 140° (20° to 160°). Diffraction (Debye-Scherrer) patterns were collected for each step of 1° . The monochromatic beam was used to interrogate eleven $\sim 100\mu m$ thick layers along the gage length. Thus, for each of the 37 loading steps, a total of 140 diffraction patterns were collected for each layer examined.

The inset of figure 3.3 shows a schematic illustration of the trend of the load time plot corresponding to the tensile test. Significant relaxation of load was observed during the course of loading and subsequent unloading. The FF scans for each load step were taken after most of the relaxation

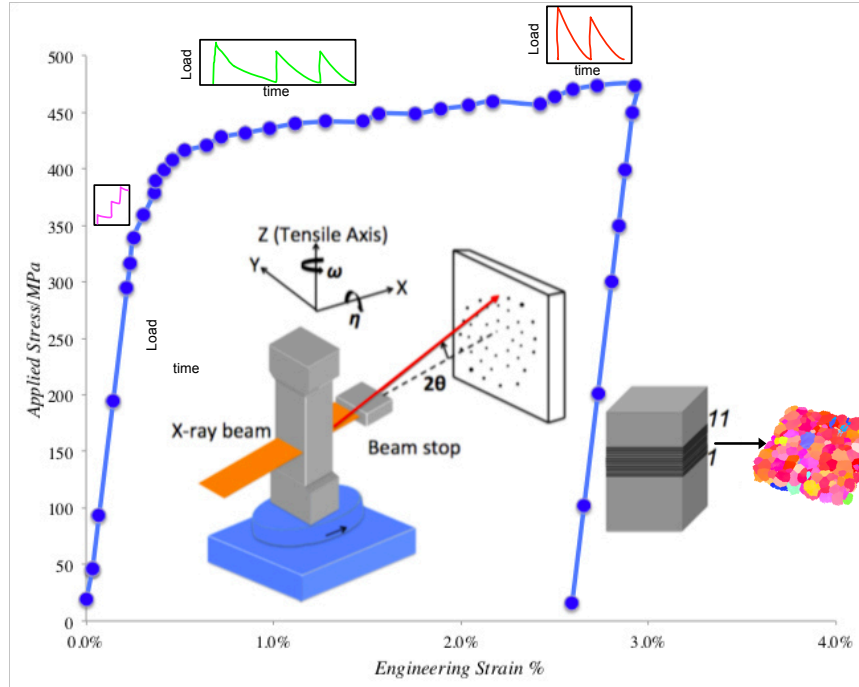


Figure 3.3: Evolution of global stress as function of engineering strain for the tensile experiment. Inset figure shows a schematic representation of the experimental setup for FF-HEDM. A schematic representation of the eleven layers examined along the gage section of the tensile is shown on the right. Inset: Schematic illustration of the load relaxation with respect to time is shown for three different strain states—prior to yield (magenta), post yielding (green) and at maximum stress (red).

had taken place. Figure 3.3 (inset) shows the schematic illustration of the load time curves for three different strain states: prior to yield (where a 2-3% relaxation was observed, represented by the magenta curve), post yield (6-8% relaxation: green curve) and at maximum stress (8-9% relaxation: red curve).

3.2.2 Post deformation surface EBSD of the tensile specimen

After the tensile experiment was completed the far side (facing the detector) of the unloaded specimen was lightly ground and electropolished. The surface was then examined using a Tescan Mira 3 scanning electron microscope equipped with an Orientation Imaging Microscopy™ system (Ametek, Mahwah NJ). Electron backscattered diffraction (EBSD) maps were obtained of the $1000\mu\text{m} \times 1000\mu\text{m}$ center of the gage length in the region examined using FF-HEDM. A step size of $2\mu\text{m}$ was used for the EBSD scan. Figure 3.4 shows the orientation map of the scanned

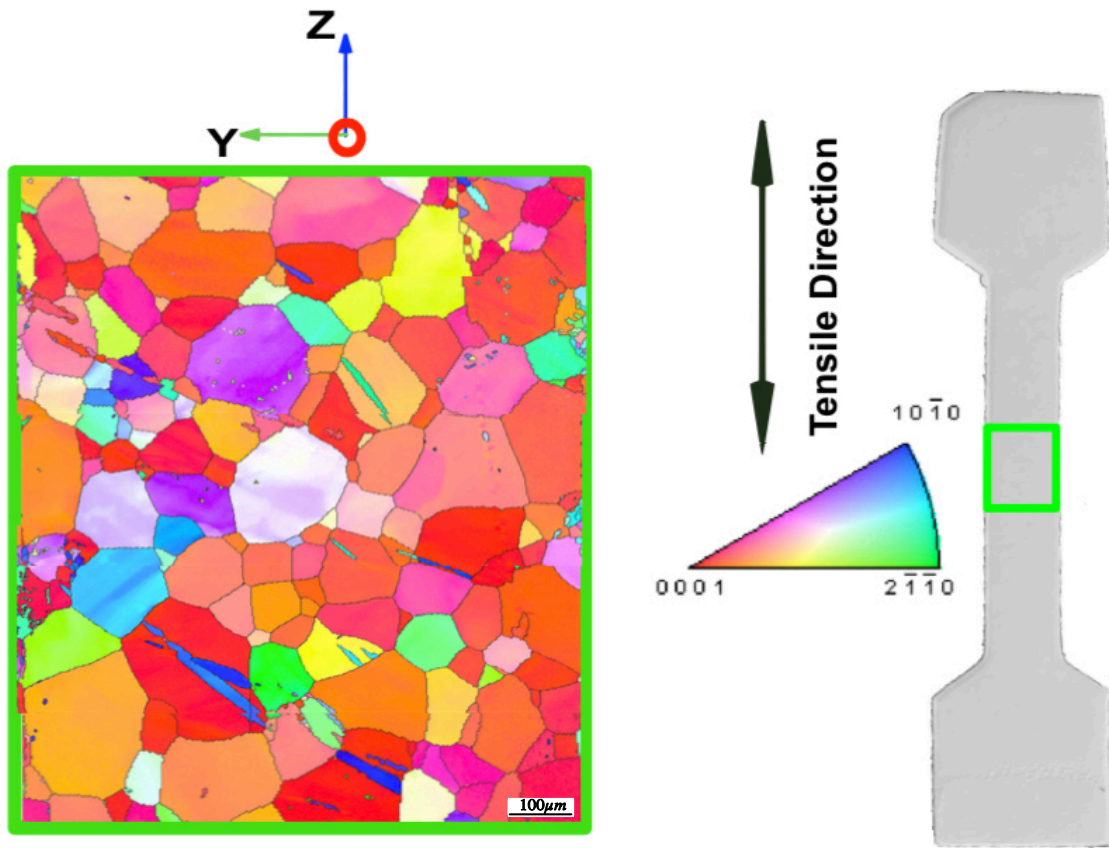


Figure 3.4: Surface tensile direction EBSD IPF map of the far side (facing detector) of the gage section of the unloaded specimen shows several twins and orientation gradients in some grains. The scanned area is highlighted in green.

region. Several discrete deformation twins and strong orientation gradients within some grains were observed in the microstructure.

3.3 Experimental setup for in-situ DAXM characterization (Chapter 6)

The bend specimen was mounted on a custom built four pointing bending stage as shown in figure 3.5. Deformation was carried out in four increments to a curvature on the tensile surface that corresponded to a bulk strain of 3.5%. For each strain increment, a highly collimated polychromatic beam of cross section $1\mu\text{m} \times 1\mu\text{m}$ was used for a coarse DAXM characterization with a step size of $6\mu\text{m}$. A detailed description of this serial probing method is given in (Eisenlohr et al., 2017).

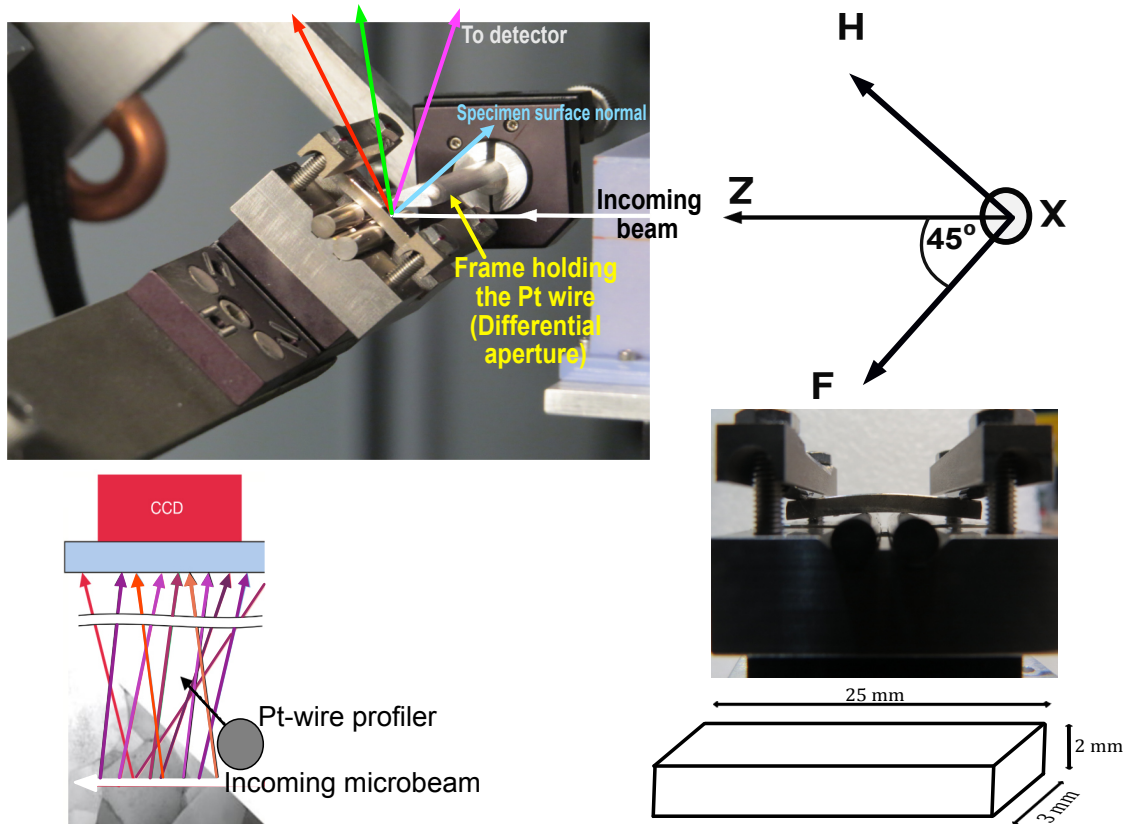


Figure 3.5: CP-Ti sample setup in the four point bending stage and dimensions are shown on the bottom right of the figure. Experimental setup for the in-situ DAXM characterization of four point bending is shown on the top left. The directions of the incoming and diffracted beams are shown schematically. The beamline coordinate system is shown on the top right: Z denotes the direction of the incoming beam; F is anti-parallel to the surface normal (denoted by the green vector) of the specimen; X is directed normal out of the page. Position and displacement direction of the differential aperture (Pt wire) are shown on the bottom left of the figure (Adapted from Larson et al. (Larson et al., 2002)).

A volume of $600\mu\text{m} \times 400\mu\text{m} \times 325\mu\text{m}$ was interrogated in this experiment. At the second strain increment, a set of more finely spaced scans was done (step size of $1.5\mu\text{m}$), along the X and H directions. Laue diffraction patterns were collected on a system of area detectors of 2048×2048 pixel resolution.

Additionally, for each bending increment the beam was switched to monochromatic mode and energy wire scans were conducted within two specific grains of interest. For the first grain, the energy wire scan was done for all the four strain increments; for the second grain it was done until the third increment due to beam time limitations. Details of these scans are elaborated in chapter 6.

CHAPTER 4

IN-SITU FAR FIELD XRD CHARACTERIZATION OF TENSILE DEFORMATION OF A COMMERCIAL PURITY TITANIUM SPECIMEN

In this chapter the tools and methodologies use to analyze data the FF HEDM tensile experiment are elaborated, followed by a detailed elucidation of the results and their discussion. The methodology used to identify twinning events from the FF HEDM data is discussed in detail. The possibility of deformation twinning nucleated as a result of slip transfer from a neighboring grain (S+T twinning) is explored in terms of local stress evolution in the parent (twinned) and neighboring grains, and geometrical consideration (based on slip transfer parameter m' and relative grain positions in 3D space). Furthermore, these relative grain positions and geometrical criteria are re-evaluated in the context of more recently collected near field (NF) data corresponding to the final unloaded stress state of the specimen.

A central question sought to be answered here is with respect to the robustness of the FF HEDM data, i.e. how well do the kinematics in terms of grain disorientation as a function of load step, match the grain averaged stress measurements.

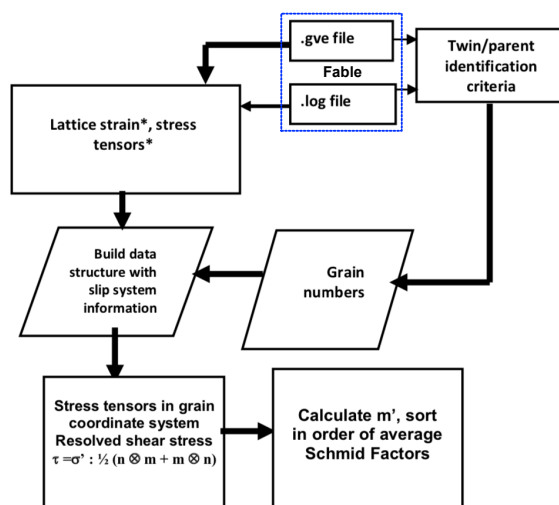


Figure 4.1: Outline of data analysis strategy that was implemented in a suite of MatLab codes. The .log files (containing orientation and grain index information), and .gve files (containing scattering vector information) are obtained using FABLE.

4.1 Analysis of the diffraction patterns

The collected diffraction patterns were analyzed using FABLE, an open source software developed jointly by the European Synchrotron Research Facility (ESRF) and the Risø National Laboratory Denmark. The analysis follows three fundamental steps. The first step identified peaks that lie above a specified threshold value using the *Peaksearch* module. The second step assigned reciprocal lattice vectors (g_{hkl}) to each of the peaks identified in the first step, using the *Transformation* module. Finally, the *Grainspotter* module indexed individual grains by correlating at least 30 g_{hkl} with a given lattice orientation. This process was repeated for each load step for all 11 layers.

4.1.1 Determination of grain centers of mass and grain averaged strain tensors

The grain centers of mass (COM) and grain average strain tensors were calculated using the least squares algorithm proposed by Margulies et al. (2002), and more recently implemented for AZ31 by Aydiner et al. (2009).

Following the formulation in equation 2.42, a modified version is used after addition of two correction terms that account for the offset in the sample coordinate system from the center of rotation (Margulies et al., 2002). This is written as shown below.

$$\epsilon_i = (l_i \ m_i \ n_i) \begin{pmatrix} \epsilon_{11} & \epsilon_{12} & \epsilon_{13} \\ \epsilon_{21} & \epsilon_{22} & \epsilon_{23} \\ \epsilon_{31} & \epsilon_{32} & \epsilon_{33} \end{pmatrix} \begin{pmatrix} l_i \\ m_i \\ n_i \end{pmatrix} - \left[\cos(\omega_i) + \frac{\sin(\omega_i) \sin(\eta_i)}{\tan(\theta_i)} \right] \frac{\Delta x}{L} - \left[\sin(\omega_i) + \frac{\cos(\omega_i) \sin \eta_i}{\tan(\theta_i)} \right] \frac{\Delta y}{L} \quad (4.1)$$

Where Δx and Δy are the offsets from the center of rotation; ω_i is angle of rotation about the tensile axis; η_i the azimuthal angle; θ_i the Bragg angle corresponding to diffraction vector i ; and L is the specimen to detector distance.

The lattice strain is calculated using the reciprocal lattice vectors for an ideal unstrained hexagonal titanium unit cell as reference. The lattice parameters used for the reference unit cell are $a_0 = b_0 = 2.95$ nm and $c_0 = 4.683$ nm; $\alpha = \beta = 90^\circ$ and $\gamma = 120^\circ$. The set of reciprocal lattice vectors in fractional crystallographic coordinates to the corresponding vectors in the Cartesian

coordinate system by the following relation.

$$g_{cart} = T g_{cry} \quad or \quad g_{cry} = T^{-1} g_{cart} \quad (4.2)$$

Where

$$T = \begin{pmatrix} a_0 & b_0 \cos(\gamma) & c_0 \cos(\beta) \\ 0 & b_0 \sin(\gamma) & \frac{c_0(\cos(\alpha) - \cos(\beta) \cos(\gamma))}{\sin(\gamma)} \\ 0 & 0 & \frac{V}{a_0 b_0 \sin(\gamma)} \end{pmatrix} \quad (4.3)$$

is the transformation matrix;

$$V = a_0 b_0 c_0 (1 - \cos^2(\alpha) - \cos^2(\beta) - \cos^2(\gamma) + 2 \cos(\alpha) \cos(\beta) \cos(\gamma)) \quad (4.4)$$

is the volume of the unstrained unit cell. g_{cart} and g_{cry} are the set of vectors in the Cartesian and fractional crystallographic coordinate systems respectively. For each indexed grain the change in interplanar spacing is determined in terms of the difference between the measured and ideal reciprocal lattice vectors.

$$\Delta g_{hkl} = \|(g_{hkl})_{measured}\| - \|(g_{hkl})_{ideal}\| \quad (4.5)$$

For each indexed grain, the elastic strain for each measured reflection (reciprocal lattice vector) is given as follows.

$$\epsilon = \frac{\Delta g_{hkl}}{(g_{hkl})_{ideal}} \quad (4.6)$$

From equations 4.1 and 4.6, an overdetermined system of linear equations can be written as:

$$AX = b \quad (4.7)$$

For n reflections, A is an $n \times 8$ matrix. Here each row of A (A_i) contains strain terms and offset from center of rotation corresponding to each measured g -vector i :

$$A_i = [l_i^2, m_i^2, n_i^2, 2l_i m_i, 2l_i n_i, 2m_i n_i, \Delta x, \Delta y].$$

b is an $n \times 1$ vector: $b_i = \epsilon_i$.

X is the vector containing the six symmetric components of strain tensor and center of mass coordinates.

The system of equations $X = A^{-1}b$ can be solved by least squares or singular value decomposition. A minimum of 17 independent reflections for each indexed orientation are necessary for a reliable solution (with a fitting error of the order of 10^{-4} or lower) (Margulies et al., 2002).

The algorithm outlined above is implemented in a suite of MatLabTM codes. The grain average stress tensor for each indexed grain is calculated as shown below. Here, C_{ijkl} is the fourth order stiffness tensor for hexagonal titanium; XYZ refers to the sample coordinate system and 123 denotes the crystal coordinate system defined by the the orientation matrix g :

$$\begin{pmatrix} \epsilon_{XX} & \epsilon_{XY} & \epsilon_{XZ} \\ \epsilon_{YX} & \epsilon_{YY} & \epsilon_{YZ} \\ \epsilon_{ZX} & \epsilon_{ZY} & \epsilon_{ZZ} \end{pmatrix} \xrightarrow{\epsilon_{\text{cry}}=g \cdot \epsilon_{\text{sam}} \cdot g^T} \begin{pmatrix} \epsilon_{11} & \epsilon_{12} & \epsilon_{13} \\ \epsilon_{21} & \epsilon_{22} & \epsilon_{23} \\ \epsilon_{31} & \epsilon_{32} & \epsilon_{33} \end{pmatrix} \xrightarrow{\sigma_{ij}=C_{ijkl} \cdot \epsilon_{kl}} \begin{pmatrix} \sigma_{11} & \sigma_{12} & \sigma_{13} \\ \sigma_{21} & \sigma_{22} & \sigma_{23} \\ \sigma_{31} & \sigma_{32} & \sigma_{33} \end{pmatrix} \xrightarrow{\sigma_{\text{sam}}=g^T \cdot \sigma_{\text{cry}} \cdot g} \begin{pmatrix} \sigma_{XX} & \sigma_{XY} & \sigma_{XZ} \\ \sigma_{YX} & \sigma_{YY} & \sigma_{YZ} \\ \sigma_{ZX} & \sigma_{ZY} & \sigma_{ZZ} \end{pmatrix}$$

4.1.2 Quantification of error in local strain calculations

In this section, the procedure to calculate the fitting error in the least squares algorithm discussed above is shown. Equation 4.7 can be rewritten as follows.

$$\epsilon = \epsilon_{11}l^2 + \epsilon_{22}m^2 + \epsilon_{33}n^2 + \epsilon_{12}lm + \epsilon_{13}ln + \epsilon_{23}mn \quad (4.8)$$

Moreover, in terms of interplanar spacing the lattice strain ϵ can be written as follows (Margulies et al., 2002).

$$\epsilon = \frac{d - d_0}{d_0} \quad (4.9)$$

The error of fit can be expressed as the residual of the sum of squares $d\epsilon$.

$$d\epsilon = \Sigma (AX - b)^2 \quad (4.10)$$

Taking into account the error of fit, the six symmetric components of the strain tensor can be written as follows.

$$\epsilon_{\pm} = [\epsilon_{11} \pm d\epsilon, \epsilon_{22} \pm d\epsilon, \epsilon_{33} \pm d\epsilon, \epsilon_{12} \pm d\epsilon, \epsilon_{13} \pm d\epsilon, \epsilon_{23} \pm d\epsilon] \quad (4.11)$$

As shown in 4.1.1, the anisotropic Hooke's law can be used to determine the error in stress measurement, which can be expressed in terms of an equivalent scalar value (von Mises stress).

The average equivalent stress error for the data evaluated in this work was found to be ~ 10 MPa, which is within 10^{-4} in terms of equivalent strain.

4.2 3D Reconstructed model of the microstructure prior to loading

In order to facilitate the study of grain interactions in 3D space, it is important to obtain an estimate of neighboring grains, grain morphology and their relative positions. Also, simulating the experiment with a computational model enables assessment of material model assumptions by direct comparison of the local stress-strain history in individual grains. To this end, a set of seed points were generated using the COM and Bunge Euler angle information of identified grains at zero strain load step for each of the 11 layers. Grain orientations that were misoriented by less than 5° and with a Euclidean distance less than $100\mu\text{m}$ between the centers of mass in two or three successive layers were assigned the same grain number. The importance of closely capturing the three-dimensional morphology of the actual microstructure has been shown in the work done by Zhang et al. (2015). Using this set of seed points in 3D space, a non-periodic model of the experimentally investigated microstructure was constructed (figure 4.2) with 10^6 volume elements, using a Voronoi tessellation module available in DAMASK (Düsseldorf Advanced Materials Simulation Kit).

4.2.1 Model parameters and simulation of tensile test

The specimen used for the tensile experiment had several grains with strong compressive residual stresses prior to loading. In order to capture this initial stress state, a uniform compressive strain of 10^{-3} was applied for each of the first three load steps. This was based on the determination of

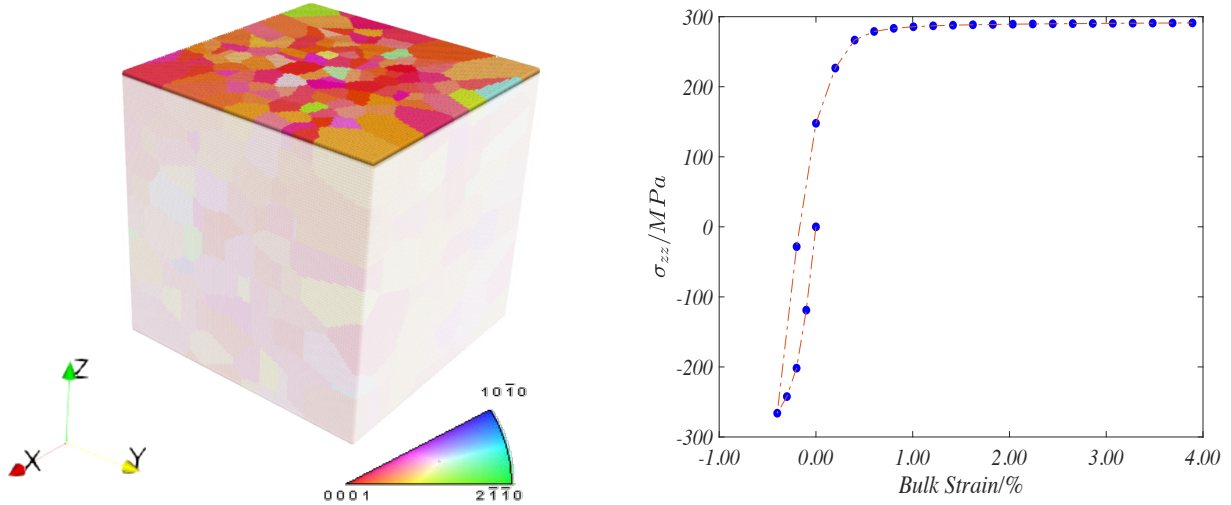


Figure 4.2: Left: Voronoi tessellated model generated from 3D XRD Data set. This microstructure shown here represents the unstrained condition, prior to the tensile test. A dilatational layer of one volume element thickness is used as the surrounding medium along the X and Y directions. The tensile direction is parallel to the Z axis. Right: Evolution of normal component of stress along the tensile direction σ_{zz} in the crystal plasticity simulation of the tensile loading. In the CP model, a uniform compressive strain of 10^{-3} is applied for each of the first three load steps; followed by a uniform tensile strain of 10^{-3} for each of the subsequent load steps.

the average initial equivalent strain in the volume interrogated by 3D XRD (which was of the order of 10^{-3}). Hereafter, a uniform tensile strain of $10^{-3}/s$ was applied for the subsequent 42 load steps to impose a bulk tensile strain of $\sim 4\%$. The evolution of the normal component of the bulk stress tensor (parallel to tensile axis) is shown in figure 4.2.

The crystal plasticity model was implemented using the DAMASK spectral solver (Eisenlohr et al., 2013). Since the model is non-periodic and the spectral solver requires imposition of periodic boundary conditions, the microstructure was sheathed in a dilatational layer (free surface) of one volume element thickness along the X and Y directions (figure 4.2, left). The constitutive description of the model is based on the phenomenological power law described in section 2.3. The material parameters used in the current model are enumerated in table 4.1.

Table 4.1: Parameters used in Crystal Plasticity model

Parameter	Value	Units
C_{11}	162.2	GPa
C_{12}	91.8	GPa
C_{13}	68.8	GPa
C_{33}	180.5	GPa
C_{44}	46.7	GPa
$\dot{\gamma}$	1×10^{-3}	s^{-1}
τ_0^{Slip} (per family)	[80,90,110,260,260,260]	MPa
τ_0^{Twin} (per family)	[220,220,250,250]	MPa

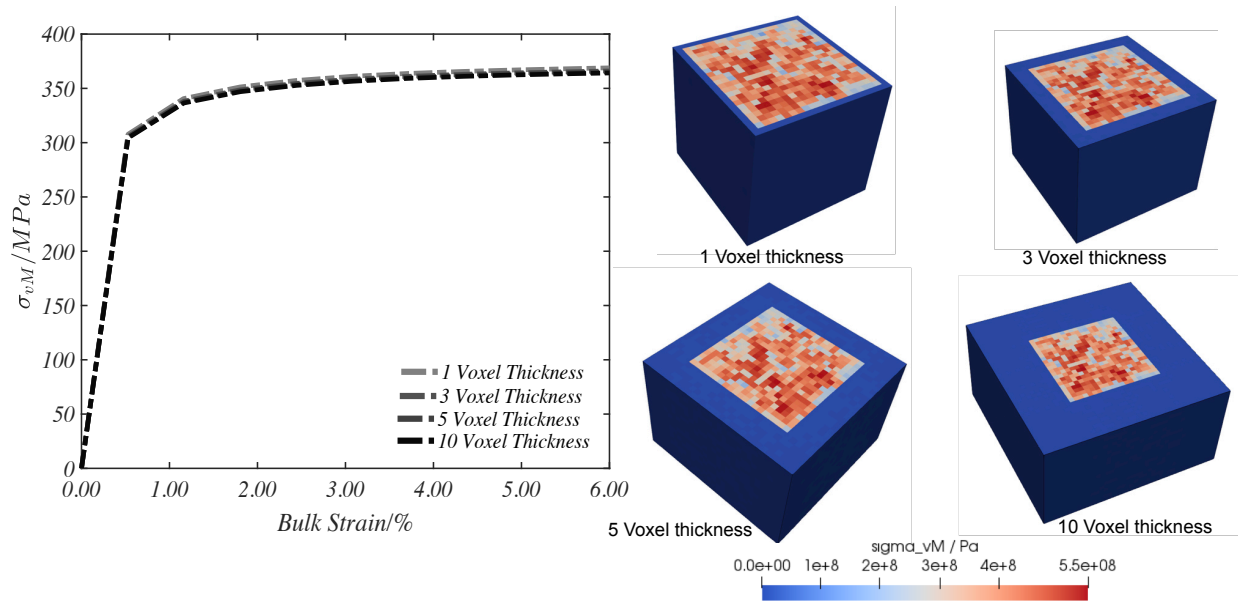


Figure 4.3: Evolution of volume averaged equivalent (von Mises) stress of the far field microstructure model as a function of bulk strain for four different thicknesses of the surrounding free surface layer. It is seen that the mechanical response is not sensitive to dilatational layer thickness.

4.2.2 Sensitivity of mechanical response of model to dilatational layer thickness

An important question arises with regard to the free surface layer used around the microstructure model—how sensitive is the model response to the layer thickness? In order to assess this, the volume averaged stress evolution of the model was evaluated for four different thicknesses of the dilatational layer. It can be observed from equivalent stress plot in figure 4.3 that the effect of dilatational layer thickness on the average mechanical response of the model is not significant.

4.3 Effect of local stress state on deformation systems

The top row of figure 4.4 shows the cumulative distribution of global Schmid factors corresponding to three load steps for basal $\langle a \rangle$, prism $\langle a \rangle$, pyramidal $\langle a \rangle$, pyramidal $\langle c + a \rangle$ and T1 twin systems. In this case the stress tensor is the same for all load steps (based on global uniaxial tension). The small changes in the cumulative distribution profiles are purely due to small crystal rotations with increasing strain.

The generalized Schmid factor, calculated using the average local stress tensor for each grain is shown on the middle and bottom rows (Dashed lines indicate data from experiment, while the solid lines correspond to the CP model). Using the local stresses, the CP model predicts lesser activity than observed for all slip systems. The middle row shows the comparison with a model that did not have the initial compressive strain imposed before tensile loading. Clearly, the strain history plays an important role with regard to the slip systems that are likely to be activated, as the predicted activity is closer to the observed activity for every slip system when the pre-compression takes place. Compared to the global stress, the likelihood of pyramidal $\langle c + a \rangle$ slip and T1 twinning being activated is much higher when the local stress state is considered. Clearly, the texture is highly favorable for pyramidal $\langle c + a \rangle$ slip, while being less conducive to $\langle a \rangle$ slip on basal, prism, or pyramidal planes.

Several significant observations can be made with regard to the comparison between the experimental and model data. Prior to loading, the experimental data show a similar propensity for pyramidal $\langle c + a \rangle$ slip and T1 twinning. The corresponding model data (with the initial compression) indicates a much lower likelihood of T1 twinning at this stage, when compared with the tension-only model and experiment. This indicates that the stress state of most grains in the model is such that they are not able to overcome the initial critical stress necessary for twinning. Both models show a similar lower likelihood of pyramidal $\langle c + a \rangle$ slip when compared with experiment prior to tensile loading. For basal $\langle a \rangle$ and prism $\langle a \rangle$ slip, the model with initial compression tracks the experimental data more closely than the tension-only model.

At approximately 0.4% bulk strain (about half way through yield), the model with initial com-

pression tracks the experimental data more closely for prism $\langle a \rangle$ and pyramidal $\langle a \rangle$ slip. It can also be seen that the fraction of grains with a propensity to form twins has increased significantly compared to the unstrained state. For T1 twinning, the tension-only model is closer to the experiment.

At 1.5% bulk strain, all of the grains should have experienced plastic deformation. The model with initial compression captures the experimental trend for prism $\langle a \rangle$, pyramidal $\langle c + a \rangle$ and T1 twinning better than the tension-only model. It can be seen that except for basal slip, the model captures the local stress state quite well for the other slip and twin systems. On the other hand, basal $\langle a \rangle$ slip tracks closer to the experiment for the tension-only model. It is apparent that once initial compressive residual stresses are overcome, the model with initial compression matches the experiment quite closely for most of the deformation systems.

4.4 Identification of twinning events

Twinning events during the in-situ tensile test were identified using the following misorientation and spatial proximity criteria:

1. The twin and corresponding candidate parent must have a c-axis misorientation of 85° and share a common a-axis.
2. Because the average grain size of the area of interest is about $100\mu m$, the centers of mass of the candidate twin and parent grain must be sufficiently close together for the twin to be plausibly within the parent grain.
3. The twinned orientation must be present in at least two consecutive load steps.

This method of identifying a twin-parent pair is illustrated in figure 4.5. The three $\{0001\}$ pole figures indicate the initial orientation of indexed grains in layer 1 (prior to tensile loading), at the load step just before the twin was detected (1.3% bulk strain) and after 1.5% bulk strain respectively. The large cluster of points close to the center of the $\{0001\}$ pole figures (where the sample tensile axis is coincident with the center of the pole figure) confirms the initial assumption that hard orientations are predominant in the specimen. It is also clear from the pole figures that the twin is

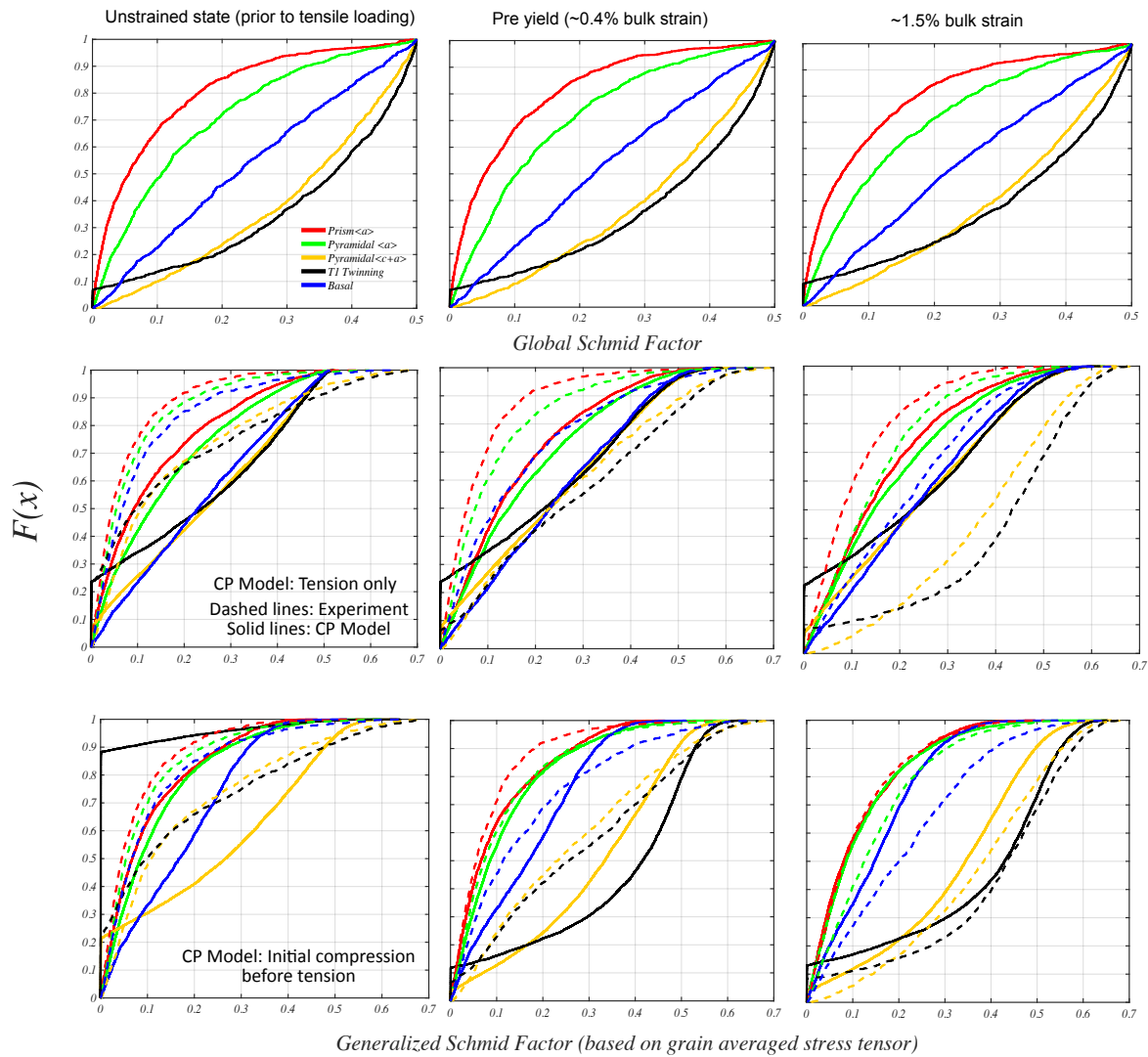


Figure 4.4: Cumulative distribution function (CDF) plots of Schmid Factors corresponding to three load steps for basal $\langle a \rangle$, prism $\langle a \rangle$, pyramidal $\langle a \rangle$, pyramidal $\langle c + a \rangle$ and T1 systems. The global Schmid factor (top row) is calculated using the global uniaxial stress tensor; while the local grain averaged stress tensor is used to obtain generalized Schmid factors (maximum 0.707) (middle and bottom rows). The middle row shows the comparison of the experimentally obtained local Schmid factors with an earlier CP model that imposes only tensile strain without initial compression. The bottom row shows the comparison of local Schmid factors with the results of the CP model with initial compression. The Schmid factors in the CDF plots are the highest per slip system family for each grain.

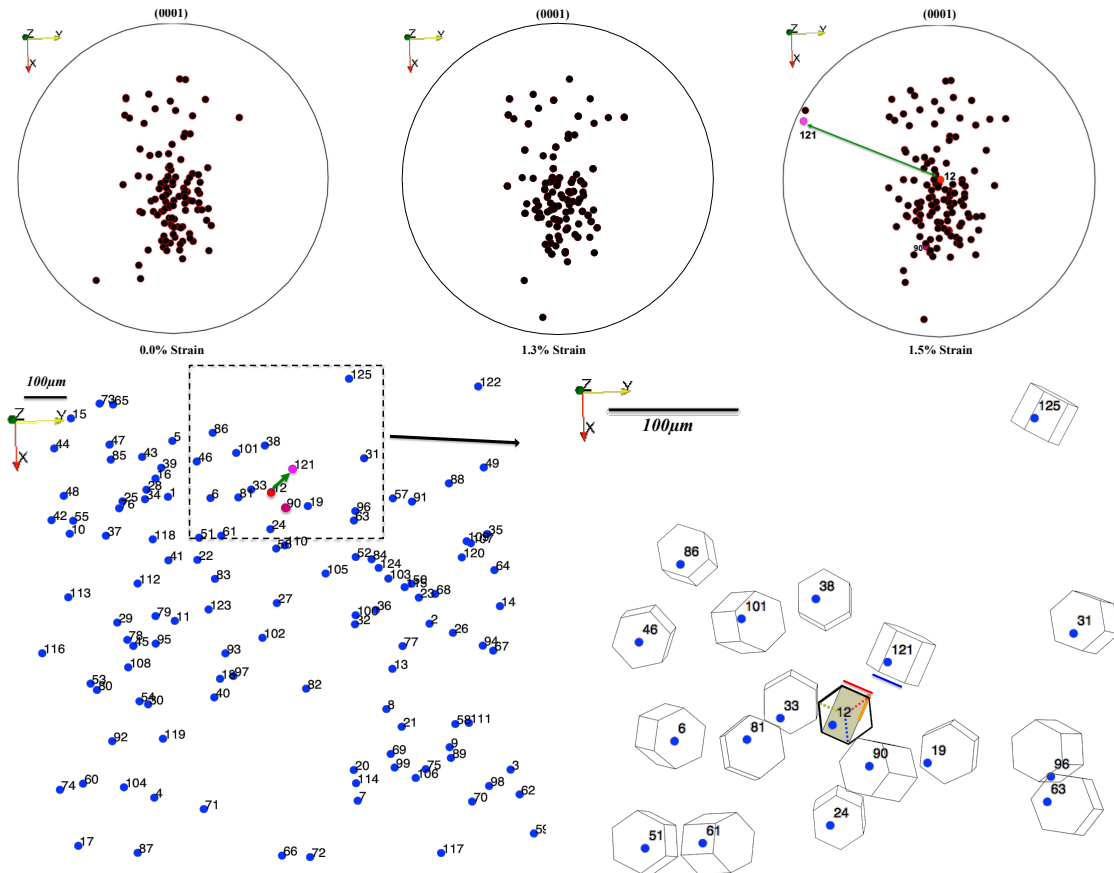


Figure 4.5: Neighborhood of all grains in layer 1 prior to deformation, at the load step just before twinning at 1.3% engineering strain, and after a twin formed at 1.5% engineering strain in orientation space (top row). The spatial map of the 2D slice is shown in the bottom row with grain identification numbers. The bottom right figure shows an enlarged view of the region of interest for the twin formation with grain unit cell orientations based upon geometrical positions in the lower left map of the slice. Tensile direction is along z direction (out of page).

not present in the load step immediately before 1.5%. The paired parent (grain in red numbered 12) and twin (magenta colored grain numbered 121) orientations are shown in the second pole figure in figure (top row right), from the measurement at 1.5% strain. It is important to note here that although there are other grains with orientations near the circumference of the pole figure that appear to be twins, they were not present in at least two consecutive load steps. The corresponding COM positions projected in 2D X-Y space are shown below the pole figures. An enlarged view of the twin-parent pair in layer 1 and its immediate neighborhood is shown with prisms to illustrate the orientations of grains in the vicinity (bottom right of figure). The common $\langle a \rangle$ -axis of the twin and its parent grain is indicated with a magenta line for the parent and blue for the twin.

Altogether, 13 twinning events were observed within the 11 layers (with 2 twins each in layers 3 and 6). The Schmid factors of the T1 twin systems were computed using the measured grain averaged stress tensor. Because this stress tensor is a local stress within the microstructure and not the global stress, the generalized Schmid factor is computed (for which the maximum possible value is $\frac{\sqrt{2}}{2}$). The evolution of the resolved shear stress (RSS) on the six T1 twin variants in the parent grains in the 11 layers are shown for each of the 13 twin events in figures 4.6, 4.7 and 4.8. In each plot of the twinned grain, the observed twin variant is indicated with red dot symbols. In the evolution of the RSS for the first layer, the activated twin variant had the highest RSS value. This is however, not always the case, as observed from the RSS plots for parent grains observed in some of the other layers (e.g 2,3 and 7), which indicates that the Schmid law (highest RSS) did not account for twin nucleation.

4.5 Results and Discussion

The focal point of this work is to examine the propensity of deformation twins being nucleated as a result of shear transfer from a compatible slip or twin system in a neighboring grain. This assessment was done using a compatibility factor (Luster-Morris parameter m')¹.

Geometrically compatible slip systems in neighboring grains can generate twinning partials at the grain boundary, resulting in a sustainable twin nucleus (Wang et al., 2009a). In this context, the value of m' can be used as a criterion to evaluate the possibility of slip transfer from a neighboring grain to an identified parent grain that generated a twin. However, a high value of m' alone is not a sufficient condition to guarantee slip transfer. In addition to the Schmid factor of the slip system in the neighbor grain and m' , a third parameter is considered. A spatial plausibility assessment can be made by taking into consideration the relative position and elevation of the grains with respect to each other. A quantitative criterion for determining a plausible high m' neighbor is outlined in figure 4.9. The likelihood of slip transfer to nucleate a twin will be high if the plane normal of the slip system in the neighbor grain is highly inclined to the vector between centers of mass of the

¹ m' is only meaningful for active slip systems

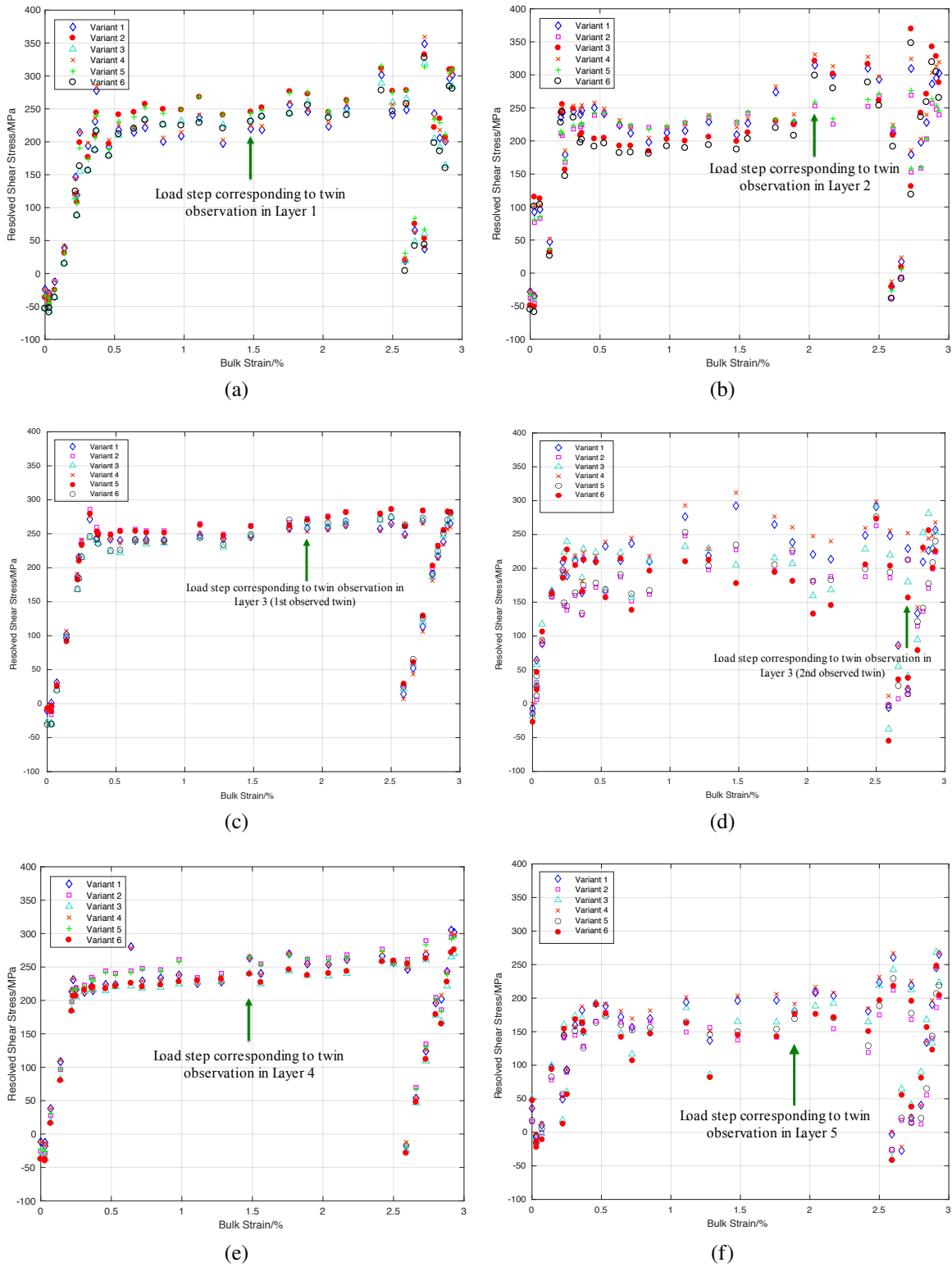


Figure 4.6: Evolution of resolved shear stress (RSS) for each of the six T1 twin systems in the parent grains identified in layers 1, 2, 3, 4 and 5. Green arrows indicate the load step where the twin was first identified, and filled red markers indicate the observed twin variant.

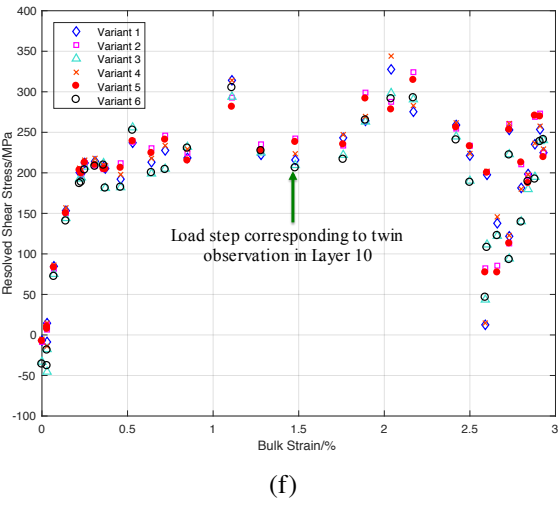
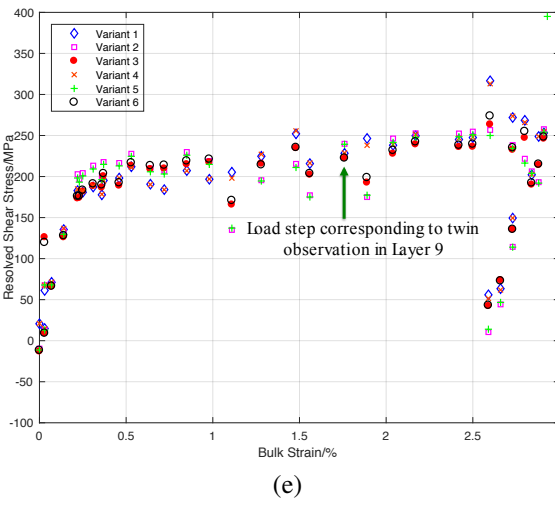
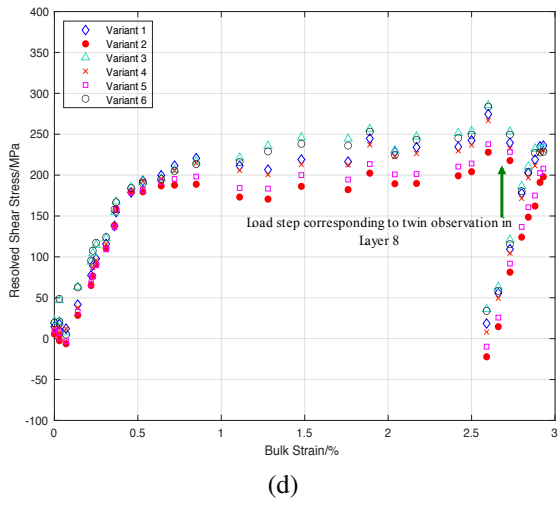
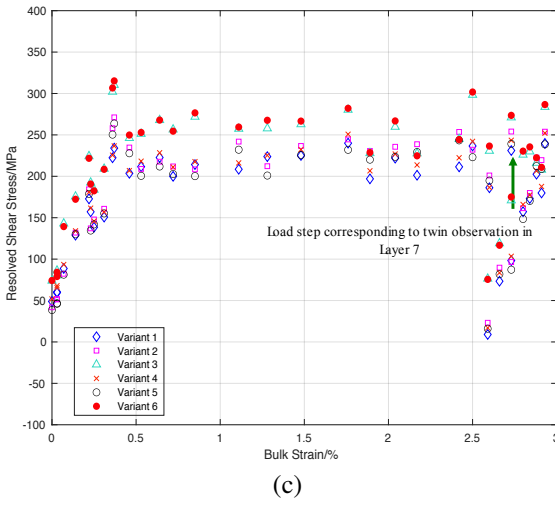
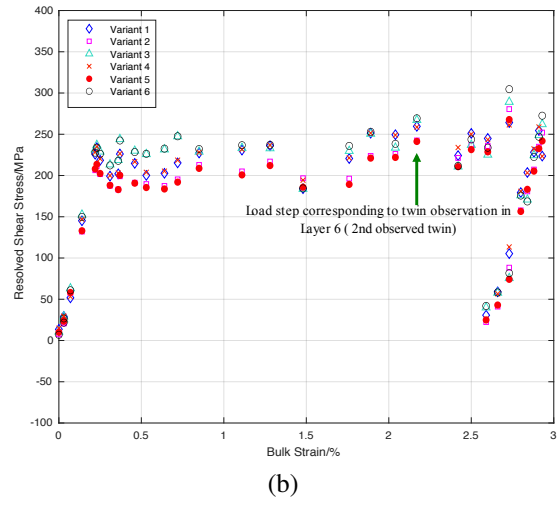
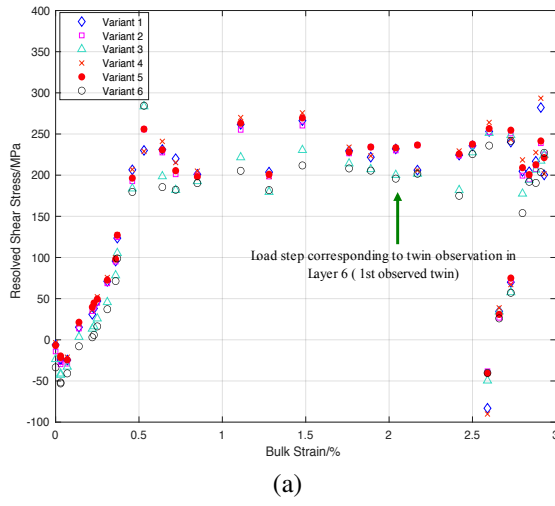


Figure 4.7: Evolution of resolved shear stress (RSS) for each of the six T1 twin systems in the parent grains identified in layers 6, 7, 8, 9 and 10. Details of symbols and color conventions are given in the caption of figure 4.6.

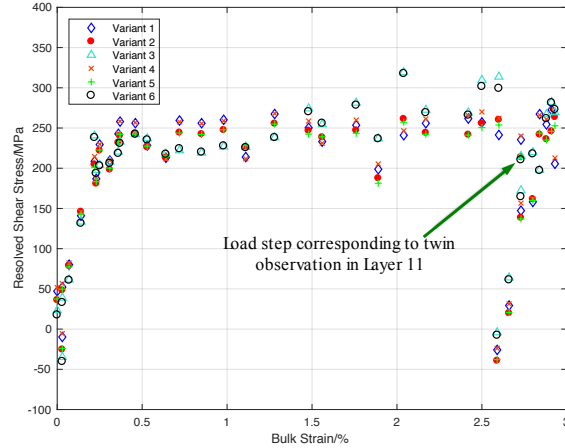


Figure 4.8: Evolution of resolved shear stress (RSS) for each of the six T1 twin systems in the parent grain identified in layer 11. Details of symbols and color conventions are given in the caption of figure 4.6.

two grains, as illustrated in figure 4.9. A high value of $\sin \theta$ implies a high probability that a slip vector trajectory will point into the neighboring grain to stimulate twin nucleation. A smaller value of $\sin \theta$ may induce a twin on one end of the grain boundary but be much less likely to stimulate a twin on the other end of the same boundary. The absolute value of $\sin \theta$, termed here as the spatial alignment factor (SAF), is considered a metric of spatial alignment of the two grains and the slip/twin systems. A SAF value of 1 indicates ideal spatial alignment, while a value of zero corresponds to the lowest likelihood for slip transfer to occur.

4.5.1 Far Field HEDM Characterization

Detailed analysis of the twins identified in six of the 11 layers shown in figure 4.10 illustrate the range of conditions observed. For details of the orientation and relative positions for the remaining twinning events, the reader is referred to appendix A.1.

4.5.1.1 Assessment of slip transfer from neighboring grains

Six different twinning events and their compatibility analysis with respect to the neighboring grains are shown in figure 4.10. The orientations (Bunge Euler angles) of the parent, twin and neighboring grains are indicated for each case. The relative position and orientation relationships

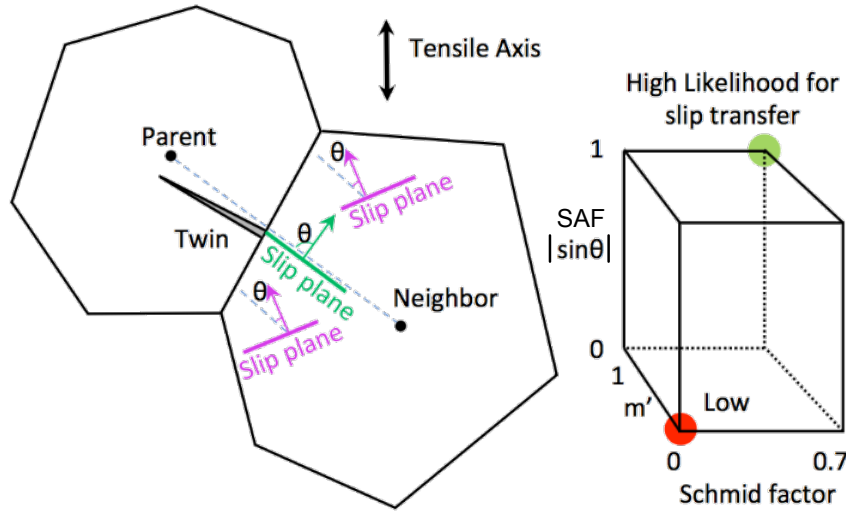


Figure 4.9: Schematic outlining the criteria used to identify the neighbor grain associated with the highest likelihood of slip transfer, thereby triggering a twin. θ is the angle between the unit vector joining the centers of masses of the parent grain and neighbor; and the unit vector normal to the slip plane in the neighbor. The three parameters (Absolute value of the Schmid Factor, Absolute value of $\sin \theta$ (Spatial alignment factor SAF) and m') can be plotted in a 3-D space. A point at the origin (red) would have the worst possible spatial alignment for slip transfer, while a point at the top right corner (green) would have the highest likelihood for slip transfer. The purple slip planes have lower SAF while the green slip plane has a higher SAF.

between the parent grain and neighbor of interest are represented in both the X-Y and X-Z planes, where the Z-axis is the tensile direction. The relative positions of the grain prisms shown are based on the COM values from which a Voronoi tessellated representation of the grain within the microstructure was generated. A corresponding prism indicating the unit cell is overlaid for each grain, with the slip and twin systems indicated by the shaded plane and Burgers vector residing in the plane. The position of the COM of the twin is indicated by the prism without a slip plane indicated. The red-green-blue a_1 - a_2 - a_3 coordinate directions are drawn inside each unit cell; one of these directions is the common $\langle a \rangle$ axis between the twin and parent grains, which allows the rotation axis for the 85° c-axis misorientation of the twin to be visualized.

In layer 1, the twin was observed at approximately 1.5% global strain. The neighborhood of the parent grain and nucleated twin, shown in figure, indicates that most of the grains in the vicinity of the identified parent grain have hard orientations, where the direction of the tensile axis is normal

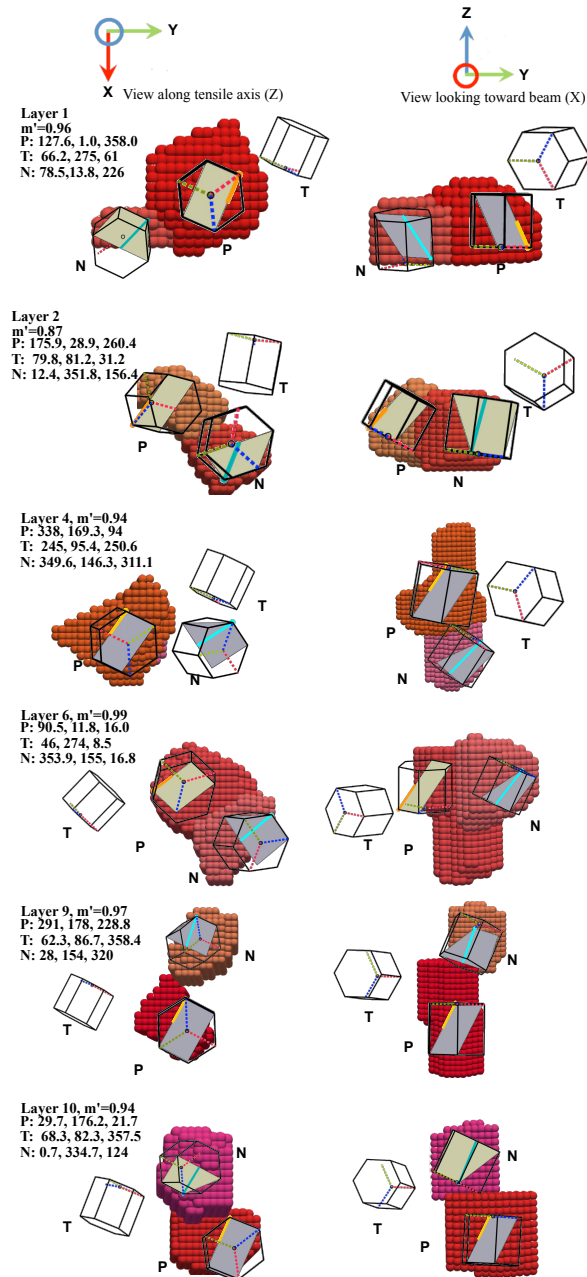


Figure 4.10: The m' relationship observed between the activated twin system and pyramidal $\langle c + a \rangle$ system of a neighboring grain is shown for six different instances (Layers 1,2, 4, 6, 9 and 10). The orientations of the parent, twin and neighboring grains are viewed along the tensile Z axis, (left column) as well as the beam X direction, (right column). The letters "P", "T" and "N" indicate the parent, twin and neighbor grains respectively. The corresponding Bunge Euler angles and m' values are also indicated for each instance. The blue vector shows the slip direction from the blue dot away from it on the positive surface of the plane, and a half length orange dot and vector indicates a twin system. The plane normal points out of the page for beige slip planes and into the page for gray planes. The dotted red, green and blue lines represent the a_1 , a_2 and a_3 directions, respectively. Colors of the grains correspond to (0001) inverse pole figure representations of the orientations.

out of the page. The likelihood of slip/shear transfer between the identified parent grain in layer 1 (grain number 12) with grains adjacent to it in the same layer are assessed using the slip transfer parameter m' . The activated twin system in the parent grain was found to have high m' relationship (~ 0.96) with a pyramidal $\langle c + a \rangle$ system in the neighboring grain number 24.

The relative positions of the two grains in layer 1 are visualized in the first row of figure 4.10, showing the parent grain along with a neighboring grain lying within the same layer; with a pyramidal $\langle c + a \rangle$ slip system that has a high m' value with respect to the activated twin system. The location of the twin is on the other side of the neighboring grain. Furthermore, the direction of shear in the neighboring grain is such that it is not likely to intersect the parent grain. Therefore the likelihood of twin nucleation as a result of slip transfer is low in this instance. This can further be verified by using the criteria outlined in figure 4.9. Despite having high values of m' and Schmid factor (0.96 and 0.55 respectively), the SAF is only 0.68, indicating poor spatial alignment conditions for effective slip transfer.

On the other hand, in layer 2 (second row in figure 4.10), the value of m' between the activated twin system and pyramidal $\langle c + a \rangle$ system of the neighbor is relatively low (0.87). In this instance, the SAF is very close to unity (0.99, or 82°). This indicates a high likelihood of shear transfer from the neighboring grain that would result in S+T twin nucleation. Similarly, it can be observed that the likelihood of S+T twinning with closely aligned pyramidal $\langle c + a \rangle$ systems is high for layers 4 (third row), 9 (fifth row) and 10 (sixth row) in figure 4.10.

The results of the slip transfer parameter calculations for 13 twinning events observed within the 11 layers are enumerated in table 4.2. The first three lines identify twins observed in a different sample of the same material examined in a prior work (Bieler et al., 2014). Layer 1 of the currently analyzed sample is labeled 2.01, and the range of Schmid factors of the potential twin variants plotted in figures 4.6, 4.7 and 4.8 for the parent grain is provided in square brackets. The rank of the Schmid factor corresponding to the observed twin variant is also indicated for each twin (red markers in figures 4.6, 4.7 and 4.8). Each row in the table identifies a neighbor grain slip system that has a high m' value with respect to the observed twin system in the parent grain. Moreover, the

relative position, the bulk strain at the point of first twin observation are also indicated. In layers 3 and 6 (2.03 and 2.06 in table 4.2), two twins were observed at different strains, so two ranges of twin Schmid factors are provided. Most of the twinned grains have more than one neighboring grain with a slip system having a high m' relationship with the twin system. In such situations, an SAF cut-off value of 0.8 (53°) is used to further reduce the list of candidates and determine whether slip transfer is plausible in each case. Instances where the likelihood of S+T twinning is high are in bold font. In most cases, the activated twin variants have high geometrical compatibility with pyramidal $\langle c + a \rangle$ systems in the neighboring grains.

Figure 4.11 shows the resolved shear stress for the activated twin variant plotted as a function of m' for the 13 observed twinning events. Slip transfer parameters for slip systems in neighboring grains for which S+T twinning is less plausible are plotted with open symbols. The size of the markers are scaled in proportion to the Schmid factor rank of the activated twin variant on a scale of 1 to 6 (6 being the highest among all the variants, 1 being the lowest). In some cases, more than one slip system in neighboring grains could facilitate twin formation of the same twin (details are in table 4.2). For example, there are four points corresponding to the twin in layer 1: pyramidal $\langle c + a \rangle$, T1 twin, basal and prism $\langle a \rangle$. Similarly for the twin in layer 4, there are two points corresponding to two different pyramidal $\langle c + a \rangle$ slip systems in the neighboring grain. Out of these two, one has a high SAF value (0.98) while the other has an SAF value of 0.63.

It can be seen from figure 4.11 that prism $\langle a \rangle$ slip systems in neighboring grains do not have a strong geometrical relationship with the twin systems of any of the identified parent grains; having both low values of m' and poor spatial alignment. Therefore, the likelihood of the observed twin nucleation by shear transfer from prismatic $\langle a \rangle$ slip systems in neighboring grains is low. The range of observed resolved shear stresses corresponding to the observed twins lie between 180 and 320 MPa. Eight of the 13 twins ($\sim 61\%$) have plausible S+T twinning from $\langle c + a \rangle$ systems in neighboring grains, indicated by filled gold symbols. There does not appear to be significant differences in the resolved shear stress between twins with plausible S+T (filled markers), and those where S+T is less plausible (open symbols). These data clearly illustrate that deformation twinning

does not necessarily comply with the Schmid law. Moreover, from the current observations, a high likelihood of geometric compatibility is seen for the twin systems with pyramidal $\langle c + a \rangle$ slip systems in adjacent grains.

These observations differ from some earlier studies. In an in-situ neutron scattering compression experiment perpendicular to the preferred c-axis direction, Nervo et al. (Nervo et al., 2016) reported high compatibility between observed clusters of subsurface T1 deformation twins and prismatic $\langle a \rangle$ slip in neighboring grains during a compression experiment of a Ti-4Al alloy. Also, Wang et al. (Wang et al., 2010a) used EBSD to characterize T1 extension twins in CPTi specimens deformed in bending with a favored c-axis texture aligned with the tensile direction (the same material, and indeed from the same specimen used in the present study); as well as with a different specimen of the same material oriented with a softer orientation along the loading axis. It was observed that only one instance of S+T twinning was apparently activated by slip transfer from pyramidal $\langle c + a \rangle$, and the rest were ostensibly triggered by prism $\langle a \rangle$ slip. Similarities with prior studies indicate that the geometrical compatibility of active twin systems with dislocation slip in neighboring grains is not strongly dependent on initial texture, directionality of loading (tensile or compressive) and orientation of the loading direction. Clearly slip transfer is unable to account for nucleation of all the observed twins, so it is likely that the non S+T twins may have resulted from grain boundary defects due to local strain concentrations at boundaries and triple junctions or strain incompatibility between the parent and adjacent grains.

A more significant observation from this study is the fact that the nature of twin nucleation from shear transfer is different in the interior and surface; as this sample was taken from the undeformed end of the same specimen where S+T twin nucleation apparently occurred as a result of shear transfer from prism $\langle a \rangle$ slip. Only pyramidal $\langle c + a \rangle$ could account for the most plausible instances of S+T twins in the interior of the microstructure. This observation is supported by the fact that the texture of the specimen prior to deformation is highly favorable for pyramidal $\langle c + a \rangle$ slip, as evident from the cumulative distribution plot for local and global Schmid factor (figure 4.2). While grains that favor prism $\langle a \rangle$ slip are not dominant, they do exist; as at least 11 grains in the

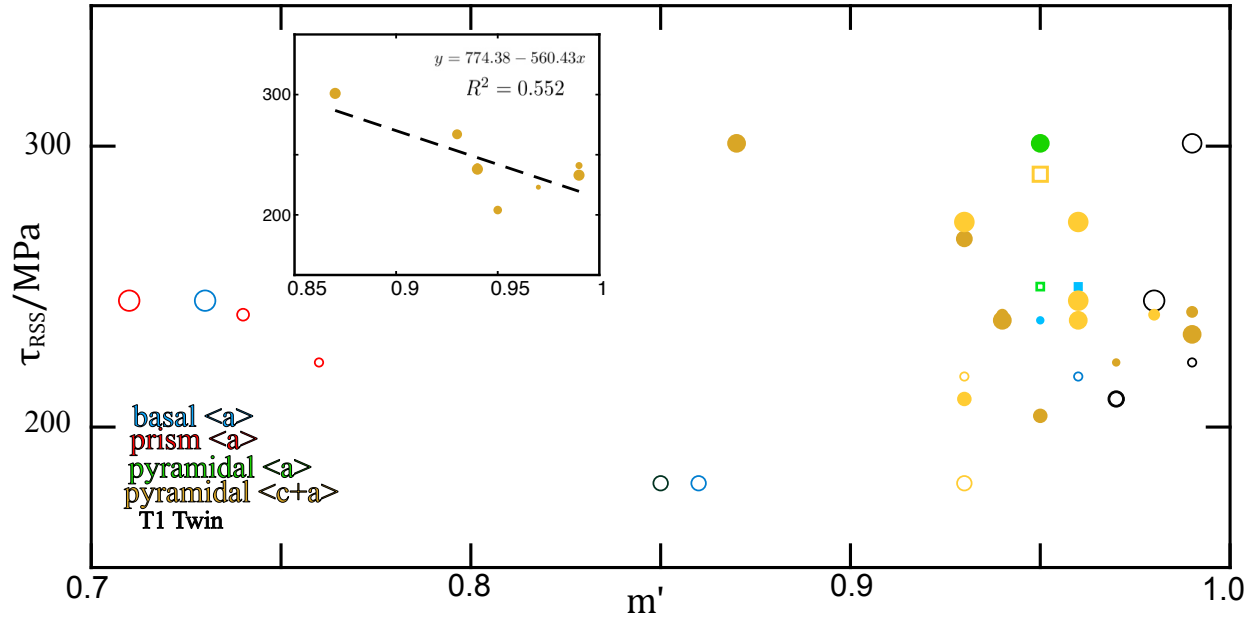


Figure 4.11: Summary of twinning events in the 11 layers as a function of m' : Size of the markers are proportional to the Schmid factor rank of the twin system. Filled circles (\bullet) indicate geometrically more plausible instances, where slip transfer may have resulted in nucleation of twins. Data from a previous study (1.01, 1.02 and 1.03 (Bieler et al., 2014) in table 4.2) are plotted as \square . Cases with $\text{SAF} > 0.6$ ($\theta > 37^\circ$) are represented as filled colored markers, where the colors represent different families of slip and twin systems. Among these, the cases with a highest likelihood of S+T twinning with $\text{SAF} > 0.8$ ($\theta > 53^\circ$) are shown in a darker gold color, while the lighter gold symbols represents instances where $37^\circ < \theta < 53^\circ$. Prism $\langle a \rangle$ is represented by red, basal $\langle a \rangle$ by blue, pyramidal $\langle a \rangle$ by green, pyramidal $\langle c + a \rangle$ by golden (transitions from lighter gold to a darker shade for more plausible cases of S+T twinning); and T1 twinning by black. Inset shows the linear regression plot, considering only the highly plausible $\langle c + a \rangle$ (dark gold) points.

interrogated volume deformed primarily by prism slip (Wang et al., 2017). None of these 11 grains, however, had a neighboring grain with a detectable twin.

4.5.1.2 Stress evolution in parent grains

The evolution of the normal component of the grain averaged stress tensor (σ_{zz}) for all the 13 twinning events is plotted in figures 4.12, 4.13 and 4.14, where the parent grain is represented with a blue line. Because deformation twinning is a response to strain accommodation between a grain and its neighbors during plastic deformation, it can be expected that the twinned grain will experience a stress relaxation upon nucleation of a twin. Therefore, the hypothesis that formation

of a twin relieves a stress buildup can be checked. Furthermore, if slip transfer occurred to nucleate a twin, the stress state in the neighboring grain should nominally track that of the twinned grain. This forms the basis of hypothesis(i), where stress evolution in a twinned grain and a neighbor are correlated. Conversely, if slip transfer did not take place, the reduction in stress in the parent grain should be compensated by an increase in stress in the neighboring grain (hypothesis(ii), anti-correlated stress).

Table 4.3 summarizes an assessment of these hypotheses. At the strain where twins nucleated, a drop in the σ_{zz} stress component values is apparent (and greater than the uncertainty) in layers 2 and 4; while an increase is observed in layers 9 and 10. In layer 4, where geometrical plausibility exists for S+T twinning, the σ_{zz} stress (shown in the figure) is lower in the parent grain than in the high m' neighbor grain. There is a drop in stress with twin formation; after which the stress in the parent grain approaches that of the neighboring grain. This observation is consistent with hypothesis(i) and is indicated by a filled dot in table 4.3. Conversely in layer 10, where S+T twinning is also deemed plausible, the stress in the parent and neighbor grain are similar. There was however, a marked increase in stress post twin formation, and a subsequent drop below the neighbor grain, suggesting an anti-correlated behavior to hypothesis(i), and is marked with an \times in table 4.3. In layer 2, where the grain geometry favors S+T twinning the stress in the parent grain was between the stress of two neighboring grains; and a drop is observed at the point of twin nucleation. Post twin formation, there was a sharp increase in stress for one of the neighboring grains; while a steady increase was noted for the high m' grain and the parent grain itself. With respect to the second twin observed in layer 6 (at 2.2% bulk strain), where S+T twinning is highly likely, an increase in stress is observed in the parent grain. Concurrently, a decrease is noted in stress for the high m' neighbor grain in an anti-correlated manner consistent with hypothesis(ii). Therefore in table 4.3 it is marked with an \times . For the twinned grain in layer 5, stress relaxation at the point of twin formation is concurrently marked by a sharp increase in stress in the high m' neighbor grain. S+T twinning here is deemed to be implausible based on geometry and spatial criteria, which is consistent with hypothesis(ii). Based on the analysis of the 13 twinning events

Table 4.2: Summary of Twinning Events Observed in 14 Layers in two specimens

Layer	ϵ	m_{self}	m' (SAF,Angle)	$m_{neighbor}$	$\sigma(\tau)$, (MPa)
1.01	1.2%	lowest	0.95	pyr⟨a⟩	(250)
1.02	1.5%	3rd highest	0.95	pyr⟨c + a⟩	(290)
1.03	1.5%	lowest	0.96	basal⟨a⟩	(250)
2.01		[0.49-0.55]			
Same Layer	1.5%	highest	0.96 (0.68, 43°)	0.55 pyr⟨c + a⟩	442 (245)
Above Parent	1.5%	highest	0.98 (0.48, 29°)	0.5 T1	442 (245)
2.02		[0.34-0.47]			
Same Layer	2.2%	2nd highest	0.95 (0.94, 70°)	0.28 pyr⟨a⟩	460 (301)
Below Parent	2.2%	2nd highest	0.99 (0.53, 32°)	0.54 T1	460 (301)
Above Parent	2.2%	2nd highest	0.87 (0.99, 82°)	0.44 pyr⟨c + a⟩	460 (301)
2.03		[0.49-0.54], [0.3-0.48]			
Below Parent	1.89%	3rd highest	0.93 (0.8, 53°)	0.44 pyr⟨c + a⟩	453(267)
Same Layer	2.73%	4th highest	0.95 (0.99, 82°)	0.56 pyr⟨c + a⟩	474 (204)
2.04		[0.36-0.42]			
Same Layer	1.5%	5th highest	0.98 (0.63, 39°)	0.47 pyr⟨c + a⟩	442 (240)
Below Parent	1.5%	5th highest	0.94 (0.98, 79°)	0.47 pyr⟨c + a⟩	442(240)
2.05		[0.31-0.54]			
Below Parent	1.89%	4th highest	0.86 (0.43, 25°)	0.32 basal	456 (180)
Below Parent	1.89%	4th highest	0.93 (0.48, 29°)	0.29 pyr⟨c + a⟩	456 (180)
2.06		[0.39-0.59], [0.49-0.60]			
Same Layer	2.04%	2nd highest	0.99 (0.89, 63°)	0.45 pyr⟨c + a⟩	456(233)
Below Parent	2.2%	5th highest	0.99 (0.87, 60°)	0.59 pyr⟨c + a⟩	460 (241)
2.07		[0.49-0.56]			
Same Layer	2.73%	highest	0.93 (0.73, 47°)	0.46 pyr⟨c + a⟩	474 (273)
Below Parent	2.73%	highest	0.96 (0.68, 43°)	0.36 pyr⟨c + a⟩	474 (273)
2.08		[0.37-0.55]			
Below Parent	2.73%	6th highest	0.93 (0.43, 25°)	0.62 pyr⟨c + a⟩	474 (218)
Below Parent	2.73%	6th highest	0.96 (0.32, 19°)	0.45 basal	474 (218)
2.09		[0.52-0.57]			
Above Parent	1.76%	6th highest	0.99 (0.66, 41°)	0.64 T1	449 (223)
Above Parent	1.76%	6th highest	0.97 (0.88, 62°)	0.57 pyr⟨c + a⟩	449(223)
2.10		[0.54-0.63]			
Above Parent	1.5%	2nd highest	0.94 (0.95, 72°)	0.49 pyr⟨c + a⟩	442(238)
Below Parent	1.5%	2nd highest	0.96 (0.71, 45°)	0.54 pyr⟨c + a⟩	442 (238)
Above Parent	1.5%	2nd highest	0.95 (0.63, 39°)	0.51 basal⟨a⟩	442 (238)
2.11		[0.48-0.56]			
Same Layer	2.73%	4th highest	0.97 (0.66, 41°)	0.61 T1	474 (210)
Below Parent	2.73%	4th highest	0.93 (0.68, 43°)	0.39 pyr⟨c + a⟩	474 (210)

Layer Interactions with neighboring grains in same layer and layers above or below,
 ϵ engineering strain where twin was first observed,
 m_{self} Schmid factor [range] and rank for observed twin,
 $m_{neighbor}$ Schmid Factor of Neighbor Slip/Twin System,
 σ global stress from stress-strain curve (MPa),
 τ resolved shear stress on neighbor slip system (MPa).

Rows in boldface indicate most plausible instances of S+T twinning.

across the 11 layers of the interrogated volume, it is observed that hypothesis(i) holds true for the instances of S+T twin nucleation; while hypothesis(ii) is not conclusive for the non S+T cases.

With increasing global strain, there occurs redistribution of stress between the parent grains and their neighbors, leading to changes in the local stress tensor field. This effect is more apparent

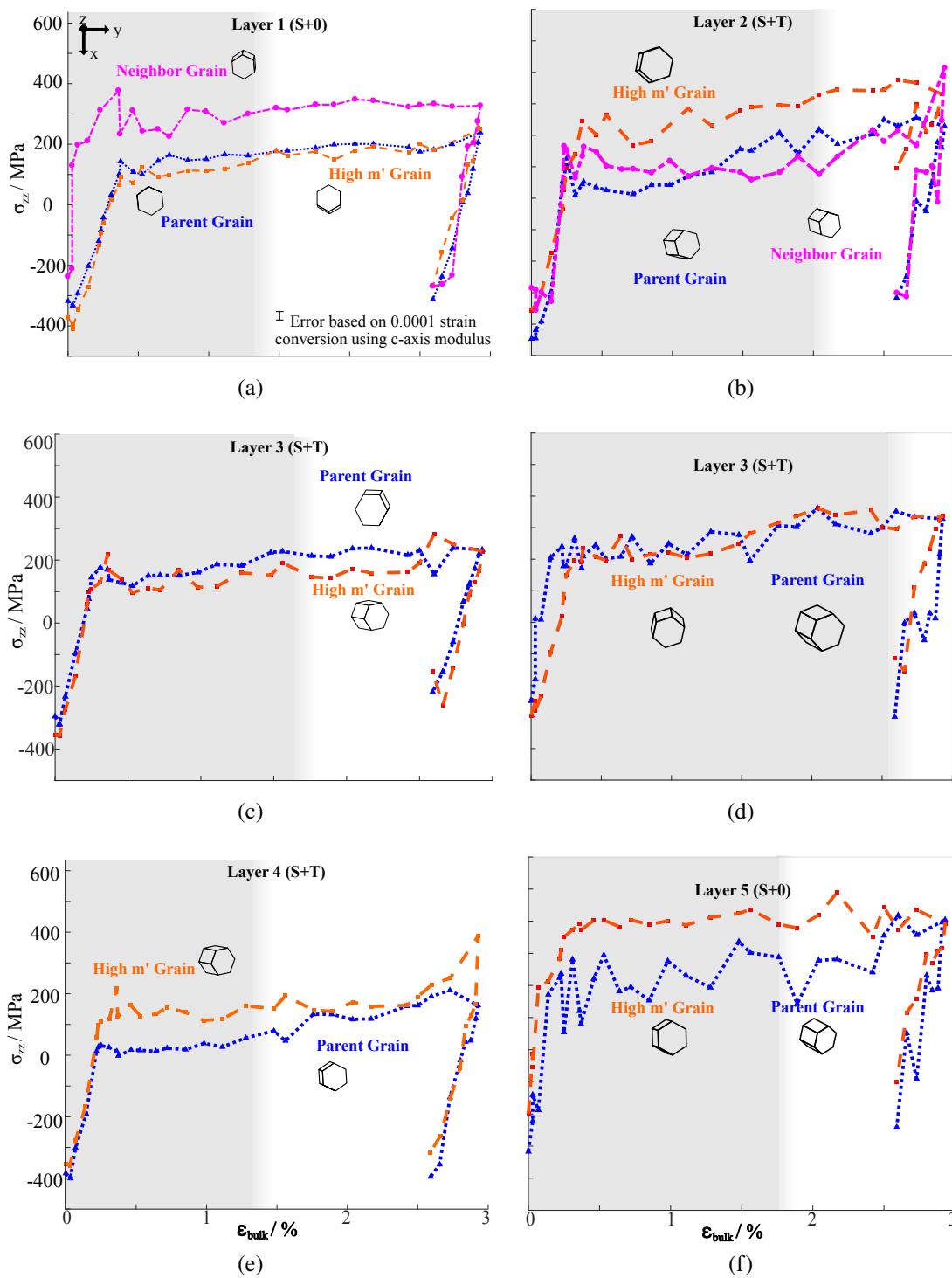


Figure 4.12: Evolution of normal component of local stress tensor (along the tensile direction) for parent and neighboring grains (layers 1, 2, 3, 4 and 5). Prisms indicate the Bunge Euler angle orientation of the grains. Transition in background shade from gray to white indicates the bulk strain at which the twin was identified.

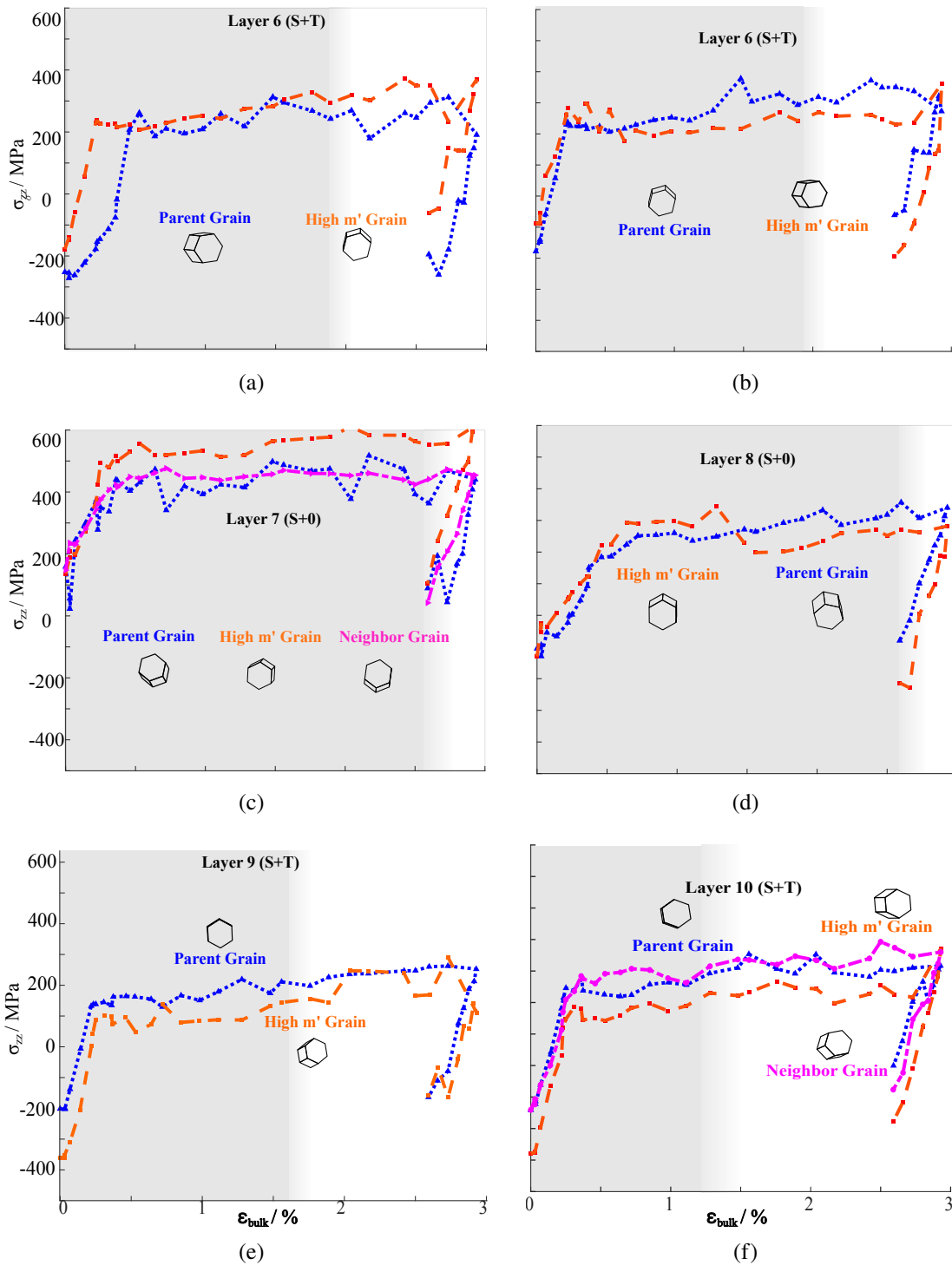


Figure 4.13: Evolution of normal component of local stress tensor (along the tensile direction) for parent and neighboring grains (layers 6, 7, 8, 9 and 10). Details on symbols and color conventions are given in the caption in figure 4.12.

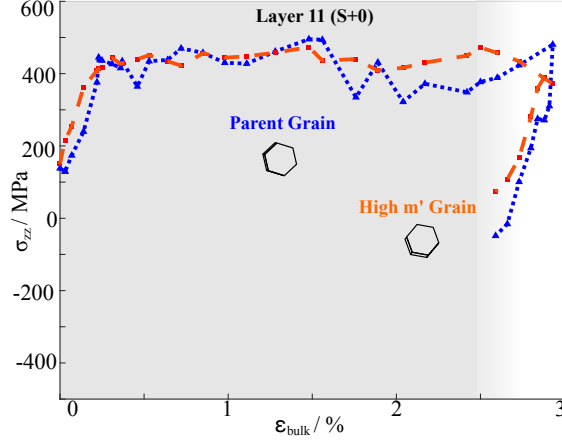


Figure 4.14: Evolution of normal component of local stress tensor (along the tensile direction) for parent and neighboring grains (Layer 11). Details on symbols and color conventions are given in the caption in figure 4.12.

Table 4.3: Summary of 13 twinning events and their stress history correlation with respect to neighboring grains.

Layer	1	2	3		4	5	6		7	8	9	10	11
			1 st	2 nd			1 st	2 nd					
Mode	S+0	S+T	S+T	S+T	S+T	S+0	S+T	S+T	S+0	S+0	S+T	S+T	S+0
Parent $\Delta\sigma$	-	↓	↓	↓	↓	↓	↓	↑	↓	↓	↑	↑	↑
Correlation	○	○	○	•	•	x	•	x	•	x	•	x	x

1st/2nd
 ○ first/second twin in current layer
 • correlated σ_{zz} , with one neighbor
 • correlated σ_{zz} , with highest m' neighbor
 x anti-correlated

in figure 4.15, where the von Mises stress is plotted in conjunction with a metric that shows the deviation of local stress from ideal uniaxial tension (expressed by the color of the symbols in the plots). The deviation from a global uniaxial tensile stress state is assessed using a dimensionless parameter ($\cos \theta$), based on the work done by Schuren et al. (2015). The $\cos \theta$ parameter is the scalar product of the normalized vector containing the six symmetric components of the local grain averaged stress tensor, and the the six component unit vector denoted ideal global uniaxial tension. A value of +1 means that the local stress state is coincident with ideal uniaxial tension; whereas -1 denotes an anti parallel (uniaxial compression) state. In layers 1, 3 (first observed twin), 4 and 9, the deviation of the local stress state from ideal uniaxial tension follows a similar trend. At the start of the loading process, the stress state is more compressive, and it traces an increasing tensile

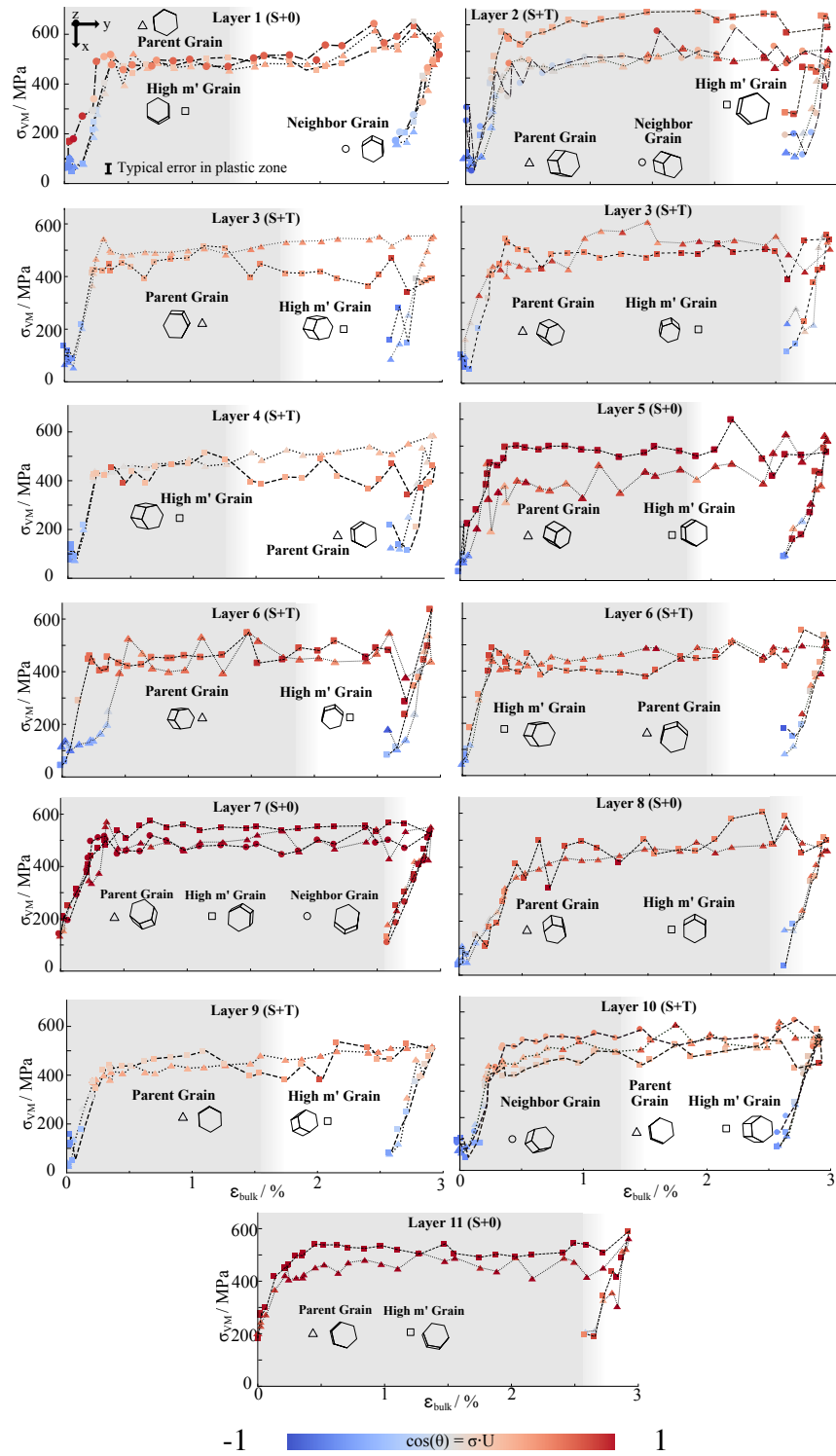


Figure 4.15: Evolution of local average von Mises stress σ_{vM} in identified parent and selected neighbor grains across the 11 layers. The load steps corresponding to twin identification is indicated by the gradual transition in background color from gray to white. The measure of local stress deviation from ideal uniaxial tension is given by $\cos \theta = \sigma \cdot U$.

trajectory with load. Upon unloading, the stress state switches back to a compressive configuration. On the other hand, the stress state of the grains in layers 7 and 11 do not exhibit any compressive character at all. In these two layers, the stress state tends towards a strong tensile character with increasing load, and the degree of which abates gradually with unloading. Similarly, in layer 5, the stress state switches from compressive to a strongly tensile character with increasing load, before falling back to a compressive state upon unloading.

The above observations are consistent with the loading history of the specimen. As mentioned earlier, the tensile specimen was cut out of a larger sample used in a four point bending experiment. It was also determined in an earlier study (Wang et al., 2014) that several grains in the microstructure had a strong compressive residual stress state. This is probably a consequence of prior deformation in the ends of the four point bending experiment of the source sample (Wang et al., 2010b). It is however, unlikely that this played a significant role in nucleation of discrete twin during the tensile loading. Clearly, grains that had a strong compressive residual stress state prior to the tensile experiment did not register a very strong tensile character with increased load. On the other hand, grains that did not have a compressive residual stress state to begin with developed a strong tensile character with increasing load.

To summarize, several expected features associated with slip transfer induced twin nucleation can be assessed using information obtained from a FF-HEDM experiment. Parallel testing of hypotheses (i) and (ii) can be made for the parent and slip transfer (high m') grains for each twinning event. The correlated stress argument looks most consistent for the twin in layer 4, while not as convincing for layer 9. The stress evolution for the twinned and slip transfer grains in layer 10 is anti correlated with hypothesis (i), suggesting that while conditions favoring S+T twinning exist, the twin likely formed by a different mechanism. For the cases that are geometrically and spatially less likely, there is mixed agreement with hypothesis (ii). Nevertheless, slip transfer does appear to be a likely, but probably not dominant mechanism for twin nucleation.

4.6 Comparison of FF 3D XRD results with surface EBSD mapping

An important question that arises for FF characterization, is whether twin-parent pairs identified can also be matched to surface EBSD maps. In this section, results from the comparison between FF and surface EBSD measurements are discussed. The objective of this comparison is to determine whether COM and orientation information obtained from FF analysis matches the surface EBSD data taken from the gage section of the specimen. Several discrete twin-parent pairs were identified on the surface of the specimen in the orientation map in figure 3.4. Three of these twins were also detected in the FF-HEDM analysis, as shown in figure 4.16. The top row shows the inverse pole figure and grain average orientation deviation (GROD) maps respectively, of the EBSD measurement spanning the gage section of the specimen. The surface considered is opposite to the side facing the incoming x-ray beam. Figure 4.16 (a) shows the comparison of the FF analysis specific to layer 1 with the surface EBSD map. The same comparison for layers 10 and 11 is shown in Figure 4.16 (b). In each case, the prisms shown in green denote the COM positions and orientations of the grains identified using FF analysis. The matching grains on the surface EBSD map are identified using black prisms. The third row of (a) and (b) shows the map of calculated misorientation between the matched grains in FF and EBSD measurements.

It is apparent that the FF grain orientations are not positioned in the same spatial relationship as the EBSD maps, suggesting uncertainty in the FF positions. It is worth noting however, that the EBSD map is a 2-D slice, while the COM from FF represents the full volume of the grain, so it is not likely that the positions would agree perfectly. It is generally known, but not commonly quantified that the agreement between COM and 3-D sectioned grains are in better agreement near the center than on the periphery (Park et al., 2017), due to the fact that peak intensity from grains in the center are more uniformly detected than grains on the periphery, leading to fewer diffraction peaks available for identification of the grain. Furthermore, it is likely that many of the actual twins may not have been large enough to be detected by 3D XRD with a certainty of 5° or less. In addition, the strong orientation gradients present in the specimen (figure 4.16, top left) could also contribute to the uncertainty of the COM position in the FF data.

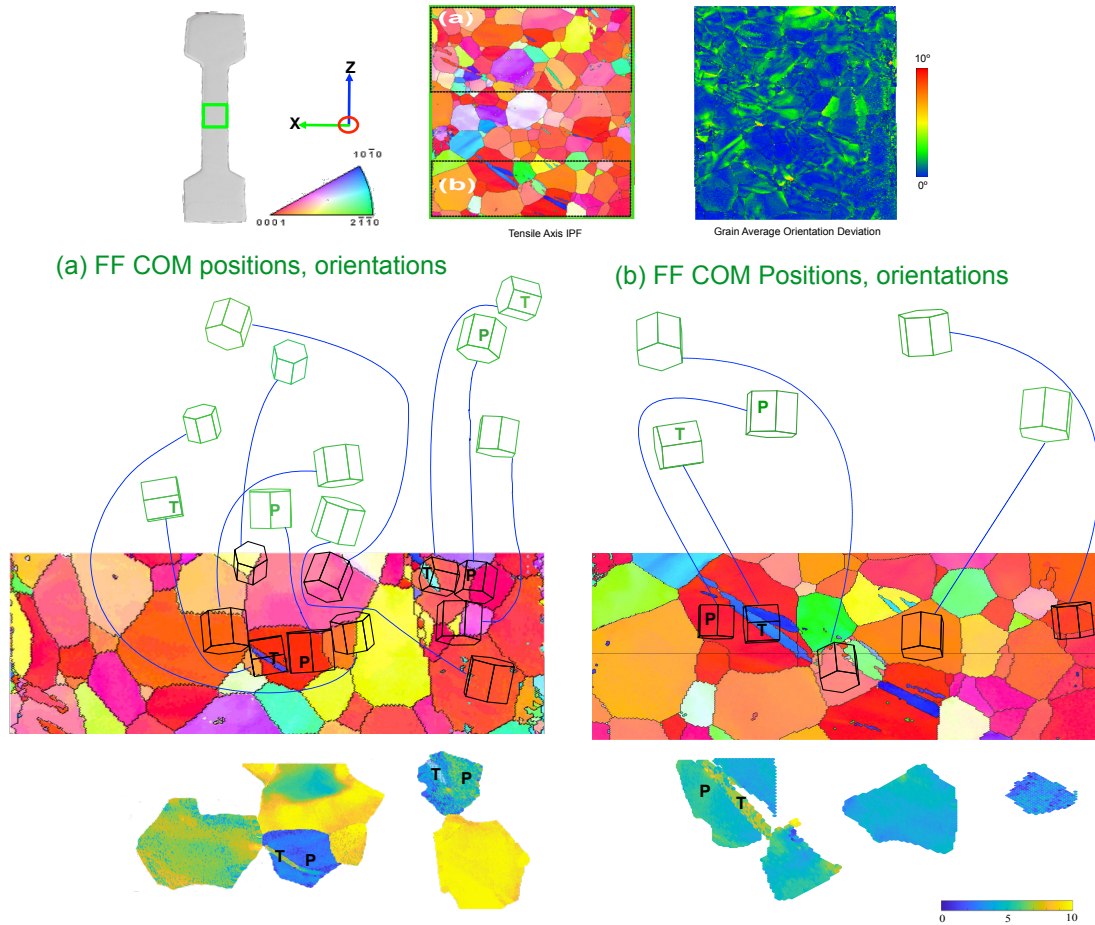


Figure 4.16: The top row shows the tensile sample and the region from which EBSD measurements were made on the surface between the sample and the detector. The top right figure shows the grain reference orientation deviation map where the reference is the average grain orientation in the EBSD data. Two different regions with twins (labeled a and b) are shown. In the second and third rows. The green prisms show the relative positions of grain centers of mass from the far field data (FF) in which twins were detected, and just beneath them, the enlarged corresponding part of the EBSD maps; the green and black prisms are not in good spatial agreement. Beneath the EBSD scans, misorientation maps between the FF COM orientation and the 2-D EBSD grain orientations show agreement within 10° .

The misorientation between the FF grain averaged orientation and each pixel in the corresponding EBSD grains are plotted in the lower row of figure 4.16, where the color represents the misorientation from the reference FF orientation. The grains with larger twins have orientations that agree within 5° with respect to the two measurements. The misorientation range of some of the neighboring grains have an orientation spread between 3° and 7° .

The orientation discrepancy was investigated to determine whether this spread in misorientation

could be attributed to a systematic error between the coordinate systems in the EBSD and FF XRD experiment, but no systematic difference in the directions of crystal X, Y or Z directions were identified. This implies that the differences in orientation also reflect the fact that the FF-HEDM measurement is an average of all voxels in the grain; while the pixels in the EBSD measurement identify a range of orientations present in only one plane of the grain. Because the actual orientations are not spatially resolved within the grains, it is not possible to compare the two orientation measurements in a one-to-one manner. Nevertheless, there is sufficiently good agreement between the two measurements to be convinced that the same grain was identified with both methods.

4.7 Cross validation of local stress tensor calculations and grain positions between Fable and MIDAS

In order to ensure consistency of the relative grain positions that were taken into account to determine favorable conditions for S+T, the FF results were also analyzed using MIDAS. Also, a near field (NF) scan was made on the deformed sample, but it was dismantled, so that the absolute position of the sample in the goniometer was lost. A couple layers of the near field data set were processed, but not sufficient to compare with far field data. During Summer 2020, near field data were measured again and analyzed, and the centers of mass can now be compared with the FF data for the final unloaded state in the next chapter. Also during Summer 2020, the FF data were reanalyzed using a more advanced post processing package called MIDAS. The results of comparison of the grain averaged stress tensor and grain centers of mass between Fable and MIDAS are discussed in this section. Details of comparison of the FF data and the recently completed NF analysis corresponding to the final unloaded state are discussed in chapter 5.

The centers of mass and local strain/stress tensors of grains indexed using Fable were compared to the results obtained using MIDAS and a near-field measurement that provides the shapes and boundary locations of each grain. At the unstrained state ~ 90% of the grains indexed with Fable match with the corresponding indexed results obtained using MIDAS. At the final unloaded state, the match for FABLE indexed grains is only about 75%. The number of grains obtained using

MIDAS at the final state is almost double, indicating that MIDAS indexing algorithm is more sensitive to sub-grain formation than Fable.

In order to analyze the variation of indexation results between Fable and MIDAS, the Euclidean distance and misorientation ($\leq 5^\circ$) between each pair of matched grains is used as a metric of error. The distribution of the Euclidean distance for the matched grains, corresponding to two loading states (unstrained prior to tensile loading, and final unloaded state) is shown in figure 4.17.

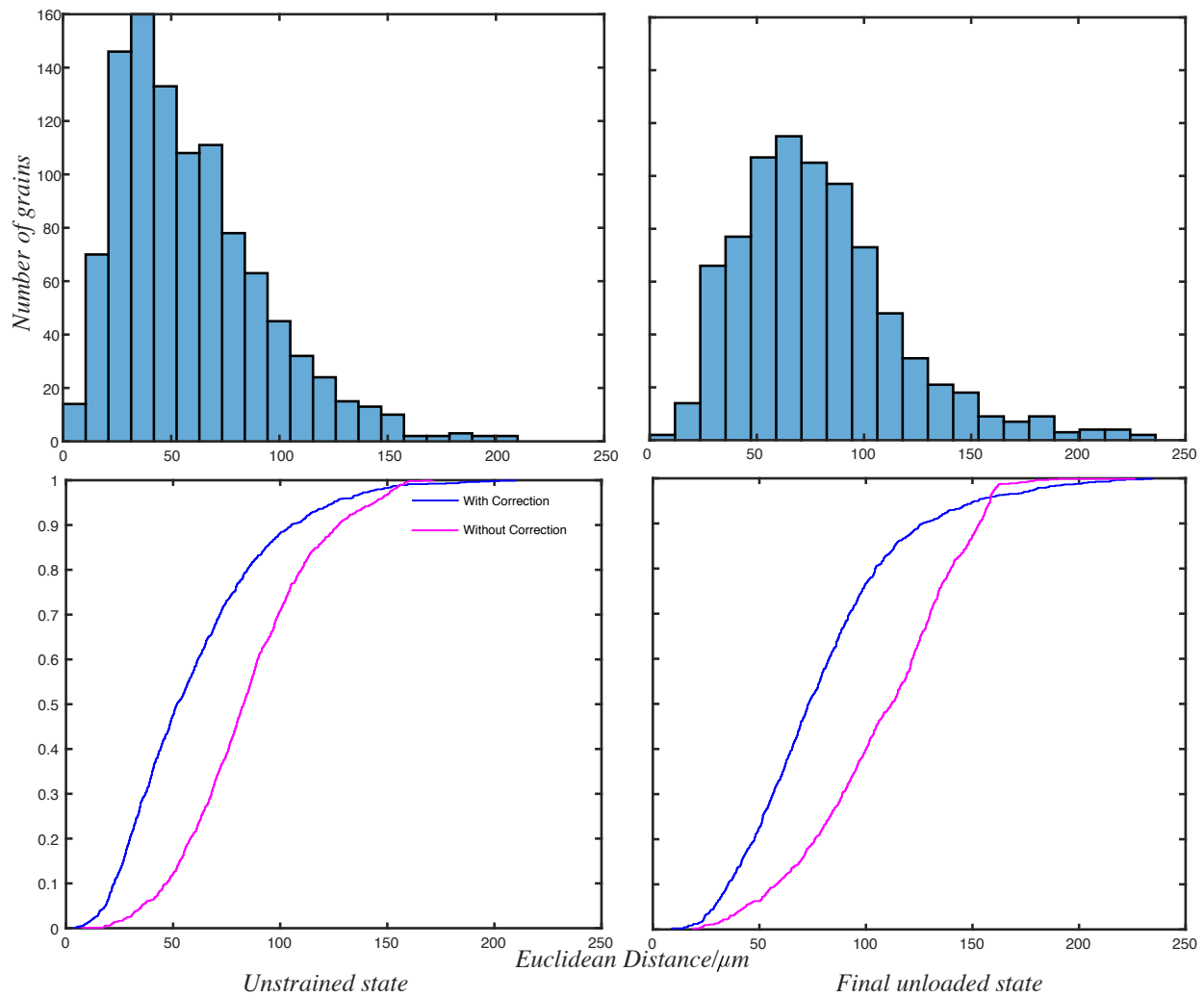


Figure 4.17: Histogram of Euclidean distance for grains consistent with indexation using Fable and MIDAS (top row), and cumulative distribution plot of the same grains (bottom row), for unstrained (prior to loading) and final unloaded states respectively. The top right plot also shows the histogram of Euclidean distance for grains consistent between FF analysis (MIDAS) for the final unloaded state.

The error between the centers of masses is found to be systematic along one specific direction.

Therefore a correction vector is applied to the initial vector joining the centers of masses of each matched pair of grains. With respect to the unstrained condition, approximately 88% of the matched grains have Euclidean distances less than $100\mu m$ (below the average grain size). The error is seen to be higher at the final unloaded state as 75% of the matched grains have Euclidean distance below the average grain size.

Upon applying the correction vector, the Euclidean distance follows a lognormal distribution for both the unstrained (prior to tensile loading) and final unloaded states, as seen from the histograms in figure 4.17.

Figure 4.18 shows cumulative distribution function (CDF) plot of grain radius for the undeformed and final unloaded states respectively. The grain radii decrease uniformly in the final unloaded state. This can be attributed to an increase in volume fraction of twins in the aggregate, as well as development of low angle boundaries within grains. Upon closer observation of the lower tail of the CDF, it is evident that features of the distribution are preserved in the deformed material (e.g. lower arrows). In the initial state, there is a notable change in slope at the upper arrows, which is still there but less apparent in the deformed state, possibly indicating division of grains due to twin formation.

The local grain averaged stress tensor calculations described in section 4.1.1 were compared with those made using MIDAS. The magnitude of the mean difference in equivalent stress for the matched grains obtained using the two approaches is ~ 60 MPa ($\sim 13\%$ of the 450 MPa flow stress). Figure 4.19 shows the cumulative distribution plots of strain/stress evolution for the matched grains, corresponding to four different load states. Overall, the local equivalent strain and stress values obtained from the two methods closely track each other, but the values of strains (and consequently, stresses) are systematically higher with the MIDAS analysis prior to plastic deformation at low elastic strains.

From the above observations, it is clear that the relative positions of the grains indexed using Fable are consistent with the results obtained using MIDAS, especially at the unstrained condition prior to tensile loading. This is important in terms of ensuring consistency of the relative grain

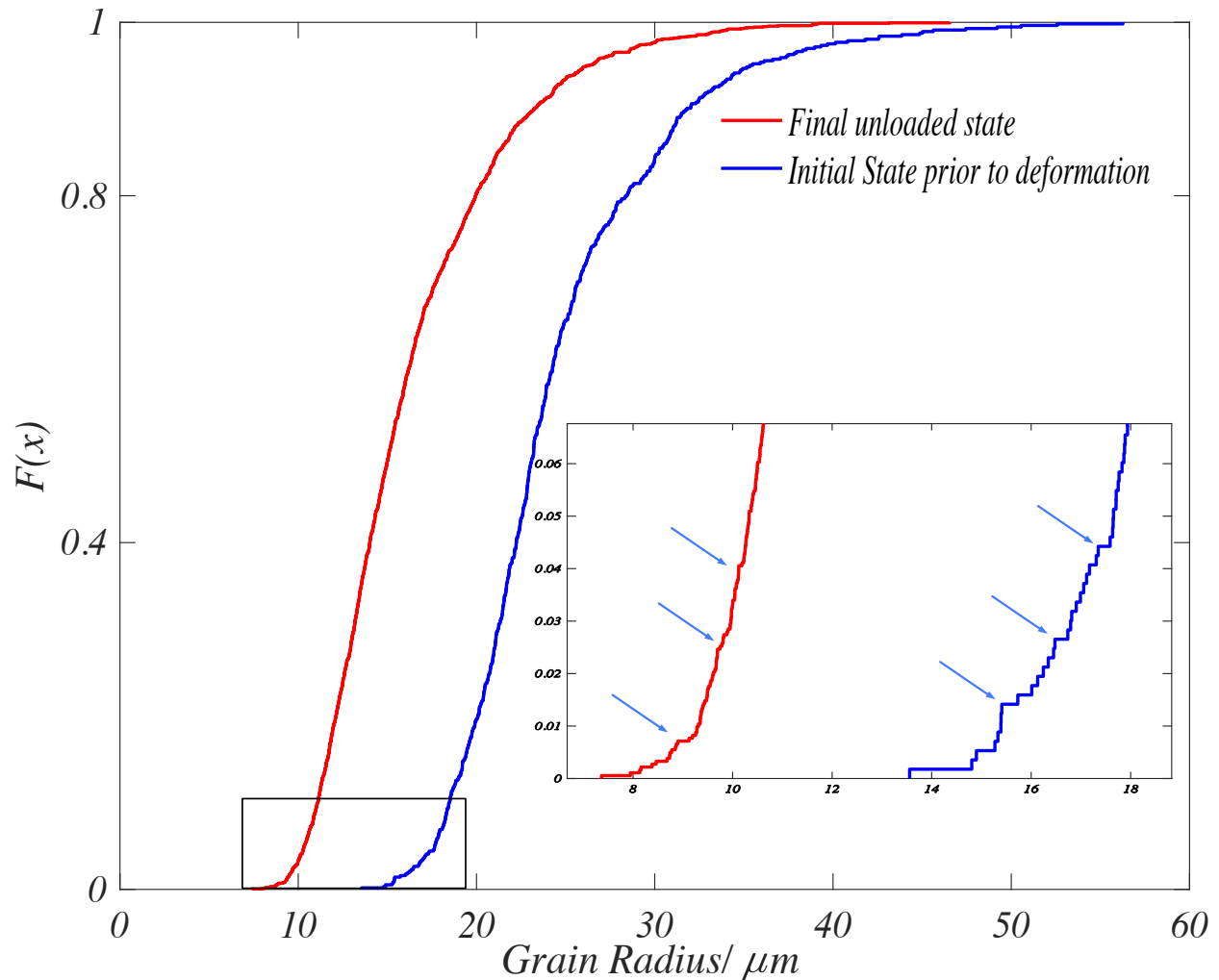


Figure 4.18: Cumulative distribution function (CDF) plots of grain radii estimated by MIDAS for the undeformed and final unloaded states respectively. Inset shows a magnified view of the tail of the CDF plots. There is a significant change in the slope towards the tail of curve, going from the state prior to deformation to the final unloaded state.

positions considered to assess possibility of S+T twinning. Furthermore, as seen from the comparative cumulative distribution plots in figure 4.19, the local equivalent strain/stress values obtained from the two methods closely track each other.

4.8 Evaluation of identified twins using Near Field HEDM

As mentioned in the previous section, NF data was collected from the dismantled tensile specimen. One advantage of the NF setting is the high spatial resolution, which is at least an order of magnitude better than FF HEDM. For a detailed analysis of positional error between the

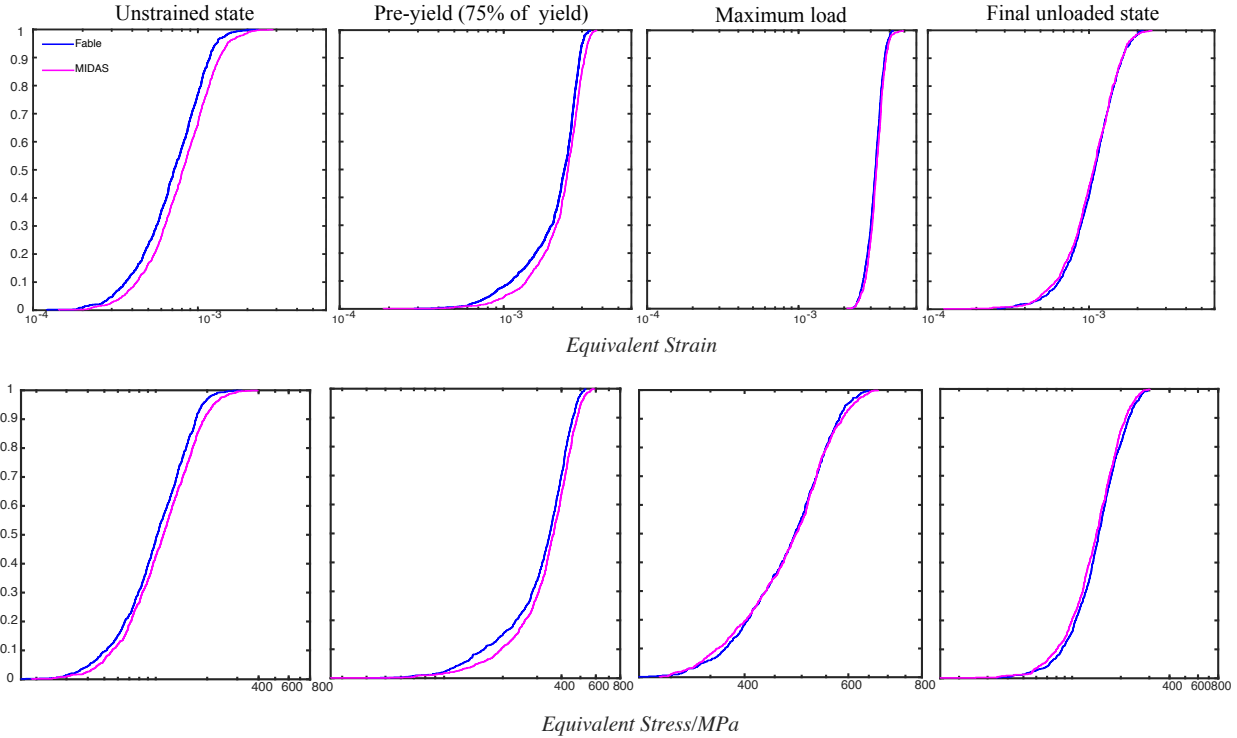


Figure 4.19: Cumulative distribution function plots for equivalent strain (top row) and von Mises stress (bottom row) evolution, showing the differences between two indexing methods. Strain and stress evolution are shown for four different load states: unstrained state prior to tensile loading, 75% of bulk strain prior to yield, maximum load and final unloaded state.

FF and NF HEDM datasets, the reader is referred to chapter 5. This enables the visualization of the morphology of parent, twin and neighboring grains. In this section, the twinning events from section 4.5.1, are re-examined in light of the NF data.

Figure 4.20 shows two projections: perspective (left) and XY plane (right), where the tensile axis is parallel to the Z axis. Several T1 twins were identified based on the $85^\circ c$ -axis misorientation from the data, more than the 13 sets identified from FF HEDM. In fact, twins were found in 34% of the grains.

For the FF data, the twinned/neighboring high m' grains were examined using conditions of geometric compatibility and relative positions in 3D space. As the NF data contains information about the grain morphology, it is possible to identify neighboring grains that have interfacial contact with the twin, thereby providing more clarity in terms of identifying candidate S+T grain pairs. To check if pyramidal $\langle c + a \rangle$ slip is responsible for plastic deformation in a grain, the evolution

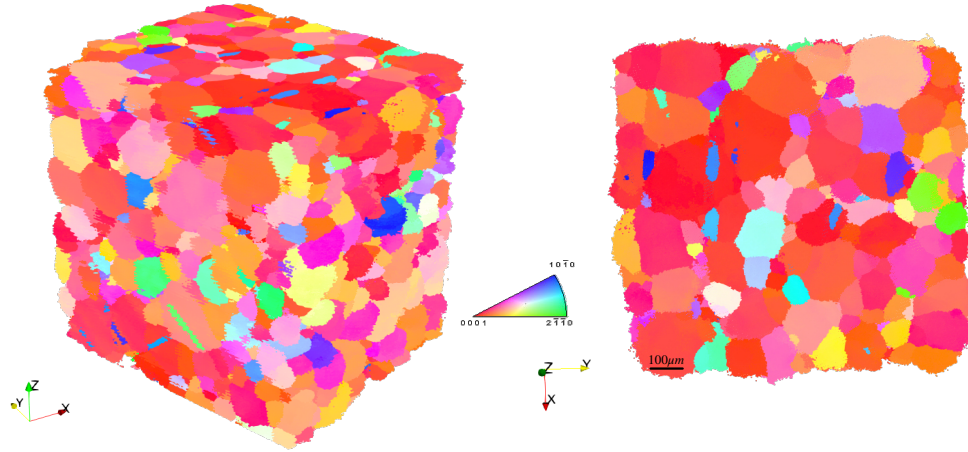


Figure 4.20: Perspective (left) and XY plane (right) projections for the gage volume interrogated by NF HEDM, shown with IPF colors. The data corresponds to the final unloaded state in the tensile experiment (after dismounting of the specimen from the tensile stage). The tensile direction was along the Z axis.

of the plastic spin axis associated with a given slip system can be assessed as a function of strain. According to this hypothesis, plastic spin axis corresponding to the slip system most responsible for plastic deformation should have the least relative misorientation. For this analysis, the plastic spin axis for each slip system is calculated by taking the cross product of the slip plane normal and Burgers vector and tracking its misorientation with respect to the axis orientation prior to tensile deformation.

Taking the information about grain morphology from the NF HEDM data, the first twinned grain considered in figure 4.10 is considered. When the shape of the twin formed is examined, it is found that it touches the surface of the same neighboring grain that was identified as the 'triggering' grain in FF HEDM. This is shown on the top left portion of figure 4.21.

The bottom left plot in figure 4.21 shows the evolution of the disorientation of the neighboring grain as a function of bulk strain, along with the c-axis misorientation evolution. If pyramidal $\langle c + a \rangle$ is indeed the driver of crystal rotation, then there should be less change in the c-axis disorientation with increasing strain than the grain disorientation, because the rotation axes of $\langle c + a \rangle$ slip are between the c-axis and the basal plane). There is an increasing deviation between the grain disorientation and the c-axis disorientation starting at a strain a little below the value where the

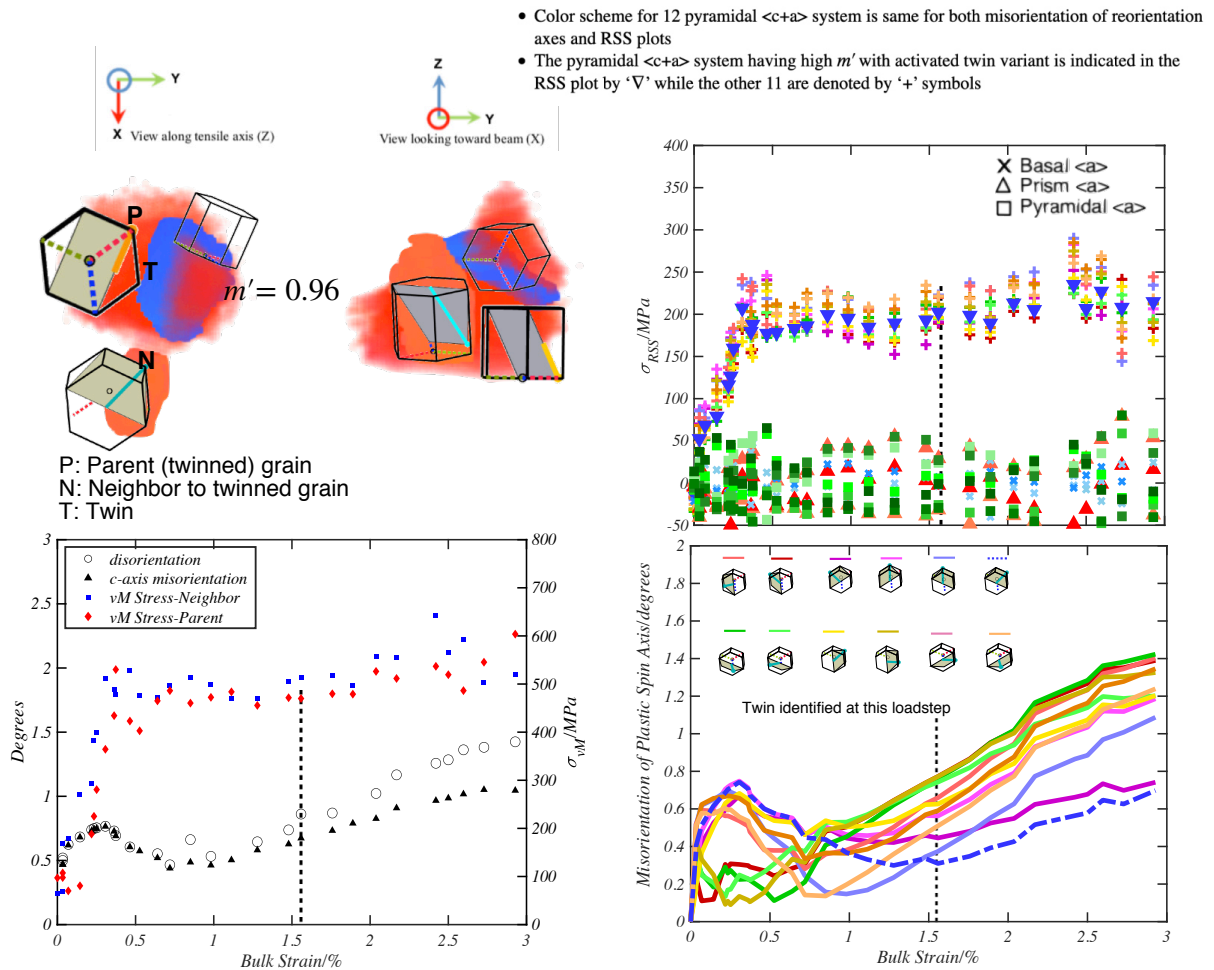


Figure 4.21: Analysis of the first parent, twin and high m' grain from figure 4.10. NF HEDM provides a more precise relative position and information on grain shape. Bottom left: plot of the c-axis disorientation of the neighboring grain as a function of bulk strain, along with the evolution of equivalent stress in both parent and neighboring grains. Top right: Evolution of resolved shear stress for 4 families of slip in the neighboring grain, and bottom right: misorientation of the plastic spin axis for each of the 12 pyramidal $\langle c + a \rangle$ slip systems as function of bulk strain. The color scheme used for the 12 pyramidal $\langle c + a \rangle$ slip systems is the same for the top right and bottom right plots. The symbol and color scheme for the slip systems is indicated in the inset text.

twin was observed.

The top right plot in figure 4.21 shows the evolution of the resolved shear stress of all four families of slip systems (basal $\langle a \rangle$, prism $\langle a \rangle$, pyramidal $\langle a \rangle$ and pyramidal $\langle c + a \rangle$) in the neighboring grain as a function of bulk strain. The resolved shear stresses of the pyramidal $\langle c + a \rangle$ slip family are much higher than the other three families, further supporting the likelihood of pyramidal $\langle c + a \rangle$ slip activity. The pyramidal $\langle c + a \rangle$ slip system that has a high m' value with respect to the activated twin variant in the parent grain is indicated in this plot by the '∇' symbol.

In the lower right plot of figure 4.21, the evolution of the plastic spin axis misorientation from the initial crystal orientation for all 12 pyramidal $\langle c + a \rangle$ systems in the neighboring grain is plotted with strain. For each load step, the misorientation of the plastic spin axis is calculated by comparing with the unstrained orientation (prior to tensile loading). Starting around the load step of twin identification, the misorientation of the plastic spin axis changes the least for the slip system with high m' relationship with respect to the active twin variant in the parent grain. This least change in the rotation axis is consistent with the greatest activity of this slip system.

Another example of a twinned grain from the FF HEDM analysis is examined in the context of NF HEDM data (The third example from figure 4.10). In this case, the neighboring grain in contact with the twin surface is not the same grain as was identified in FF HEDM. The relative positions of the parent, twin and neighboring grains for this example, along with the relevant plots are shown in figure 4.22.

In this case, the disorientation of the grain is very small, suggesting balanced activity of slip systems that result in little orientation change. However, the slip system with the highest m' relationship with respect to the active twin variant does have the highest resolved shear stress, but it also has the greatest misorientation of the plastic spin axis, from which it is difficult to conclude that its activity was primary. Indeed, the slip system that would balance the rotation caused by this system is the light orange system (directly below the one with the dashed line in the key), and it has the second highest resolved shear stress and its rotation axis tracks very closely with the purple system.

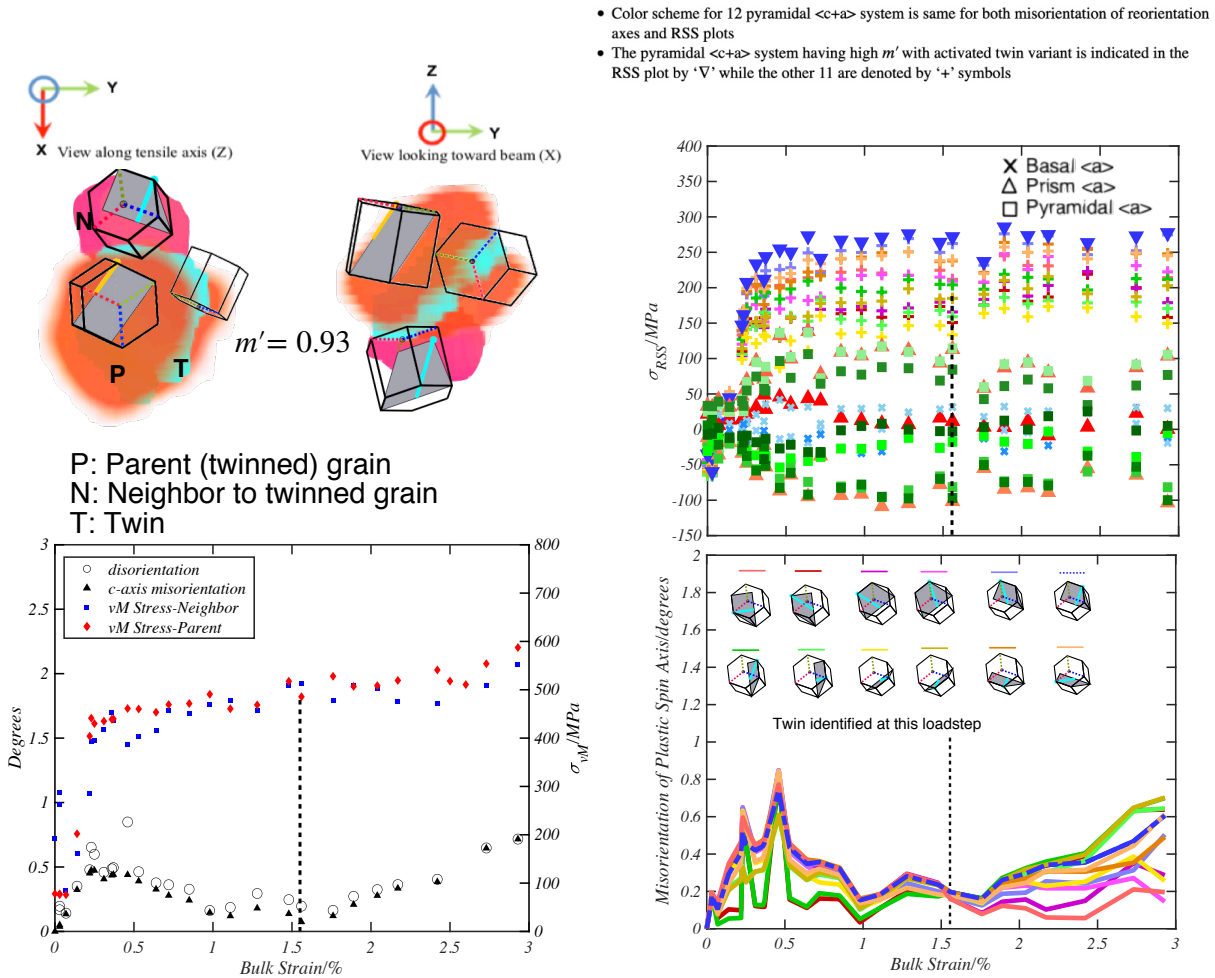


Figure 4.22: Revisit of the third parent, twin and high m' grain from figure 4.10. NF HEDM enables a more precise relative position and information on grain shape. Bottom left: plot of c-axis disorientation of the neighboring grain as a function of bulk strain, along with the evolution of equivalent stress in both parent and neighboring grains. Top right: Evolution of resolved shear stress for 4 families of slip in neighboring grain, and bottom right: misorientation of the plastic spin axis for each of the 12 pyramidal $\langle c + a \rangle$ slip systems as function of bulk strain. The color scheme used for the 12 pyramidal $\langle c + a \rangle$ slip systems is the same for the top right and bottom right plots. The symbol and color scheme for the slip systems is indicated in the inset text.

Each of the 13 twinned grains were examined in light of the NF HEDM characterization done for the final unloaded step. In two of the instances (twins in layers 5 and 8, as identified during the FF HEDM analysis), it was not possible to identify the twins in the corresponding NF HEDM data. This could be a result of detwinning during the unloading process or very small twin volume fraction within the parent grains. In case of four others (twins in layers 2, 3 and the first instance in layer 6 identified in the FF HEDM analysis), the twin was embedded inside the parent grain without contacting any neighboring grain. Therefore a total of 7 twinning events were examined using the approach outlined in figures 4.21 and 4.22.

Similar to figure 4.11, the data from the 7 twinning instances examined in light of the NF HEDM data are plotted in figure 4.23 (solid circles) with the data from figure 4.11. Only the points where pyramidal $\langle c + a \rangle$ has high m' with respect to the activated twin variant are shown. As in 4.11, the points are scaled in proportion to the Schmid factor rank of the active twin variant. There are three points that match with the previous data, as shown by the translucent points from NF that coincide with the FF points. It can be observed that the more confident NF values are in the same range as those observed with the FF analysis. The difference with respect to the other points is because of the choice of different neighbor grains based on grain position and morphology information from NF HEDM. From the standpoint of grain position and geometrical alignment of pyramidal $\langle c + a \rangle$ slip system with the active twin variant, all look to be plausible candidates for slip transfer for the latter seven cases. However, it cannot be said with certainty that the twins observed indeed nucleated as a result of pyramidal $\langle c + a \rangle$ slip transfer.

It can therefore be seen that it is important to quantify the uncertainty associated with grain positions in the FF HEDM analysis. Moreover, in order to make an assessments of complex mesoscopic loading situations such as S+T twinning, it is critical to understand the limits of grain averaged stress measurement. A detailed analysis of results from matching (grain position and crystallographic orientation) FF HEDM data with corresponding NF HEDM data is made in chapter 5. Additionally, a quantitative comparison of kinematic (lattice rotation) and grain averaged stress measurements of the FF HEDM technique is made in chapter 6.

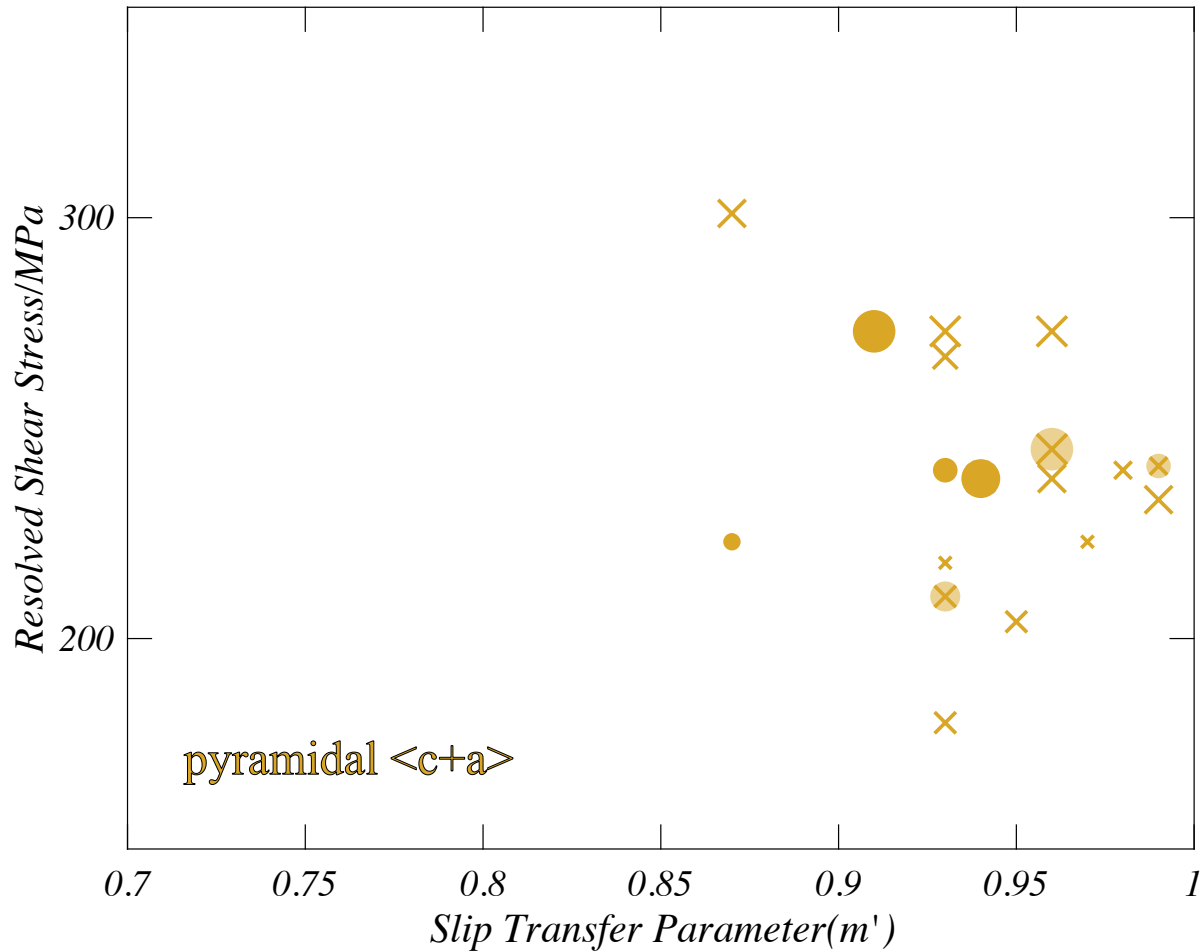


Figure 4.23: Resolved shear stress plot as a function of m' for the seven twinning events validated with NF HEDM data plotted in the same manner as figure 4.11. Here, all of the slip systems with a favorable geometric compatibility with respect to the active twin variant in the parent grain are of pyramidal $\langle c + a \rangle$ type. The data points from the FF HEDM analysis that correspond to high m' relationship with respect to the active twin variant are indicated by 'x'. The size of the markers are proportional to the Schmid factor rank of the active twin variant. The NF points that coincide with the FF results are indicated by translucent circles.

CHAPTER 5

A COMPARATIVE STUDY OF THE ACCURACY OF FF HEDM METHOD WITH RESPECT TO NF HEDM

In this chapter, FF HEDM data on grain positions and orientation are compared with corresponding data from the NF HEDM experiment. As explained in chapters 2 and 4, the uncertainty associated with grain positions in 3D space using FF HEDM is relatively high (of the order of $10\mu\text{m}$). Therefore a systematic quantification of the positional error becomes important for validation of the slip transfer analysis conducted in chapter 4. In this context, it is known that NF HEDM is able to determine grain positions with a better uncertainty than FF HEDM by at least an order of magnitude. Hence, comparison of the grain positions using both FF and NF HEDM techniques is a good approach for cross validation.

The NF HEDM data used for comparison in this study was collected for the load step corresponding to the final unloaded condition, after the specimen was removed from the stage. As such, the NF HEDM data was measured seven years after the FF HEDM characterization was completed. As no changes in the room temperature microstructure are expected, the NF dataset serves as a useful benchmark for comparison of the FF HEDM data.

The different sources of position and orientation errors for the FF and the NF datasets are discussed. Details of an algorithm used to compare the 3D positions and crystallographic orientations of the FF and NF datasets are laid out. Additionally, a comparison of size estimations of matched grains (FF with NF) is made for each technique, using the grain radius as a metric.

5.1 Classification of errors from the FF and NF HEDM experiments

The types of the errors present in identifying grain positions and unique crystal orientations using FF and NF HEDM methods can be classified into the following three categories. In this chapter, the terms 'centers of mass' and 'centroids' have the same meaning. A schematic representation of the error classification is shown in Figure 5.1.

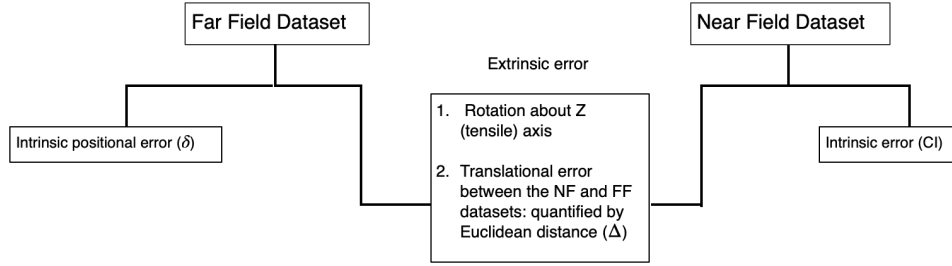


Figure 5.1: Classification of errors from the FF and NF HEDM experiments.

1. Intrinsic error from the FF measurements (δ): This error quantifies the uncertainty associated with grain position (center of mass) determination in FF HEDM. Based on literature, this error is $\sim 10 \mu\text{m}$ (Park et al., 2017).
2. Intrinsic error from the NF measurements (expressed in terms of confidence index, CI): defined as the fraction of simulated Bragg peaks from a data point that matches the experimental scattering data. This term is a function of both the position in 3D space as well as crystal orientation. A simulated Bragg peak from a data point (voxel) is considered to be *qualified* if it intercepts the detector at multiple positions. For a crystal orientation to be considered, the number of qualified peaks (N_{qual}), is a function of $Q_{max} = \max|g_{hkl}|$, which imposes a limit on the set of $\{h k l\}$ and number of diffraction peaks considered (Li and Suter, 2013). The resultant value of CI is a floating point number between 0 and 1 for each NF data point (Li and Suter, 2013; Turner et al., 2016).
3. Extrinsic error, which relates the NF and FF datasets: This can be subdivided into two categories. The first is the rotation necessary to bring the crystal orientation of the corresponding FF and NF grains into coincidence. The second category is the translational error between respective centroids in the NF and FF datasets, quantified using Euclidean distance (Δ).

5.2 Estimation of grain volume

Sharma et al. (2012b) have shown that the volume of an indexed grain (V_g) in FF HEDM can be estimated using the following relation.

$$V_g = \frac{m_{hkl}}{2} V_{gage} \frac{I_g}{k I_p} \Delta\Theta \quad (5.1)$$

$$\Delta\Theta = \arcsin[\sin \theta \cos(\Delta\omega + \cos \theta |\sin \eta| \sin(\Delta\omega))] - \theta \quad (5.2)$$

where, m_{hkl} : multiplicity of crystallographic plane, k : number of diffraction images in which the diffraction spot was present, V_{gage} : illuminated volume, I_g : integrated intensity of diffraction spot, I_p : intensity per diffraction ring on the image if the sample were a powder.

Assuming a spherical shape, the grain radius can then be estimated as follows.

$$R_g = \sqrt[3]{\frac{3V_g}{4\pi}} \quad (5.3)$$

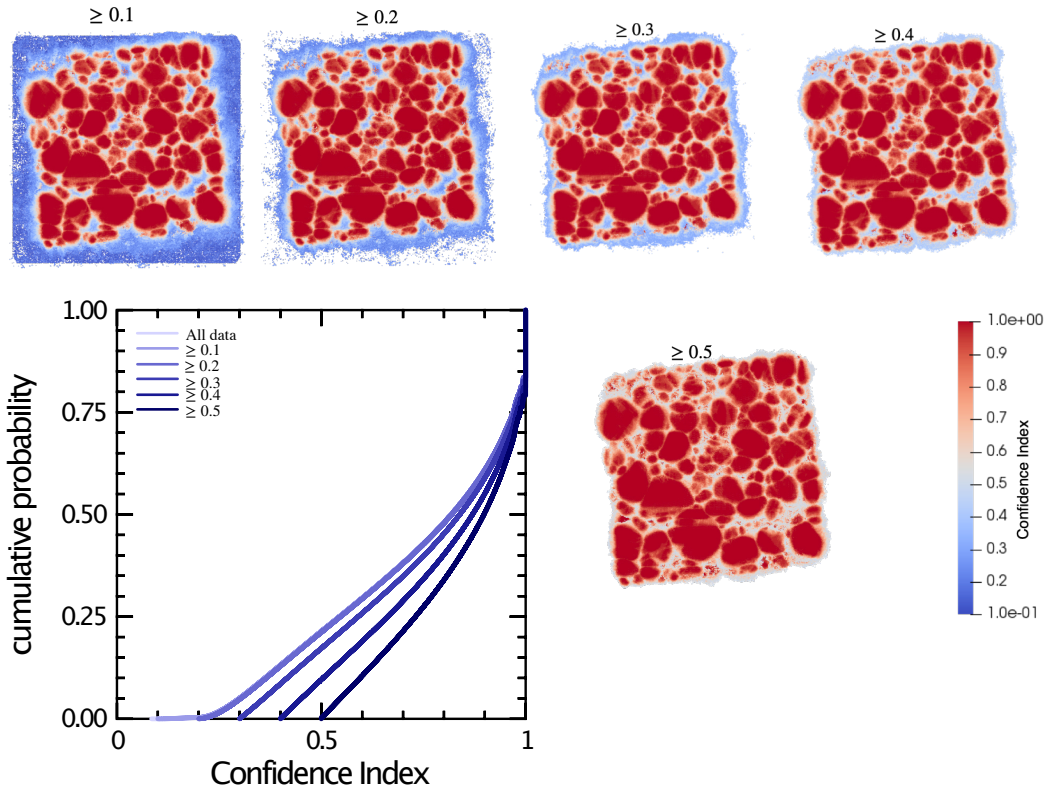


Figure 5.2: Maps showing distribution of the confidence index (CI) in the interrogated microstructure projected on the XY plane (looking down along tensile axis over the entire interrogated volume). Cumulative distribution plots of CI (unfiltered data and with different threshold values) are shown in bottom left. The cumulative distribution curves converge at a CI value ~ 0.95 .

5.3 NF HEDM: Reduction of data on the basis of Confidence Index

The purpose of this step is to filter out voxels that constitute noise in the NF HEDM dataset. Figure 5.2 shows maps illustrating the spatial distribution of the confidence index (CI) for the gage volume (the projection shown is on the XY plane, looking down along the tensile axis). Using thresholding values in an iterative manner (in this case, they are arbitrarily chosen in increments of 0.1), the noise threshold in the NF data can be identified. The cumulative distribution curves for the reduced data with different threshold values from 0 to 0.5 converge at a CI value of approximately 0.95. By inspection, if a CI threshold greater than 0.5 is used, significant voids are created in the microstructure, indicating a loss of meaningful data points. Therefore, a cut-off CI value of 0.5 was chosen to filter the dataset. This resulted in a 21% reduction of data points: from $\sim 8.9 \times 10^6$ voxels to $\sim 7 \times 10^6$ voxels.

5.4 Matching of centroids between NF and FF HEDM datasets

As mentioned in section 5.1, there are two sources of extrinsic variation between the FF and NF datasets—in orientation space and in real 3D space. In this study, coincidence of the datasets in orientation space was accomplished by a counter clockwise rotation of the FF data by 20° about the Z axis. Matching of centroids between FF and NF was done by considering both crystal orientation and position in 3D space.

5.4.1 Data reduction

Prior to the matching process, it is important to consider the difference in size between the two datasets. The number of points (indexed voxels with 3D positions and orientations) for the NF data is three orders of magnitude larger than the corresponding FF data. Therefore, it is necessary to reduce the size of the NF data in order to make a meaningful comparison. Accordingly, the average 3D coordinate and average orientation for each grain in the NF data was calculated. This results in a comparable number of data points in the both FF (1702) and NF (1562) datasets. It is pertinent to mention here that during the averaging process of the NF data, a grain that is split by an embedded

twin is considered to be a single grain instead of two separate grains.

Two approaches for calculating the average crystallographic orientation were used for data reduction. The first approach, is based on the methodology outlined in the work by Cho et al. (2005), where the list of orientations are reduced to the fundamental zone and converted to quaternion space. Then the average orientation is given by a resultant quaternion comprising the arithmetic mean of each individual component of the input orientations. One drawback of this averaging approach is that symmetrically equivalent orientations in the boundaries of the fundamental zone can be considered highly disoriented, leading to erroneous results for average orientations.

The Python based module for calculating average orientation available under DAMASK has an optimized algorithm that accounts for symmetrically equivalent orientations. For the reduced FF and NF HEDM datasets, the results using both approaches yield the same result with the maximum disorientation between the two methods not exceeding 3° . Figure 5.3 shows the cumulative distribution function plot of the disorientation between the two orientation averaging approaches for the reduction of the NF dataset. Here the same population of voxels are averaged: first using the quaternion averaging method, and then the DAMASK averaging algorithm. At least 90% of the points have disorientations $\leq 1.5^\circ$. It should also be noted that no apparent difference was observed in matched grains between the NF and FF datasets using either method of averaging crystal orientation.

5.4.2 Algorithms used for matching grains between FF-NF datasets

Two different approaches were used to search for matching grains between the two datasets. The two (forward and reverse) algorithms are summarized in figures 5.4 and 5.5 respectively. In both cases, a point cloud of NF centroids around each FF data point is considered. Once a NF point is matched to a FF grain, the NF voxel list is updated, so that the same voxel is not considered when matching another FF grain.

In the first approach (figure 5.4), the misorientation of a given FF data point is calculated with respect to the entire set of NF data points. Then a misorientation tolerance criterion is applied, i.e.

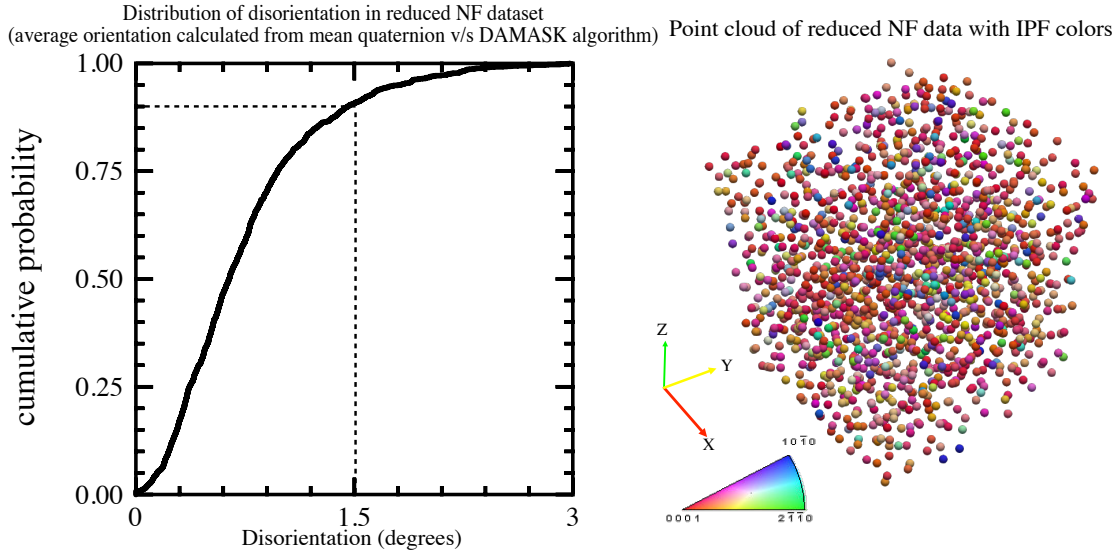


Figure 5.3: Cumulative distribution plot of the disorientation between two different grain averaging techniques for the reduction of the NF data. The same group of orientations are averaged: the first approach being simple quaternion averaging, and the second using the more optimized grain averaging algorithm available in DAMASK. The maximum disorientation between the mean quaternion approach and the DAMASK algorithm is less than 3° . At least 90% of the points have a disorientation of 1.5° or less. The point cloud of the reduced NF data is shown on the right with IPF colors denoting crystal orientation with respect to the Z axis.

the list of NF data points with a misorientation less than or equal to the tolerance is generated. If this list is non-empty, then the Euclidean distances between the FF point and points in this reduced list are calculated. The NF data point in this list that has the smallest Euclidean distance is chosen to be the matching grain. This process is iterated over the entire set of points in the FF dataset.

In the second approach (figure 5.5), the nearest neighbor point cloud using a specified ball radius is generated first. The misorientation tolerance is then applied, and if the list of filtered points is non-empty, the point with the smallest Euclidean distance is chosen as the matching grain.

In order to assess whether the results of the matching process would be different in each approach, the datasets were analyzed using NF both forward and reverse algorithms.

The Euclidean distance distributions for the matching grains using the two different algorithms are shown in figure 5.6. For both cases, a misorientation tolerance of 5° is applied. Clearly, the results of the matching operation is independent of the type of algorithm (forward or reverse) used to implement it. The CDF plot for a smaller subset of the data, i.e. only those centroid pairs with

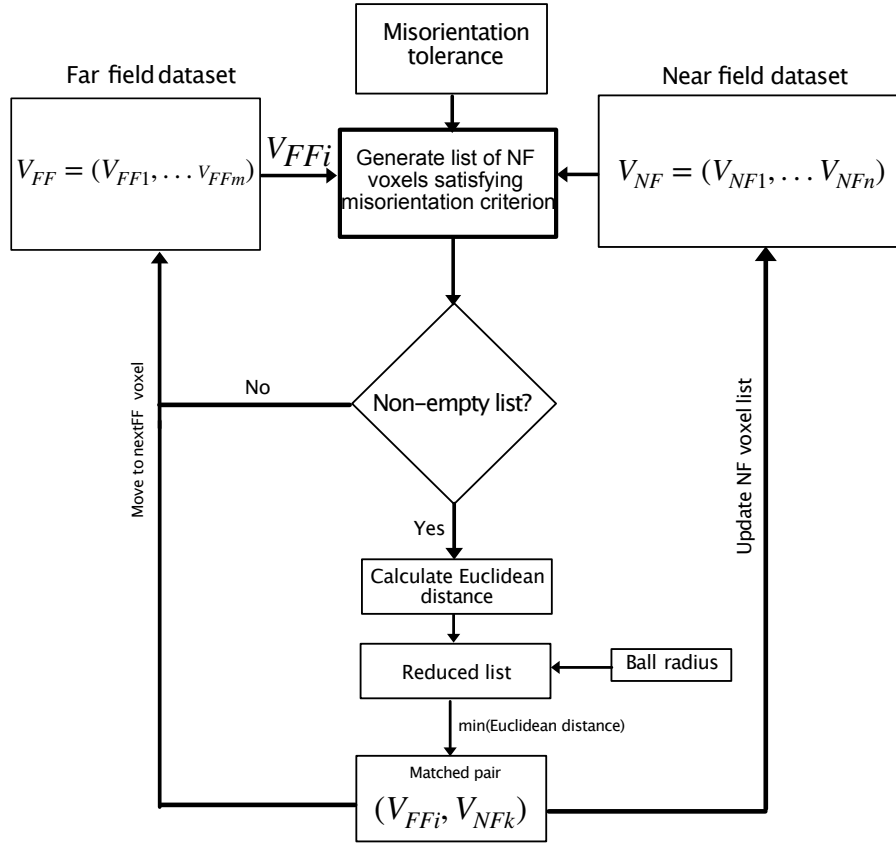


Figure 5.4: Forward algorithm used for matching grains between the FF and NF datasets, where the misorientation criterion is applied before the ball radius.

FF-NF Euclidean distance of $\leq 200 \mu m$ is shown in the inset on the right hand side of figure 5.6.

5.4.3 Grain size comparison between matched grains in FF/NF datasets

In addition to position and crystal orientation, an important consideration in the matching exercise is the grain size. This involves examining how well the reported grain radii from FF data match the grain sizes from the NF data. In order to make an equivalent comparison, the sizes of the matched grains in the NF dataset are expressed in terms of grain radius as follows.

Figure 5.7 shows the arrangement of voxels in a 2D slide of the NF HEDM dataset. A series of lines can be drawn to reduce it to a hexagonal grid arrangement. If a regular hexagonal comprising six voxels is considered, the distance between two adjacent voxels is $\sim 2.88 \mu m$. The series of lines is drawn such that each voxel is enclosed in 2D space by an equilateral triangle.

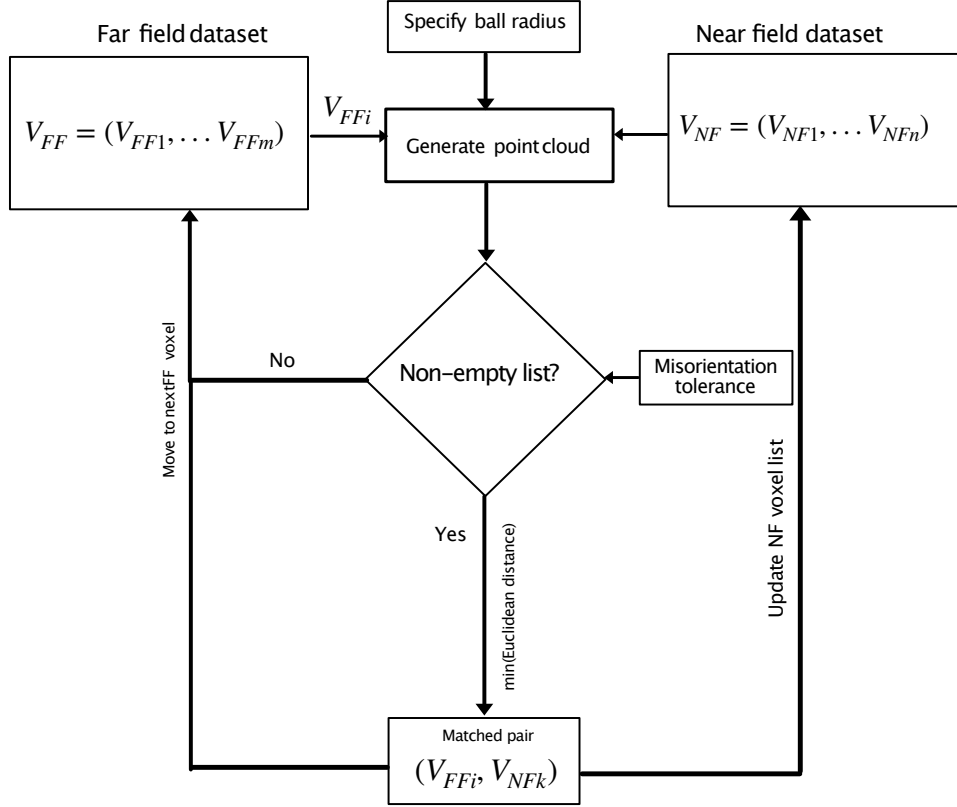


Figure 5.5: Reverse algorithm used for matching grains between the FF and NF datasets, where the ball radius criterion is applied first and the misorientation threshold is applied in the second step.

The length of a side of the enclosing equilateral triangle, L is given as follows.

$$L = \frac{2.88 + (0.5 \times 2.88)}{\sin(\frac{\pi}{3})} \quad (5.4)$$

From the above equation, the value of L comes out to $5\mu\text{m}$. Assuming a thickness of $10\mu\text{m}$ for a slice of the NF HEDM data, the volume of an triangular element is given as: $V_0^{NF} = \frac{1}{2} \times L(2.88 + (0.5 \times 2.88)) \times 10 = 108.28(\mu\text{m})^3$.

If the number of constituent voxels in a grain is N , then the total volume of the grain is given as: $V_g^{NF} = N \times V_0^{NF}$.

Therefore, assuming a spherical grain shape the radius can be calculated as follows.

$$R_g^{NF} = \sqrt[3]{\frac{3V_g^{NF}}{4\pi}} \quad (5.5)$$

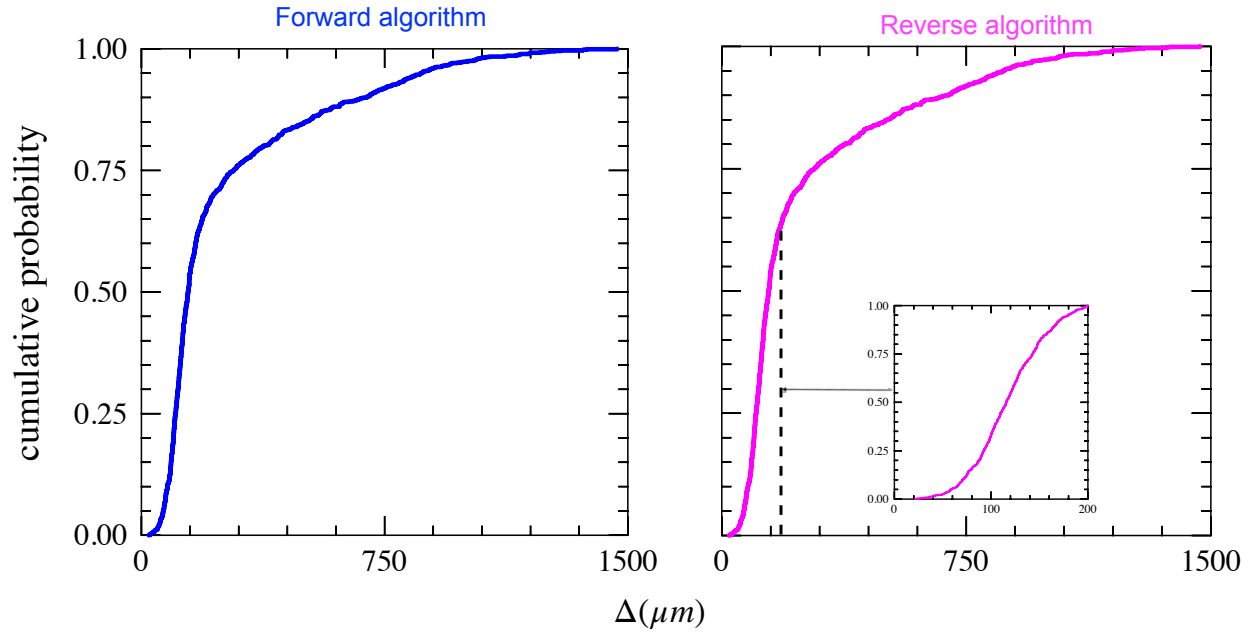


Figure 5.6: Cumulative distribution function plots for matched grains using forward algorithm (left) and reverse algorithm (right), using a misorientation tolerance of 5° . In both the matching operations, a ball radius of $1500 \mu m$ was used (entire domain of the NF dataset). Both the approaches yield identical results. Inset on the right hand side shows CDF plot for a much smaller subset, i.e. only centroids within a $200 \mu m$ ball radius are considered.

Figure 5.8 shows the cumulative distribution plots of the grain radii for the FF and NF datasets corresponding to the final unloaded stress state. The reported FF grain radii do not show a good match with the calculated grain radii for the matched NF grains. The median value of the FF grain radii is smaller than the NF grain radii by a factor ~ 2.9 ($15.5 \mu m$ in FF and $44.3 \mu m$ in NF). Moreover, the FF grain radius values show a wider variance than the corresponding NF values. If the FF radius values are multiplied by a factor of 2.9, a better match between the two datasets is observed.

5.4.4 Implementation of matching algorithm

Figure 5.9, shows the lines connecting the centroids of the matched FF and NF grain pairs using a maximum ball radius of $200 \mu m$. The plot on the left side has the connecting vectors scaled and shaded in proportion to the calculated NF grain radius (R_g^{NF}), i.e. a smaller NF grain radius has

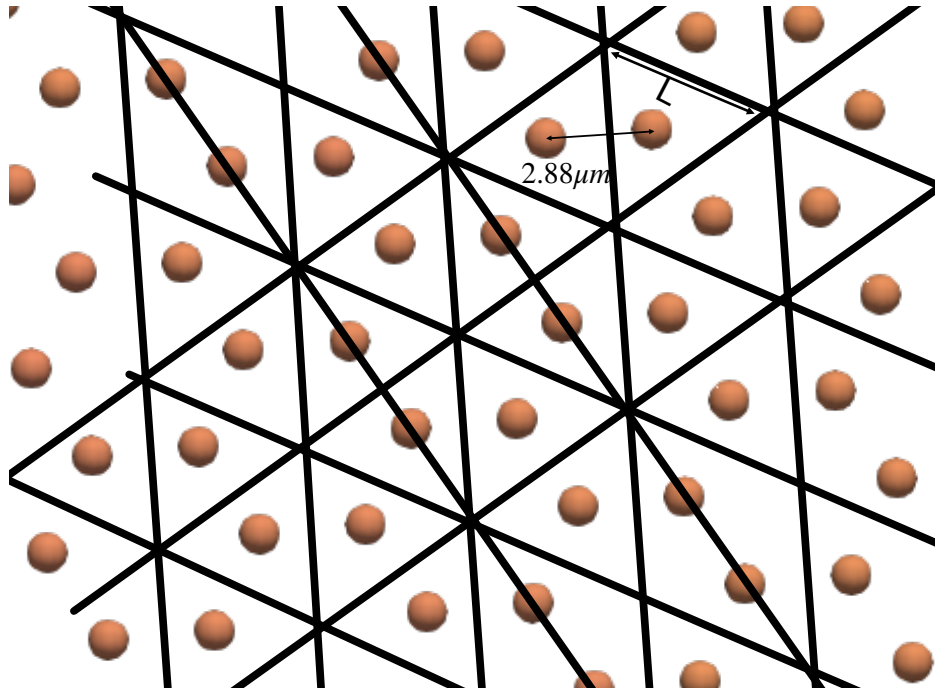


Figure 5.7: Arrangement of voxels in a 2D slice of the NF HEDM data, looking down the tensile (Z) axis.

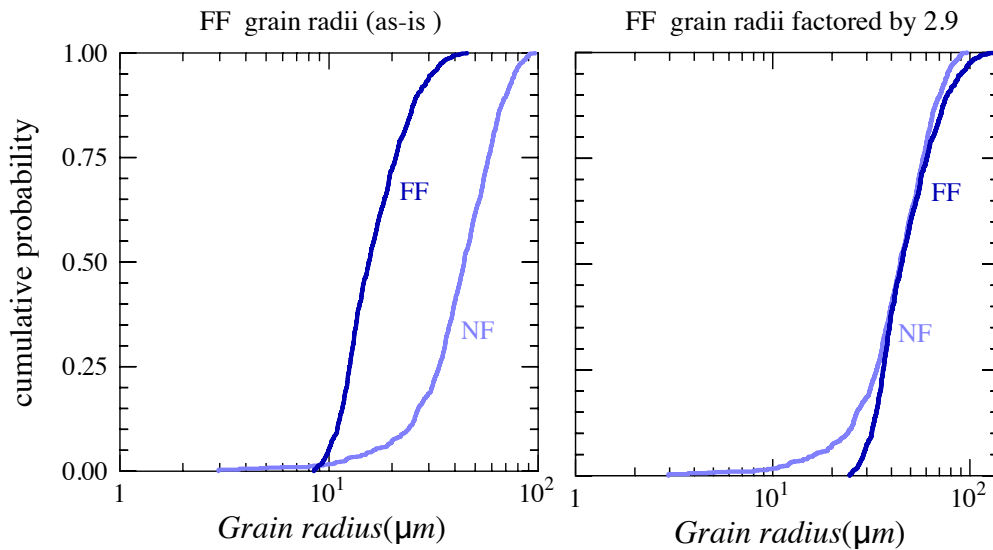


Figure 5.8: Cumulative distribution plots for FF and NF grain radius value for the matched grains with a cut-off ball radius of $200\mu m$. The figure on the left shows the comparison between the two datasets with the as-is FF grain radius values. The figure on the right shows the comparison after the FF grain radius values were multiplied by a factor of 2.9, which gives a closer match with the NF data.

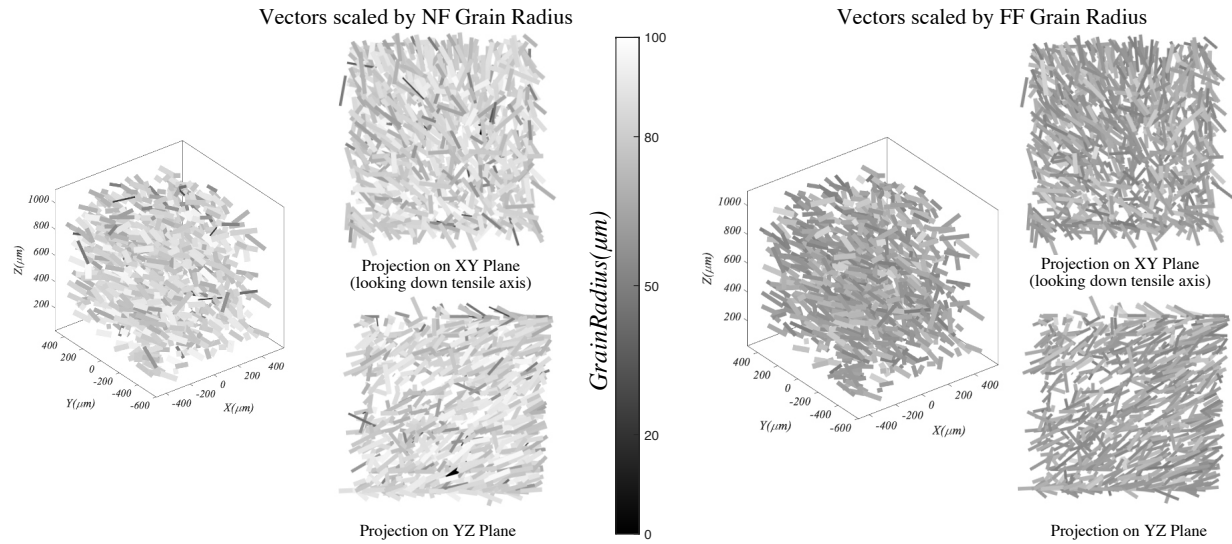


Figure 5.9: Comparison of grain centroid positions from FF and ND HEDM results, corresponding to the final unloaded state of the specimen. Only the centroids with NF-FF Euclidean distance $\leq 200\mu m$ are considered here. The left side of the figure shows the connecting vectors scaled and shaded in proportion to the calculated values of NF grain radius. The same set of plots are repeated on the right side, with the connecting vectors scaled and shaded in proportion to FF grain radius, without a corrective scaling factor.

a thinner darker line. The right plot has the connecting vectors scaled and shaded in proportion to the reported FF grain radius without the correction factor of 2. The more similar shade of gray illustrates the narrower distribution of FF grain sizes. Also, the projections along the Z and X axes shows a dominant directionality between the two data sets.

5.4.5 Application of translational correction between FF/NF datasets

From the projection of the 3D plot in figure 5.9 on the YZ plane, a systematic translational shift of the NF data can be seen with respect to the FF points. Therefore, the average translation vector was used to improve the spatial match of the two datasets. Accordingly, the vector sum of all the connecting lines were calculated, which is then divided by the total number of matching pairs of centroids (821). The resultant vector ($\vec{\Delta r}_{unit}$) and its magnitude, along with its projection in the YZ plane are shown in figure 5.10. From the CDF plot, translating all of the FF centroids along the direction and by the magnitude of the correction vector results in an improved spatial match of the

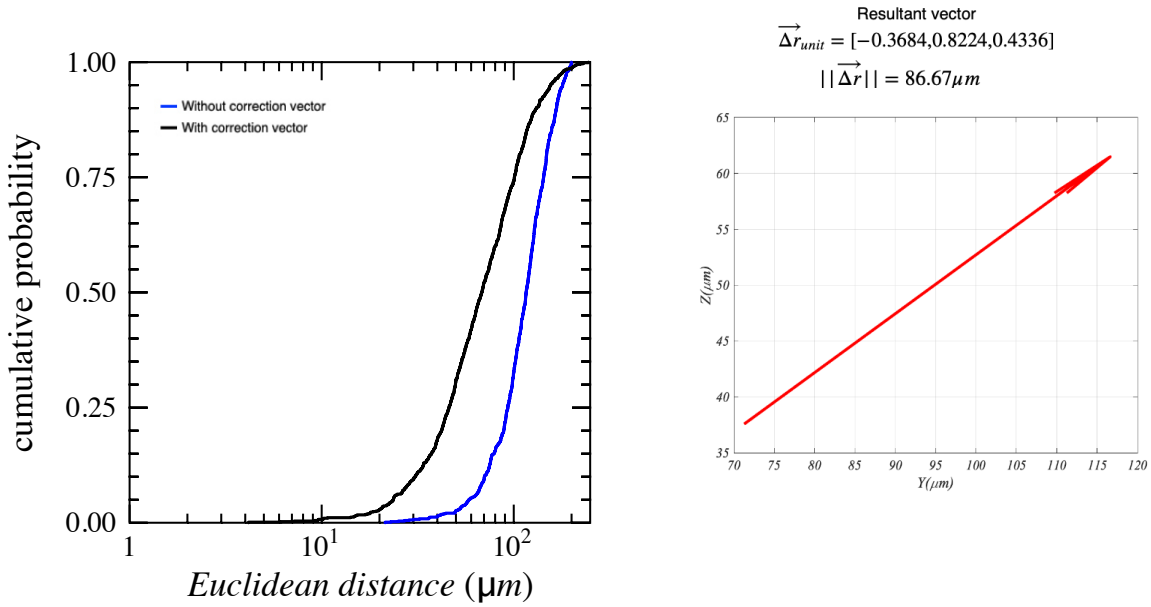


Figure 5.10: Left: CDF plot of same data from Figure 5.9, with and without the correction vector. From the leftward shift of the CDF curve, using the correction vector results in a better spatial match between the two datasets. Right: projection of the calculated correction vector in the YZ plane. Its magnitude and direction are also indicated.

FF/NF datasets and illustrated in 5.11.

5.4.6 Relationship between NF grain size and matching centroids in FF

An important outcome of matching of the FF/NF datasets is to identify the relationship between the NF grain size and the corresponding matched grains in FF. A working hypothesis here is that there should be a positive correlation between the reported FF grain radius and the number of constituent voxels in the matched NF grain.

Comparing the distribution of grain size in the NF dataset to the subset of FF grains that were matched, the FF grains have a larger size, as shown in the CDF plot in figure 5.12 (top right). For the matched grains, a weak linear correlation ($R^2 = 0.2061$) can be seen. The motivation behind applying a threshold voxel size of NF grains is based on the hypothesis that smaller grains may contribute towards noise during the matching process. If a threshold is applied, the value of the correlation coefficient (R^2), i.e. smaller grains below a given number of voxels are not considered. The value of R^2 increases up to a maximum value (0.4634) for a threshold of 400 NF voxels, and

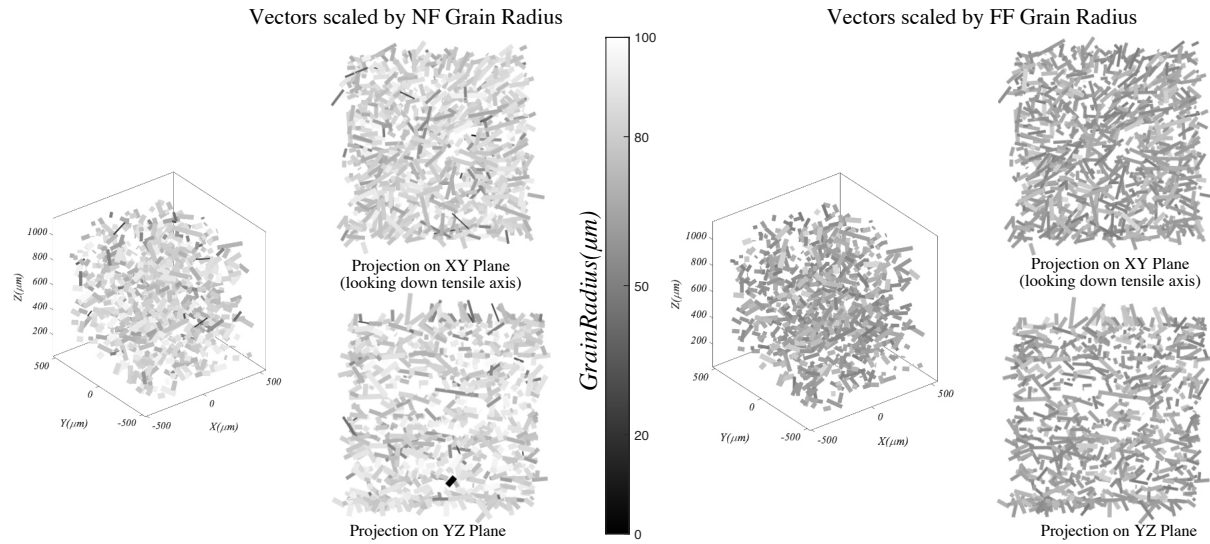


Figure 5.11: Replotting of the same data as in figure 5.9, except in this case the correction vector is applied to the FF data points. The the FF data appears much better aligned with the corresponding NF data points.

then decreases after that. Therefore the best fit for linear correlation is obtained if grains larger than 400 voxels are considered, but no improvement in R^2 is achieved if the threshold is increased beyond this value.

The weak linear correlation between the grain size of the matched FF and NF grain datasets suggests that the reported values of FF grain radius is not a close approximation of the actual grain size. Since the resolution of the NF characterization is finer ($2.5\mu m$), the metrics used for estimating grain size from this dataset (number of constituent voxels or calculated grain radius) provides a more credible estimate of the grain size.

In terms of the algorithms used to match between the FF and NF datasets, both the forward and reverse approaches converge to the same result. Therefore, it does not matter whether the misorientation or the ball radius criteria are applied first.

Additionally, the relative error in grain position from FF HEDM shows a strong inverse relationship as a function of grain size. At load steps corresponding to significant plastic deformation, the relative positional error becomes significant in smaller sized grains. For the grains that were matched between the FF and NF datasets corresponding to the final unloaded state, the reported

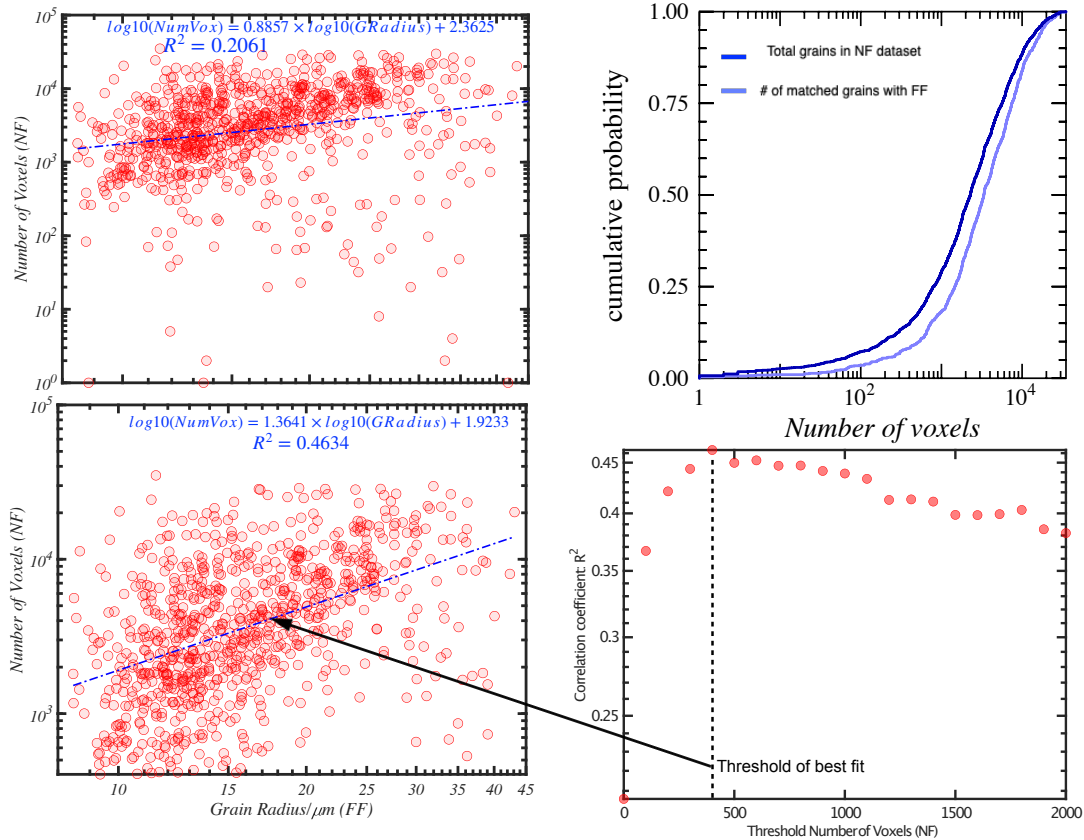


Figure 5.12: Top right: cumulative distribution plots of grain sizes, in terms of number of constituent voxels. For the subset of grains matched with FF dataset, there is a shift to right, indicating a larger average grain size. Left: For matched grains, grain size plotted as a function of the unscaled grain radius. Bottom right: variation of the correlation coefficient as a function of threshold number of voxels.

grain radius values from FF varies from the corresponding NF values by about a factor of 2. Moreover, at larger plastic strains, smearing of diffraction patterns could result in larger relative positional errors. Therefore, when using grain position data from FF HEDM, it is important to consider the deformation state of the specimen.

CHAPTER 6

COMPARISON OF KINEMATICS OF CRYSTAL ROTATION AND GRAIN AVERAGED STRESS MEASUREMENTS OBTAINED FROM FF HEDM

The motivation behind this chapter stems from the need to assess the reliability of grain averaged stress measures in predicting complex mechanical events such as slip induced twin nucleation (S+T twinning). For a given grain, FF HEDM enables the calculation of relative lattice reorientation as a function of strain. Here, the objective is to quantify how well this kinematic descriptor of plastic deformation can be reconciled with the grain averaged stress measurements obtained using FF HEDM. From the standpoint of kinematics, the relative lattice reorientation can be obtained from FF HEDM as a function of load step. On the other hand, based on lattice strain, the grain averaged stress tensor can also be calculated. The latter can be projected onto the slip systems that are most likely to play a role in crystal rotation, and compared with the observed crystal rotation. Quantification of how well these two measurements match each other is an important step towards assessing the limits of the FF HEDM technique.

6.1 Calculation of plastic spin axes for active slip systems

A useful way to determine if a particular slip system is active during plastic deformation is to check how well aligned the corresponding plastic spin axis is to the lattice reorientation at that load step. If n and b are the slip plane normal and the slip direction respectively, then the plastic spin axis is given as follows.

$$\begin{aligned}\vec{L} &= \vec{b} \times \vec{n} \\ \text{or } \vec{L} &= \vec{n} \times \vec{b}\end{aligned}\tag{6.1}$$

The direction of the resultant plastic spin axis has to correctly reflect the sense of lattice rotation brought about by the slip system considered, as can be seen from the schematic representation of the sense of shear effecting lattice rotation due to slip (figure 6.1). To be consistent with observed

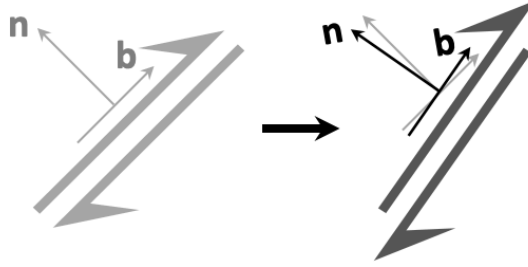


Figure 6.1: Schematic representation showing the sense of shear and plastic spin effected by crystallographic slip, that results in lattice rotation. n denotes the slip plane normal, while b denotes the slip direction.

rotations and the direction of shear informed by the resolved shear stress, equation 6.1 is modified as follows.

$$\vec{L} = \text{sgn}(RSS)(\vec{b} \times \vec{n}) \quad (6.2)$$

where RSS is the resolved shear stress for the considered slip system, calculated using the grain averaged stress tensor.

6.2 Comparison of slip system plastic spin axis and lattice reorientation

This section details the methodology used to quantify how well the measured kinematic orientation evolution compares with the expected rotation based upon a simple estimate based upon the most highly stressed slip systems using the stress obtained from FF HEDM stress. For the purposes of this study only prism $\langle a \rangle$, basal $\langle a \rangle$ and pyramidal $\langle c + a \rangle$ slip systems are considered to be active, and to simplify this analysis as starting point, the critical resolved shear stress for all of these families are consider equal.

The prism denoting the lattice orientation prior to tensile loading in the sample frame is shown on the top left of figure 6.2. The top row of stereographs shows the lattice spin axis for each load step in the plastic regime up to the point of maximum tensile load ($\sim 3\%$ bulk strain). These spin axes vary with increasing strain, and the progression is indicated by a change in the shade of gray from

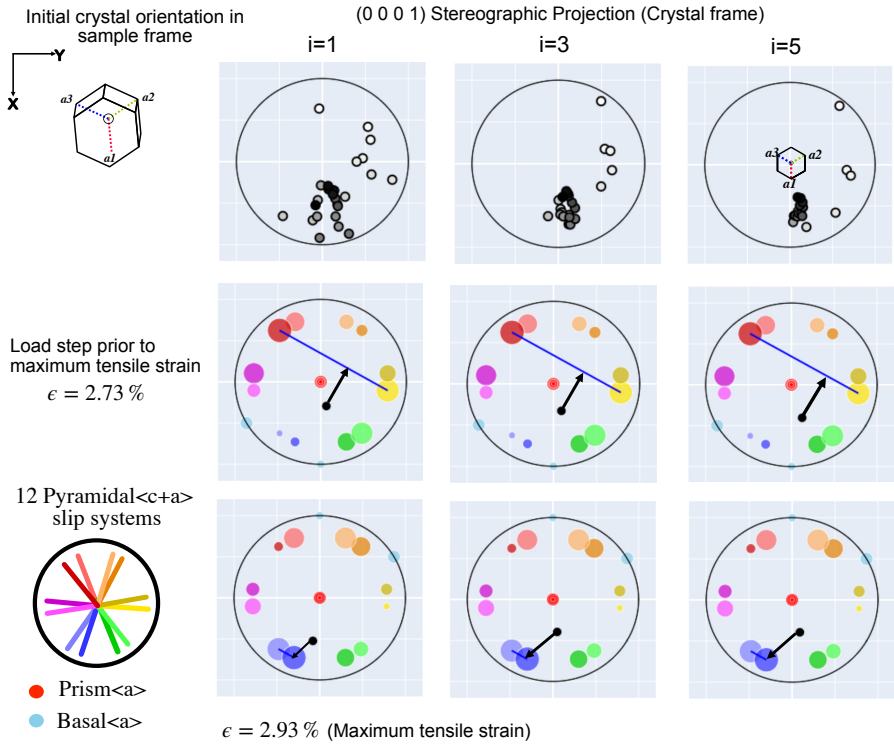


Figure 6.2: The upper left prism identifies the initial grain orientation in the sample frame with the three $\langle a \rangle$ axes labeled. The top row shows three (0001) stereographic projections showing the lattice spin axis at each load step from from the beginning of the plastic regime (white) to $\sim 3\%$ (black). The $\langle a \rangle$ axes of the crystal frame are identified at the center of the upper right stereographic projection. Increasing the spacing i between load steps from 1 to 5 (left to right) smooths the fluctuations between load steps. Middle and bottom rows: Stereographic projections show the plastic spin axes for (basal $\langle a \rangle$) (light blue circles on perimeter), prism $\langle a \rangle$ (red circles in the center) and pyramidal $\langle c + a \rangle$ (rainbow colors). The rainbow color scheme for the 12 pyramidal $\langle c + a \rangle$ slip system spin axes are shown in the lower left-hand corner (the two spin axes for different directions on the same plane are close together with dark and light tones of the same color (plane), and more widely spaced adjacent spin axes are for the same slip direction on different planes, which have either a darker or lighter color of the two planes). The symbols for each spin axis are scaled in proportion to their resolved shear stress magnitude. The black point identifies the observed spin axis. A blue arc connects a blend of the two most highly stress slip systems (largest symbols). The observed spin axis has an arrow pointing to the blend of the top two slip systems that is closest (largest dot product), In the middle and bottom rows, the most favored slip systems are different, indicating significant fluctuations in the stress state, but the black arrows indicate that that the observed spin axis is closer to the blend of the highly stressed slip systems. With smoothing, the black arrow gets longer (dot product becomes smaller).

white to black, where the lightest points represent the transition from elastic to plastic deformation. The darkest point identifies the rotation axis during the final tensile load step prior to unloading. In the column with $i = 3$, the crystal rotation axis is computed based upon the orientations before and after the reference load step, to increase the range of the orientation change. Similarly, for $i = 5$, the rotation axis between two load steps before and two load steps after the reference load step is computed. As i is increased, the oscillation of the grain plastic spin axes decrease as the fluctuations between load steps are smoothed out.

For a given load step, the two most favored slip systems are chosen based on the magnitudes of the resolved shear stress values (calculated using the grain averaged stress tensor). Then the two slip system plastic spin axes for the two 'most favored' slip systems are calculated using equation 6.2. Assuming that the actual slip activity could result from a linear combination of these two slip systems, a series of intermediate spin axes resulting from different weights of the two are generated. These intermediate axes are then compared to the *observed* lattice spin axis using a dot product to see how close they are to each other. For each grain, the dot product of the *observed* lattice plastic spin axis at a given load step is calculated with respect to the blend of the two most highly stressed plastic spin axes. The maximum value of this dot product and the corresponding fraction of the highest resolved shear stress slip system in the blended pair are recorded.

An example of this exercise for a twinned grain at the last two load steps corresponding to bulk strain values of $\sim 2.73\%$ and $\sim 2.93\%$ is shown in the middle and bottom rows of figure 6.2. The three families of slip systems (basal $\langle a \rangle$, prism $\langle a \rangle$ and pyramidal $\langle c + a \rangle$) are plotted on stereographs in the crystal frame for each of the three values of i . In the middle row, the two slip systems with the highest magnitudes of resolved shear stress are pyramidal $\langle c + a \rangle$ slip systems with spin axes that are on different sides of the stereograph (the large yellow and red circles). The black point representing the crystal spin axis is near the center of the stereograph, and an arrow points to the intermediate combination of the red and yellow slip systems with the minimum dot product. In contrast, at the last loading step, the two most highly stressed systems have very similar spin axes (two pyramidal $\langle c + a \rangle$ systems on the same plane indicated by two large blue points).

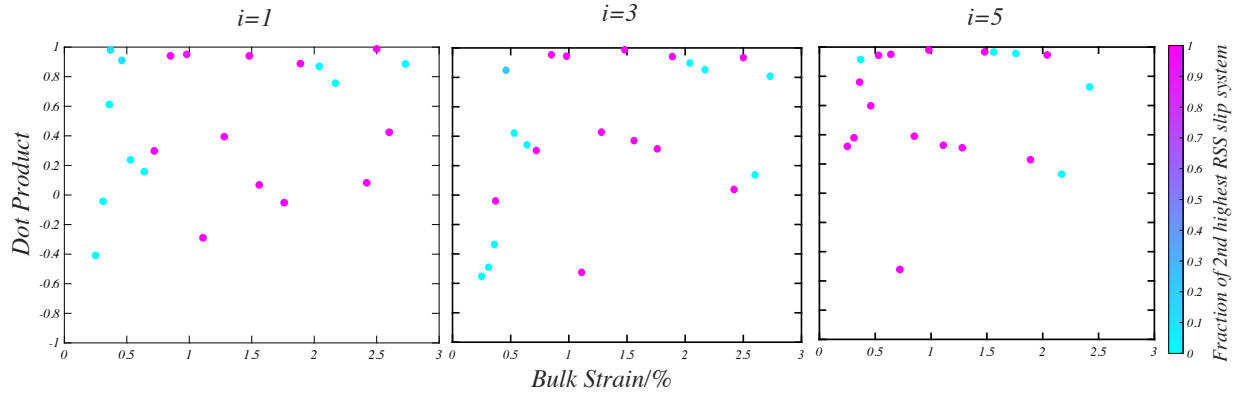


Figure 6.3: Maximum dot product between lattice spin axis and blended slip system plastic spin axes (linear combination of the highest and second highest resolved shear stress slip systems), for the twinned grain in figure 6.2. The effect of smoothing (increasing i) leads to less fluctuation, and suggests alternating sets of active slip systems. The colors of the markers indicate the fraction of the slip system with the second highest resolved shear stress in the blended axis.

The lattice spin axis for the final load step (colored black) is different from the prior load step, and is closer to these two blue slip system spin axes than other $\langle c + a \rangle$ slip systems. Clearly, the average stress tensor differs between these two load steps, and the observed rotation axis changes in a direction that reflects the change in the stress tensor.

Smoothing resulting from increasing the load step increment used to compute the observed lattice spin axis leads to a more concentrated set of spin axis points (less fluctuation). However, as the value of i increases, the distance between the observed spin axis and the most favored slip system spin axes increases. This indicates that the last load step differed from the trend of plastic spin in the prior part of the deformation process.

The results of this analysis for the twinned grain are shown in the plots in figure 6.3. Here, the maximum dot product is plotted as a function of bulk strain. Each datum point is colored by the fraction of the slip system along the blended axis as indicated by the color bar. In the twinned grain, a little less than half of the dot products are high values, indicating that there are large fluctuations in the evolving stress tensor. This indicates that the concept of this analysis potentially able to relate the observed grain spin axis history to favored slip systems, and refinements to this approach may provide an improved agreement between this analysis strategy and the observations.

The process outlined in figure 6.3 is used for each load step in the plastic regime for three

different classes of grains represented in three rows (figure 6.4). The first type of grains are those where deformation twins were formed. The second type of grains are neighbors to the twinned grains that have a favorable geometrical and spatial alignment for slip transfer (high m' grains). The third type of grains are arbitrarily chosen from the gage volume interrogated by FF HEDM. Each plot has the history of observed vs. highly stressed slip systems dot products from six grains from each of the three categories are chosen for this comparison. For each class of grains, and for each value of i , the average value of the dot product is calculated and identified with a horizontal dashed line. The average value of the dot product increases slightly with increasing i for the twinned grains. In case of the other two classes of grains, there is a slight decrease in the average values for $i = 3$, but it increases for $i = 5$.

These results are further summarized in the cumulative distribution plots of the maximum value of the dot product for the same three categories of grains in figure 6.5, indicating the considerable spread in the values of the dot product. Nevertheless, the twinned grains have more values of the dot product that are closer to one. This can also be seen in the cumulative distribution plot in figure 6.5 where at least 46% of the points have values ≥ 0.8 . If this blend of the two most favored slip systems dominates the reorientation, the values of the CDF should be low until the dot product approaches 1, which is most clearly observed in the twinned grains. On the other hand, figure 6.5 shows that for the two other categories of grains (neighboring and arbitrarily chosen grains), the effect of smoothing is not as significant.

Additionally, the effect of changing the spacing between load steps is more profound in case of the twinned grains category as well. As the spacing is increased from 1 to 5, the percentage of data points with a dot product of 0.8 or higher increases. This indicates that despite the complexity associated with twinning, this method may be able to account for significant activity of pyramidal $\langle c + a \rangle$ slip that is associated with twinning, as this analysis currently tends to ignore the contributions of basal or prism slip, which may be more significant in the randomly chosen grains.

From the analysis shown in this chapter, it is clear that the variation between the kinematics of plastic deformation (as measured by lattice spin), and the grain averaged stress tensor measurement

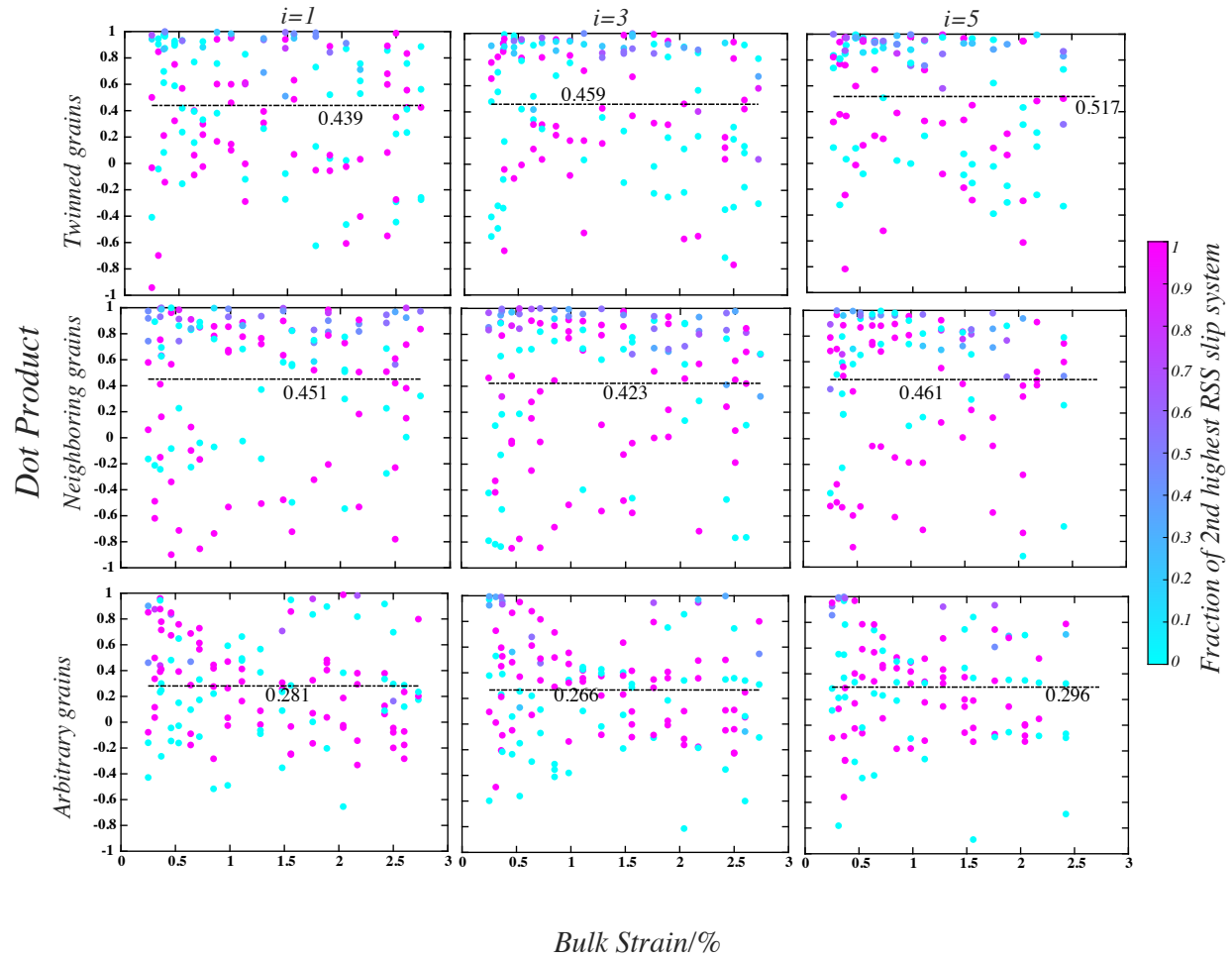


Figure 6.4: Maximum dot product between the observed lattice spin axes and blended high resolved stress slip system axes (slip systems with highest and second highest resolved shear stress), plotted as a function of bulk strain for six members of three types of grains; twinned grains, neighbors to the twinned grains, and arbitrarily chosen grains. For each plot, the average value of the dot product is plotted as a dashed horizontal line and annotated in each plot.

from FF HEDM is quite significant. Therefore, analysis of complex load transfer events in a polycrystal such as deformation twinning, the use of grain averaged measurements may not be sufficient for understanding what takes place, particularly in regions near grain boundaries where even greater variations in local stress state are expected. To gain better understanding of the influences of slip in one grain on its neighbor, the ability to measure the local stress tensor with a finer spatial resolution, such as the capability offered by DAXM is required for improved understanding of local plastic deformation processes.

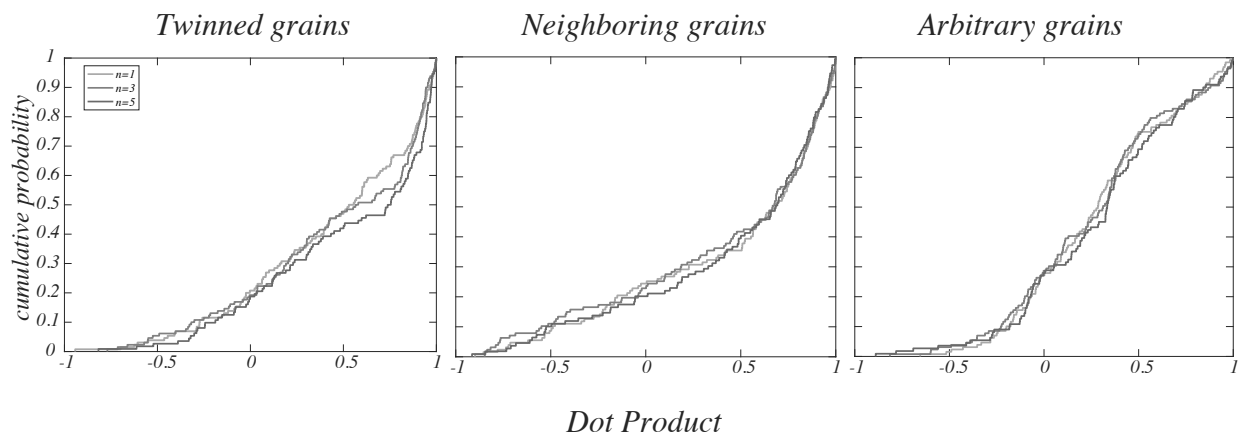


Figure 6.5: Cumulative distribution plots for the maximum dot product for the three categories of grains shown in 6.4. The effect of spacing between load steps is more significant for the twinned grains than for the other two classes of grains.

CHAPTER 7

IN-SITU DAXM CHARACTERIZATION OF A COMMERCIAL PURITY TITANIUM SPECIMEN SUBJECTED TO A FOUR POINT BENDING TEST

The approaches used for analysis of data obtained from the in-situ DAXM characterization at different load steps are described. The experimental setup and overall geometry for the in-situ characterization of the bending experiment are shown in figure 3.5. The spatially resolved deviatoric strain tensor is calculated for each bending increment. In addition, a methodology to calculate slip system specific GND density based on lattice rotation gradient is outlined. This is followed by a detailed description of the results and their discussion in section 7.4. The heterogeneity of stress state at grain boundaries is illustrated by tracking the variation in spatially resolved principal stress and principal directions for the second bending increment (section 7.4.2). Finally the relationship between local accumulation of GND density and slip transmissibility at the second bend increment is explored in section 7.4.3.

7.1 Texture of CP-Ti specimen

The four point bending specimen used for this experiment has a predominantly soft texture with respect to the loading direction i.e. prism slip is readily activated (Figure 7.1). Within the region examined by DAXM, two grains are considered to be of particular interest: a hard oriented grain, where prism slip is not expected to be readily activated; and a soft oriented grain adjacent to it. Indeed, evaluation of the surface global Schmid factor indicates that prism $\langle a \rangle$ slip is less likely to be active in the hard grain; while it is highly favored for the soft grain (Figure 7.2).

7.2 White beam diffraction

The experimental setup for the in-situ bending experiment has been discussed in section 3.3. Prior to bending, a DAXM scan of the region of interest was done with a step size of $4\mu\text{m}$. After the specimen was placed in the bending stage, DAXM scans were done following each

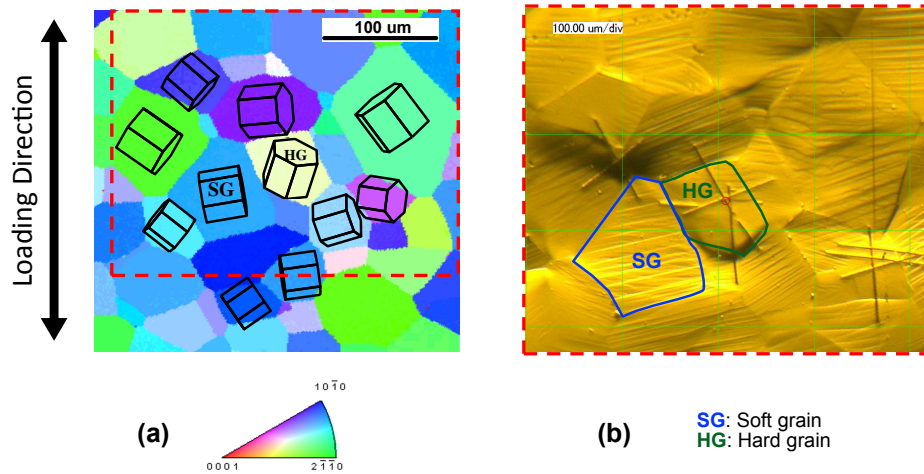


Figure 7.1: (a) OIM Map of the undeformed microstructure of the 4 point bending specimen prior to bending. The region interrogated by DAXM is outlined with a dashed rectangle. Prisms indicating orientations of the soft and hard grains are shown. (b) Optical image of the microstructure at the end of the final bending increment ($\sim 3.5\%$ macroscopic strain). The soft and hard oriented grains are outlined in blue and green respectively.

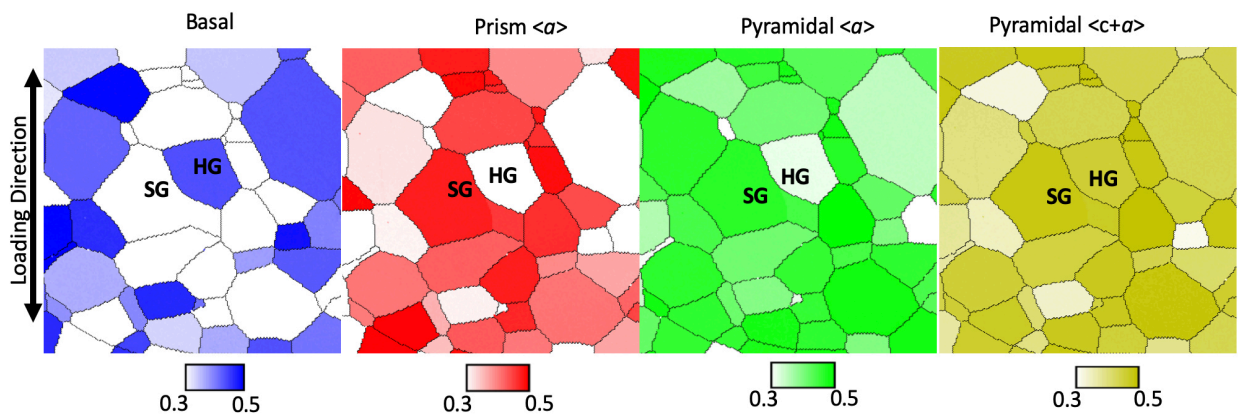


Figure 7.2: Surface global Schmid factor maps for specimen prior to bending. The overall texture is conducive to basal and prism $\langle a \rangle$ slip.

bending increment. The orientation maps of the scanned regions for undeformed and four bending increments are shown in figure 7.3 (a)-(e). At the second bend increment ($\sim 1.7\%$ bulk strain), line scans were made along the H and X directions with a step size of $1.5\mu\text{m}$ (figure 7.3(c)). All of the work described hereafter is from this second increment of strain.

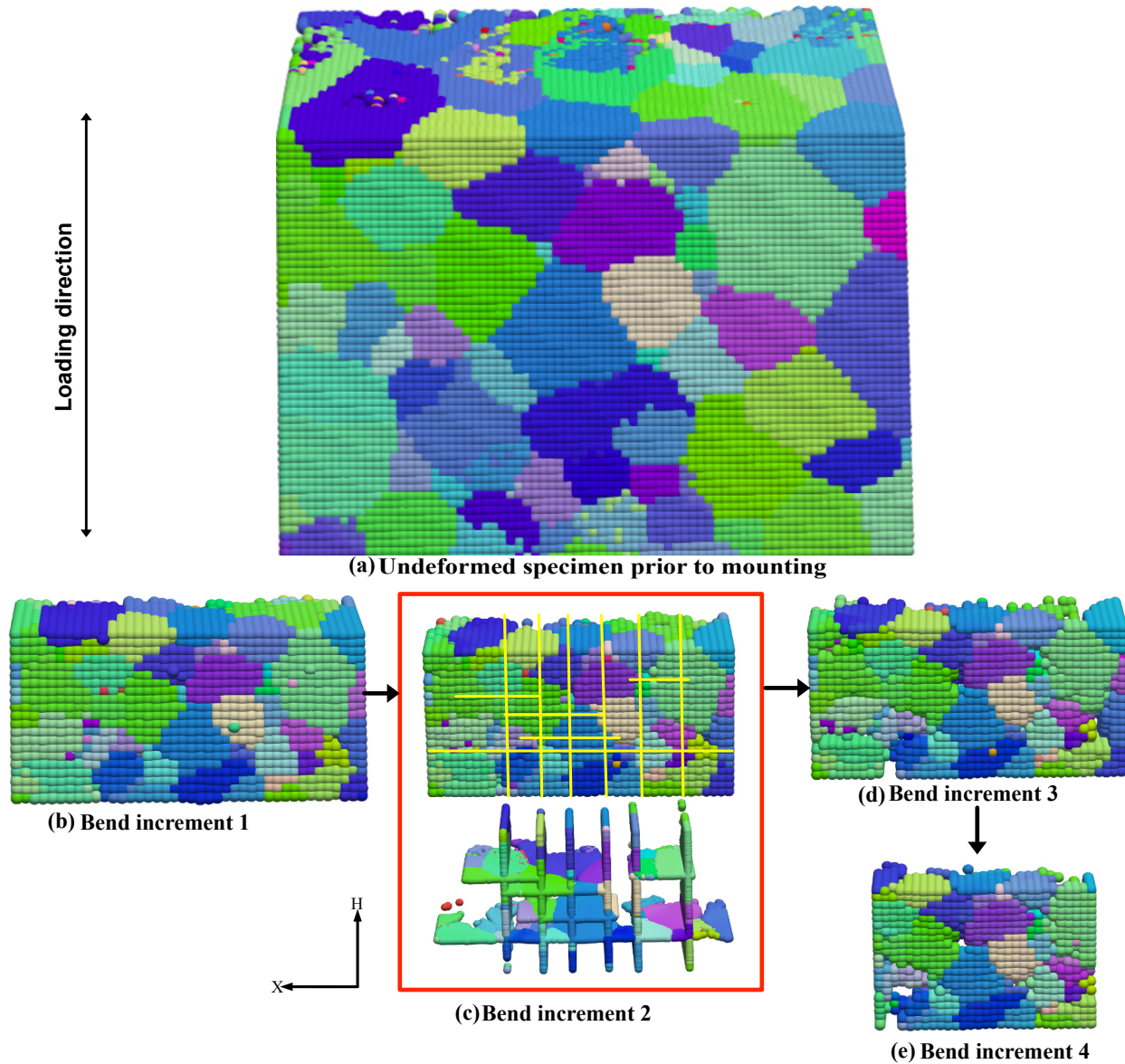


Figure 7.3: Orientation maps from the indexed DAXM results. The undeformed specimen was interrogated before mounting with a step size of $4\mu\text{m}$ (a). For the subsequent bending increments 1, 2, 3 and 4 ((b) through (e)) a coarser step size ($6\mu\text{m}$) was used. The vertical and horizontal lines (colored yellow) overlaid on the coarse dataset in (b) indicate the locations of finer $2\mu\text{m}$ step size H and X scans that are shown beneath the coarser map.

7.2.1 Local deviatoric strain tensor estimation from DAXM data

The Laue reflections obtained from white beam diffraction enables the mapping of the shape change of the unit cell with respect to the undistorted lattice. Optimization schemes were used to evaluate the deformation gradient which forms the basis for calculating the deviatoric strain tensor. This is implemented in the LaueGo module developed at the APS, which was used to analyze the data in an IGOR Pro environment.

Figure 7.4 shows the spatially resolved equivalent strain distribution for the DAXM measured volume for the unstrained state and the four subsequent bending increments (Interrogated volumes shown in figure 7.3). Below the plot, maps at a particular cross section are shown (the unstrained state has a vertical step size of $4\mu\text{m}$ and the four bending increments have a coarser $6\mu\text{m}$ step size). In the unstrained condition, the outlines of the grain boundaries are also shown in figure 7.4 (left, bottom row). While the sample is unstrained, there are clearly varying internal strains within the grains as indicated by the color gradients, where local accumulation of high equivalent strain above 0.001 can be observed in the vicinity of grain boundaries and triple junctions. With loading, the local strain state becomes more uniform, with subtle variations in color where grain boundaries are located, and they become more apparent with increasing strain. The topic of stress/strain heterogeneity near grain boundaries is examined in more detail in section 7.4.2. In the first, second and third bending increments at least 97% of the voxels have equivalent strains less than 0.005, 0.008 and 0.015 respectively. The inset shows the equivalent strain at each increment, indicating that after the fourth increment, an overall relaxation of the equivalent elastic strain took place (purple datum point). This indicates that a redistribution of elastic strain occurred within the sample.

7.3 Geometrically necessary dislocation density calculation from DAXM data

In this section the methodology used to calculate the GND density from DAXM data is detailed. This follows the mathematical and physical basis laid out by Das et al. and Guo et al. (Das et al.,

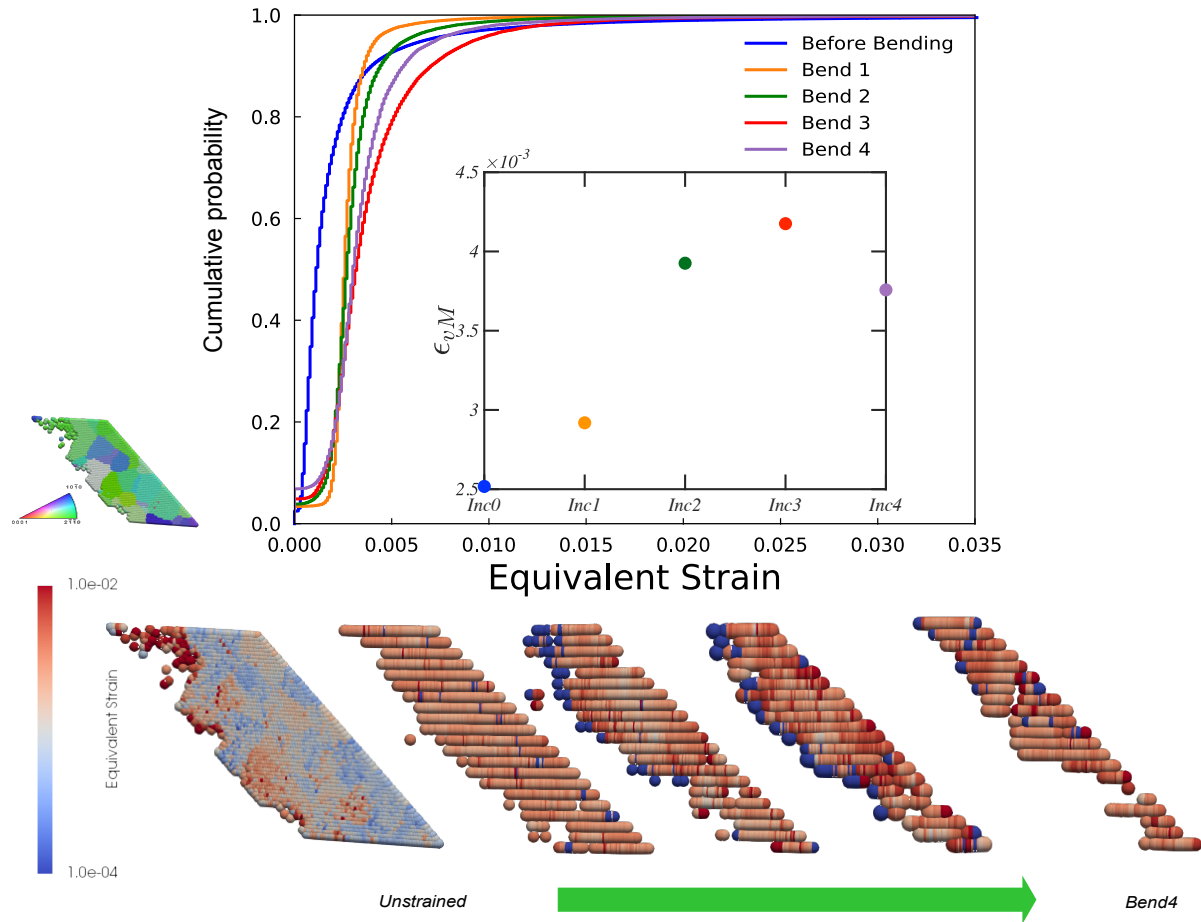


Figure 7.4: Local equivalent strain distribution map corresponding to the unstrained state and after four subsequent bending increments. The cumulative distribution function compares the equivalent strain corresponding to the unstrained state prior to bending (blue), and the four subsequent bending increments. The inset shows the evolution of the equivalent strain averaged over the entire interrogated volume for five strain states. The lower row shows the spatially resolved equivalent strain maps for the unstrained and four deformation states. The IPF color map for the microstructure corresponding to the unstrained state is shown on the left hand side of the top row. The unstrained scan was done prior to the bending experiment and covered a larger volume with a finer step size. The other scans were taken after each load step during the bending experiment.

2018; Guo et al., 2020) in section 2.6. The DAXM dataset used for GND calculation is the fine grid of H-X scans collected at the second bending increment ($\sim 1.7\%$ bulk strain). The approach used for GND calculation is summarized in figure 7.5. First, the reciprocal lattice vectors for each voxel obtained from the reconstructed DAXM data are used to calculate the real space lattice vectors and the orthogonal orientation matrix. The rotation gradient with respect to neighboring voxels in the three principal (orthogonal) directions is obtained. Finally, the optimization function is set up to minimize the total elastic energy of dislocations.

For each voxel, a ball of surrounding voxels is identified using a K-dimension nearest neighbor search algorithm. In the current work, the nearest neighbor search is implemented using the KD (K-dimensional) tree module available in SciPy. The disorientation matrix between each voxel and each of the voxels within the ball is computed as follows,

$$\omega_{ij} = R_{Center} \cdot R_{Neighbor}^T \quad (7.1)$$

where R_{Center} and $R_{Neighbor}$ are the orthogonal orientation matrices for the kernel and neighboring voxel respectively. The disorientation values are used to calculate the lattice rotation gradient tensor by a least squares fit onto a hyperplane of dimension $n - 1$.

$$\begin{bmatrix} w^1 \\ \vdots \\ w^n \end{bmatrix} = \begin{bmatrix} X_1^1 & X_2^1 & X_3^1 \\ \vdots & \vdots & \vdots \\ X_1^n & X_2^n & X_3^n \end{bmatrix} \begin{bmatrix} \frac{\partial w}{\partial X_1} \\ \frac{\partial w}{\partial X_2} \\ \frac{\partial w}{\partial X_3} \end{bmatrix} \quad (7.2)$$

For each neighboring voxel n , $w^n = (w_1^n, w_2^n, w_3^n)$ are the components of the infinitesimal lattice rotation vector such that $w_1^n = \frac{(\omega_{32} - \omega_{23})}{2}$, $w_2^n = \frac{(\omega_{13} - \omega_{31})}{2}$ and $w_3^n = \frac{(\omega_{21} - \omega_{12})}{2}$. (X_1^n, X_2^n, X_3^n) are the coordinates of the n^{th} nearest neighbor voxel in three-dimensional space.

For each voxel p in the DAXM dataset, $\left(\frac{\partial w}{\partial X_1}\right)_p$, $\left(\frac{\partial w}{\partial X_2}\right)_p$ and $\left(\frac{\partial w}{\partial X_3}\right)_p$ are the lattice rotation gradients. The lattice rotation gradient tensor for a given voxel in the dataset is written as follows.

$$\alpha_{ij}^\omega = \begin{bmatrix} \frac{\partial w_1}{\partial X_1} & \frac{\partial w_2}{\partial X_1} & \frac{\partial w_3}{\partial X_1} \\ \frac{\partial w_1}{\partial X_2} & \frac{\partial w_2}{\partial X_2} & \frac{\partial w_3}{\partial X_2} \\ \frac{\partial w_1}{\partial X_3} & \frac{\partial w_2}{\partial X_3} & \frac{\partial w_3}{\partial X_3} \end{bmatrix} \quad (7.3)$$

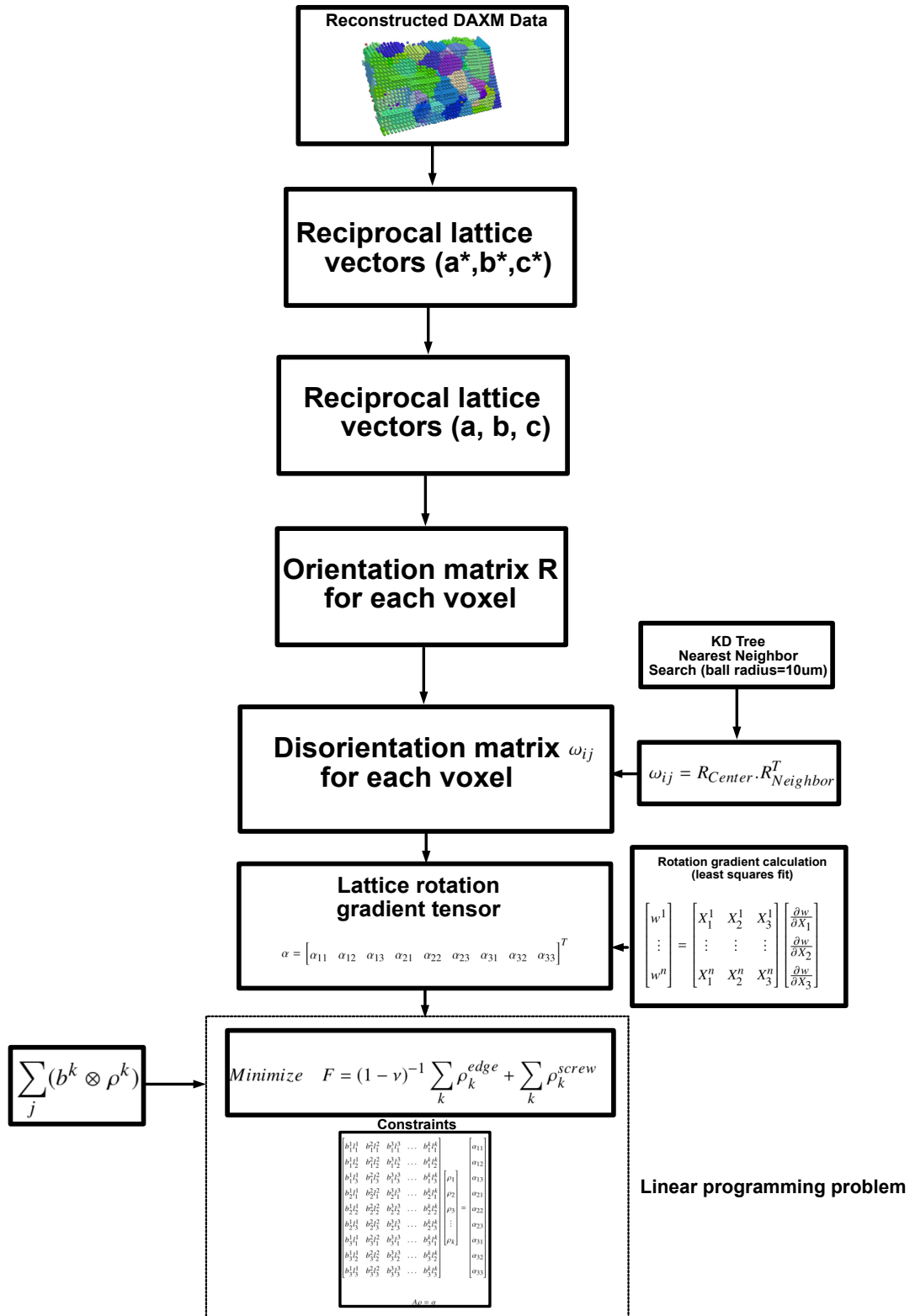


Figure 7.5: Schematic outlining strategy used to calculate GND density from DAXM dataset.

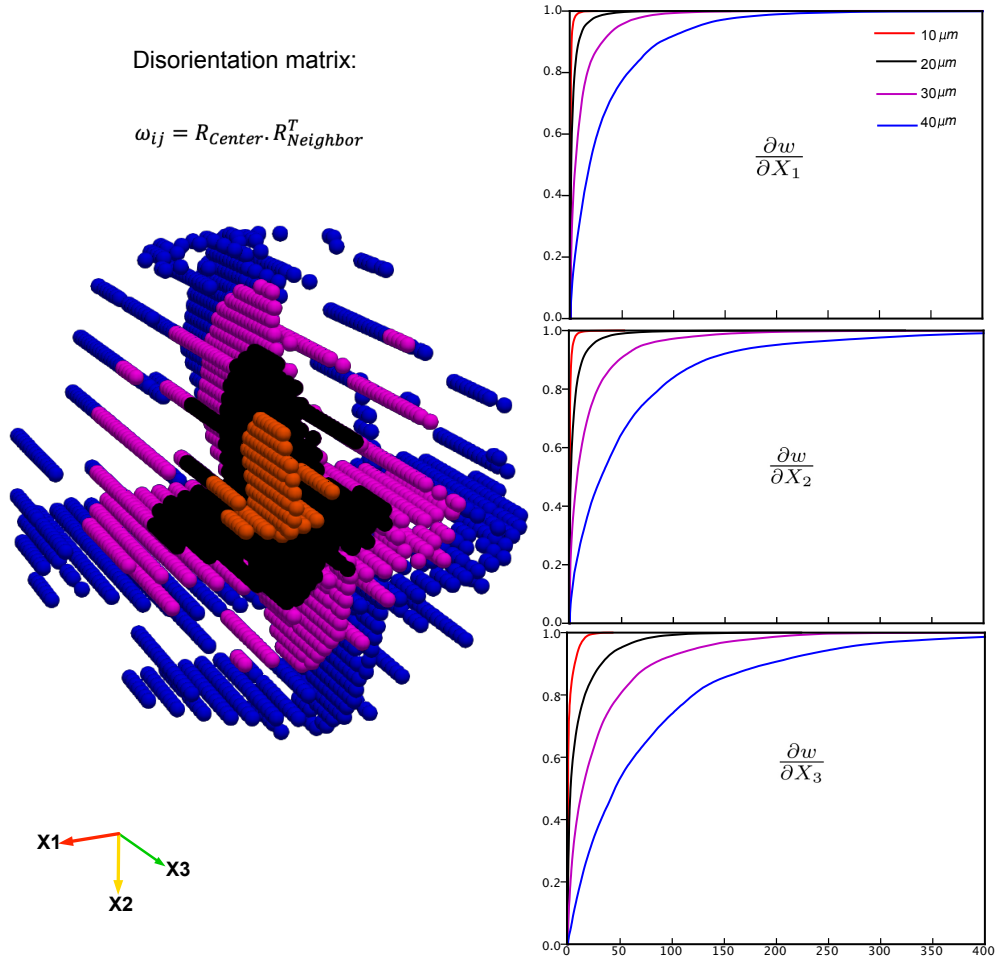


Figure 7.6: Left: The sphere surrounding a kernel for an exemplary voxel within the combined (Coarse scan + Fine scan) DAXM dataset for bend increment 2 is shown for ball radii range of 10-40 microns. Cumulative distribution function (CDF) plots of the residual sum of squares error for each of the three components of the rotation gradient tensor. The error increases with increasing ball radius used for the nearest neighbor search.

Figure 7.6 shows the cumulative distribution plot of the the error of fit (residual) for each component of the rotation gradient tensor, based upon the four different values of ball radius.

The error of fit (residual) for each voxel is calculated by evaluating the square of the L_2 norm using the following equation.

$$R_{\frac{\partial w}{\partial X}} = (||W - P||_2)^2 \quad (7.4)$$

Where,

$$W = \begin{bmatrix} w^1 \\ \vdots \\ w^n \end{bmatrix}$$

and

$$P = \begin{bmatrix} X_1^1 & X_2^1 & X_3^1 \\ \vdots & \vdots & \vdots \\ X_1^n & X_2^n & X_3^n \end{bmatrix} \begin{bmatrix} \frac{\partial w}{\partial X_1} \\ \frac{\partial w}{\partial X_2} \\ \frac{\partial w}{\partial X_3} \end{bmatrix}$$

The cumulative distribution plots in figure 7.6 show that the residual along each principal direction is sensitive to the ball radius chosen for the nearest neighbor search. Also, the density of voxels along the vertical (X_3) direction is greater than in the rest of the surrounding volume of the sphere due to the combination of fine and coarse datasets. Clearly, the error increases with increasing ball radius. For the present work, a ball radius of $10\mu\text{m}$ is used for nearest neighbor search. In theory, using a ball radius below $10\mu\text{m}$ would yield even smaller residual values. The limitation to using a smaller ball radius however, arises due to the ($6\mu\text{m}$) resolution of the coarser DAXM dataset. A ball radius less than $6\mu\text{m}$ would yield a sparser point cloud leading to highly skewed values of rotation gradients discussed next.

7.3.1 Rotation gradient calculation of DAXM dataset

The GND analysis is focused along the fine (H-X) line scan data collected at the second bend increment ($\sim 1.7\%$ global strain). For calculating the lattice rotation gradient, the H-X scan data are used in combination with the coarser dataset for the same load step as shown in figure 7.7. Using only the fine resolution data around a kernel with a sparse number of voxels along the X_1 direction leads to skewed values of rotation gradients. As seen from the different sphere sizes in figure 7.6, the density of voxels is lower along the X_1 direction, compared to X_2 and X_3 . Using a minimum ball radius of $10\mu\text{m}$ includes at least two sets of three or more voxels from the coarse dataset along the X_1 or X_2 directions. A kernel with ball radius below $6\mu\text{m}$ has a lower density

of voxels along $X1$ or $X2$. Contributions from the sparse data set were weighted the same as from the fine data set.

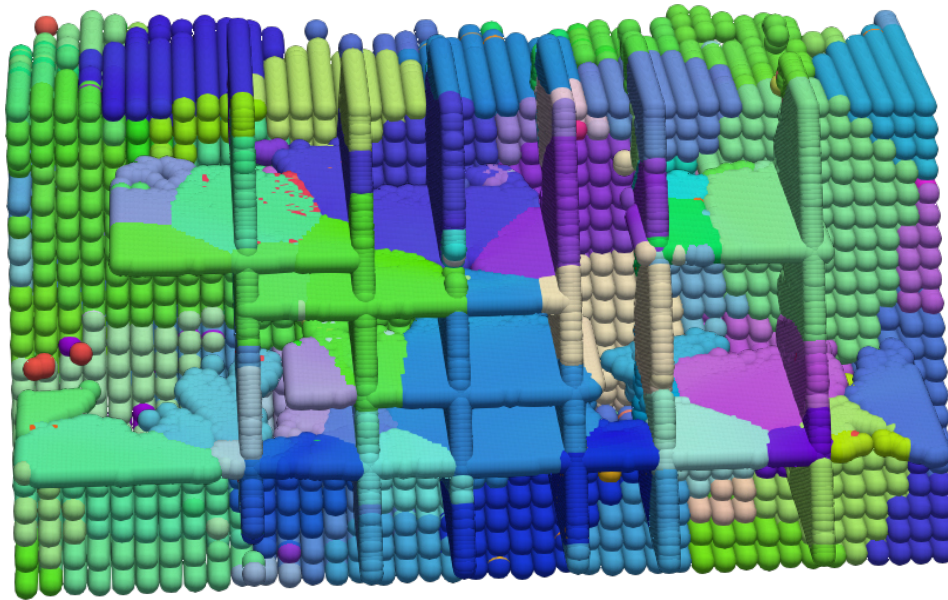


Figure 7.7: Bend increment 2: Line scan DAXM dataset superposed on coarse serial probed DAXM dataset. The two datasets are combined for purposes of the lattice rotation gradient calculation.

Figure 7.8 shows the nine components of the rotation gradient tensor for the fine scan dataset at the second bending increment. As expected, the magnitude of the rotation gradient components is high in the vicinity of grain boundaries.

7.3.2 Calculation of dislocation density from the rotation gradient

The current work uses the formulation of the Nye-Kröner-Bilby (NKB) equation that follows from equations 2.34 and 2.35. In equation 2.35, the contribution to the dislocation tensor α from the lattice rotation gradient is considered to be much greater than the elastic strain gradient. Therefore the second term can be neglected here.

Equations 2.36 and 2.37 are rewritten below in terms of the components of the lattice rotation gradient tensor.

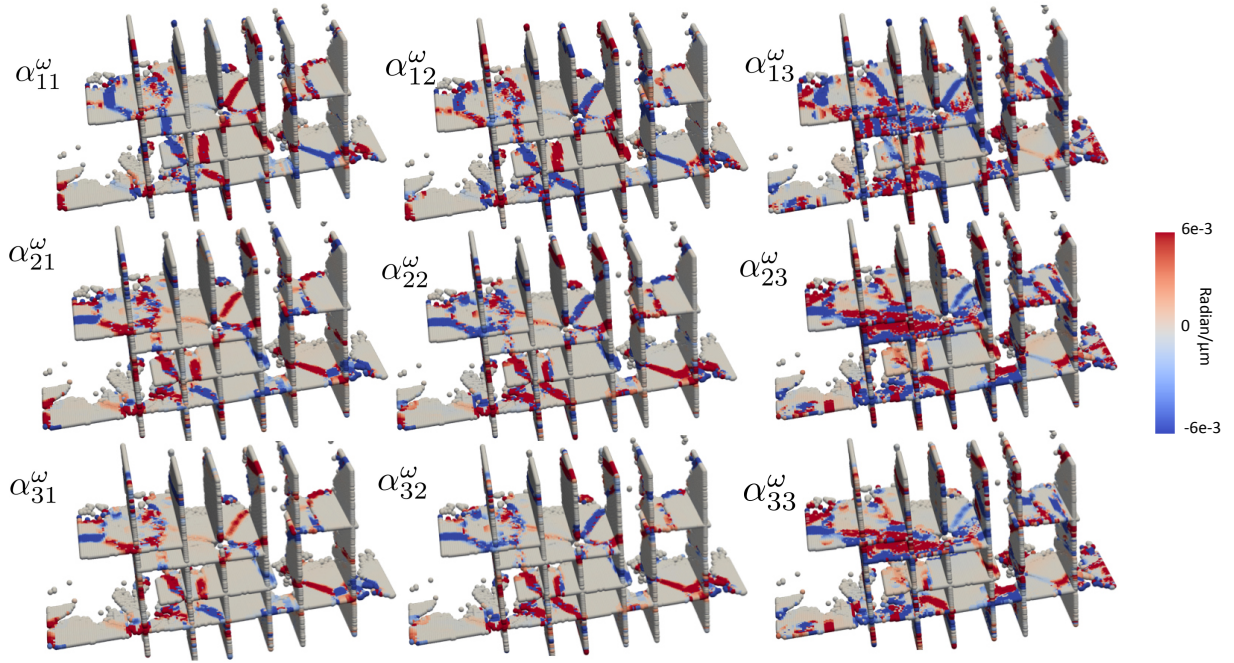


Figure 7.8: Bend increment 2: Maps showing the distribution of the nine components of the rotation gradient tensor for the fine scan grid.

$$\sum_j (b^k \otimes \rho^k) = \begin{bmatrix} b_1^1 l_1^1 & b_1^2 l_1^2 & b_1^3 l_1^3 & \dots & b_1^k l_1^k \\ b_1^1 l_2^1 & b_1^2 l_2^2 & b_1^3 l_2^3 & \dots & b_1^k l_2^k \\ b_1^1 l_3^1 & b_1^2 l_3^2 & b_1^3 l_3^3 & \dots & b_1^k l_3^k \\ b_2^1 l_1^1 & b_2^2 l_2^1 & b_2^3 l_2^1 & \dots & b_2^k l_2^1 \\ b_2^1 l_2^1 & b_2^2 l_2^2 & b_2^3 l_2^2 & \dots & b_2^k l_2^2 \\ b_2^1 l_3^1 & b_2^2 l_3^2 & b_2^3 l_3^3 & \dots & b_2^k l_3^3 \\ b_3^1 l_1^1 & b_3^2 l_2^1 & b_3^3 l_3^1 & \dots & b_3^k l_3^1 \\ b_3^1 l_2^1 & b_3^2 l_2^2 & b_3^3 l_2^3 & \dots & b_3^k l_2^3 \\ b_3^1 l_3^1 & b_3^2 l_3^2 & b_3^3 l_3^3 & \dots & b_3^k l_3^3 \end{bmatrix} \begin{bmatrix} \rho_1 \\ \rho_2 \\ \rho_3 \\ \vdots \\ \rho_k \end{bmatrix} = \begin{bmatrix} \alpha_{11} \\ \alpha_{12} \\ \alpha_{13} \\ \alpha_{21} \\ \alpha_{22} \\ \alpha_{23} \\ \alpha_{31} \\ \alpha_{32} \\ \alpha_{33} \end{bmatrix} = \begin{bmatrix} \frac{\partial w_3}{\partial X_3} - \frac{\partial w_2}{\partial X_2} \\ \frac{\partial w_2}{\partial X_1} \\ \frac{\partial w_3}{\partial X_1} \\ \frac{\partial w_1}{\partial X_2} \\ \frac{\partial w_1}{\partial X_1} - \frac{\partial w_3}{\partial X_3} \\ \frac{\partial w_3}{\partial X_2} \\ \frac{\partial w_1}{\partial X_3} \\ \frac{\partial w_2}{\partial X_3} \\ \frac{\partial w_2}{\partial X_2} - \frac{\partial w_1}{\partial X_1} \end{bmatrix} \quad (7.5)$$

$$A\rho = \alpha \quad (7.6)$$

where,

$$\alpha = \left[\alpha_{11} \quad \alpha_{12} \quad \alpha_{13} \quad \alpha_{21} \quad \alpha_{22} \quad \alpha_{23} \quad \alpha_{31} \quad \alpha_{32} \quad \alpha_{33} \right]^T,$$

$$A = \begin{bmatrix} b_1^1 l_1^1 & b_1^2 l_1^2 & b_1^3 l_1^3 & \dots & b_1^k l_1^k \\ b_1^1 l_2^1 & b_1^2 l_2^2 & b_1^3 l_2^3 & \dots & b_1^k l_2^k \\ b_1^1 l_3^1 & b_1^2 l_3^2 & b_1^3 l_3^3 & \dots & b_1^k l_3^k \\ b_2^1 l_1^1 & b_2^2 l_1^2 & b_2^3 l_1^3 & \dots & b_2^k l_1^k \\ b_2^1 l_2^1 & b_2^2 l_2^2 & b_2^3 l_2^3 & \dots & b_2^k l_2^k \\ b_2^1 l_3^1 & b_2^2 l_3^2 & b_2^3 l_3^3 & \dots & b_2^k l_3^k \\ b_3^1 l_1^1 & b_3^2 l_1^2 & b_3^3 l_1^3 & \dots & b_3^k l_1^k \\ b_3^1 l_2^1 & b_3^2 l_2^2 & b_3^3 l_2^3 & \dots & b_3^k l_2^k \\ b_3^1 l_3^1 & b_3^2 l_3^2 & b_3^3 l_3^3 & \dots & b_3^k l_3^k \end{bmatrix},$$

and

$$\rho = \left[\rho_1 \quad \rho_2 \quad \rho_3 \quad \dots \quad \rho_k \right]^T$$

Here ρ_k is the density corresponding to the k^{th} type of dislocation. b_i^k and l_j^k are the components of the Burgers vector and line direction of the k^{th} type of dislocation. The total dislocation density therefore, is given by $\sum_1^k \rho$. The coefficient matrix A with dimensions $9 \times k$ is built by taking into consideration four families of slip systems—basal,prism $\langle a \rangle$,pyramidal $\langle a \rangle$ and pyramidal $\langle c + a \rangle$. Twin systems or secondary slip systems are not considered in this formulation. Here, k is the total number of slip systems considered, while $i, j = 1, 2, 3$ are the three components of the Burgers vector b^k and line direction l^k in 3D space.

As mentioned in section 2.6, if $k > 9$, a unique solution for the dislocation density ρ does not exist. Since A and α are known, equation 7.5 can be solved using L^1 optimization. Here the total elastic energy of the dislocations is minimized. The elastic energies of the edge and screw dislocation are related to the Poisson ratio ν by the following relation.

$$\frac{E_{edge}}{E_{screw}} = \frac{1}{1 - \nu} \quad (7.7)$$

¹If edge/screw contribution from the slip system is uniquely identified it is marked with an '✓'. Screw dislocations from basal $\langle a \rangle$, prism $\langle a \rangle$ and pyramidal $\langle a \rangle$, that cannot be explicitly isolated are marked with '**'

Table 7.1: Slip Systems considered for GND density calculation

Slip System Type	Slip Plane Normal/Slip Direction	Edge ¹	Screw ¹
Basal $\langle a \rangle$	(0001)[2 $\bar{1}\bar{1}$ 0]	✓	*
Basal $\langle a \rangle$	(0001)[$\bar{1}$ 2 $\bar{1}$ 0]	✓	*
Basal $\langle a \rangle$	(0001)[$\bar{1}\bar{1}$ 20]	✓	*
Prism $\langle a \rangle$	(01 $\bar{1}$ 0)[2 $\bar{1}\bar{1}$ 0]	✓	*
Prism $\langle a \rangle$	($\bar{1}$ 010)[$\bar{1}$ 2 $\bar{1}$ 0]	✓	*
Prism $\langle a \rangle$	(1 $\bar{1}$ 00)[$\bar{1}\bar{1}$ 20]	✓	*
Pyramidal $\langle a \rangle$	(0 $\bar{1}$ 11)[2 $\bar{1}\bar{1}$ 0]	✓	*
Pyramidal $\langle a \rangle$	(10 $\bar{1}$ 1)[$\bar{1}$ 2 $\bar{1}$ 0]	✓	*
Pyramidal $\langle a \rangle$	($\bar{1}$ 101)[$\bar{1}\bar{1}$ 20]	✓	*
Pyramidal $\langle a \rangle$	(1 $\bar{1}$ 01)[11 $\bar{2}$ 0]	✓	*
Pyramidal $\langle a \rangle$	(01 $\bar{1}$ 1)[$\bar{2}$ 110]	✓	*
Pyramidal $\langle a \rangle$	($\bar{1}$ 011)[1 $\bar{2}$ 10]	✓	*
Pyramidal $\langle c + a \rangle$	($\bar{1}$ 101)[2 $\bar{1}\bar{1}$ 3]	✓	✓
Pyramidal $\langle c + a \rangle$	($\bar{1}$ 101)[1 $\bar{2}$ 13]	✓	✓
Pyramidal $\langle c + a \rangle$	(10 $\bar{1}$ 1)[$\bar{1}\bar{1}$ 23]	✓	✓
Pyramidal $\langle c + a \rangle$	(10 $\bar{1}$ 1)[$\bar{2}$ 113]	✓	✓
Pyramidal $\langle c + a \rangle$	(0 $\bar{1}$ 11)[$\bar{1}$ 2 $\bar{1}$ 3]	✓	✓
Pyramidal $\langle c + a \rangle$	(0 $\bar{1}$ 11)[11 $\bar{2}$ 3]	✓	✓
Pyramidal $\langle c + a \rangle$	(1 $\bar{1}$ 01)[$\bar{2}$ 113]	✓	✓
Pyramidal $\langle c + a \rangle$	(1 $\bar{1}$ 01)[$\bar{1}$ 2 $\bar{1}$ 3]	✓	✓
Pyramidal $\langle c + a \rangle$	($\bar{1}$ 011)[11 $\bar{2}$ 3]	✓	✓
Pyramidal $\langle c + a \rangle$	($\bar{1}$ 011)[2 $\bar{1}\bar{1}$ 3]	✓	✓
Pyramidal $\langle c + a \rangle$	(01 $\bar{1}$ 1)[1 $\bar{2}$ 13]	✓	✓
Pyramidal $\langle c + a \rangle$	(01 $\bar{1}$ 1)[$\bar{1}\bar{1}$ 23]	✓	✓

Therefore the objective function F to be minimized can be expressed as follows (Das et al., 2018; Guo et al., 2020).

$$\text{Minimize } F = (1 - \nu)^{-1} \sum_k \rho_k^{edge} + \sum_k \rho_k^{screw} \quad (7.8)$$

subject to the constraints defined by equations 7.5 and 7.6; where $\rho^{edge} = (\rho^{edge})_{\langle a \rangle} + (\rho^{edge})_{\langle c + a \rangle}$ denotes the edge dislocation contribution (including $\langle a \rangle$ and $\langle c + a \rangle$ slip systems). Similarly $\rho^{screw} = (\rho^{screw})_{\langle a \rangle} + (\rho^{screw})_{\langle c + a \rangle}$ represents the screw dislocation contributions. The linear programming problem (equation 7.8) can be solved using standard solvers. In this particular case, the *LINPROG* module available in MatLab was used. An important assumption is that dislocations

are either of pure edge or pure screw type.

In the case of the screw dislocation contributions from basal $\langle a \rangle$, prism $\langle a \rangle$ and pyramidal $\langle a \rangle$ slip, an aggregate screw dislocation density for each $\langle a \rangle$ direction is obtained but cannot be explicitly isolated in terms of individual slip systems.

Table 7.1 lists the slip systems considered for the constraint equation 7.5. If the edge or screw dislocation contributions from the slip system can be uniquely identified, the column is marked with an '✓'. Screw dislocations from $\langle a \rangle$ type of slip systems (basal, prism and pyramidal), that cannot be explicitly isolated are marked by '*'.

7.4 Results and discussion

Figure 7.9 shows the total and slip system family subset GND maps from each family for the fine scan data corresponding to the second bending increment. Local agglomeration of both total and slip system family GND density can be observed near grain boundaries and triple junctions.

7.4.1 Localized GND concentrations at grain boundaries

The localized GND concentrations were analyzed for twelve grain boundaries (including three triple junctions) within the microstructure of the finer scan DAXM dataset (the 5 regions encompassing these boundaries are shown in figure 7.10). Region 1 is a vertical fin comprising of two boundaries of interest: one low angle grain grain boundary within the same grain, and the other being a high angle grain boundary (purple and pink colored grain). Region 2 encompasses a triple junction, where one of the constituent grains has a hard orientation with respect to the loading axis (beige grain on the right). Regions 3 and 5 also contain triple junctions, while region 4 is a high angle grain boundary.

7.4.2 Assessment of local stress heterogeneity using principal components

An important consideration to understand the meso-scale mechanical response is the spatial variation in the local stress state. For example, it is especially interesting to assess how the spatially

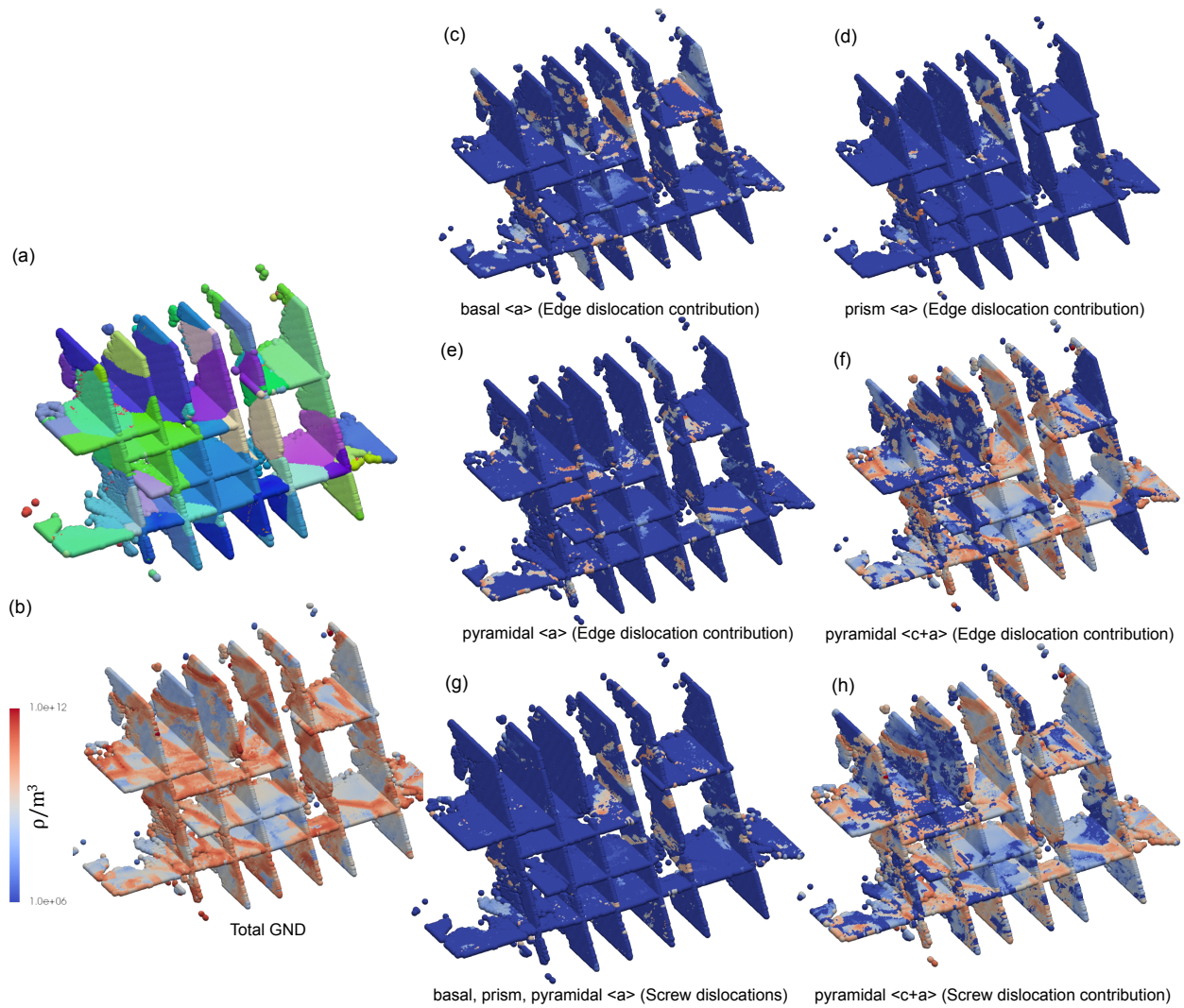


Figure 7.9: Bend increment 2: GND density maps, showing total GND density (b) and GND densities specific to slip system families. Screw dislocation contributions of $\langle a \rangle$ type are in (g). Comparing the total GND density with the IPF map (a), it can be seen that the GND concentrations coincide with the grain boundaries.

resolved stress tensor varies with respect to grain averaged values in the vicinity of grain boundaries. Thus, the principal values and directions of the local stress tensor are used to quantify heterogeneity of the driving force for mechanical response within the polycrystal. This is done by calculating the Eigen values and Eigen vectors of the local stress tensor and comparing with the equivalent results from the grain averaged stress tensor. Specifically, five distinct regions from the microstructure interrogated by the line DAXM scans are examined (figure 7.10). These regions include three triple junctions (regions 2, 3, and 5) and three other grain boundaries (two high angle grain boundaries (HAGB) and one low angle grain boundary (LAGB)).

The variation in magnitude and direction of the principal stress is visualized using "stress jacks"; where the three principal directions are superposed onto a colored sphere that represents each voxel, where the color represents the local crystal orientation. The magnitude and sense of each principal stress component are denoted by the color of the respective vector. The principal stress and directions for each voxel in two exemplary areas involving the purple grain are shown in figures 7.11 and 7.12. For comparison, the corresponding grain averaged stress tensors and the principal components for the purple grain and its neighbors above it also computed,

$$\sigma_{ij}^{Average} = \frac{\sum_{k=1}^n \sigma_{ij}^k}{n} \quad (7.9)$$

where n is the total number of constituent voxels in the grain, and $i, j = 1, 2, 3$. Only the voxels from the coarse resolution dataset were used to calculate the average stress state of each grain, to eliminate overemphasis from the fine scan regions. Similarly, the individual components of the stress tensor averaged over the entire volume interrogated in the coarse DAXM data set comprising about 70 grains is determined, indicating that the principal stress directions are not perfectly aligned with the assumed global uniaxial tension.

The principal components in this analysis are referred to as *first*, *second* and *third* in order of decreasing magnitude, and they are labeled for the average stress tensors in figures 7.11 and 7.12. To put these two maps into a larger context, maps of about six grains showing these three components are presented in figure 7.13. It is noteworthy that the first principal stress component

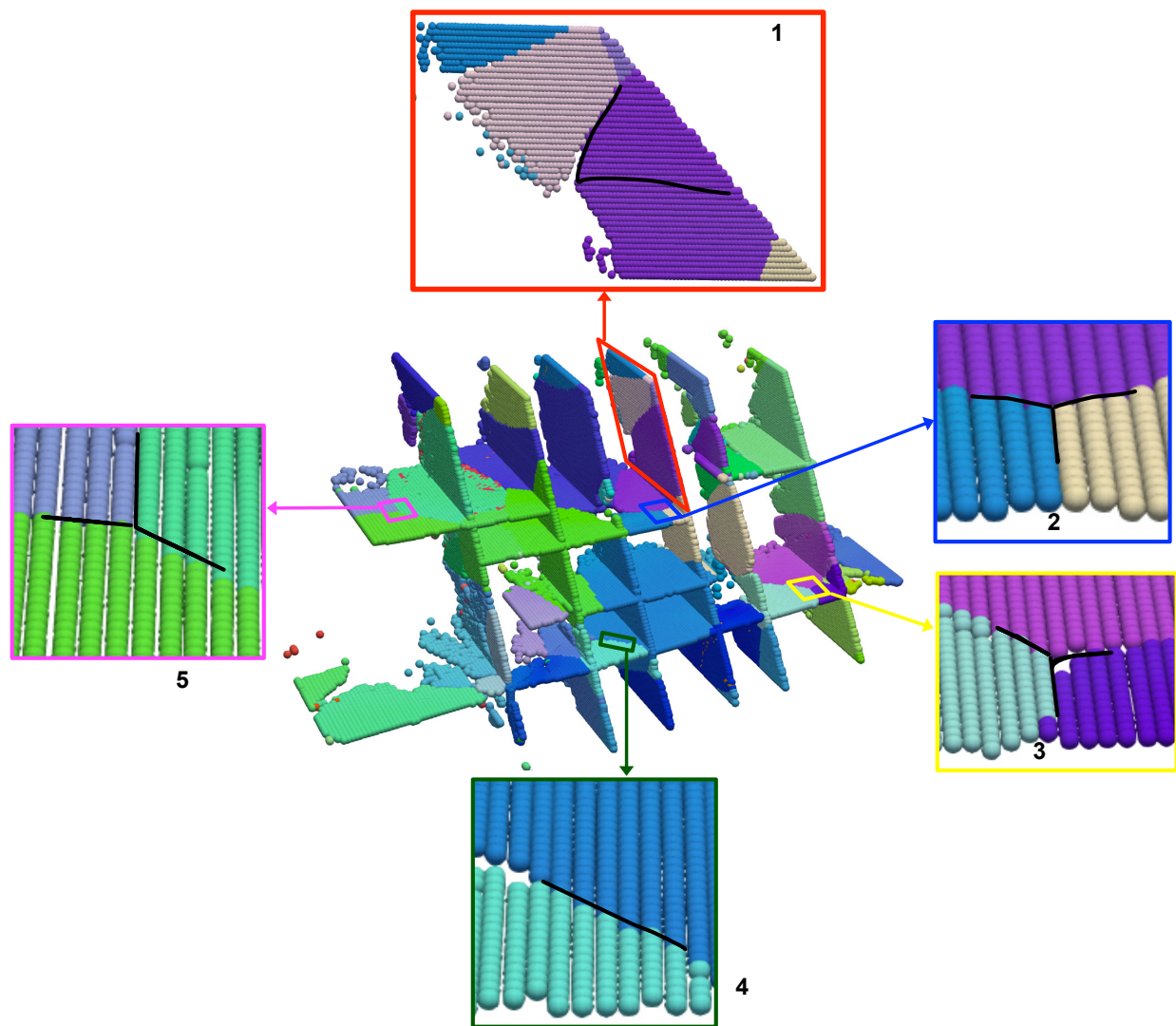


Figure 7.10: Bend increment 2: Orientation map of the regions of interest where the scaled slip transfer parameter is plotted as a function of residual Burgers vector. Region 1 comprises a grain boundary and an intragranular region with an orientation gradient; region 2, 3 and 5 are triple junctions; and region 4 is a grain boundary.

is mostly compressive, but the second component is mostly tensile, and has similar magnitude, indicating that the stress state is largely bi-axial.

7.4.2.1 Local stress heterogeneity within and above the purple grain

The principal stress map for a region within the purple grain is shown in figure 7.11. The intragranular zone between the black lines indicates a region with locally varying stresses that differ significantly from neighboring voxels as well as the average stress (only the right side of this region has a stress close to the grain average). Above and below the two lines, the stress jacks are more uniformly oriented. The region along the grain boundaries with two neighboring grains above is shown in figure 7.12. The local variation in stress tensor among the three grains in the triple junction (pink, lavender, and purple grains) indicate that all three grains have significantly different stress states near the boundary, and that these stresses differ significantly from their respective grain averaged stress jacks. Some voxels adjacent to grain boundaries have high stress values. The region in the purple grain below the grain boundary has a different stress state than the more uniform stresses several voxels below the grain boundary.

Examining the principal stress maps in figure 7.13 identified by the three components, it can be seen that there is significant variation in both direction and sense of the first (maximum) principal component (left) in the vicinity of the grain boundary above the purple grain and even within the intragranular region identified in figure 7.11 with variable stress tensors. The sense of the first principal stress changes from compressive near the center of both grains to tensile along the grain boundary and some locations within the intragranular zone of high local stress variation within the purple grain. This variation in the first principal direction corresponds with high GND density locations described later in section 7.4.3.

Considering the third principal stress and direction, the stress is mostly tensile but lower in magnitude than the second component in most of the region. The sense of stress switches from tensile near the grain centers to compressive in the vicinity of the grain boundary and the intragranular zone with high local GND density. Moreover, taking all three principal stresses and

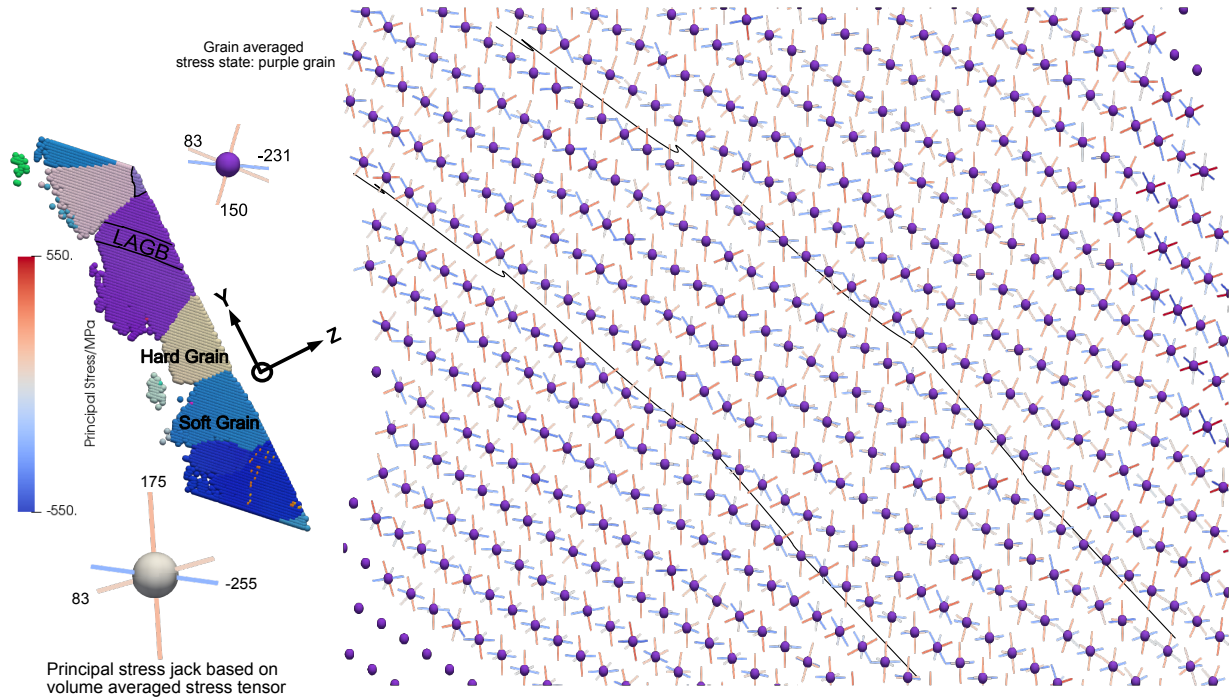


Figure 7.11: Principal Stress distribution for the intragranular region in the purple grain shows varying local stress states indicated by different "principal stress jacks" that differ from the average stress tensor for the purple grain shown on the left. The color of each line in the stress jack indicates the value of the principal stress component in MPa, which are annotated on the average stress jacks. The tensile direction is parallel to the Y axis in the coordinate system shown while Z is the surface normal. The stress jacks are oriented according to the XYZ axes, indicating that the largest compressive principal stress is roughly perpendicular to the stress axis. The average principal stress jack corresponding to the entire measured volume is also shown on the light gray sphere.

directions into account, intragranular transition zones are observed in most of the grains where waviness is apparent.

7.4.2.2 Local stress heterogeneity in region 2 triple junction with hard and soft grains

Examining the triple junction in region 2 between the purple grain and the hard (beige) and soft (blue) grains (figure 7.14), it can be seen that the local principal stress and directions align closely with the grain averaged state, except for the row of voxels that form the boundaries with the blue and beige neighboring grains. In the soft (blue) grain, the directions of the compressive (blue) principal component gradually changes as the grain boundary is approached from the left. The positive principal direction becomes much larger as one gets closer to the grain boundary and

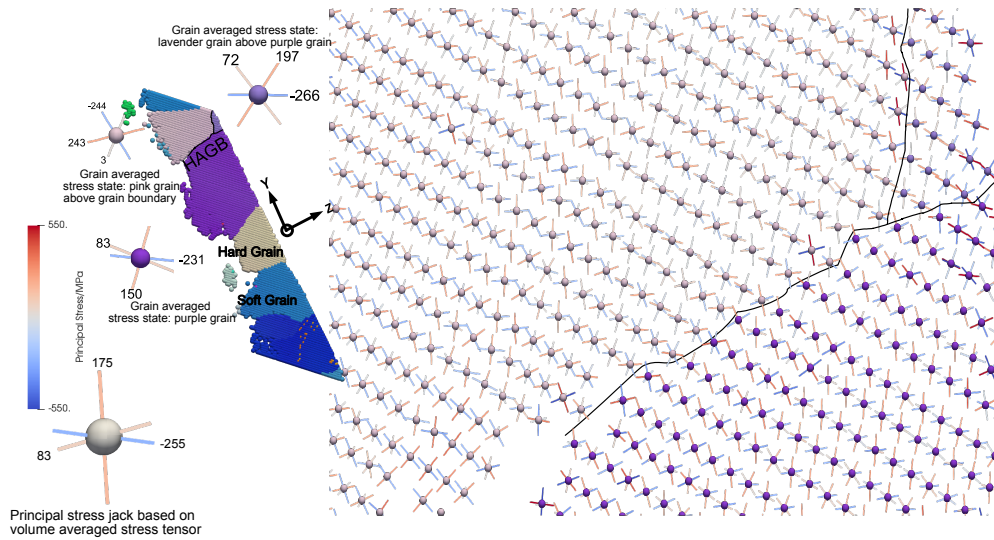


Figure 7.12: Principal Stress map for the high angle grains near the boundaries above the purple grain, including the corresponding grain average "principal stress jacks" for the pink and lavender grains above the purple grain, which have a significantly different stress state than the purple grain. The tensile axis is parallel to the global Y direction (shown on the right of figure). The principal stress values are annotated on the grain average and volume average stress jacks. The stress in the pink and lavender grains are much different from the purple grain, and the stress state near the boundaries differ significantly from the grain interiors.

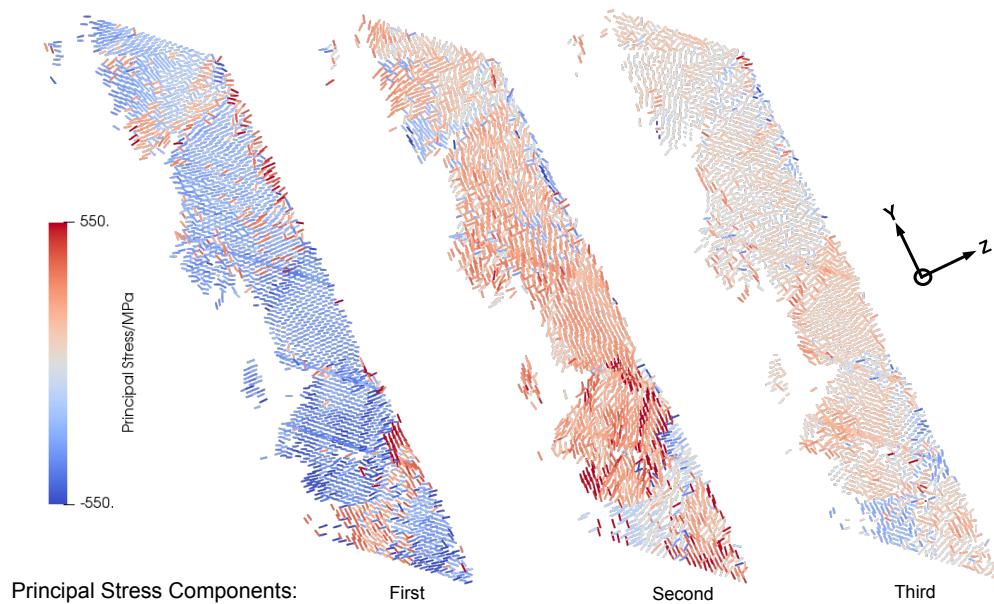


Figure 7.13: Bend increment 2: Principal Stress maps for the entire vertical fin containing the LAGB and HAGB of region 1, with each principal component shown separately.

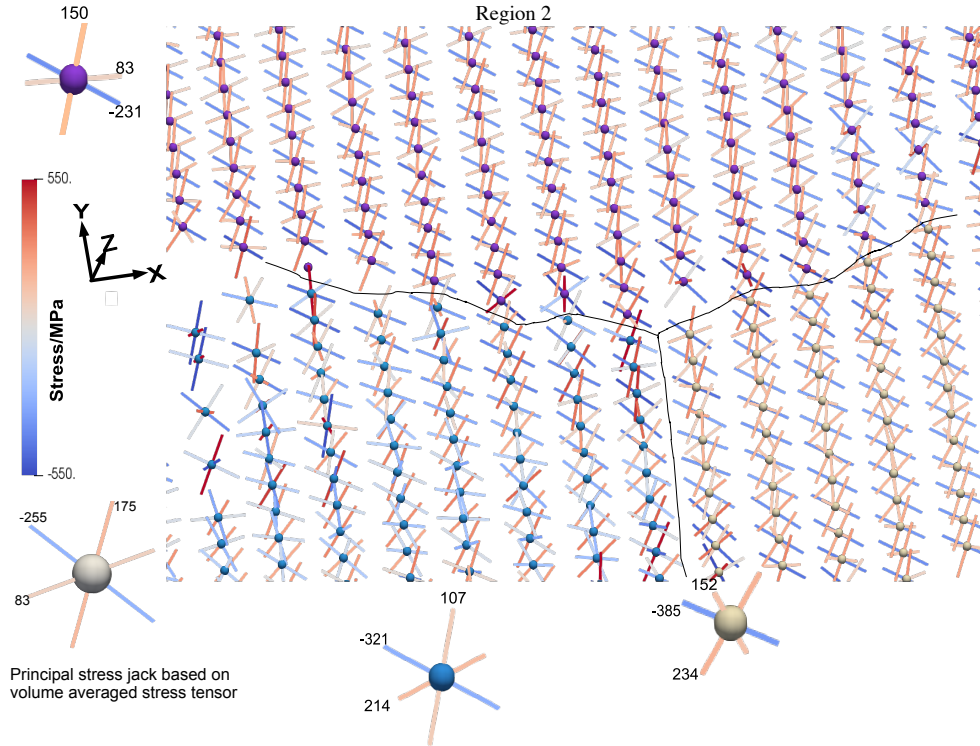


Figure 7.14: Principal Stress direction map for the triple junction in region 2, where the viewpoint is identified by the X-Y-Z arrows. The grain boundaries are delineated by black lines. Principal stress jacks corresponding to average stress tensor for each individual grain, along with their magnitudes and sense are also shown for comparison. The tensile axis is parallel to the global Y axis shown on the left of the figure.

triple junction. The stress tensor in the beige (hard) grain orientation is quite uniform and similar to the grain averaged state. For the purple grain, the stress is close to the average stress tensor except near the triple junction. The principal stress and principal direction maps of the remaining three regions considered in this analysis are shown in appendix E.

From the above observations it can be surmised that changes in sense and direction of local principal stress can be used to identify regions where local strain accommodation at grain boundaries may involve stresses that activate slip systems that differ significantly from regions in the grain interior. There are regions where significant deviation from the grain averaged stress state occur also tend to have high local GND agglomeration, as described in section 7.4.3. Moreover, grains with soft orientations noticeably have strong deviations from the average stress state in the vicinity of grain boundaries. On the other hand, the local stress in the hard oriented grain in region 2 does

not deviate significantly from the average stress state.

7.4.3 Description of parameters used in analysis of slip transfer at the voxel level

Figure 7.15 shows the total GND density map for the intergranular (grain boundary) and intragranular voxels for region 1. The GND map of Region 1 (figure 7.15) shows a band of high GND density in the middle of the purple grain. The spatially resolved deviation from the average grain orientation in figure 7.16 shows that this region is disoriented from the average grain orientation by about a degree, and is hence labeled a low angle grain boundary (LAGB) region. Specific regions such as the pairs of voxels circled are analyzed using strategies described below, and provided in appendix F.

An important underlying assumption in this analysis is that m' would have an inverse relationship with respect to the magnitude of residual Burgers vector, i.e. instances where slip transfer readily takes place (m' values approaching 1) would correspond to lower magnitudes of residual Burgers vector. m' plotted as a function of residual Burgers vector are discussed in detail for specific regions in the H-X scan dataset.

Let α and β be two adjacent voxels and s_α and s_β be two interacting slip systems in grains α and β , respectively. If slip transmission from α to β is considered, the residual Burgers vector left within a grain boundary can be expressed by the following equation.

$$b_{Residual} = b_{Out}^{s_\beta} - b_{In}^{s_\alpha} \quad (7.10)$$

where $b_{Residual}$ is the residual Burgers vector; $b_{Out}^{s_\beta}$ and $b_{In}^{s_\alpha}$ are the Burgers vectors corresponding to the transmitting and receiving voxels respectively.

The second parameter used to assess the likelihood of slip transfer is the Luster-Morris parameter (m'). The third parameter is the generalized Schmid factor on each slip system as evaluated using the stress tensor from each voxel.

In the present analysis, several different combinations of parameters are used to plot the relationship between $|b_{Residual}|$, m' and slip system specific GND density for a pair of interacting

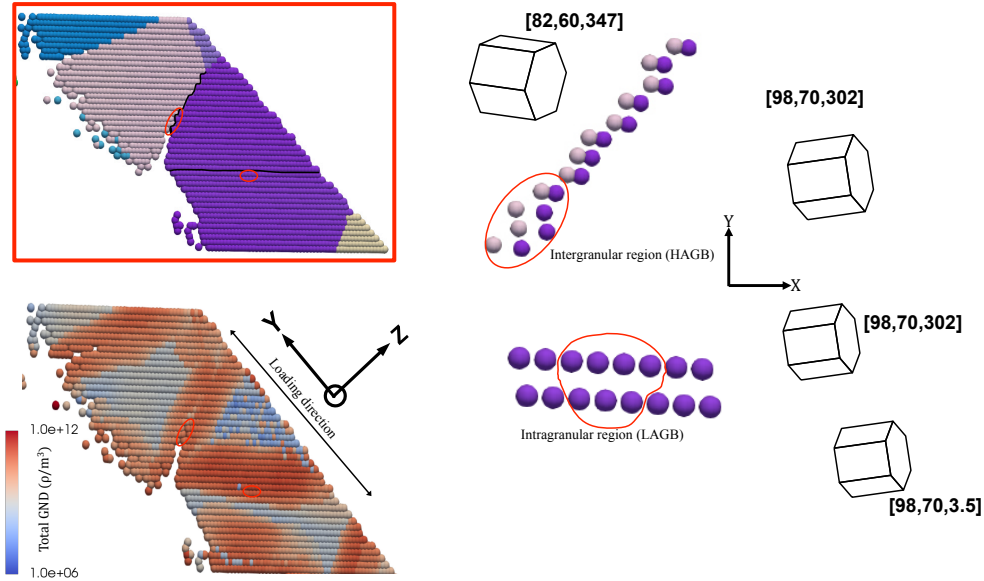


Figure 7.15: Orientation and total GND density maps for region 1. The voxels chosen for slip transfer analysis in the high angle grain boundary ($\sim 28^\circ$ misorientation) and intragranular (low angle grain boundary with misorientation $< 1.5^\circ$) regions are shown (circled voxels). The Bunge Euler angles denoting the average grain orientations are also noted here. It is important to note here that prisms denoting the crystal orientations are drawn from the perspective of the sample normal direction, with Y pointing vertically up and X to the right.

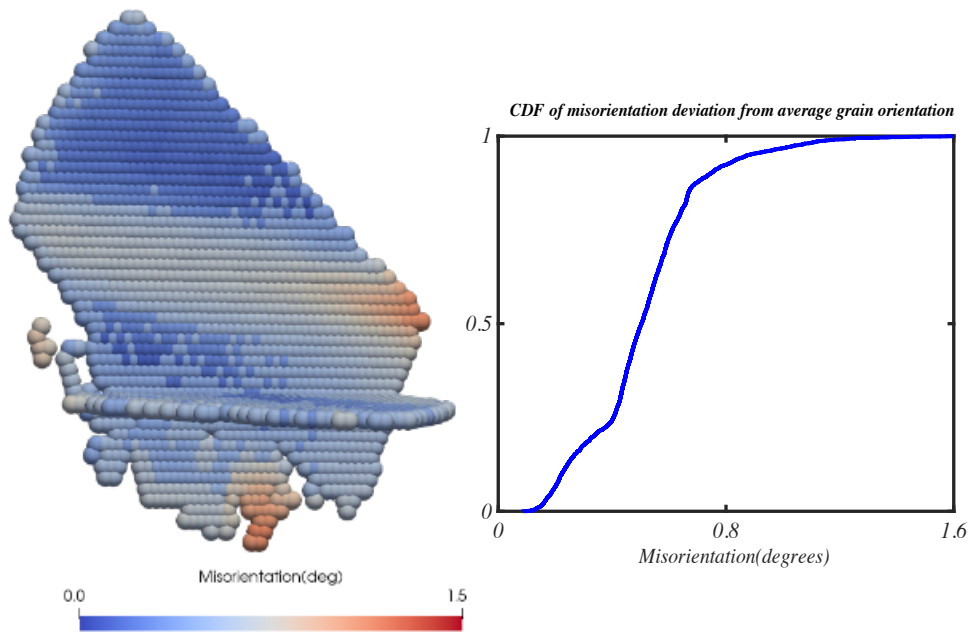


Figure 7.16: Map showing spatially resolved deviation from the average grain orientation in the lower grain of region 1 (Left). The cumulative distribution of misorientation deviation within this grain is shown on the right. The region with a relatively higher deviation coincides with the high local GND accumulation region

voxels. These combinations are listed in table 7.2. The independent variable used here is the magnitude of the residual Burgers vector $b_{Residual}$, while m' is the dependent variable. Both of these values can be scaled by the maximum or minimum values of the slip system specific GND density ($max(\rho_\alpha, \rho_{beta})$ or $min(\rho_\alpha, \rho_\beta)$) for the voxel pair.

Table 7.2: Combinations of parameters used to assess relationship between residual Burgers vector, m' and GND density

Independent Variable	Dependent Variable	Basis of choice of transmitting voxel
$ b_{Residual} $	m'	Arbitrary
$min(\rho_\alpha, \rho_{beta}) \times b_{Residual} $	$\frac{m'}{min(\rho_\alpha, \rho_{beta})}$	Arbitrary or $max(LSf)$
$max(\rho_\alpha, \rho_{beta}) \times b_{Residual} $	$\frac{m'}{max(\rho_\alpha, \rho_{beta})}$	Arbitrary or $min(\rho_\alpha, \rho_{beta})$

An important question arises here, as to the basis for choosing the transmitting slip system for a pair of voxels. In this study three different approaches are used—the first being an arbitrary choice of voxels on one side of the grain boundary as transmitters. For the second approach the slip system with the greater local Schmid factor (LSf) is considered to be the transmitter. The third approach uses the minimum value of slip system specific GND density as the criterion for the transmitting voxel based upon the assumption that the slip system with the lower GND density will transmit more readily. The reader is referred to appendix F for more details of this analysis and preliminary outcomes.

7.5 Summary assessment of inter-and intra-granular heterogeneous deformation

From this preliminary assessment of heterogeneous stress and local GND density, it is evident that local variations of stress, particularly in the vicinity of grain boundaries are significant, and these variations have to be taken into account in order to describe the local dislocation activity. Although the stress tensor averaged over the interrogated volume approaches ideal uniaxial tension in some grains, it is clear that the local stress tensors vary widely from the global stress, especially near grain boundaries. Assuming an average grain size of $100\mu\text{m}$, the investigated volume contains approximately 70 grains: therefore it is a much smaller subset of the bulk volume of the specimen,

where the number of grains is of the order of 10^5 . The measurements and analysis possible with DAXM show that true understanding of instances of local slip interactions at the grain boundary cannot be examined effectively using even grain averaged stress tensors.

CHAPTER 8

CONCLUSIONS AND SCOPE FOR FUTURE WORK

8.1 Far Field HEDM

8.1.1 Twin identification and role of slip transfer in twin nucleation

As described in chapter 4, a total of 13 discrete twin-parent pairs were identified using FF 3D XRD. Among these twins, the activated variant did not necessarily have the highest local Schmid factor values. From just the FF HEDM analysis, it would appear that five of the twins may have nucleated as a result of slip transfer of pyramidal $\langle c + a \rangle$ slip across the grain boundary. When assessing the plausibility of slip transfer across a grain boundary, it is important to take into consideration both the geometrical and spatial compatibility.

One important observation from this study is that the subsurface slip activity in a polycrystal can be different from slip activity on the surface. Earlier surface studies pointed towards relatively high prism $\langle a \rangle$ slip activity leading to twin nucleation, whereas subsurface investigations reveal a much higher likelihood of pyramidal $\langle c + a \rangle$ slip leading to twin nucleation. Indeed, prism $\langle a \rangle$ slip systems were not found to have high geometric compatibility with the activated twin variants observed. Comparison with similar studies in titanium shows that the type of slip system most likely to nucleate a T1 twin is dependent on the loading direction and initial texture (Abdolvand et al., 2015a; Nervo et al., 2016)

A semi quantitative metric of the initial local stress in each grain was obtained by comparing the measured grain averaged stress tensor with ideal uniaxial tension. The stress state of several of the parent grains approached the uniaxial tensile state following an initial nearly uniaxial compressive state with increasing global load (which were present due to internal stresses in the sample). The magnitude of stress in the analyzed twinned grains registers a drop or remains steady around the point of twin formation. In some less common cases, an stress increase was observed. This confirms

that twin formation is often associated with stress relaxation in the parent grain and accommodation of the stress drop by neighboring grains in the polycrystal. The final stress state of the parent grain is dependent on how the accommodation of strain takes place in the neighborhood.

For the FF HEDM data, a quantified comparison between the kinematic descriptor (lattice reorientation) and grain averaged stress state is made, indicating that the actual relationship is more complex than the metric can identify. This also helps to identify the limits of using FF HEDM for understanding complex mesoscopic loading states in polycrystalline materials.

8.1.2 Comparison of FF results with Near Field and surface EBSP mapping

Comparison of FF results with surface EBSD mapping at the final unloaded state yielded partial matches for twin parent pairs and grains in their neighborhood. Only three twin-parent pairs were matched within a misorientation threshold of 5° . Comparison of the angle-axis misorientation between the XRD and EBSD did not reveal any systematic mounting error leading to variation in misorientation for the twins identified. Large variations in spatial positions between the surface EBSD and FF 3D XRD were noted indicating significant uncertainty in FF grain positions. To ensure that the results of the FF dataset obtained using Fable were credible, the data were also analyzed using the more sophisticated MIDAS package. A good match between the two sets of results was obtained, in terms of grain center of mass positions and grain averaged strain/strain tensors, but MIDAS provided a larger number of indexed grains (section 4.7). Thus, it is possible that the large variations in misorientation and spatial positions could be an intrinsic outcome of comparing a 2D EBSD slice with a 3D XRD dataset of a deformed sample. The strong orientation gradients present in the specimen probably contributed to this wide range of orientation variation. The results of matching with EBSD are not as favorable as some of the reported work on polycrystalline hexagonal metals with more random texture, such as Louca and Abdolvand (2021).

The FF HEDM data corresponding to the final unloaded state was also compared with the NF data, using criteria of Euclidean distance between the grain center of mass and the misorientation between the two FF and NF orientations. Two different algorithmic approaches were used for the

comparison exercise. In the first approach, the misorientation criterion is applied before the distance criterion, while the order was reversed for the second approach. Both algorithms converged to the same result for matching grains in the two datasets.

For the matched set of grains between FF and NF HEDM, the median grain radius of the NF data is greater than the reported FF grain radius by a factor of ~ 3 . There is a weak linear correlation between the reported FF grain radius and the number of constituent voxels in the matched NF grains. Overall, the grain volume estimated by NF is more credible compared to the FF grain radius values due to the finer spatial resolution of the NF method. Many more twinned grains were found in the NF dataset than the 13 twinning events identified in the FF data. Out of the 13 twins identified from the FF HEDM analysis 11 twins were also found in the NF dataset. Out of this population of 11 twins, 7 had interfacial contact with neighboring grains. Therefore slip transfer analysis was repeated for only these 7 twinning instances. It is pertinent to mention here that out of the 7 twins that were identified between FF and NF datasets, the neighboring grains deemed to have good geometrical compatibility (high m' with respect to activated twin variant) and spatial proximity in FF analysis were the same for 3 instances in the NF dataset. During the NF analysis the remaining 4 twins had different neighboring grains with interfacial contact with the twin. It was observed from the NF data set indicated that $\sim 34\%$ of the grains contain T1 twins.

8.2 DAXM analysis

8.2.1 Assessment of heterogeneity in stress state due to local constraints

Assessment of the spatially resolved principal stress and their directions suggest strong heterogeneity in the local stress magnitude and direction within an individual grain. This reveals strong constraint effects from neighboring grains. The variation in principal stress magnitude, sense and direction is more pronounced in the vicinity of grain boundaries. Therefore, it is highly likely that the local stress state may have a greater influence on which slip systems are active as revealed by the GND accumulation than the pure geometrical relationship between two grains.

8.3 Scope for future work

These data sets provided continuing opportunity for deeper analysis. Using the far field 3D XRD analysis, several discrete pairs of twin-parent grain pairs were identified that were likely active in slip transfer. However, the analysis conducted did not seek evidence for whether twins initiated $\langle c + a \rangle$ slip or vice versa. From analysis of rotations in the grain, it is possible to discern if $\langle c + a \rangle$ slip took place on the identified slip system using orientation changes such as that used by Leyun Wang et al.. It is also however, important to consider combinations of slip systems that could account for the observed crystal orientation evolution.

Also, the number of matched grains between 3D XRD and surface EBSD mapping is low (<40%). It would be more efficient to develop an automated process to identify twin parent pairs from the FF HEDM data, compared to the manual method employed in the current study. Though there is no obvious way to do this conveniently, it would be helpful if in-situ EBSD could be conducted concurrently with the 3D-XRD characterization. The NF data was only available for the final unloaded state of the tensile experiment. For grain matching between FF and NF datasets, it would be very helpful if a corresponding NF characterization of the data is also conducted prior to tensile loading.

In the DAXM study, the GND content was calculated using the lattice rotation gradient and the effect of long range elastic stress fields was not considered. Therefore the formulation is highly localized. A non-local formulation would take into account the influence of elastic stress fields that could result in a better resolved GND mapping. Moreover, this mesoscopic approach does not capture the more complex mechanics of dislocations at the atomistic level. For completeness, a multiscale approach associating the meso-scale results with atomistic simulations would be provide further opportunity to explore the large amount detail available in this data set.

APPENDICES

APPENDIX A

ADDITIONAL FAR FIELD ANALYSIS RESULTS

A.1 Grain positions showing propensity of S+T twinning

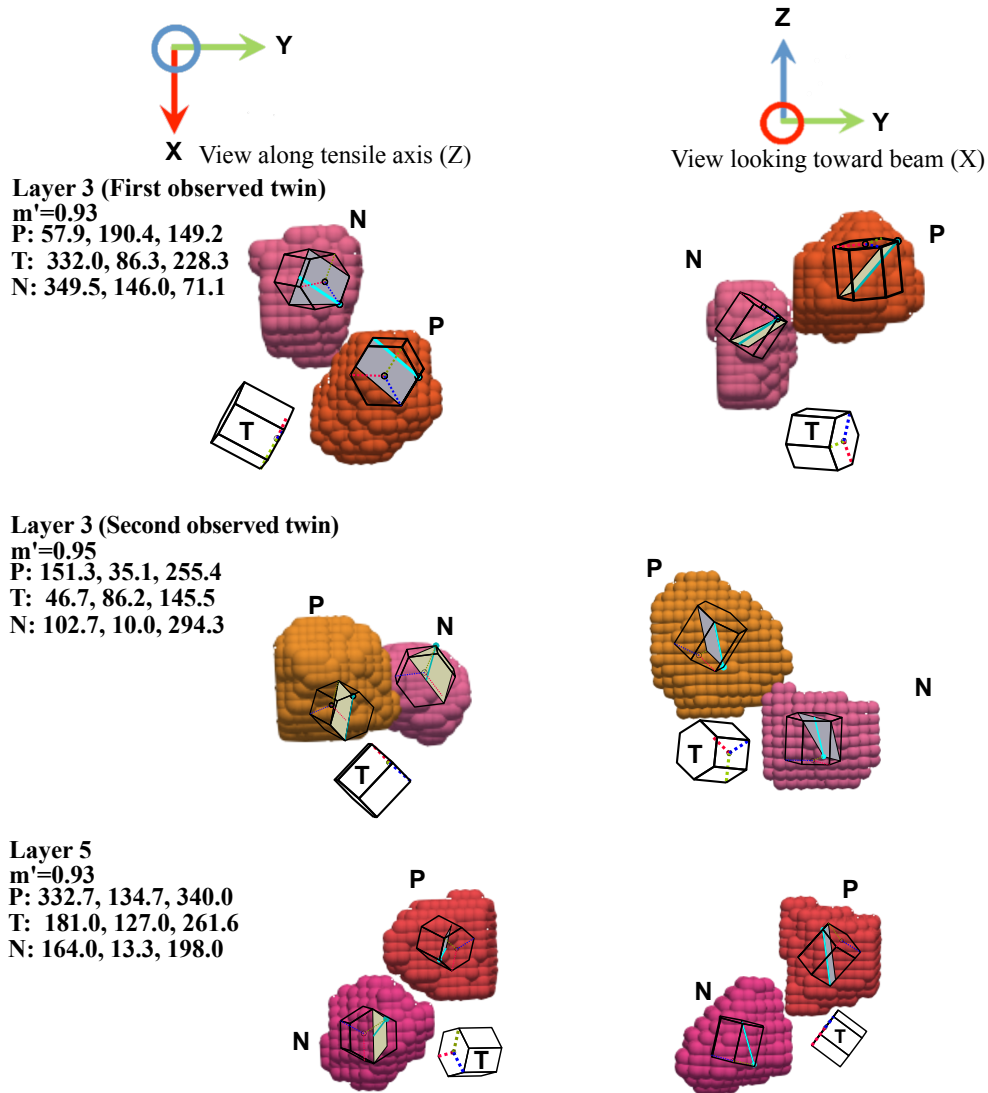


Figure A.1: The m' relationship observed between the activated twin system and pyramidal $\langle c + a \rangle$ system of a neighboring grain is shown for layers 3 and 5. The orientations of the parent, twin and neighboring grains are viewed along the tensile Z axis, (left column) as well as the beam X direction, (right column). For description of the symbols, the reader is referred to figure 4.10.

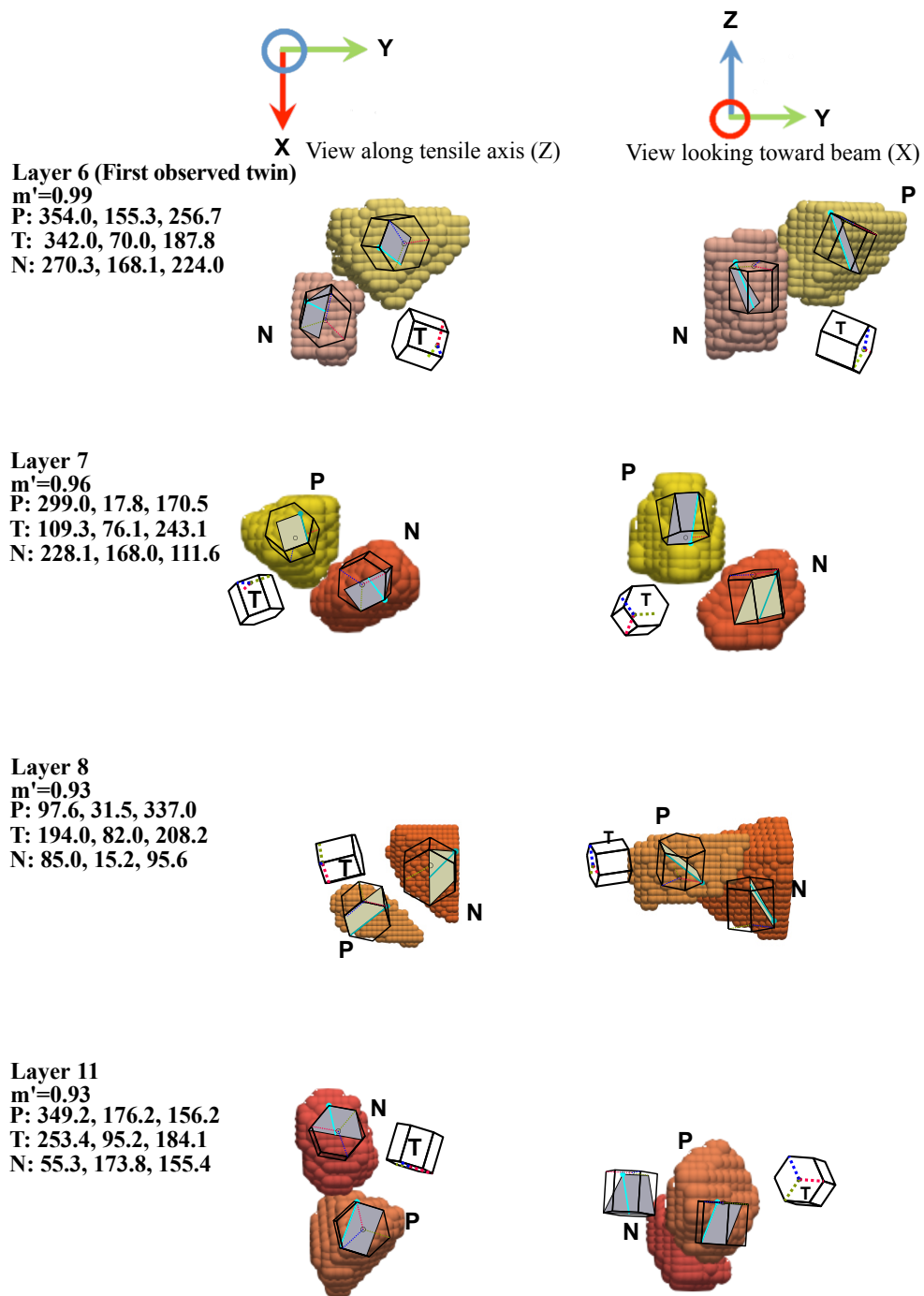


Figure A.2: The m' relationship observed between the activated twin system and pyramidal $\langle c + a \rangle$ system of a neighboring grain is shown for layers 6, 7, 8 and 11. The orientations of the parent, twin and neighboring grains are viewed along the tensile Z axis, (left column) as well as the beam X direction, (right column). For description of the symbols, the reader is referred to figure 4.10.

APPENDIX B

PARENT/TWIN/NEIGHBOR SLIP TRANSFER ANALYSIS FROM NF HEDM

In this part of the appendix, the remaining five twinning events identified in FF HEDM that were validated by NF HEDM are shown. For description of the plotted parameters the reader is referred to section 4.8

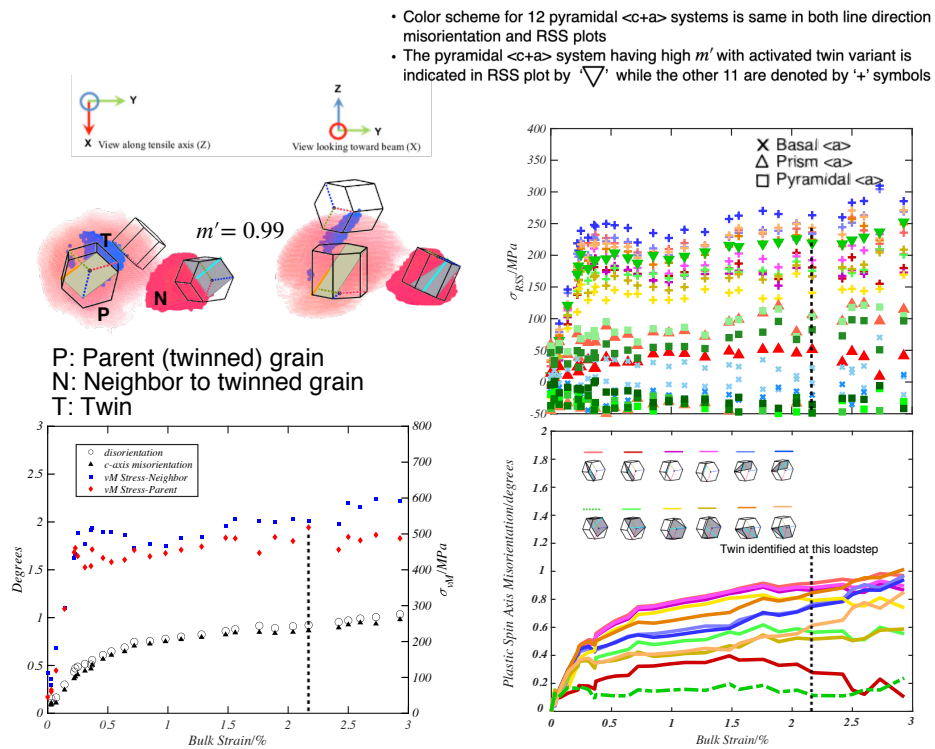


Figure B.1: Parent/Twin/High m' neighbor for twin identified in layer 6 in FF HEDM and validated by NF HEDM.

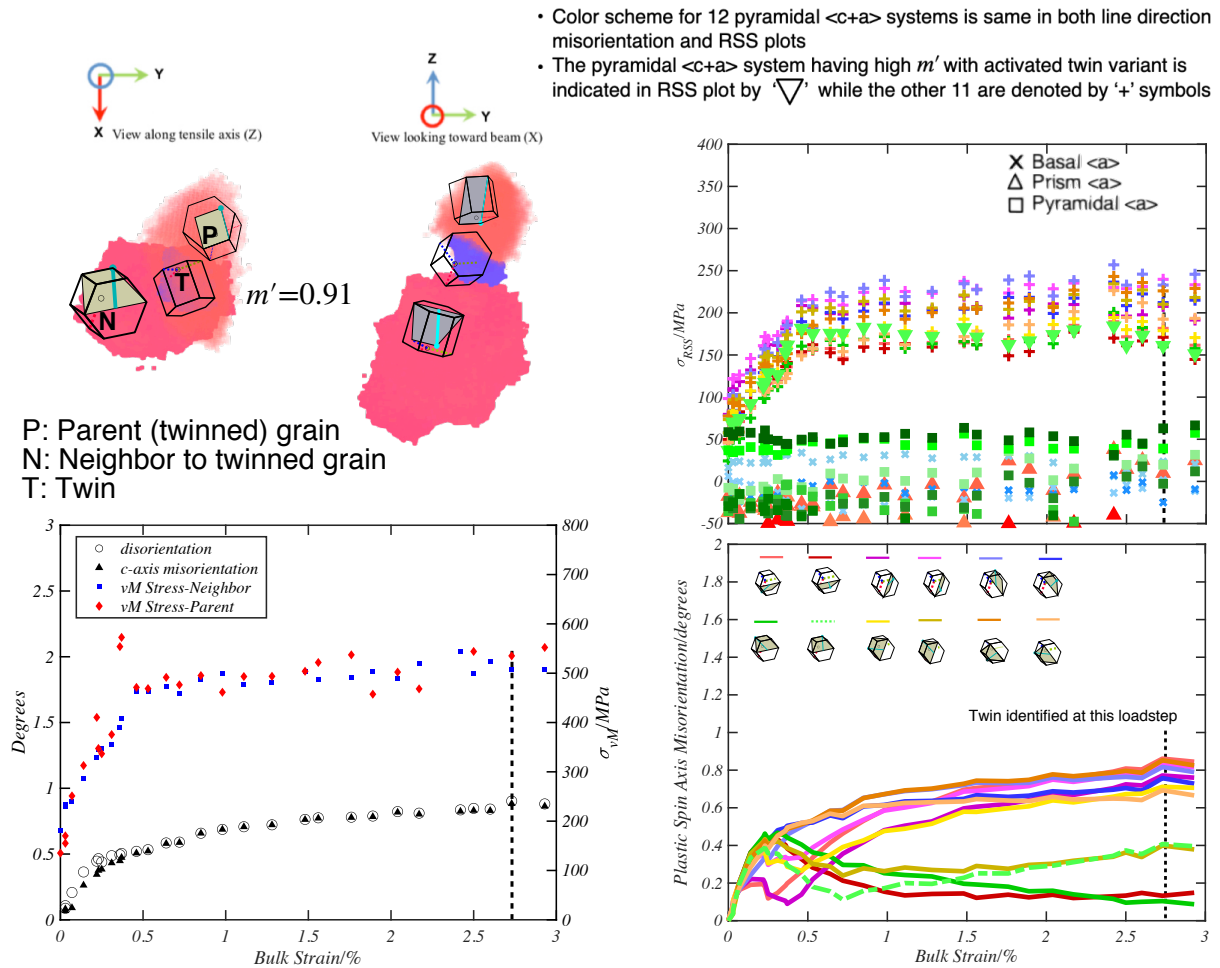


Figure B.2: Parent/Twin/High m' neighbor for twin identified in layer 7 in FF HEDM and validated by NF HEDM.

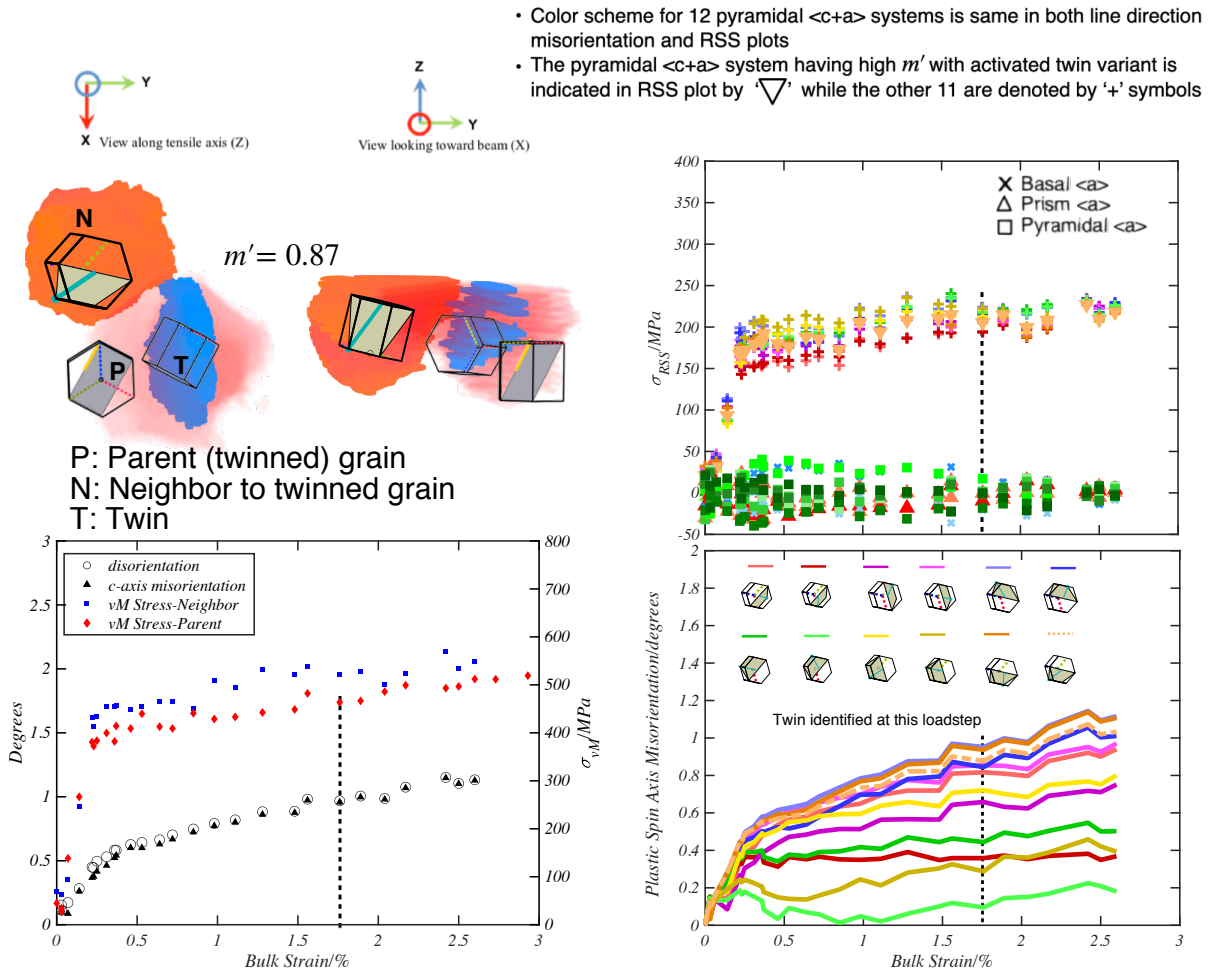


Figure B.3: Parent/Twin/High m' neighbor for twin identified in layer 9 in FF HEDM and validated by NF HEDM.

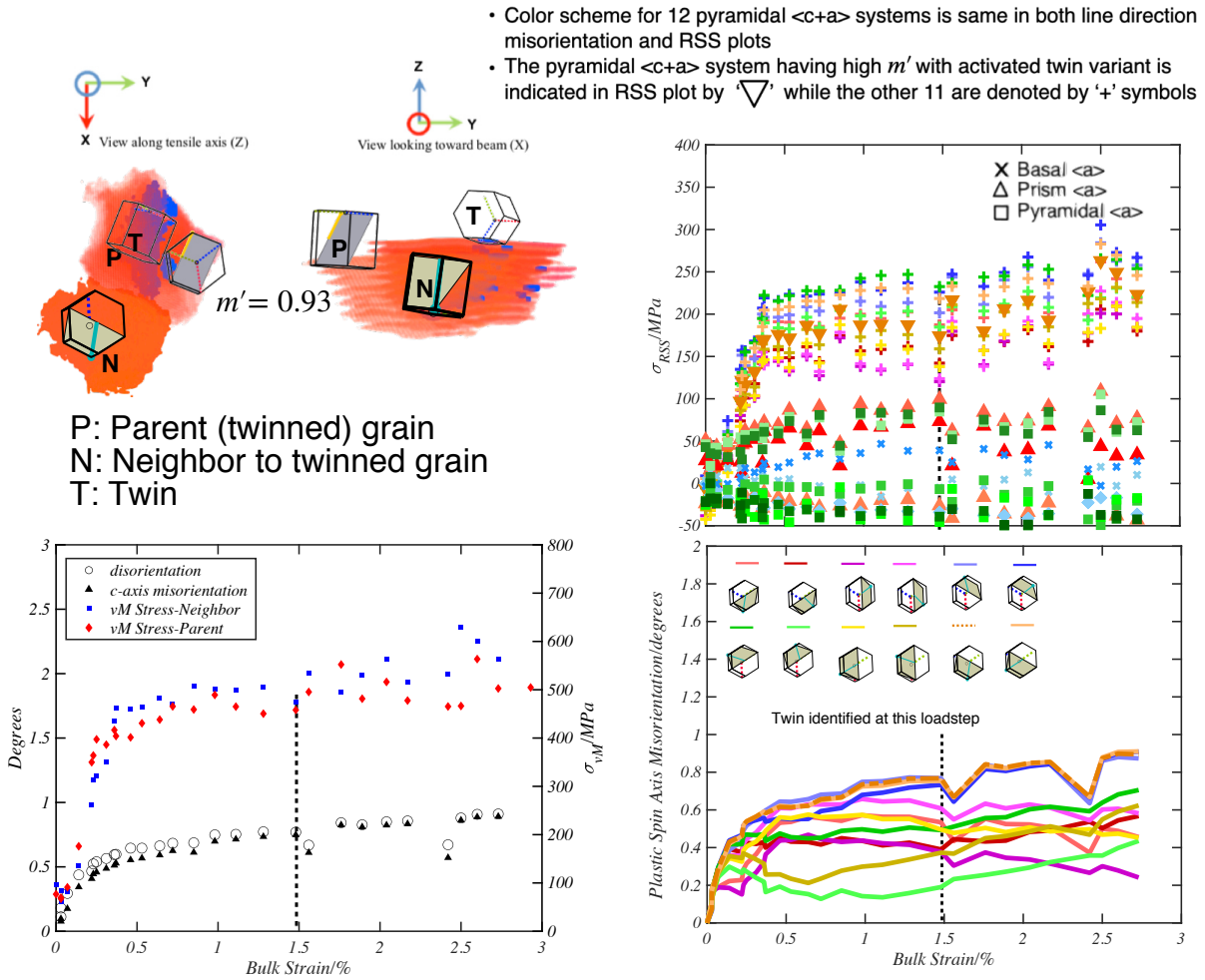


Figure B.4: Parent/Twin/High m' neighbor for twin identified in layer 7 in FF HEDM and validated by NF HEDM.

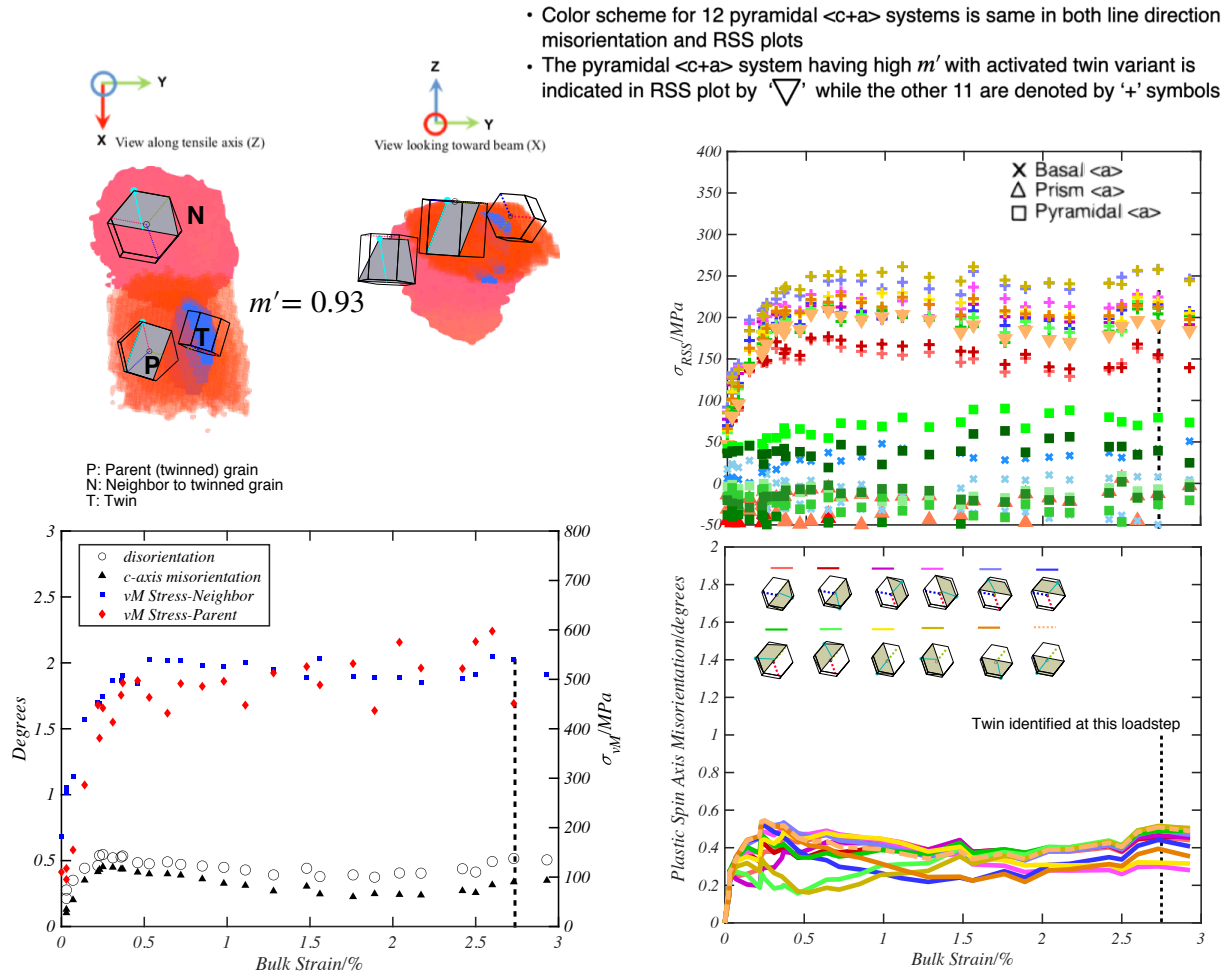


Figure B.5: Parent/Twin/High m' neighbor for twin identified in layer 7 in FF HEDM and validated by NF HEDM.

APPENDIX C

STEREOGRAPHS OF EVOLUTION OF LATTICE PLASTIC SPIN AXIS AS A FUNCTION OF BULK STRAIN

Here the evolution of the lattice plastic spin axis is shown as a function of bulk strain for a twinned grain and its neighbor. For each load step, the arc comprising of plastic spin axes resulting from linear combinations of the two slip systems with the highest resolved shear stress is also shown. For details on the notations and symbols, reader is referred to 6.2.

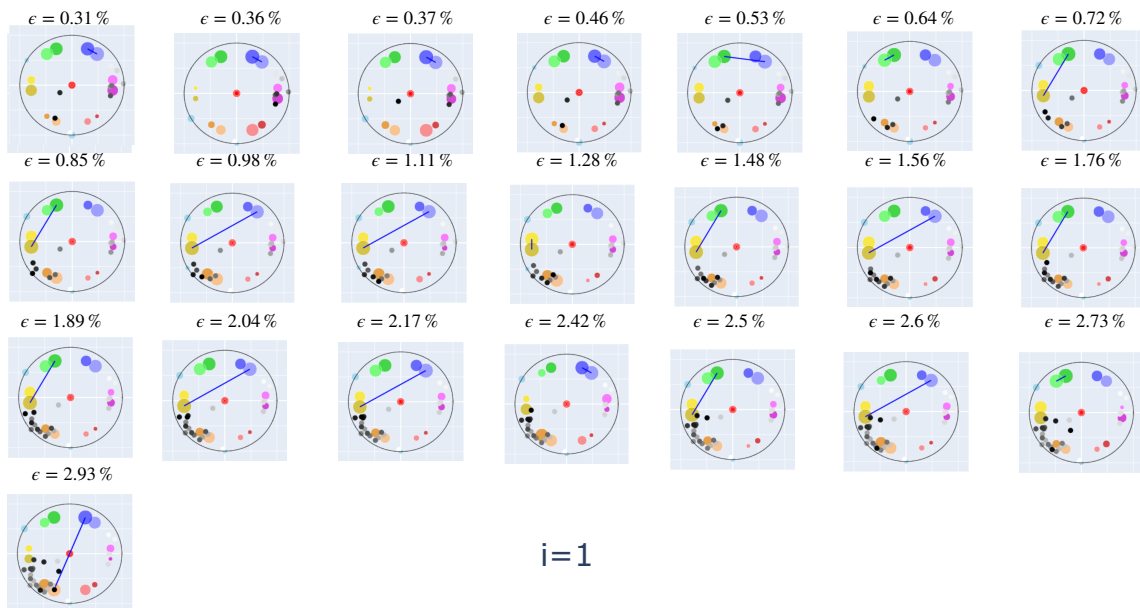


Figure C.1: Stereographic projection of the evolution of the lattice plastic spin axis is shown for different values of bulk strain for a twinned grain.

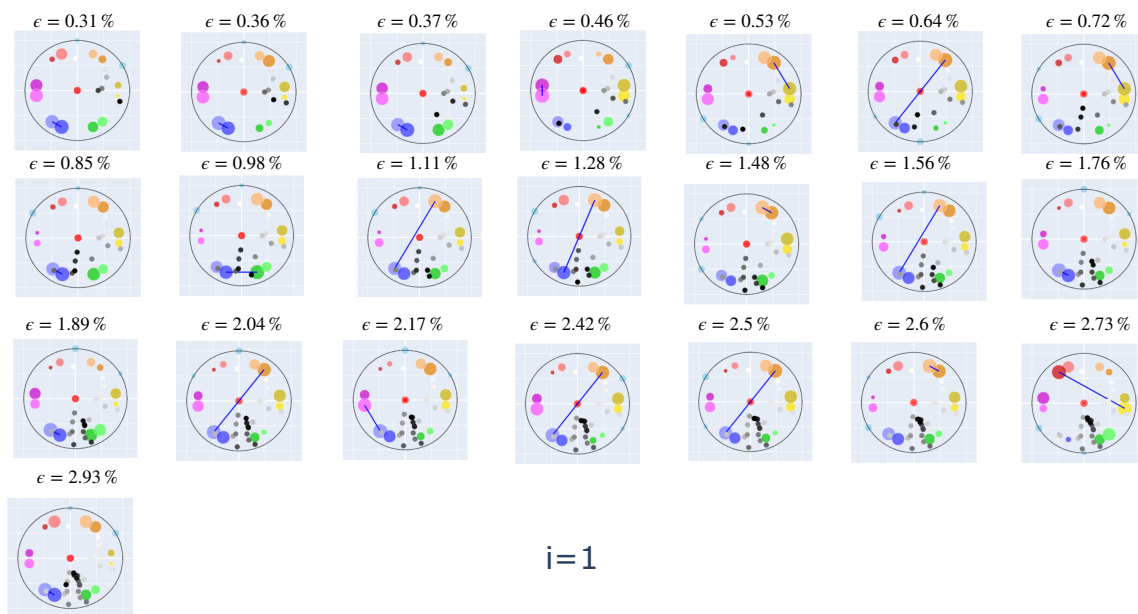


Figure C.2: Stereographic projection of the evolution of the lattice plastic spin axis is shown for different values of bulk strain for the neighbor with a high m' relationship with respect to the active twin variant in the grain shown in figure C.1

APPENDIX D

HYDROSTATIC STRAIN TENSOR MEASUREMENT USING MONOCHROMATIC SETTING OF DAXM

D.0.1 Hydrostatic strain

Since the magnitude of the reciprocal lattice vectors cannot be uniquely determined using the polychromatic mode in DAXM, only the deviatoric component of the strain tensor can be determined, since it is directly associated with the lattice curvature. By setting the beam to monochromatic mode, an incident beam of known energy can be used to obtain the magnitude of the reciprocal lattice vector for a given set of planes that can be indexed. If the deviatoric strain tensor is known then the local hydrostatic component can be calculated as shown below.

The decomposition of the full strain tensor into its deviatoric and hydrostatic components can be written as follows.

$$\epsilon_{Full} = \begin{pmatrix} \epsilon_{11} & \epsilon_{12} & \epsilon_{13} \\ \epsilon_{21} & \epsilon_{22} & \epsilon_{23} \\ \epsilon_{31} & \epsilon_{32} & \epsilon_{33} \end{pmatrix} + \begin{pmatrix} \epsilon_{hydro} & 0 & 0 \\ 0 & \epsilon_{hydro} & 0 \\ 0 & 0 & \epsilon_{hydro} \end{pmatrix} \quad (D.1)$$

where ϵ_{hydro} is the hydrostatic component of the strain tensor. It is significant to mention here that the hydrostatic strain is considered to be a scalar quantity in the above formulation. In general, the hydrostatic strain can vary in the three orthogonal directions. A second important consideration in this formulation is that the magnitude of the reciprocal lattice vector is determined based on a single Laue peak at each strain state.

The full lattice distortion can be expressed as a function of ϵ_{hydro} as follows.

$$D(\epsilon_{hydro}) = I + \epsilon_{Full} = \begin{pmatrix} 1 + \epsilon_{11} + \epsilon_{hydro} & \epsilon_{12} & \epsilon_{13} \\ \epsilon_{21} & 1 + \epsilon_{22} + \epsilon_{hydro} & \epsilon_{23} \\ \epsilon_{31} & \epsilon_{32} & 1 + \epsilon_{33} + \epsilon_{hydro} \end{pmatrix} \quad (D.2)$$

The lattice distortion tensor D_{hydro} can now be used to evaluate the real space lattice vector in strained condition using the following relation.

$$\overrightarrow{R_{Strained}} = D(\epsilon_{hydro}) \cdot \overrightarrow{R_0} \quad (D.3)$$

Equivalently, equation D.3 can be written in terms of the reciprocal lattice vectors.

$$\overrightarrow{Q_{Strained}(h, k, l)} = D(\epsilon_{hydro})^{-1} \cdot \overrightarrow{Q_0(h, k, l)} \quad (D.4)$$

For a set of reciprocal lattice vectors a^* , b^* and c^* the magnitude of the Q vector is given as follows.

$$\|Q\| = \left\| h \cdot \overrightarrow{a^*} + k \cdot \overrightarrow{b^*} + l \cdot \overrightarrow{c^*} \right\| \quad (D.5)$$

The EW scan measures the magnitude of the Q vector. Therefore from equation D.5 , the relationship between the measured Q vector and lattice distortion tensor can be written as:

$$Q_{measured} = \|Q_{Strained}(h, k, l)\| = \|D(\epsilon_{hydro})^{-1} \cdot Q_0(h, k, l)\| \quad (D.6)$$

Rearranging the terms in equation D.6, the fitness function is obtained as follows.

$$\|Q_{measured} - \|D(\epsilon_{hydro})^{-1} \cdot Q_0(h, k, l)\|\| = 0 \quad (D.7)$$

Equation D.7 is a function of a single scalar ϵ_{hydro} . In order to solve the optimization problem a continuous interval which contains a solution satisfying equation D.7 is considered. In this case the interval $[-0.02, 0.02]$ is considered to contain a solution that satisfies the fitness function, i.e. the hydrostatic stress lies within this closed interval. The estimation of the hydrostatic strain can be done using an implementation of Brent optimization algorithm available under SciPy.

D.0.2 Energy wire scan using monochromatic beam diffraction

In order to obtain the complete local strain tensor description with the hydrostatic component, it is necessary to determine the magnitude of the reciprocal lattice vector for a given set of crys-

tallographic planes. This can be accomplished by making the incident x-ray beam monochromatic for a range of known energies (resulting in a series of energy wire (EW) scans). This enables the calculation of the hydrostatic strain component associated with lattice dilatation.

In this work, EW scans were done at the approximate surface centers of the hard and soft oriented grains. For both grains, scans were done prior to bending, and at the same location following each subsequent bend increments. The scan for the final bend increment in the soft grain could not be completed due to beam time constraints. Figure D.1 shows the variation of the magnitude of the reciprocal lattice vector with depth for the hard and soft grains at different bending increments.

As expected, peak broadening is observed for both grains with increasing bulk strain. In the unstrained state, the peak intensity for the softer grain is an order of magnitude higher than for the hard oriented grain, due to reflections from different crystallographic planes. With increasing bulk strain the peak intensity decreases for the soft grain, indicating an increasing amount of defects such as dislocations. For the hard grain, the peak intensities for bend increments 3 and 4 are more similar to each other, indicating that there is some change in lattice orientation and defect content at the final strain state but less than in the soft grain. For the first bending increment, a change in energy is noted from the unstrained state for both the soft and hard oriented grains. In the soft orientation, the intensity peak shift to the right indicates an increase in the magnitude of the reciprocal lattice vector ($|Q|$), or compression in real space. The peak intensity for the soft grain moves to the right after strain is applied. Thereafter, little change in $|Q|$ is apparent for the bend increments 2 and 3. On the other hand, the hard oriented grain shows a peak shift to the left, indicating a tensile change in real space. There is a sequential shift of the intensity peak through the first, second and third bending increments. For the final bending increment there is a noticeable shift to the right, resulting in decrease of $|Q|$. These changes reflect effects of elastic anisotropy during loading and changes in grain shape with plastic strain.

In the current study, the EW scans are taken from the center of a coarse grain in a single phase material. Furthermore the specimen was subjected to a relatively low strain, whereby the lattice dilatation would be very small. Therefore, within a single grain, the assumption of a scalar value of

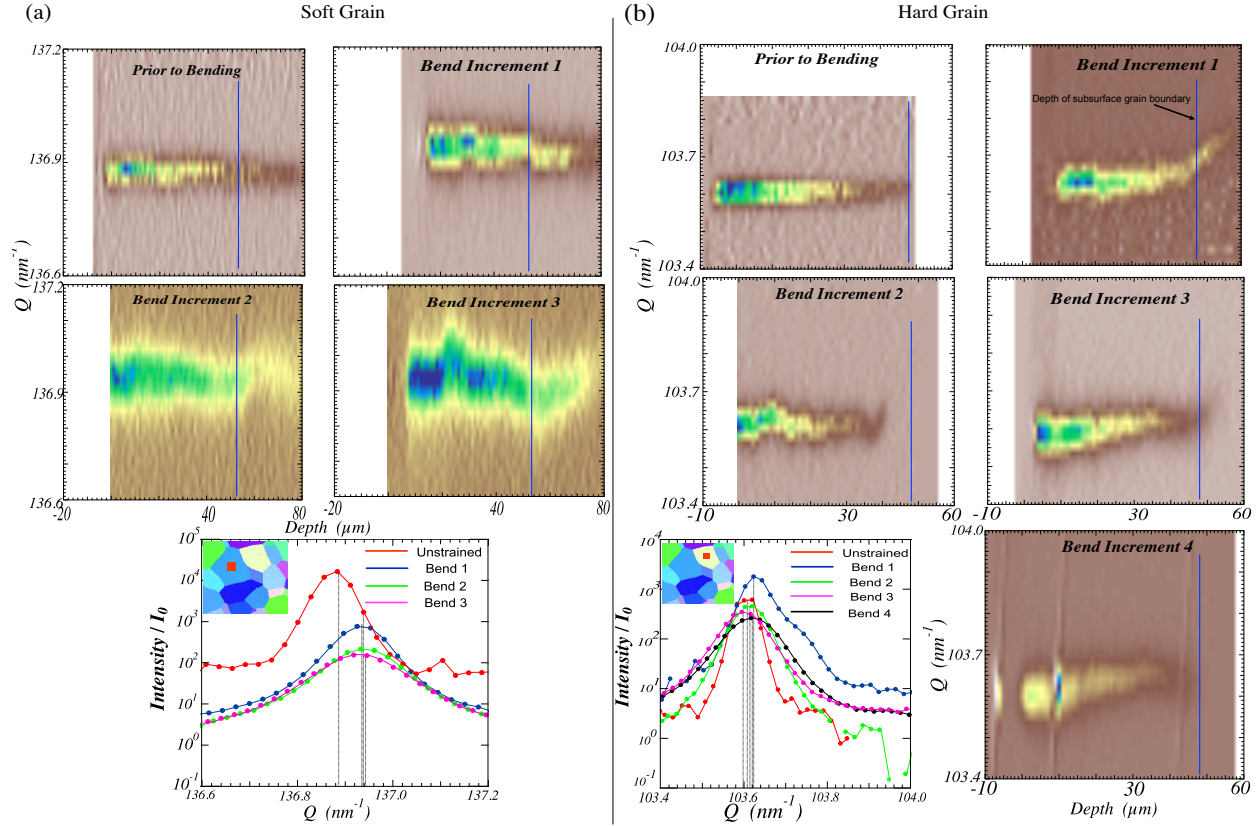


Figure D.1: Laue patterns obtained from energy wire scans of (a) soft grain (unstrained condition through bend increment 3), (b) hard grain (unstrained condition through bend increment 4). The variation of reciprocal lattice vector magnitude with depth is shown for each bend increment. The plots on the third row of (a) and (b) show the intensity profiles as a function of the reciprocal lattice vector magnitude. The approximate locations in the grain interior used for the energy wire scans in the hard and soft grains are shown (marked in red) as insets in the intensity plots. The depths at which the subsurface grain boundary exists is shown by blue vertical lines in the Q v/s depth plots for both the hard and soft orientations.

hydrostatic strain is valid. Moreover, These results indicated that within a single grain, the spatially resolved lattice dilatation can also be considered to be uniform.

As the interrogated volume approaches the grain boundaries the assumption of a scalar value of hydrostatic strain is not valid, because of complex interactions with neighboring grains. This is evident in the change in Q as one approaches the boundary in the hard grain at bend increment 1. In bend increments 2-4, the peak intensity drops and becomes unmeasurable. Ideally, spatially resolved EW scans have to be conducted to obtain the reciprocal lattice vector magnitude corresponding to each voxel, which is a time-consuming exercise in an actual experiment. In the present work, EW

scans were conducted near the center of two grains. The important assumption made for subsequent calculation of the hydrostatic strain is the absence of strong orientation and stress gradients in these locations.

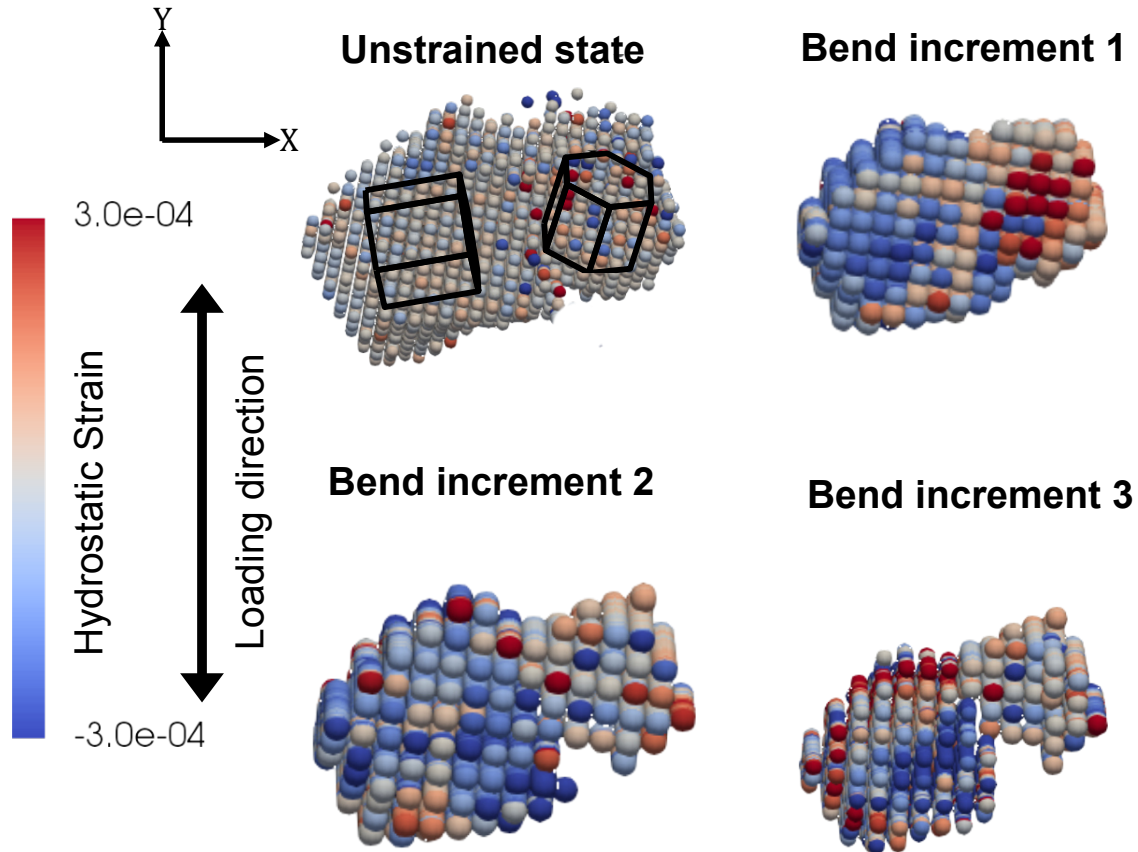


Figure D.2: Local hydrostatic strain maps for the soft (left) and hard (right) grains, shown for bend increments 0 (unstrained state) to 3. The prisms indicating the orientations of the hard and soft grains with respect to the loading direction are also shown.

Figure D.2 shows the spatial distribution of hydrostatic strain in the hard and soft oriented grains; corresponding to the unstrained state and first three bending increments. A larger spread of local hydrostatic strain is observed for the soft grain compared to the hard grain. The character of the hydrostatic strain for the softer orientation changes from near zero to compressive with increasing bulk strain. In the case of the harder orientation, the character of the dilatation changes from near zero to tensile at the first bend increment; and changes to compressive with increasing

bulk strain. In both cases the magnitudes of the hydrostatic strain are found to be small; therefore lattice dilatation is not significant.

APPENDIX E

PRINCIPAL STRESS AND PRINCIPAL DIRECTION MAPS FOR REGIONS 3,4 AND 5

For the three grains associated with the triple junction in region 3 (figure E.1), a change in sense of the first principal stress component from compressive to tensile (darker red) from the center towards some of the grain boundary neighborhood voxels is observed in the lower two grains, where the direction also changes as one gets closer to the boundary. It is also pertinent to note that that average stress state in the lower left grain is nearly biaxial, since the magnitude of the third principal component is relatively low. In the upper (interior) grain, there is a band that traverses from left to right where there is a strong (more vertical) tensile component that is in a different direction than the average, and there are more compressive regions in the upper left and lower right regions close to grain boundaries.

Considering the grain boundary in region 4 (figure E.3), the first principal components for both the top and bottom grain are characterized by a near-balance in tensile and compressive states, where the compressive component is stronger in the upper (interior) grain and stronger tensile in the lower (surface) grain. There is a band emanating from the grain boundary toward the upper right that shows a different direction of the tensile component. For the bottom grain the tensile component becomes stronger close to the grain boundary, along with small change in direction.

In the case of the triple junction in region 5 (figure E.2) the stress state in the left two grains is quite uniform, and a near-balance of tensile and compression in the first two principal stresses. There is a band of strong tensile stress near but away from the lower right grain boundary in the lower left grain, and the stress along the boundary differs from the grain interior. The upper right (interior) grain has isolated voxels with significantly different stress states, and there is a subtle waver of different stress direction in the middle of the grain. The second component of the principal stress for the top right grain changes significantly in direction and sense (compressive to tensile) near the boundary with the top left grain. It can be seen that the grain averaged principal stress state in the three grains is almost biaxial, as one of the three components has a much lower magnitude

compared to the other two.

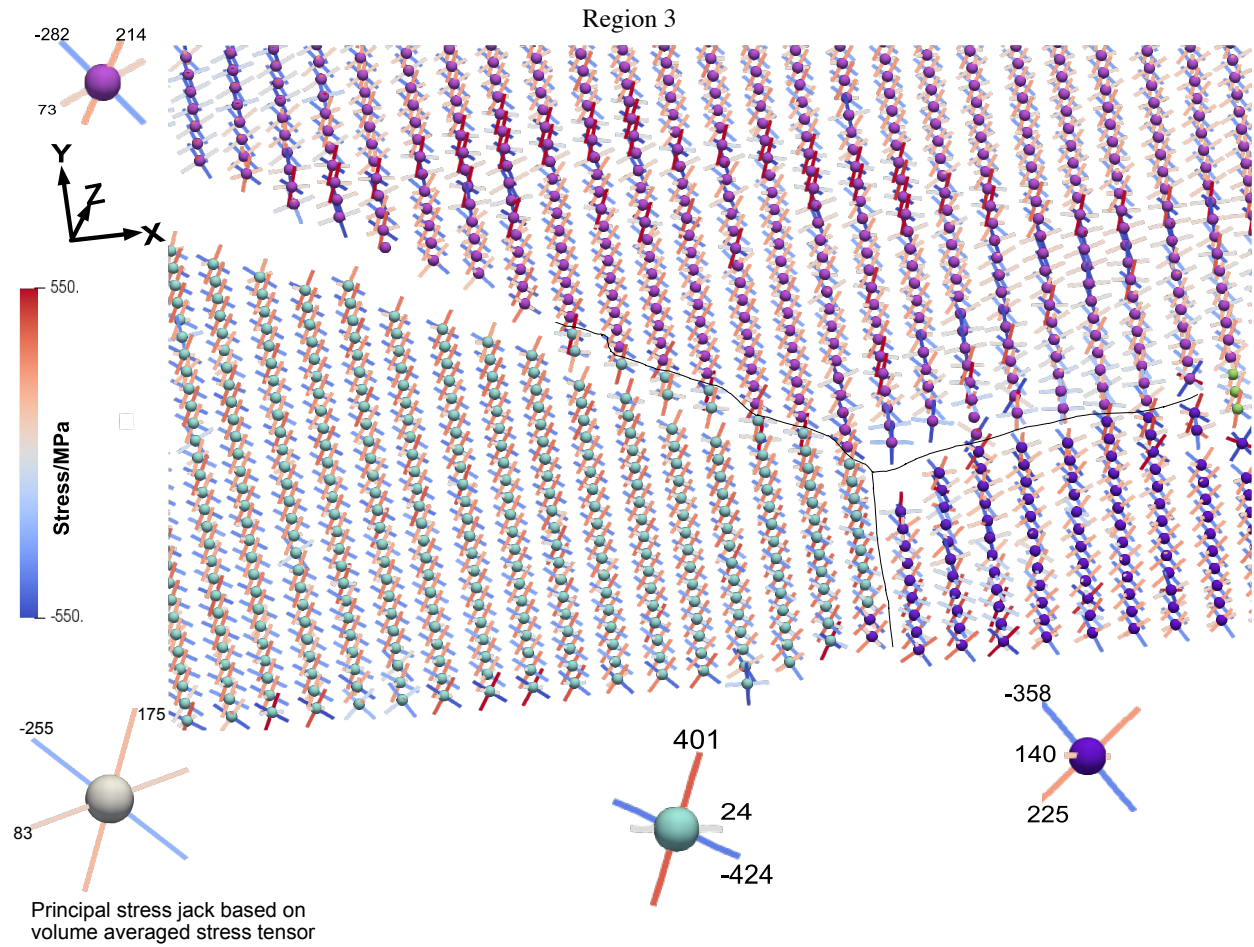


Figure E.1: Principal Stress direction map for the triple junction in region 3. The grain boundaries are delineated by black lines. Principal stress jacks corresponding to average stress tensor for each individual grain, along with their magnitudes and sense are also shown for comparison.

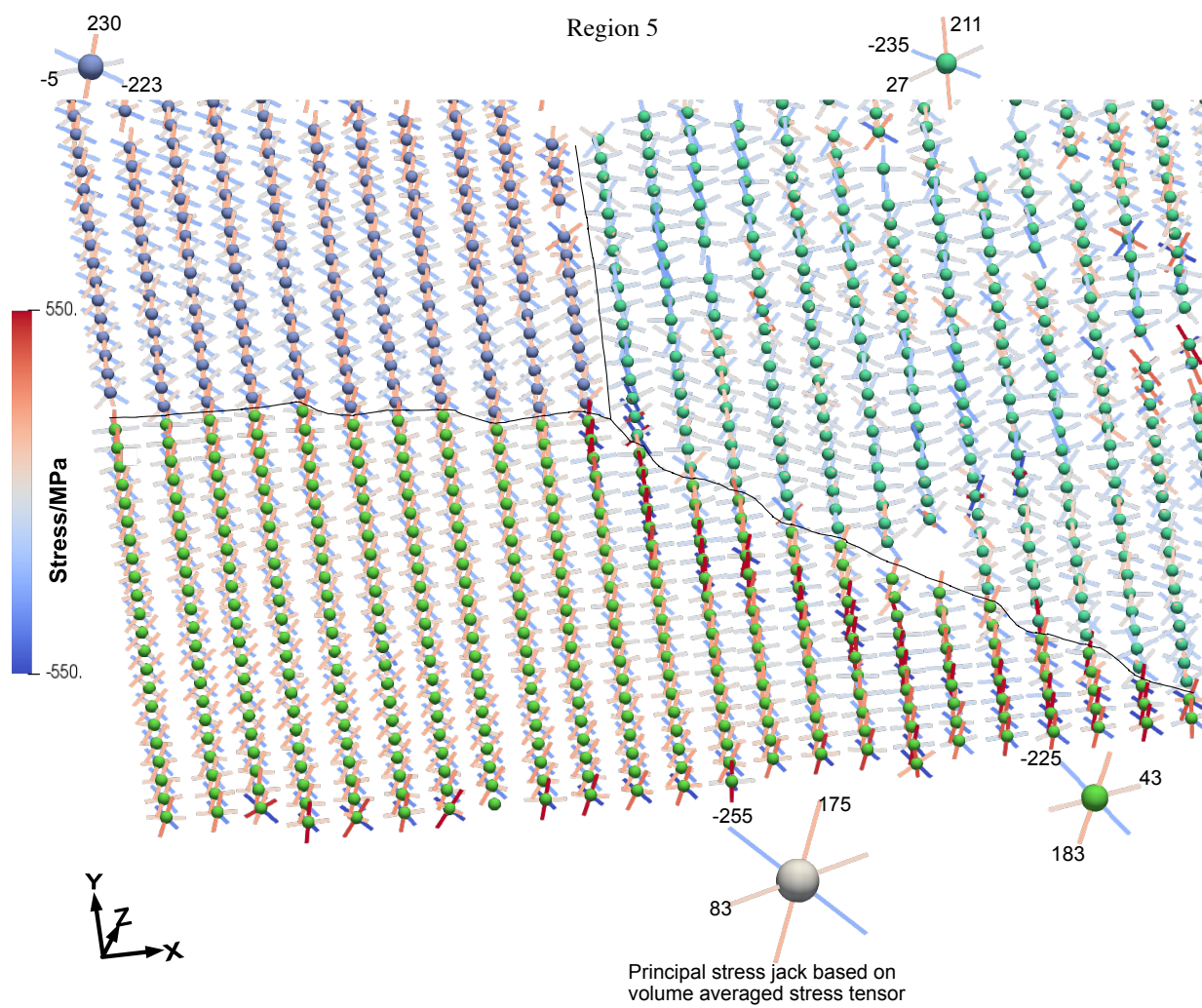


Figure E.2: Bend increment 2: Principal Stress distribution for the triple junction in region 5.

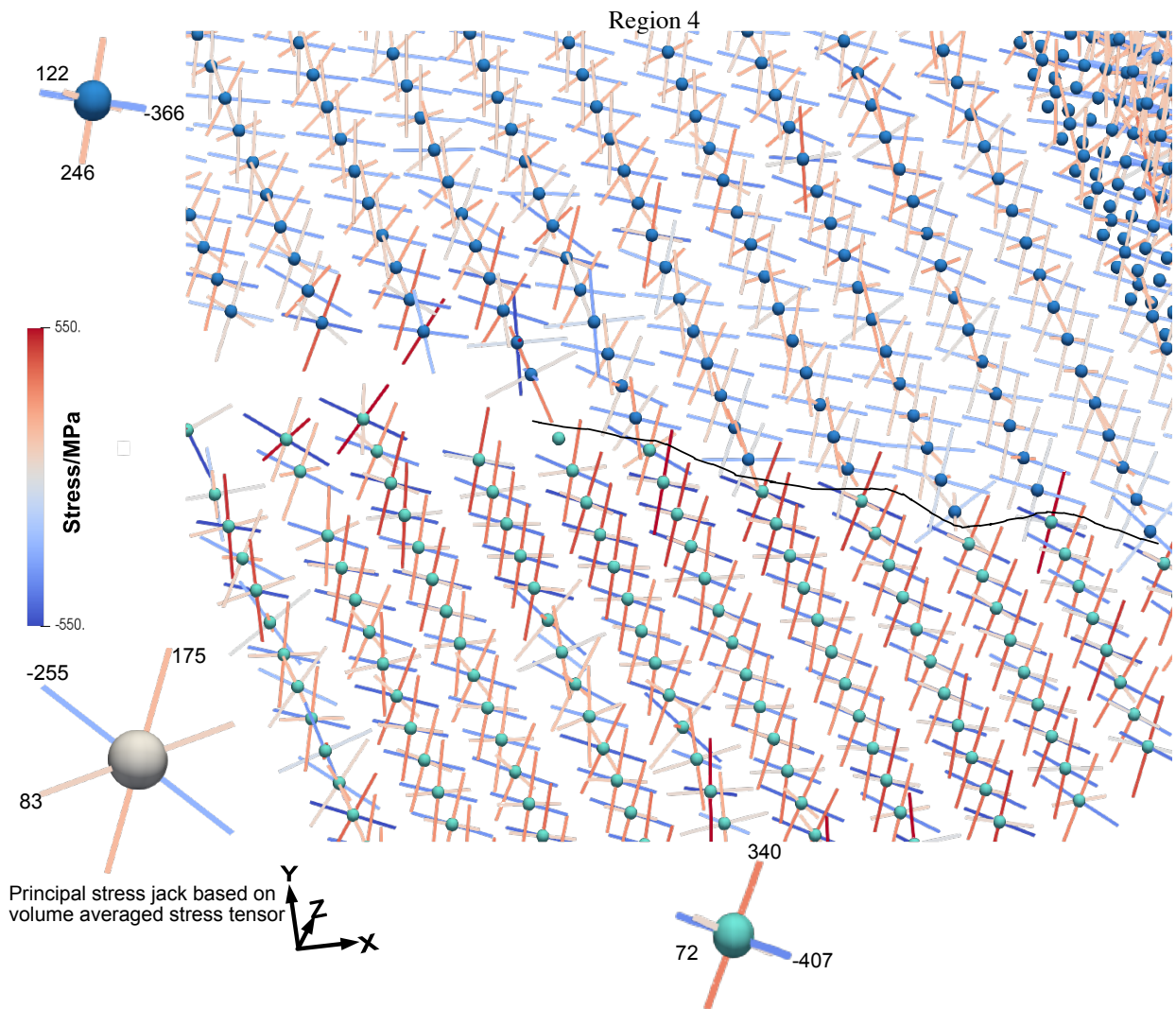


Figure E.3: Bend increment 2: Principal Stress distribution for the triple junction in region 4.

APPENDIX F

CORRELATION OF GND CONTENT WITH RESIDUAL BURGERS VECTOR AND SLIP TRANSFER PARAMETER

F.0.1 Analysis of intragranular high local GND density accumulation area

It can be expected that instances where the likelihood of slip transfer is high (m' values closer to 1), would correspond to lower magnitudes of residual Burgers vector. Correspondingly, a lower value of m' should correspond to higher magnitudes of $b_{residual}$. Figure F.2 shows the plots of m' as a function of $|b_{residual}|$ for the LAGB and HAGB of region 1. Each symbol in these plots corresponds to one pair of slip system interactions for four adjacent voxel pairs. Each voxel in this interacting pair has a unique crystallographic orientation and deviatoric stress tensor associated with it. The face color and shape of each symbol indicate the transmitting slip system chosen (in this case arbitrarily as described in section 7.4.3 and listed in table 7.2). The edge color of each symbol denotes the slip system in the receiving voxel. As an example, if a transmitted basal slip system interacts with a prism slip system in the receiving voxel, the symbol is a triangle with blue face color and red edge color. In addition, the size of each symbol¹ is scaled with the sum of the local Schmid factors of the interacting slip systems for the voxel pair considered.

F.0.1.1 Analysis of m' and $|b_{residual}|$

Figure F.2 shows the results of four voxel pairs along the grain boundaries. For each type of initiating slip system (basal, prism $\langle a \rangle$, pyramidal $\langle a \rangle$ and pyramidal $\langle c + a \rangle$) in each voxel pair, only the instances with the five highest local Schmid factor sums are plotted (20 data points per plot).

From purely geometrical considerations, an inverse relationship should exist between the value of m' and $|b_{residual}|$, which is evident in some of the plots, where slip transfer would be expected for slip system pairs in the upper left corner, and blocked slip at the boundary in the lower right.

¹Symbol Size is proportional to the sum of the local Schmid factors (LSf); size = $500 \times \text{sum}(LSf_{s_\alpha}, LSf_{s_\beta})^3$

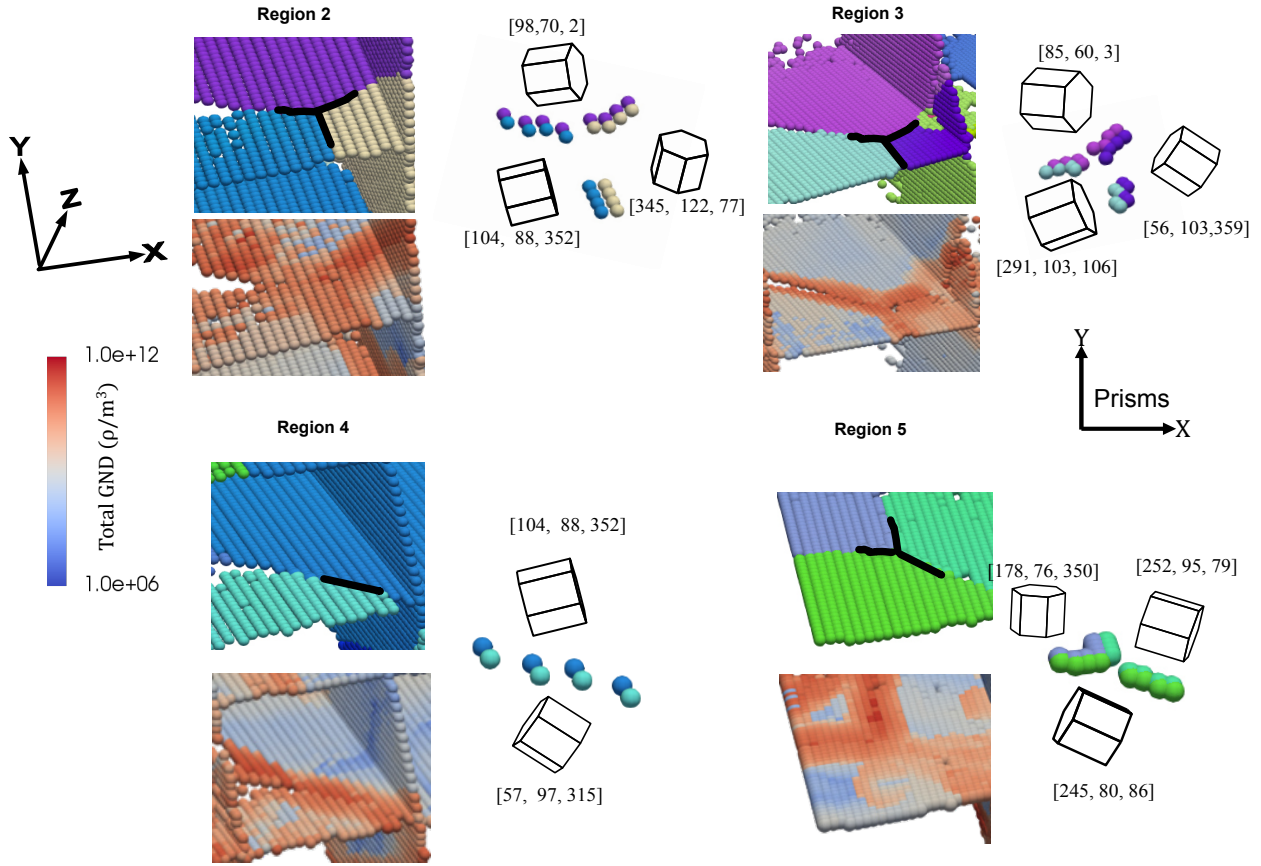


Figure F.1: Orientation and total GND density maps for regions 2, 3, 4 and 5, corresponding to the second bending increment. The voxels on either side of the grain boundary used for slip transfer parameter calculations are shown on the right of each orientation map. The Bunge Euler angles denoting the average grain orientations are also shown. Prisms denoting orientations are drawn from the perspective of the sample normal, with Y pointing up and X pointing to the right (coordinate system shown on the right side of image). The sample coordinate system is shown on the left hand side of image. The tensile direction is parallel to the Y direction.

However, there is no discernable trend in these plots, so the next step is to take into account the role of slip system specific GND density that reflects accumulation of a high density of GNDs or transmission of dislocations through the boundary, resulting in a low density.

F.0.1.2 Analysis of m' and $|b_{residual}|$ with GND density

The local slip system specific GND densities in each voxel pair can be considered by choosing a scaling parameter for m' based on either the maximum or the minimum values of GND density pertinent to the slip system pair. Therefore, the scaled slip transfer parameter (m'') may be expressed

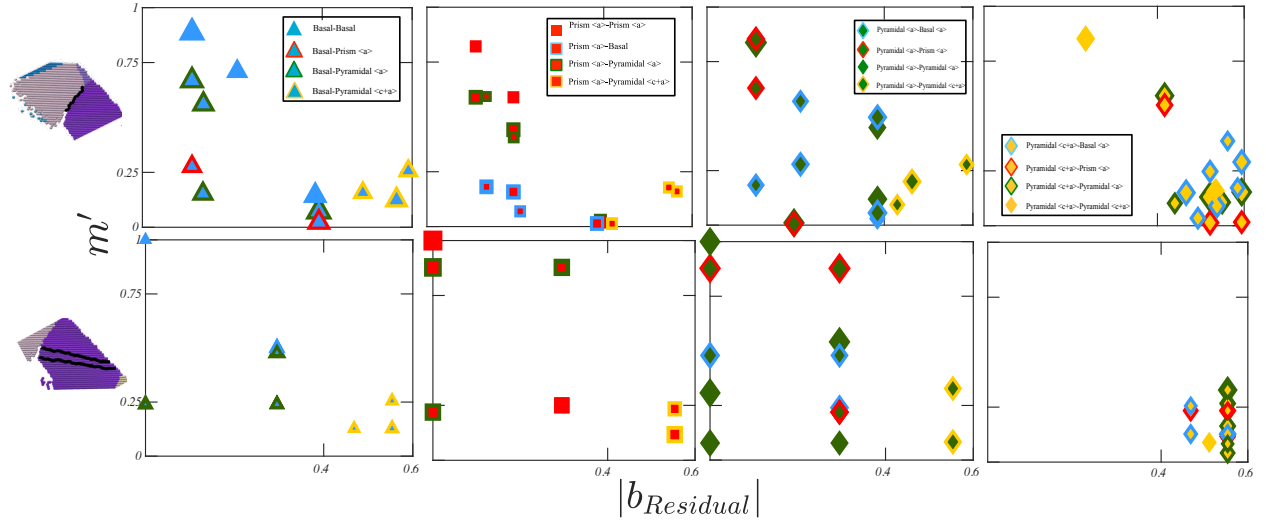


Figure F.2: The Luster-Morris parameter plotted as a function of magnitude of residual Burgers vector for the LAGB (top row) and HAGB (bottom row) in region 1. Legends in the plots show the color/shape convention used to denote the interacting slip system in a voxel pair. This convention is followed for the subsequent plots. The symbol size for each datum point is scaled with the sum of the local Schmid factors for the interacting slip systems.

by one of the following equations.

$$m'' = \frac{m'_{\alpha\beta}}{\max(\rho^{s_\alpha}, \rho^{s_\beta})} \quad \text{or} \quad m'' = \frac{m'_{\alpha\beta}}{\min(\rho^{s_\alpha}, \rho^{s_\beta})} \quad (\text{F.1})$$

where $m'_{\alpha\beta}$ is the slip transfer parameter, considering slip systems s_α and s_β for voxels α and β respectively.

Figure F.3 shows the plots of the scaled values of m' and $|b_{Residual}|$ for the LAGB in region 1. Plots using $\max(\rho_\alpha, \rho_\beta)$ and $\min(\rho_\alpha, \rho_\beta)$ as scaling parameters are shown on the left and right columns respectively in figure F.3. Comparing with the LAGB row of plots in figure F.2, use of these scaled parameters exaggerates the inverse relationship between the residual Burgers vector magnitude and slip transfer parameter, such that a slope to the points is evident. Using the minimum dislocation density causes points to be more concentrated. As discussed in section 7.4.3, the transmitting slip systems are arbitrarily chosen to emanate from voxels on one side of the grain boundary.

F.0.1.3 Analysis with GND density and choice of transmitting slip system by LSf

Another approach is to specifically choose the transmitting slip system as the one with the higher local Schmid factor between s_α and s_β based upon the assumption that the more favored slip system is the initiating system. These data are then sorted by initiator slip system type (basal, prism $\langle a \rangle$, pyramidal $\langle a \rangle$ and pyramidal $\langle c + a \rangle$). The same data as in figure F.3, are plotted using this modified approach in figure F.4. In this case, the number of symbols plotted in each figure will not necessarily be equal, as one grain may have more highly favored slip systems than the other. This is evident in the fewer number of initiating systems on the basal plot, and the larger number of initiating systems in the prism plot and pyramidal $\langle a \rangle$ plots. The number of datum points appearing in each plot are indicated in figure F.4.

F.0.1.4 Analysis with GND density and choice of transmitting slip system by $\min(\rho_{s_\alpha}, \rho_{s_\beta})$

The third strategy for choosing the initiating slip system is based on the minimum value of slip system specific GND density between the interacting systems. Figure F.5 shows the m'' and scaled $|b_{Residual}|$ plots generated for the LAGB in region 1 using this approach. For the LAGB using $\min(\rho_{s_\alpha}, \rho_{s_\beta})$ as the transmitter criterion results in higher number of data points plotted for basal and pyramidal $\langle a \rangle$ slip compared with $\max(LSf)$ (figure F.4).

F.0.1.5 Analysis of slip systems filtered by $m' \geq 0.8$

The data plotted for the LAGB in region 1 (figures F.3, F.4 and F.5) are filtered based on a slip transmissibility criterion (only points with $m' \geq 0.8$ are considered) and re-plotted in figures F.6, F.7 and F.8 respectively.

For the LAGB in region 1, no basal slip system is found to have a favorable geometrical alignment ($m' \geq 0.8$) for slip transfer. Similarly, there was only one plausible instance of pyramidal $\langle c + a \rangle$ with a high likelihood for transfer. The number of basal and pyramidal $\langle c + a \rangle$ systems likely to transmit did not change with the criteria used for choice of the initiator (figures F.6, F.7 and F.8).

Clearly there is a significant variation in the number of high m' prism $\langle a \rangle$ and pyramidal $\langle a \rangle$ across the three choice criteria. In case of the arbitrary choice criterion, there are nine instances of favorable geometric alignment for transfer of prism $\langle a \rangle$ slip across the boundary ($m' \geq 0.8$), out of which four instances have near perfect geometrical alignment ($m' \sim 1.0$). When the maximum LSf is considered as the criterion for choice of transmitting slip system, the number of plausible instances is found to be eight (with 2 having $m' \sim 1.0$). The number of plausible instances for prism $\langle a \rangle$ slip increases to eleven (with four near perfect cases), when $\min(\rho_\alpha, \rho_\beta)$ is considered as the choice criterion. All of the eight data points correspond to low values of GND density. There are also seven possible instances where a high likelihood of pyramidal $\langle a \rangle$ slip transfer can take place. When pyramidal $\langle a \rangle$ slip is considered the number of plausible slip transfer instances using the three criteria are six (one near perfect), seven (two near perfect) and four (2 near perfect) respectively.

It is worth noting that no favorable conditions for transfer of basal slip were determined using both the maximum LSf and minimum GND density as choice criteria for the transmitting system. When prism $\langle a \rangle$ slip is considered using maximum LSf and minimum GND density criteria yield eight and eleven favorable instances respectively. Out of these six instances are identical between the two choice criteria used. In the case of pyramidal $\langle a \rangle$ slip, the number of favorable instances found using the two criteria are seven and four respectively, out of which three are identical. It is pertinent to mention here that across the three criteria examined, the same slip system pair for pyramidal $\langle c + a \rangle$ is found to be the only plausible instance of slip transfer.

Because this neighborhood has very low misorientations, geometrically every slip system should be highly favored for slip transfer, but the criteria of dislocation density and local stress state provides additional constraints on what slip transfer processes are more likely to be active. The lack of many slip systems participating in plausible slip transfer suggests that there is much dislocation entanglement in this neighborhood.

Some of the slip system pair interactions for basal, prism $\langle a \rangle$, pyramidal $\langle a \rangle$ and pyramidal $\langle c + a \rangle$ initiating systems are illustrated in figure F.9. Here the size of each prism pair illustrating the

crystallographic orientations are scaled in proportion to the sum of the LSf of the interacting slip systems. Although near-perfect geometrical alignment for basal slip transfer exists, the variation in the local stress state makes the activation of basal slip less likely. From the standpoint of near ideal geometrical alignment and local stress state, there is high likelihood for transfer of prism $\langle a \rangle$ and pyramidal $\langle a \rangle$ slip. The only favorable instance of pyramidal $\langle c + a \rangle$ slip transfer is also shown (bottom right of figure F.9).

F.0.2 Analysis of slip transfer in the HAGB

Plots of the scaled slip transfer parameter as a function of scaled magnitude of $b_{Residual}$ for HAGB in region 1 using the three different criteria for transmitting slip choice are shown in figures F.10, F.11 and F.12 respectively. The data is plotted in an identical manner as described for figures F.3, F.4 and F.5 respectively for the LAGB case.

For the HAGB in region 1, five favorable instances of basal slip transfer, in terms of geometrical alignment and local Schmid factor, are found irrespective of the criteria used for choice of transmitting system. If the transmitting slip system is arbitrarily chosen, no favorably aligned candidates for prism $\langle a \rangle$ slip transfer ($m' \geq 0.8$) were found. When the maximum Schmid factor is considered as the criterion for transmitting slip system choice, two plausible instances of prism $\langle a \rangle$ are found. Using the criterion of minimum GND density, only one favorable instance for transfer of prism $\langle a \rangle$ slip is identified. Overall, the likelihood of prism $\langle a \rangle$ slip transferring across the grain boundary is low. Similarly the likelihood for pyramidal $\langle a \rangle$ slip transfer is also low. Three favorable candidates for possible transfer of pyramidal $\langle a \rangle$ slip are noted when the maximum Schmid factor criterion is used to choose the transmitting system.

The five instances where basal slip transfer is favored are identical irrespective of the choice criteria used. Two instances of favorable pyramidal $\langle a \rangle$ slip transfer are identical using both maximum Schmid factor and minimum GND density conditions. The sole favorable instance of pyramidal $\langle c + a \rangle$ slip transfer is also identical using both conditions.

F.0.3 Analysis of slip transfer in triple junction grain boundaries

Figures F.16, F.17 and F.18 show the plots of m'' as a function of scaled $|b_{Residual}|$ for each of the three grain boundaries constituting the triple junction in region 2. For the analysis of this region, $\min(\rho_\alpha, \rho_\beta)$ is used as the basis for determining the transmitting slip system in a pair of voxels.

Figure F.16 shows the plots of m'' plotted as a function of scaled $b_{residual}$ for the grain boundaries that constitute the triple junction in region 2. The first grain boundary (first column of plots in figure F.16) is between a relatively hard oriented grain (beige, inset) and a soft oriented grain (blue, inset). There were no instances that favored transfer of basal slip across the boundary. Only one instance that could favor transfer of prism $\langle a \rangle$ slip was identified ($m' \sim 0.9$). This is consistent with very low likelihood of activation of prism $\langle a \rangle$ slip; especially if slip transfer is deemed to occur from the hard oriented grain to the softer grain. There was one possible instance each, favoring transfer of pyramidal $\langle a \rangle$ and pyramidal $\langle c + a \rangle$ slip respectively. The locations of the datum points corresponding to these favorably aligned instances of slip transfer are circled in figure F.16.

The second grain boundary in region 2 (figure F.17) is between the blue and purple grains shown in the inset. There was only one favorable instance each for transfer of basal and prism $\langle a \rangle$ slip respectively. Four cases with favorable geometrical alignment for transfer of pyramidal $\langle a \rangle$; and one such instance for pyramidal $\langle c + a \rangle$ were found, but the plotted values are lower and to the right than the other two grain boundaries.

The third grain boundary in region 2 (F.18) is formed by the hard grain and softer oriented purple grain. No instances favoring transfer of basal or pyramidal $\langle c + a \rangle$ slip were identified, but there were three scenarios where prism $\langle a \rangle$ slip appears likely. Four pyramidal $\langle a \rangle$ systems with high likelihood of transmitting were also identified.

Plots for the grain boundaries in regions 3, 4 and 5 are included in the appendix G.

In several of the slip system pairs considered, it is observed that in cases where the likelihood of slip transfer is high ($m \geq 0.9$), the magnitude of slip system specific dislocation density is low. Figures F.19, F.20, F.21 and F.22 show m' plotted as a function of the maximum and minimum

values of slip system specific dislocation density, using voxel pair instances from the twelve grain boundaries encompassed by regions 1, 2, 3, 4 and 5. Here the transmitting slip systems (basal,prism $\langle a \rangle$, pyramidal $\langle a \rangle$ and pyramidal $\langle c + a \rangle$ respectively) are chosen using the minimum GND density of the voxel pair.

In figure F.19, m' and GND densities are plotted for cases where basal slip is considered as the transmitting system. In the plot on the left hand side, where m' varies with respect to the maximum GND density, an envelope of data points can be found where m' decreases with increasing values of GND density. Furthermore, interactions with $\langle c + a \rangle$ have much lower m' values than potential slip transfer with the other three slip systems. A similar trend can be seen for the case of prism $\langle a \rangle$ and pyramidal $\langle a \rangle$ initiator slip systems (figures F.20 and F.21 respectively). This trend is less obvious when pyramidal $\langle c + a \rangle$ slip is considered as the initiator in figure F.22, suggesting that pyramidal $\langle c + a \rangle$ slip as the initiation system is much less likely, which may reflect the preferred soft orientations that predominate in this material.

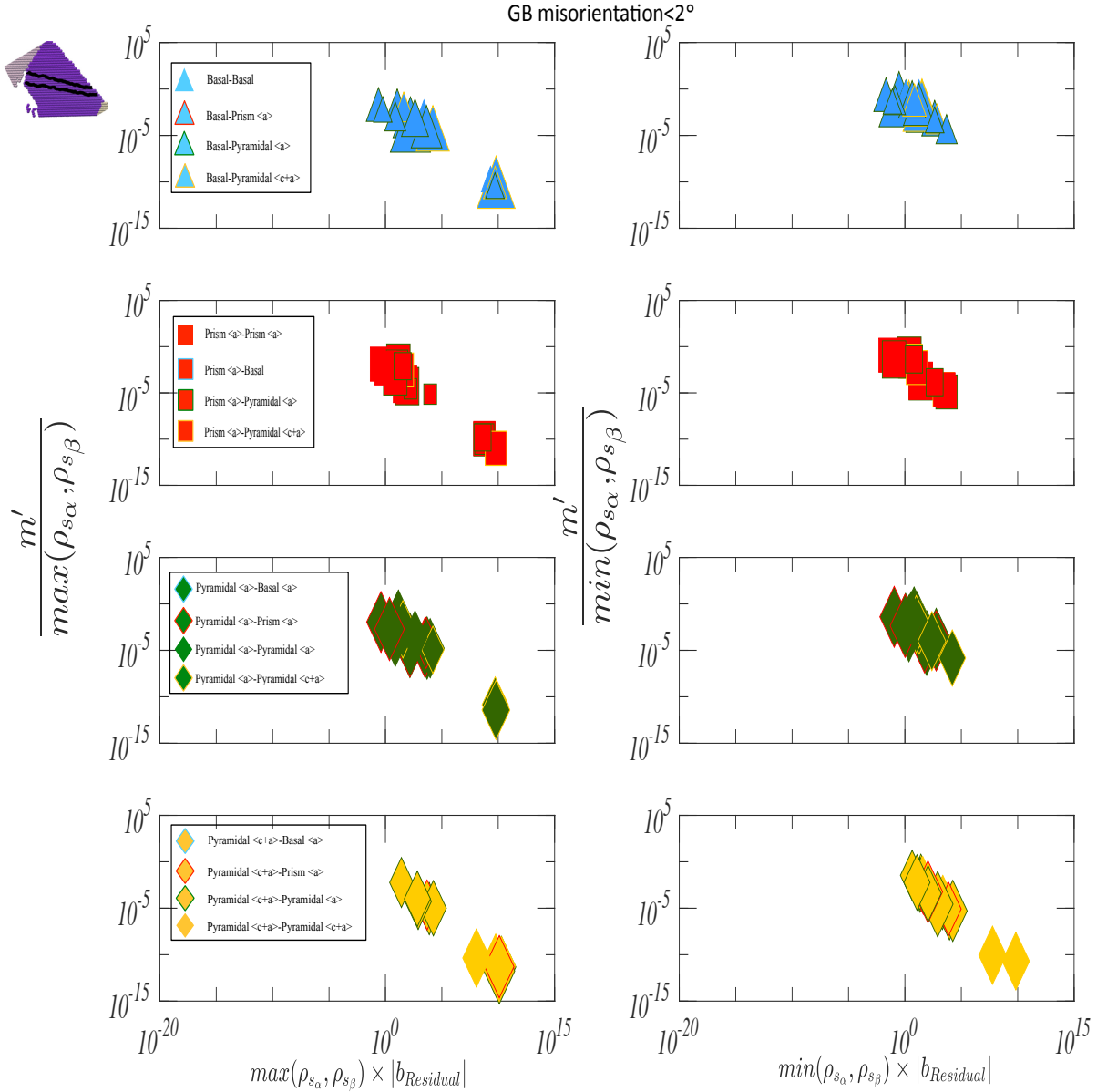


Figure F.3: LAGB in region 1 scaled by GND density: Left column shows $m'' = \frac{m'}{\max(\rho_{s_\alpha}, \rho_{s_\beta})}$ plotted as a function of $\max(\rho_{s_\alpha}, \rho_{s_\beta}) \times |b_{Residual}|$; while $m'' = \frac{m'}{\min(\rho_{s_\alpha}, \rho_{s_\beta})}$ as a function of $\min(\rho_{s_\alpha}, \rho_{s_\beta}) \times |b_{Residual}|$ plots are shown on the right column. Each plot corresponds to one of four transmitting slip systems considered. Four voxel pairs along the grain boundary are considered here. For each transmitting slip system type in each voxel pair, only the five highest local Schmid factor sums are plotted (A total of 20 plots per plot). The choice of the transmitting slip system is arbitrarily made as described in section 7.4.3.

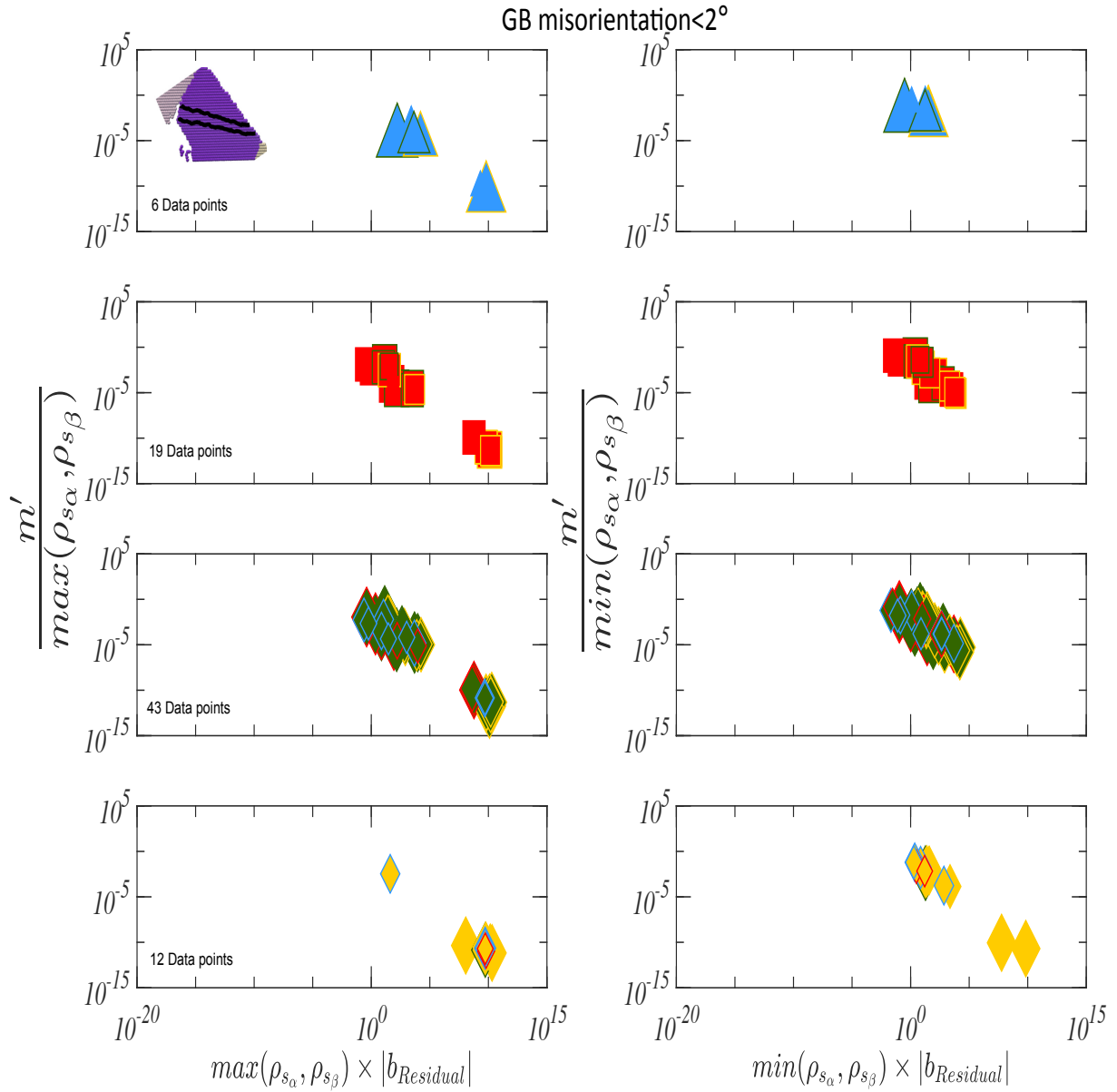


Figure F.4: For four voxel pairs in the LAGB in region 1, each row of plots corresponds to the initiator slip system families with the *higher local Schmid factor* considered as the transmitting system, leading to more datum points in the pyramidal $\langle a \rangle$ slip system plot as initiators than other systems. For each initiating slip system family member in each voxel pair, only the datum points with the five highest local Schmid factor sums are considered. The number of datum points plotted for each initiator slip system type are indicated. The number of datum points per slip system family for the plots scaled by maximum and minimum GND density (left and right columns respectively) are identical.

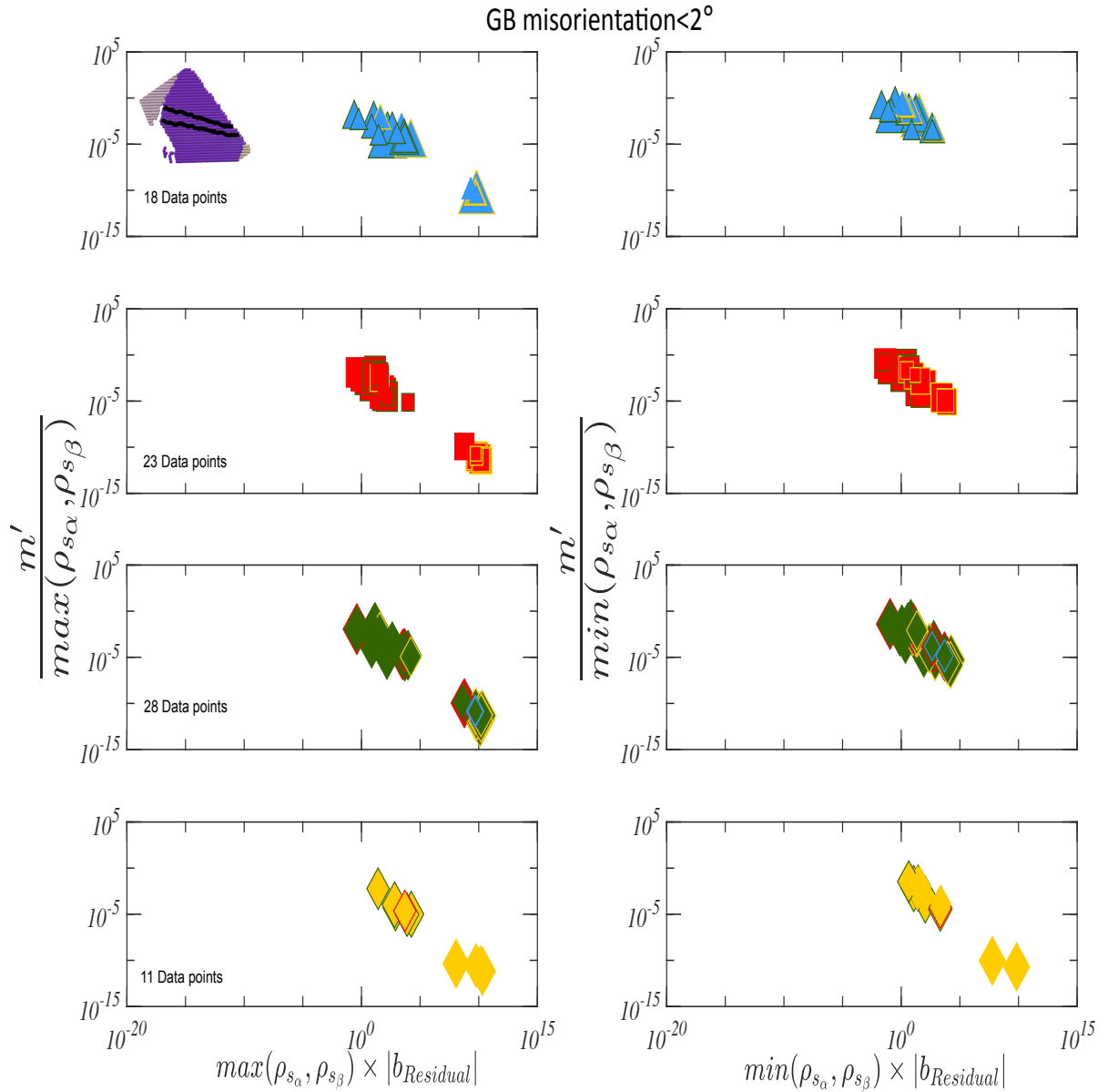


Figure F.5: For four voxel pairs in the LAGB in region 1, each row of plots corresponds to the initiator slip systems with the *lower GND density* is considered as the transmitting system, leading to more datum points in the basal and prism $\langle a \rangle$ slip system plot as initiators than when the Schmid factor is considered in figure F.4. For each voxel pair, only the data points with the five highest local Schmid factor sums are considered. The number of data points plotted for each initiator slip system type are indicated.

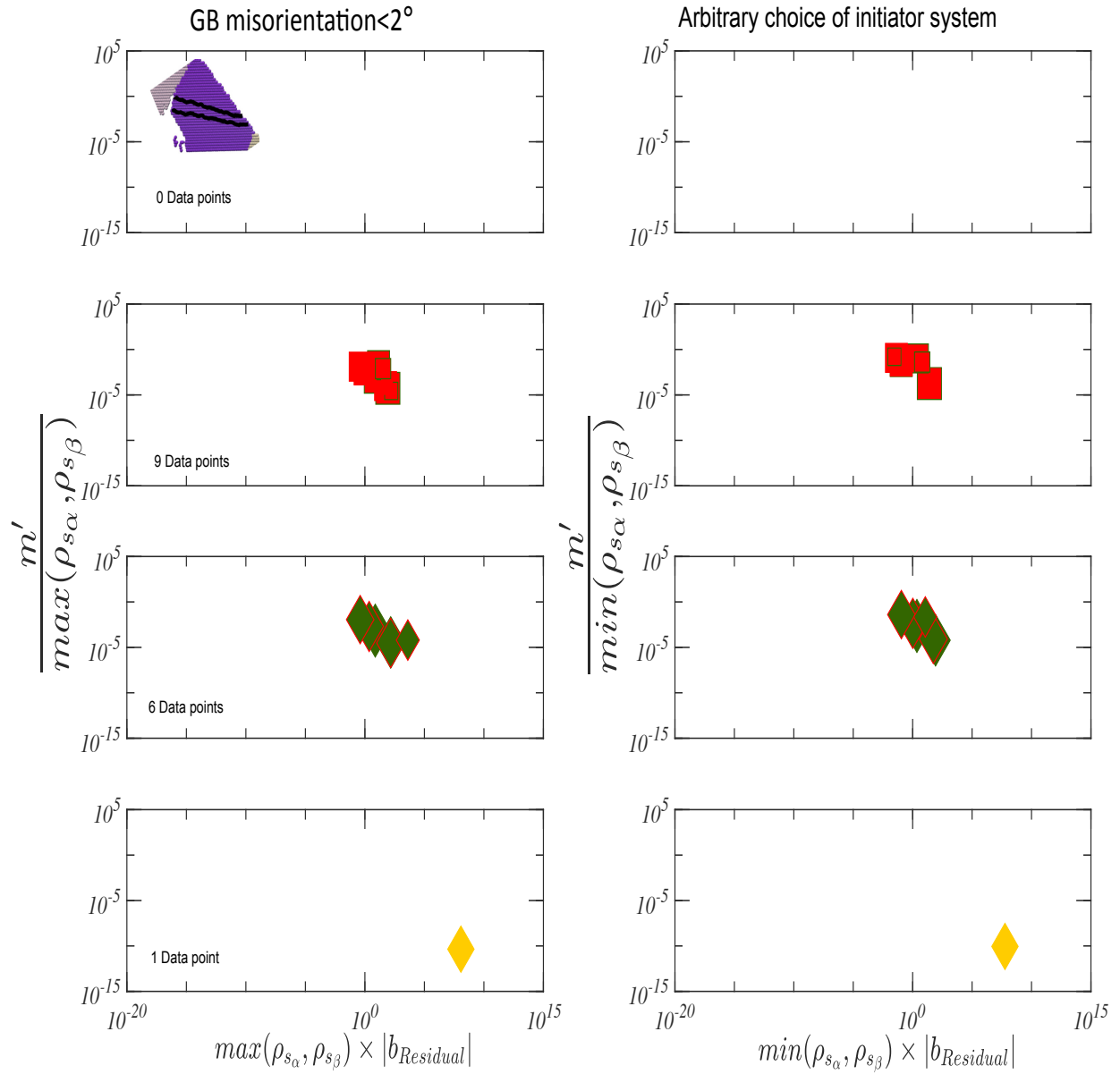


Figure F.6: LAGB region 1: m'' v/s scaled $|b_{Residual}|$ plots for the same data points shown in figure F.3, filtered using a criterion of $m' \geq 0.8$.

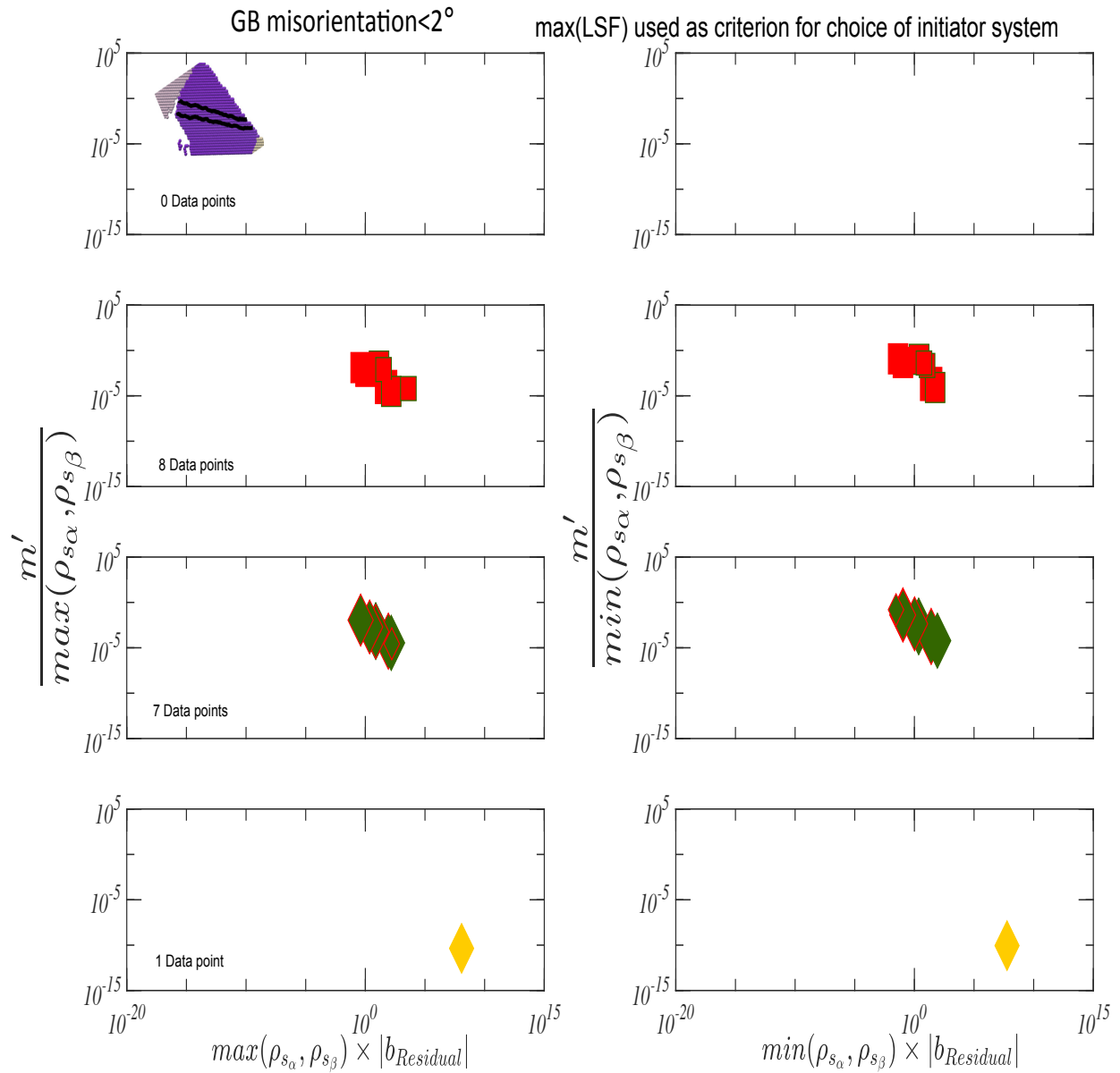


Figure F.7: LAGB region 1: m'' v/s scaled $|b_{Residual}|$ plots for the same data points shown in figure F.4, filtered using a criterion of $m' \geq 0.8$.

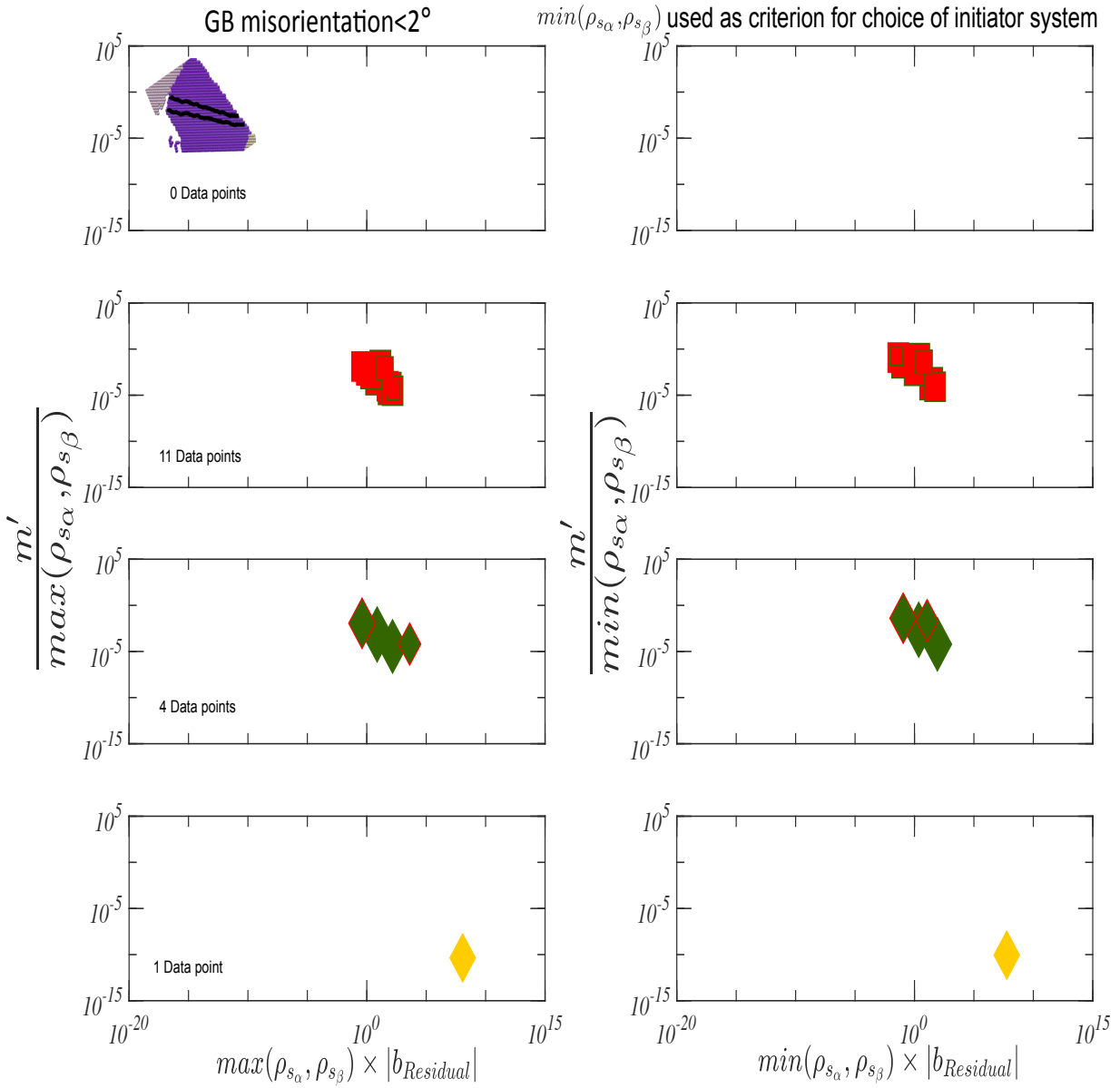


Figure F.8: LAGB region 1: m'' v/s scaled $|b_{Residual}|$ plots for the same data points shown in figure F.5, filtered using a criterion of $m' \geq 0.8$.

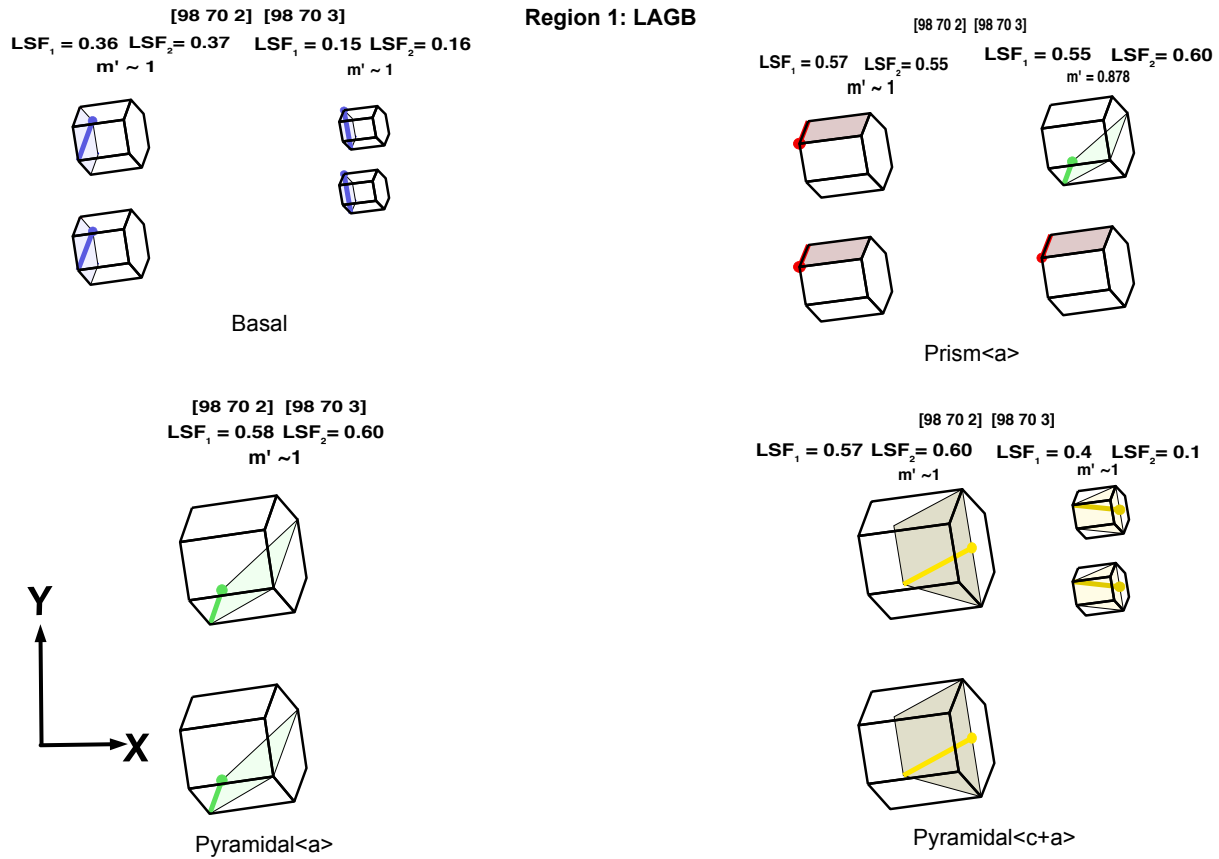


Figure F.9: Some instances of slip system interactions for basal, prism<a>, pyramidal<a> and pyramidal<c + a> initiating systems for the LAGB voxels in region 1 are shown. The LSF values, which were calculated using the local stress tensor, and the Bunge Euler angles and m' values are noted. The size of the prisms is proportional to the sum of the LSF values of the sum of the Schmid factors for the slip system pair. Prisms are drawn from the perspective of the sample normal, with Y pointing upwards and X pointing towards the right.

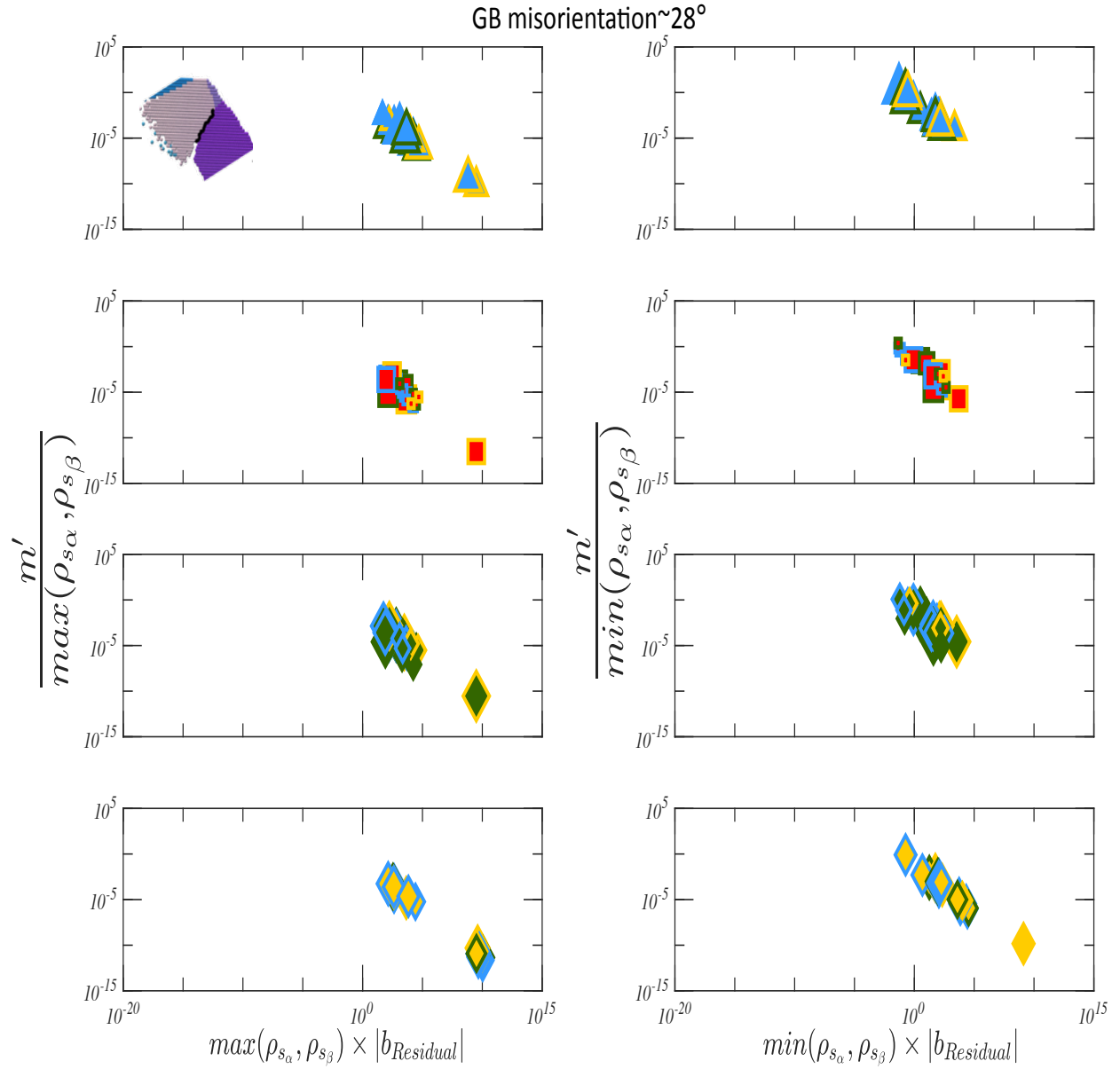


Figure F.10: HAGB region 1: Scaled slip transfer parameter m'' plotted as a function of scaled residual Burgers vector. The methodology used to plot the data is identical to F.3. In this case the initiator in an interacting pair of slip systems is chosen arbitrarily as described in section 7.4.3.

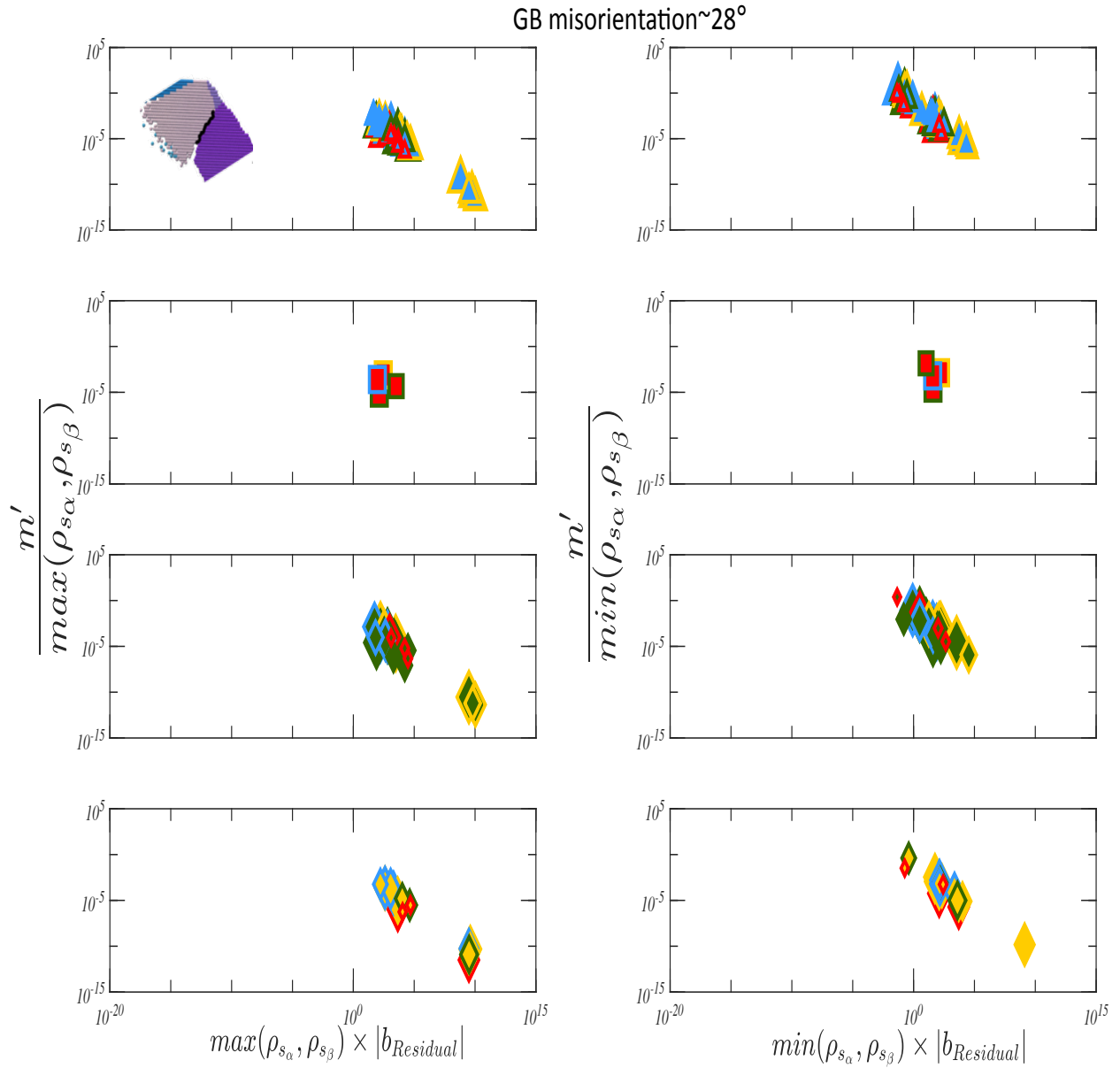


Figure F.11: HAGB region 1: Scaled slip transfer parameter m'' plotted as a function of scaled residual Burgers vector, using the maximum of LSF as criterion for choosing the transmitting slip system.

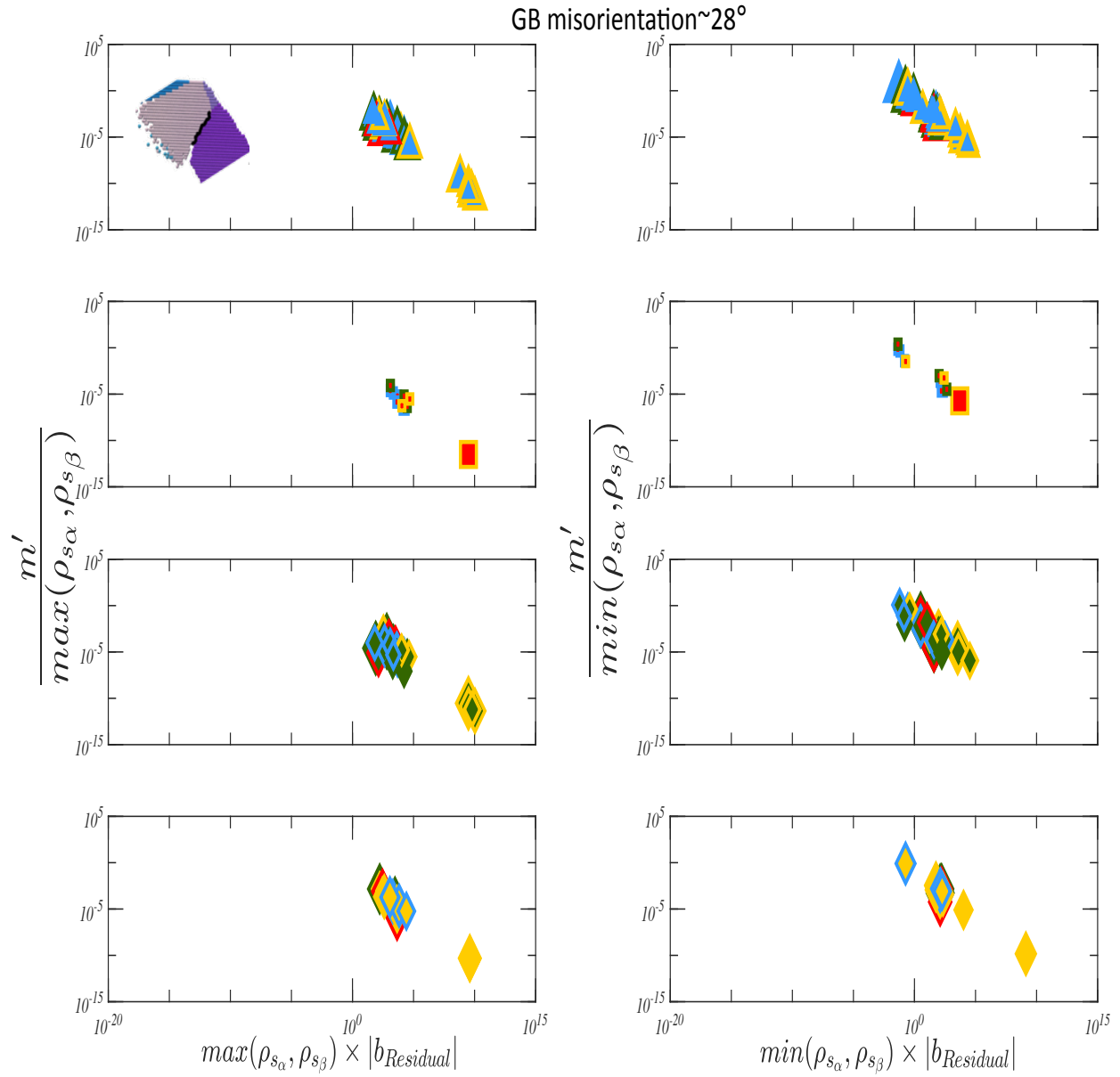


Figure F.12: HAGB region 1: Scaled slip transfer parameter m'' plotted as a function of scaled residual Burgers vector, using the minimum of GND density as criterion for choosing the transmitting slip system.

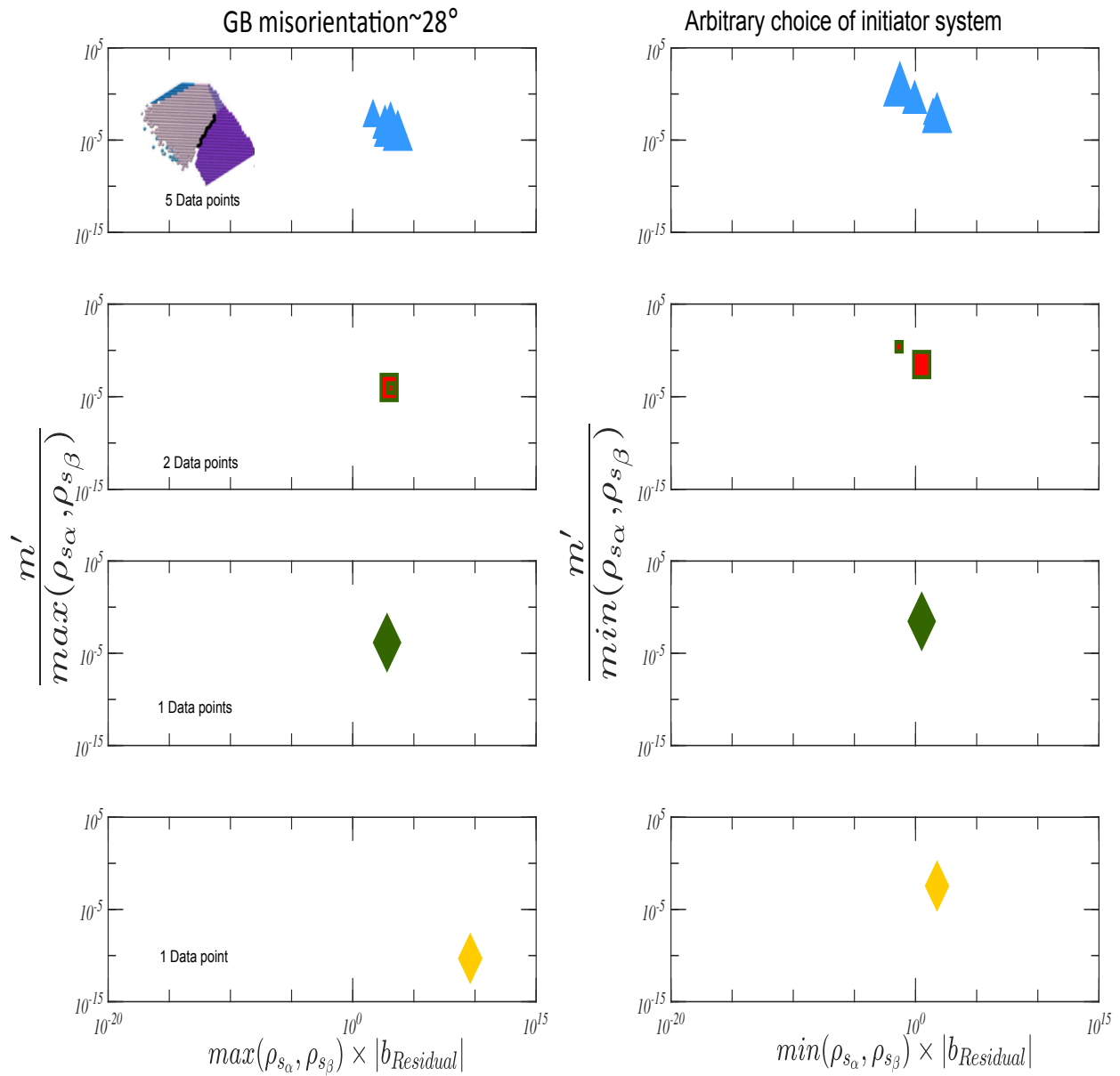


Figure F.13: HAGB region 1: Same data as plotted in figure F.10: only points with $m' \geq 0.8$ are plotted here .

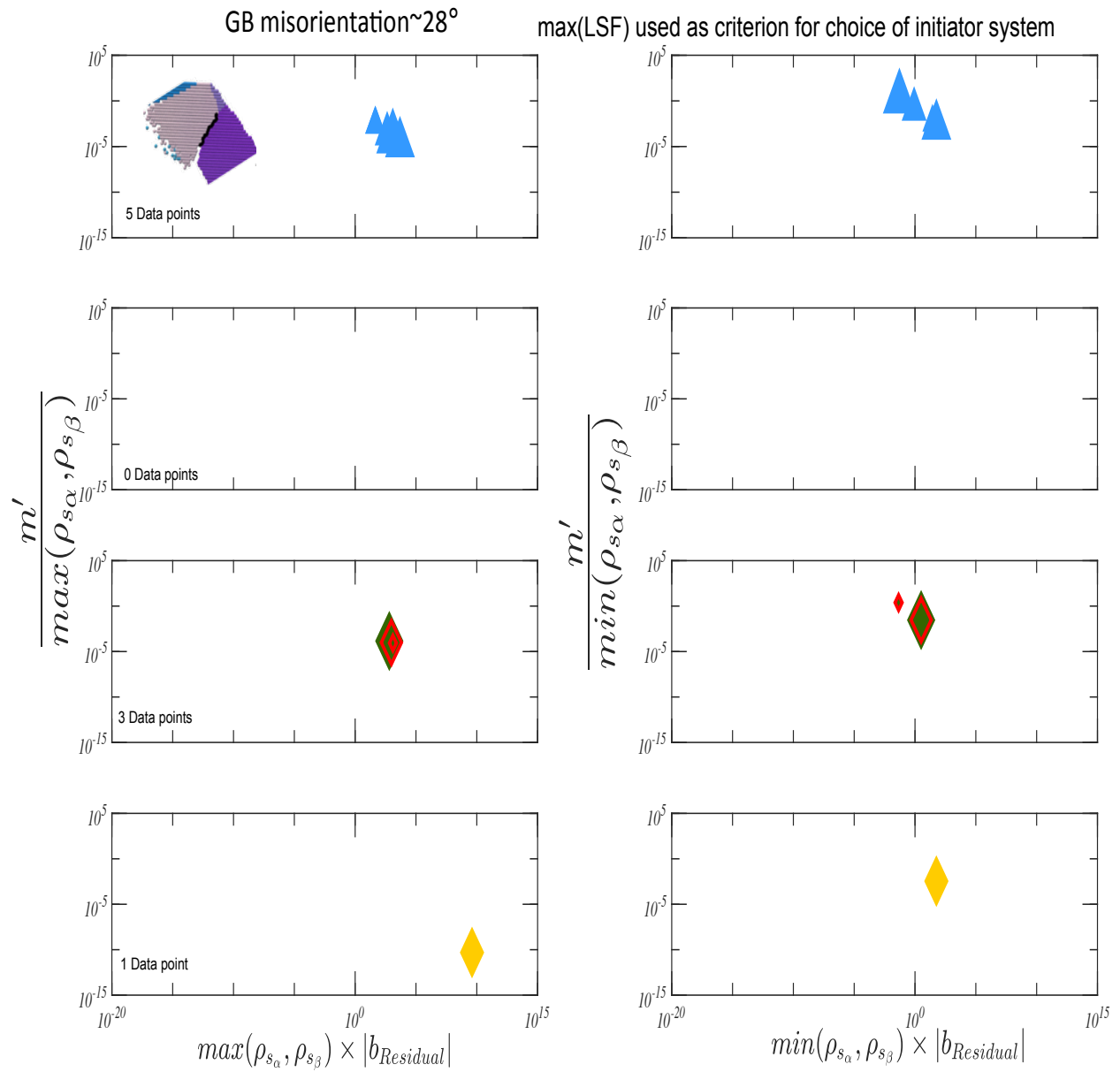


Figure F.14: HAGB region 1: Same data as plotted in figure F.11: only points with $m' \geq 0.8$ are plotted.

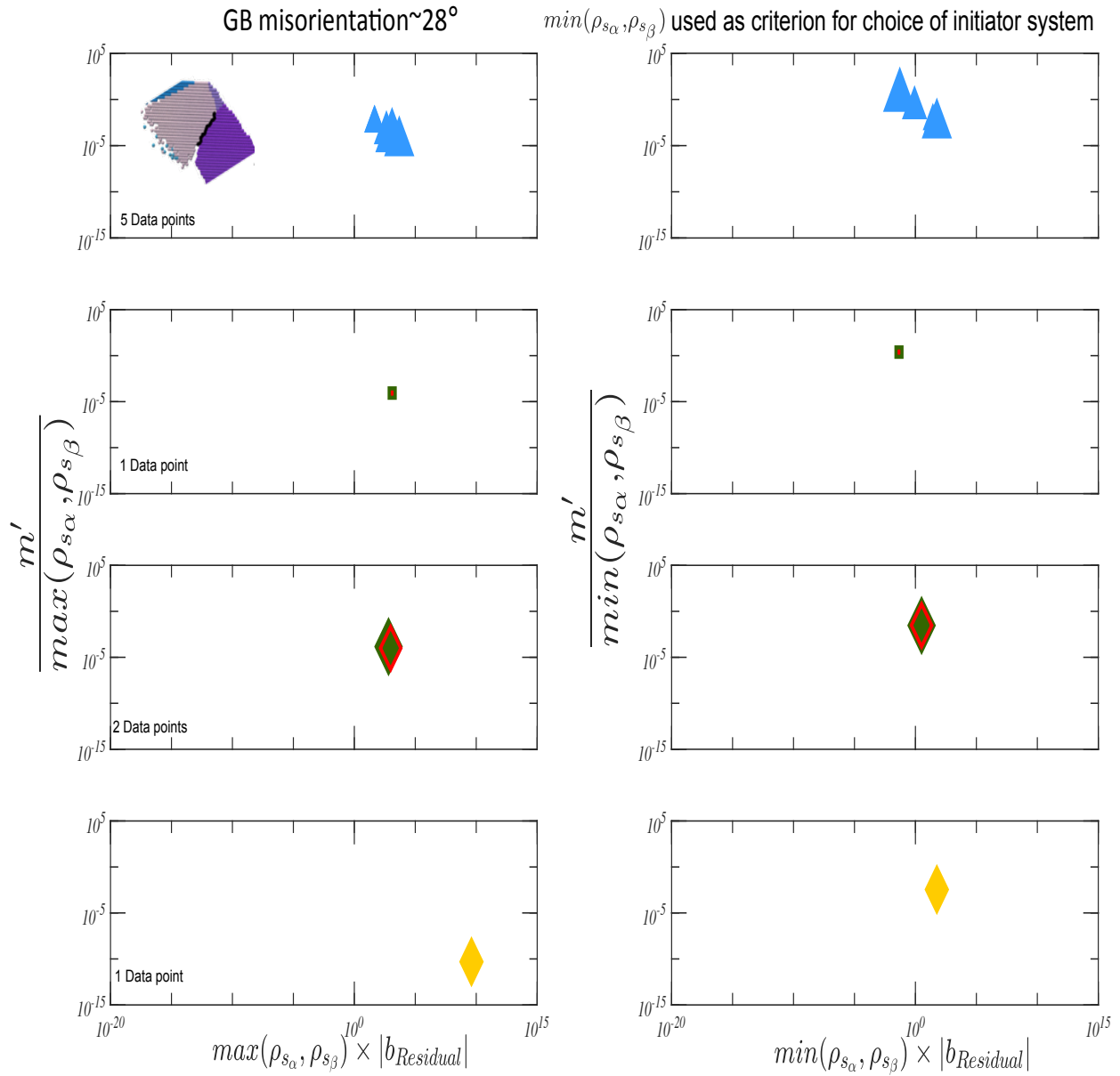


Figure F.15: HAGB region 1: Same data as plotted in figure F.12: only points with $m' \geq 0.8$ are plotted.

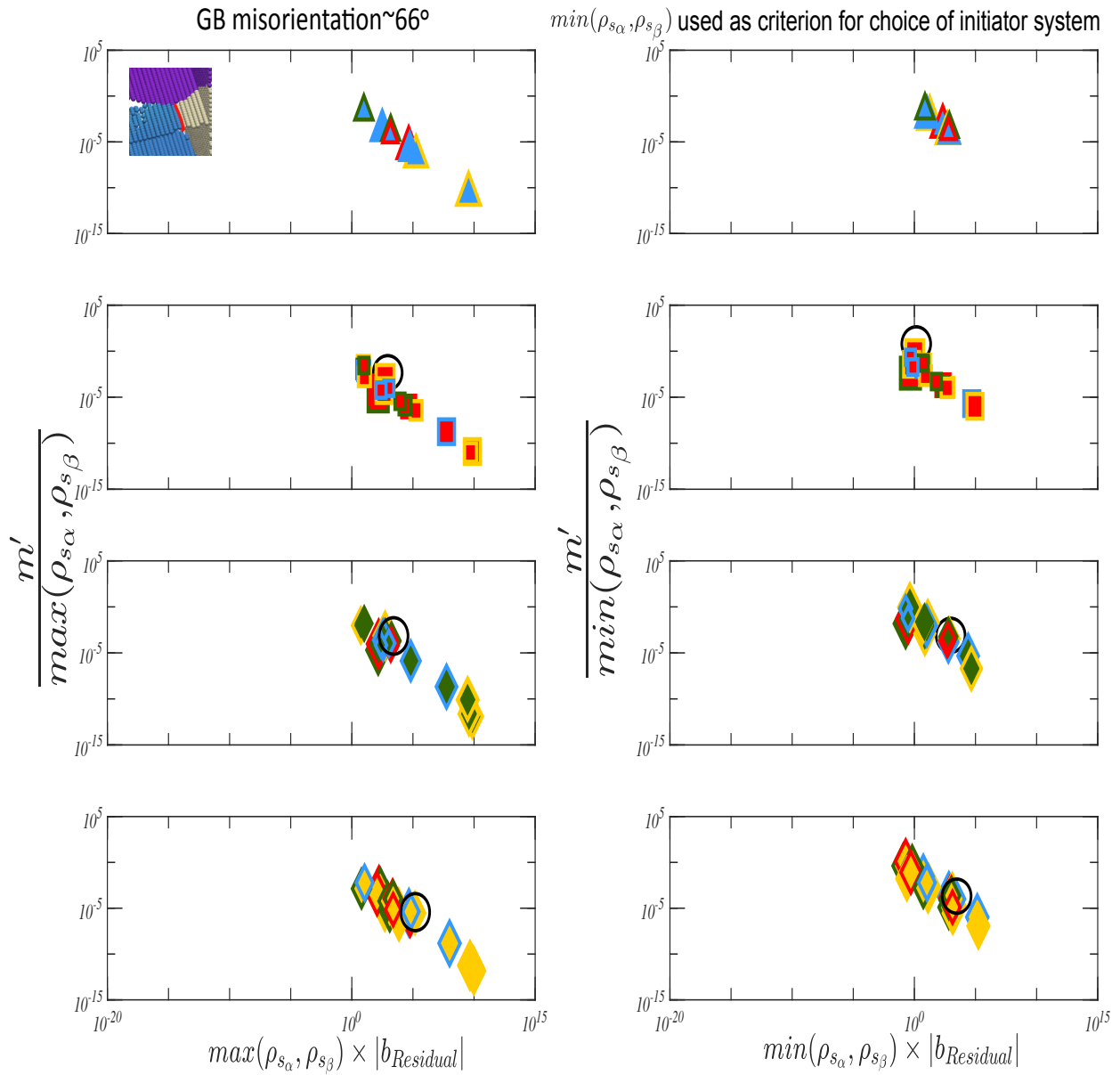


Figure F.16: Using the minimum GND density criterion for the transmitting grain, m'' is plotted as a function of scaled residual Burgers vector magnitude for the boundary between the hard (beige) and soft oriented (blue) grains in region 2. Data plotted is for four pairs of voxels situated along the grain boundary. Only the top five points (sorted by descending order of sum of LSf values) per voxel pair are considered here. The locations of the points that correspond to a high likelihood of slip transfer are encircled.

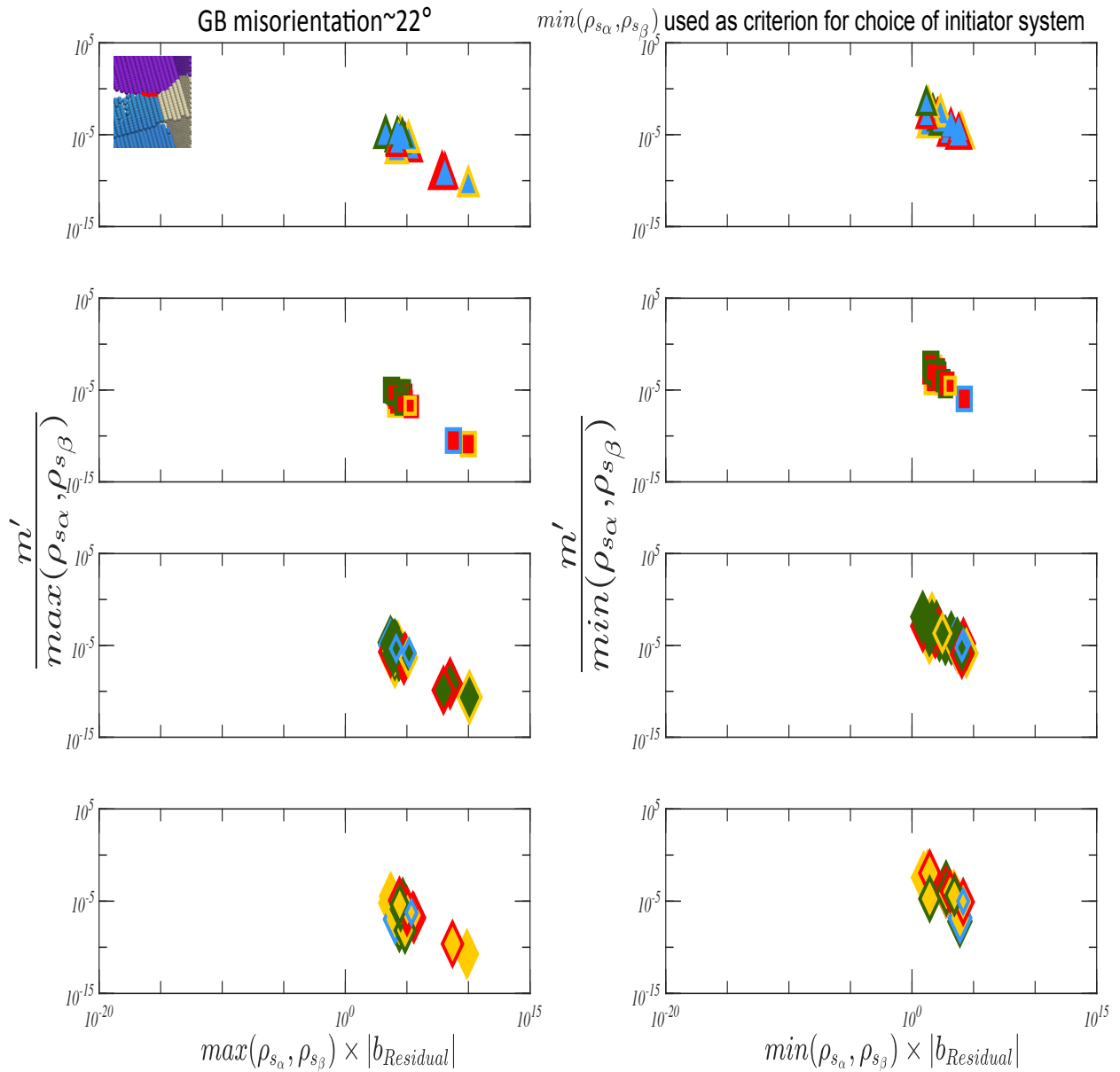


Figure F.17: Using the minimum GND density criterion for the transmitting grain, m'' is plotted as a function of scaled residual Burgers vector magnitude; for the boundary formed by the two softer oriented grains (blue and purple) in region 2. This boundary has the lowest likelihood for slip transfer of the three. Data plotted is for four pairs of voxels situated along the grain boundary. Only the top five points (sorted by descending order of sum of LSf values) per voxel pair are considered here.

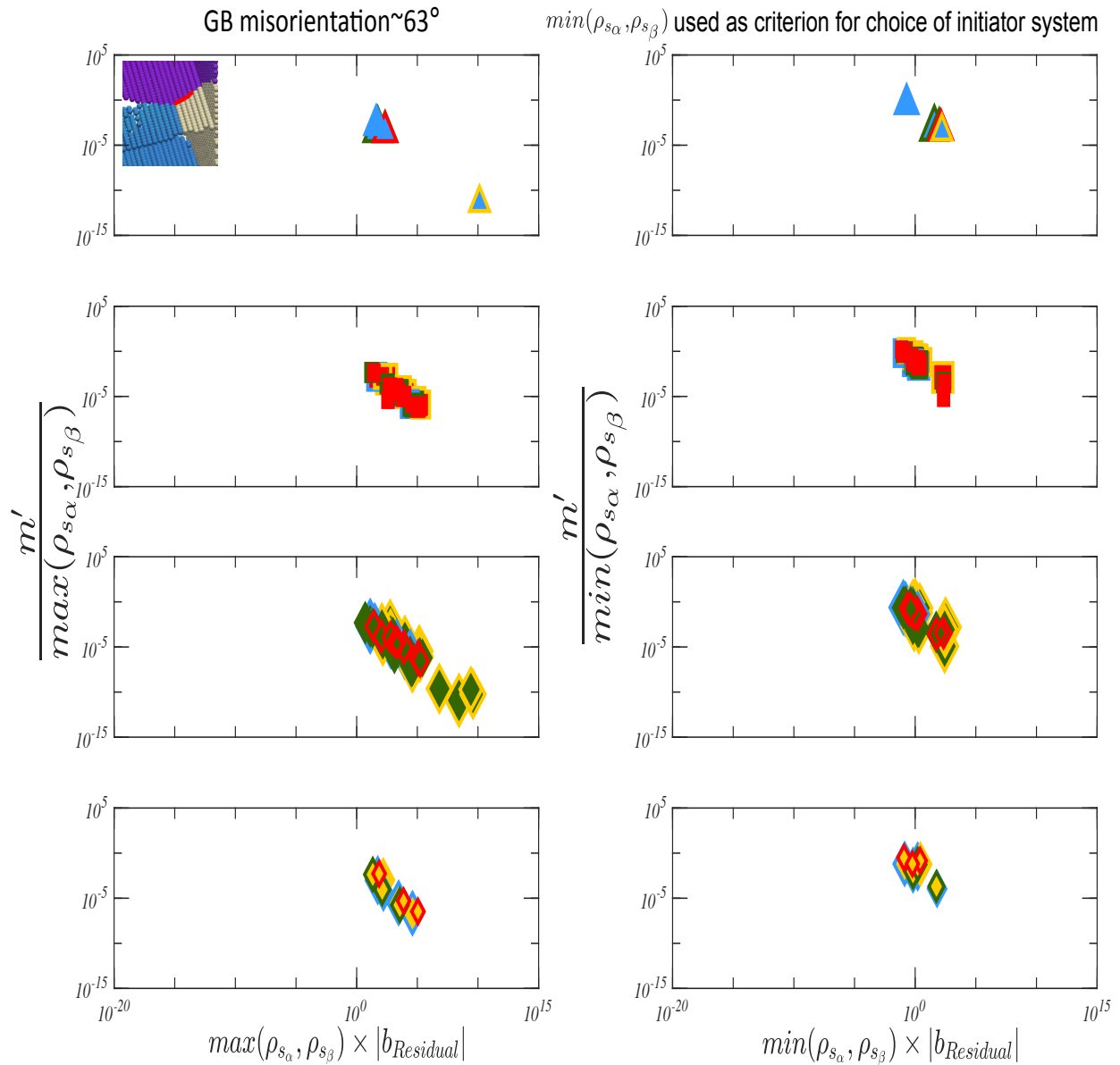


Figure F.18: Using the minimum GND density criterion for the transmitting grain, m'' is plotted as a function of scaled residual Burgers vector magnitude for the boundary between the hard beige and soft oriented purple grain in region 2. Data plotted is for four pairs of voxels situated along the grain boundary. Only the top five points (sorted by descending order of sum of LSf values) per voxel pair are considered here.

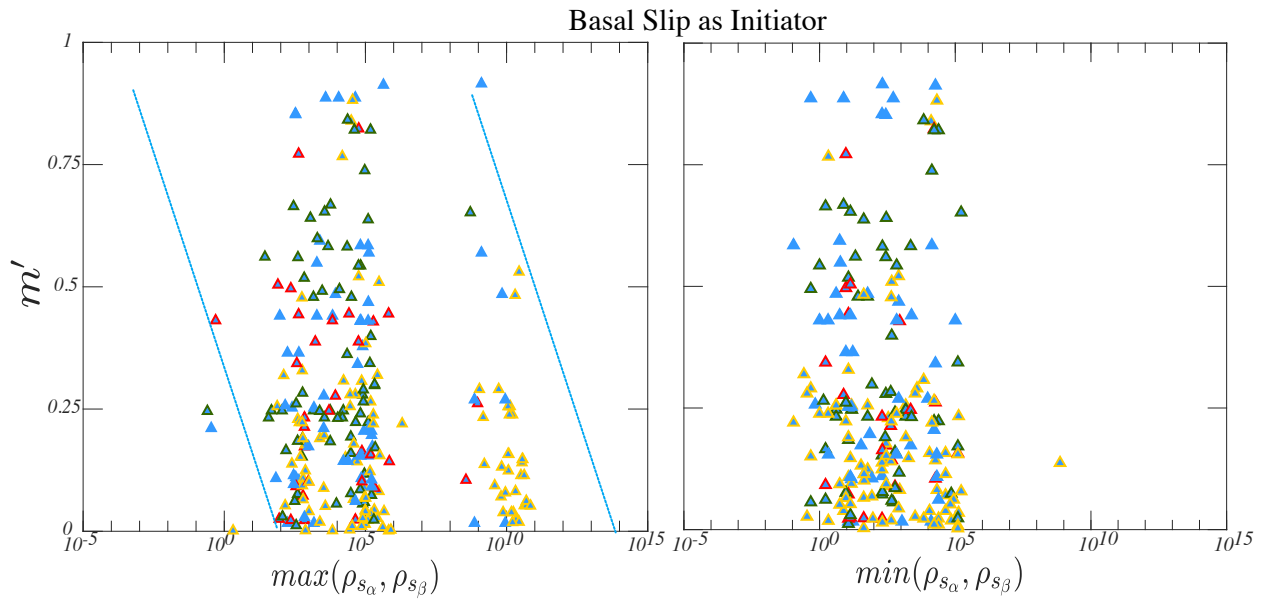


Figure F.19: m' plotted as a function of $\max(\rho_{s_\alpha}, \rho_{s_\beta})$ and $\min(\rho_{s_\alpha}, \rho_{s_\beta})$, considering basal slip as the transmitting system. The transmitting slip system is chosen on the basis on minimum slip system specific GND density in voxel pair. The data plotted are from 12 grain boundaries encompassed by regions 1, 2, 3, 4 and 5. The envelope of data points for the $\max(\rho_{s_\alpha}, \rho_{s_\beta})$ case shows an inverse correlation between GND density and slip transmissibility are enclosed within the lines in each plot. The description of the symbol shape and color scheme of the data points is explained in section F.0.1

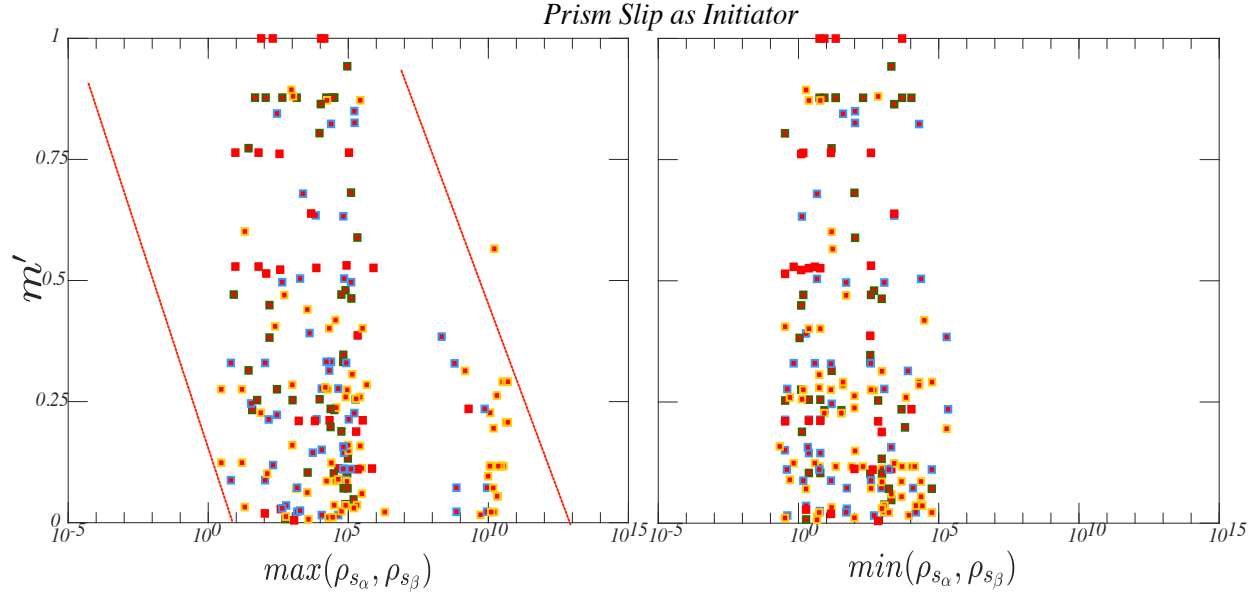


Figure F.20: m' plotted as a function of $\max(\rho_{s_\alpha}, \rho_{s_\beta})$ and $\min(\rho_{s_\alpha}, \rho_{s_\beta})$, considering prism $\langle a \rangle$ slip as the transmitting system. The transmitting slip system is chosen on the basis on minimum slip system specific GND density in voxel pair. Data plotted from 12 grain boundaries encompassed by regions 1, 2, 3, 4 and 5. The envelope of data points for the $\max(\rho_{s_\alpha}, \rho_{s_\beta})$ case shows an inverse correlation between GND density and slip transmissibility are enclosed within the lines in each plot.

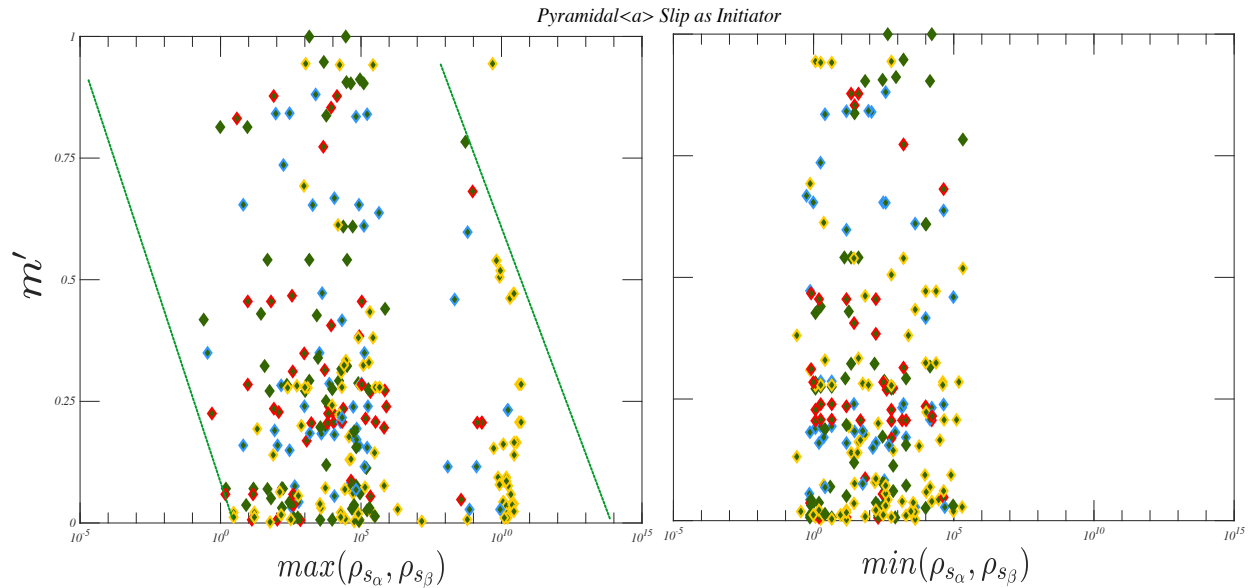


Figure F.21: Bend increment 2: m' plotted as a function of $\max(\rho_{s_\alpha}, \rho_{s_\beta})$ and $\min(\rho_{s_\alpha}, \rho_{s_\beta})$, considering pyramidal $\langle a \rangle$ slip as the transmitting system. The transmitting slip system is chosen on the basis on minimum slip system specific GND density in voxel pair. Data plotted from 12 grain boundaries encompassed by regions 1, 2, 3, 4 and 5. The envelope of data points for the $\max(\rho_{s_\alpha}, \rho_{s_\beta})$ case shows an inverse correlation between GND density and slip transmissibility are enclosed within the lines in each plot.

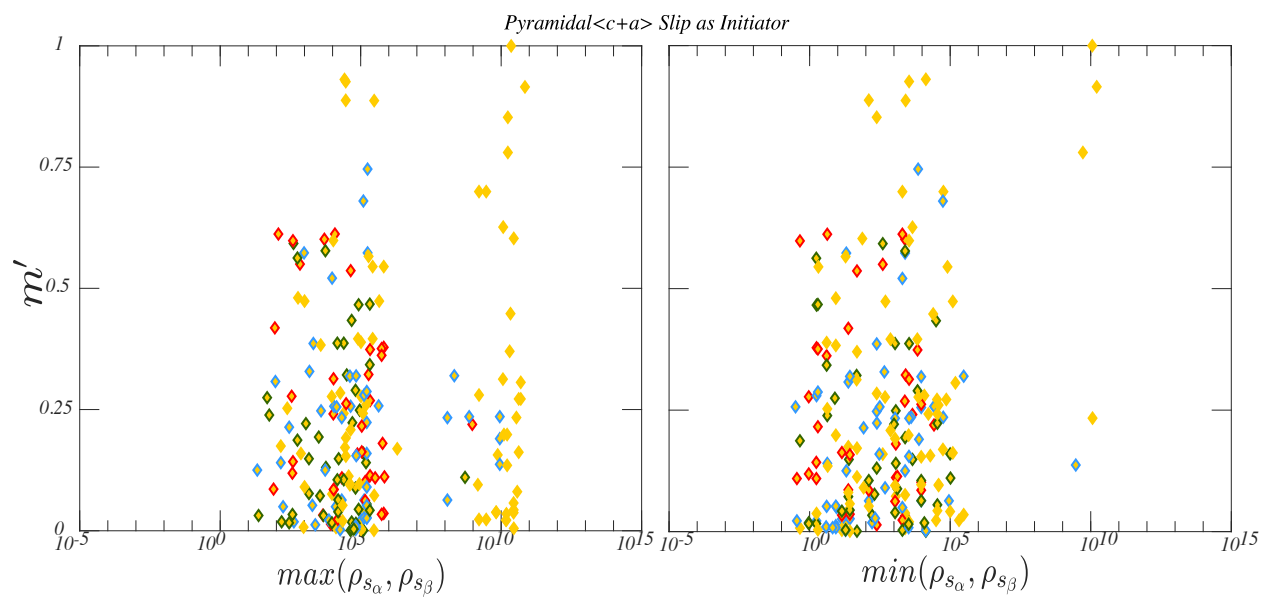


Figure F.22: Bend increment 2: m' plotted as a function of $\max(\rho_{s_\alpha}, \rho_{s_\beta})$ and $\min(\rho_{s_\alpha}, \rho_{s_\beta})$, considering pyramidal $\langle c + a \rangle$ slip as the transmitting system. The transmitting slip system is chosen on the basis on minimum slip system specific GND density in voxel pair. Data plotted from 12 grain boundaries encompassed by regions 1, 2, 3, 4 and 5.

APPENDIX G

SLIP TRANSFER PARAMETER V/S RESIDUAL BURGERS VECTOR PLOTS

In this section, the plots of scaled values of the Luster Morris parameter as a function of scaled magnitude of residual Burgers vector are shown for regions 3, 4 and 5 of the microstructure described in 7.4.3. Details of the parameter descriptions can be found in 7.4.3 and F.0.1. The plots shown are for interacting slip systems in four voxel pairs on either side of a grain boundary. For details on the symbol conventions used, the reader is referred to F.0.1. In all of the plots shown in this section, the initiating slip system for each voxel pair is chosen based on the minimum value of the slip system specific GND density.

The plots for the three constituent grain boundaries in the triple junction for region 3 are shown in figures G.1, G.2 and G.3. For the first grain boundary shown in figure G.1, only one basal $\langle a \rangle$ system was found to have a high likelihood of slip transfer ($m' \geq 0.8$); whereas no instances of prism $\langle a \rangle$, pyramidal $\langle a \rangle$ and pyramidal $\langle c + a \rangle$ are likely to transfer.

In case of the second grain boundary in region 3 (figure G.2), the only likely slip system to transfer is pyramidal $\langle a \rangle$ (3 instances). For the third grain boundary in region 3 (figure G.3), the number of slip systems with favorable geometrical compatibility for transfer of basal $\langle a \rangle$, prism $\langle a \rangle$ and pyramidal $\langle c + a \rangle$ are 2, 1 and 2 respectively.

For the grain boundary in region 4, the only geometrically favorable instances of slip transfer correspond to pyramidal $\langle a \rangle$ and pyramidal $\langle c + a \rangle$ (1 each) (figure G.4).

For the first grain boundary of the triple junction in region 5 (figure G.5), the only favorable instances of slip transfer correspond to basal $\langle a \rangle$ (2) and pyramidal $\langle c + a \rangle$ (2) systems. With respect to the second grain boundary in region 5 (figure G.6), the favorable instances for slip transfer correspond to basal $\langle a \rangle$ (3), prism $\langle a \rangle$ (4) and pyramidal $\langle a \rangle$ (2). There were no instances with a favorable geometrical compatibility for slip transfer for the third grain boundary in region 5 (figure G.7).

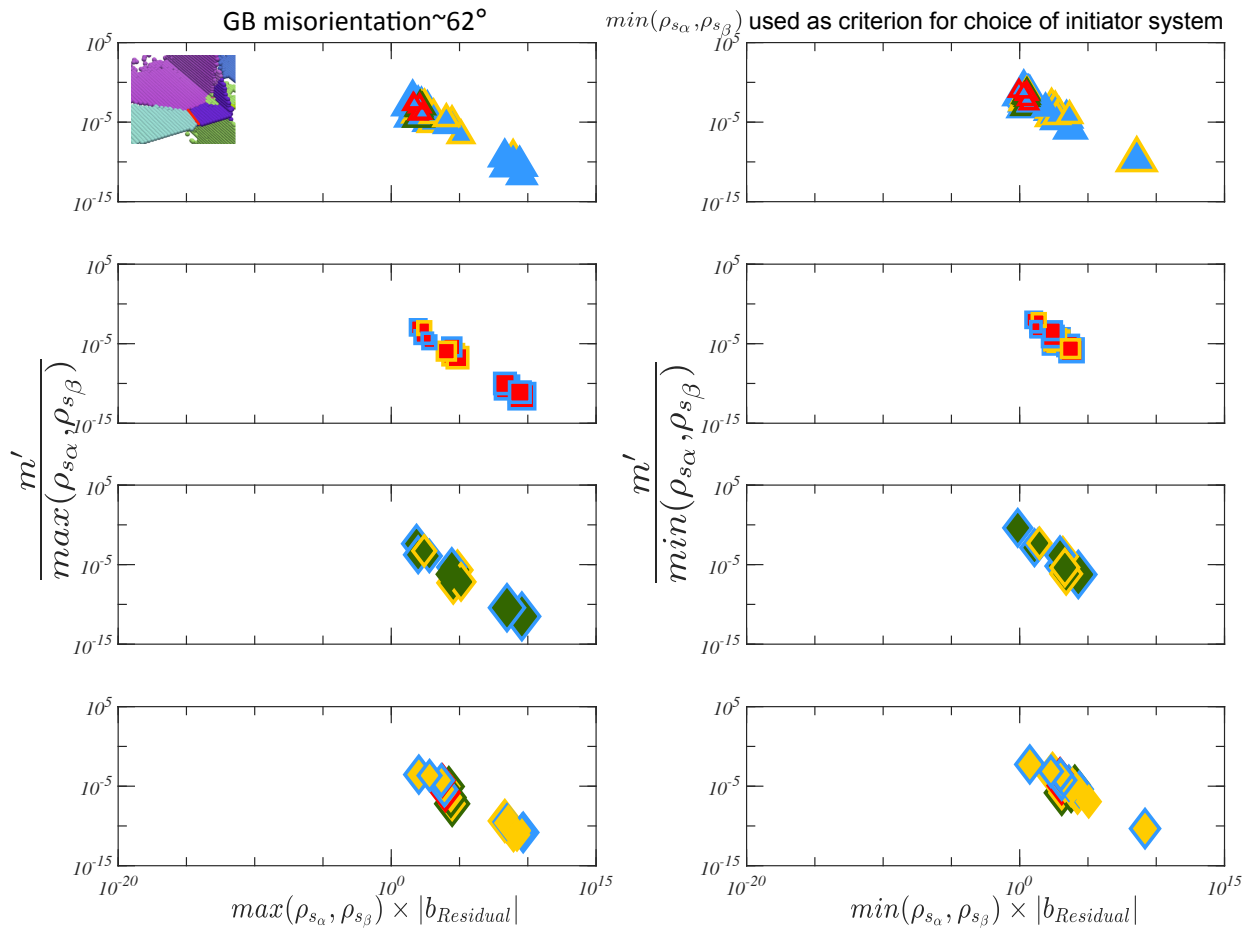


Figure G.1: Bend increment 2: Scaled slip transfer parameter plotted as a function of scaled residual Burgers vector magnitude for the first grain boundary (shown in the inset) constituting the triple junction in region 3 of microstructure described in 7.4.3. The choice of the transmitting slip system is made on the basis of minimum GND density of the voxel pair.

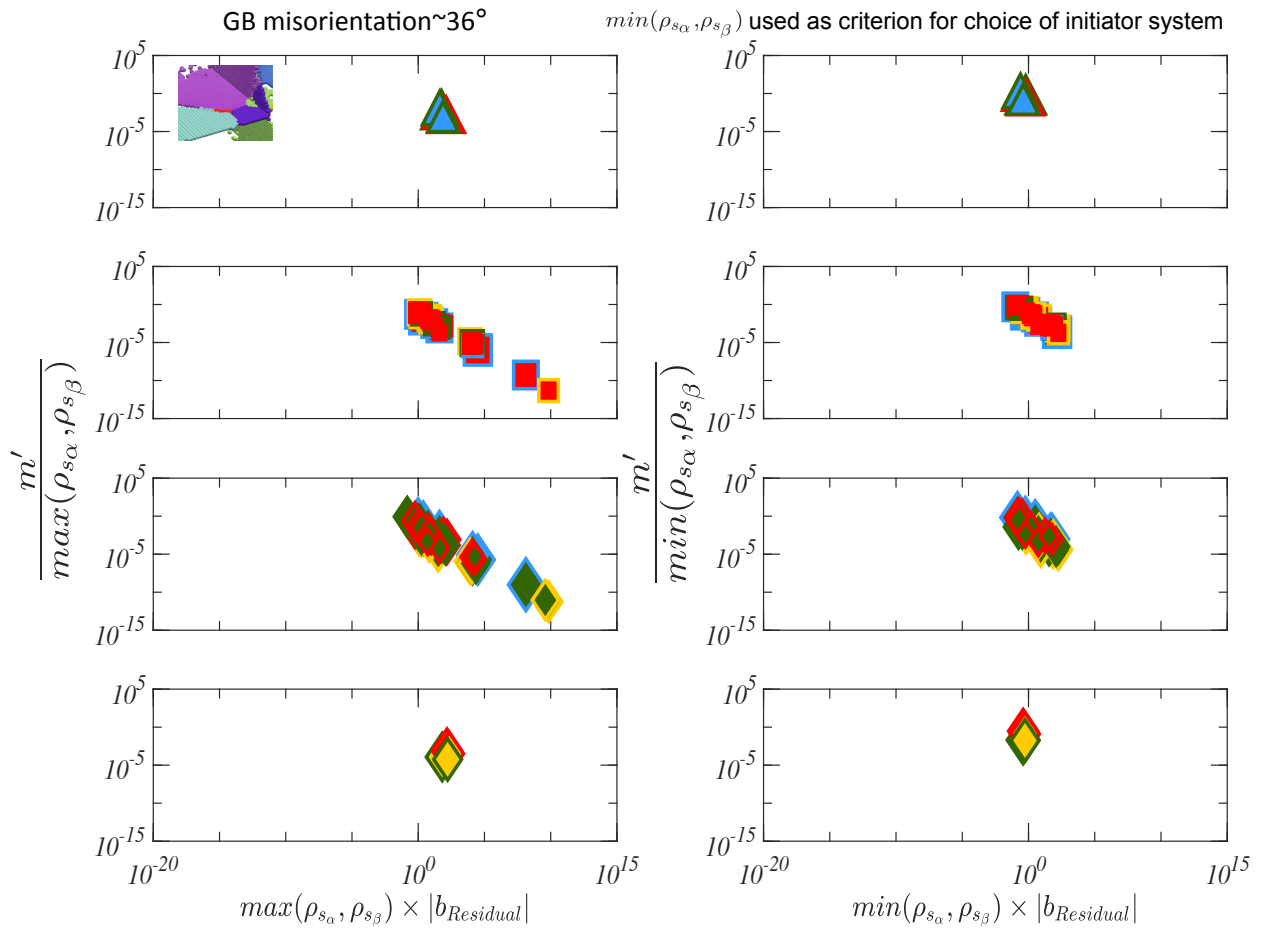


Figure G.2: Bend increment 2: Scaled slip transfer parameter plotted as a function of scaled residual Burgers vector magnitude for the second grain boundary (shown in the inset) constituting the triple junction in region 3 of microstructure described in 7.4.3. The choice of the transmitting slip system is made on the basis of minimum GND density of the voxel pair.

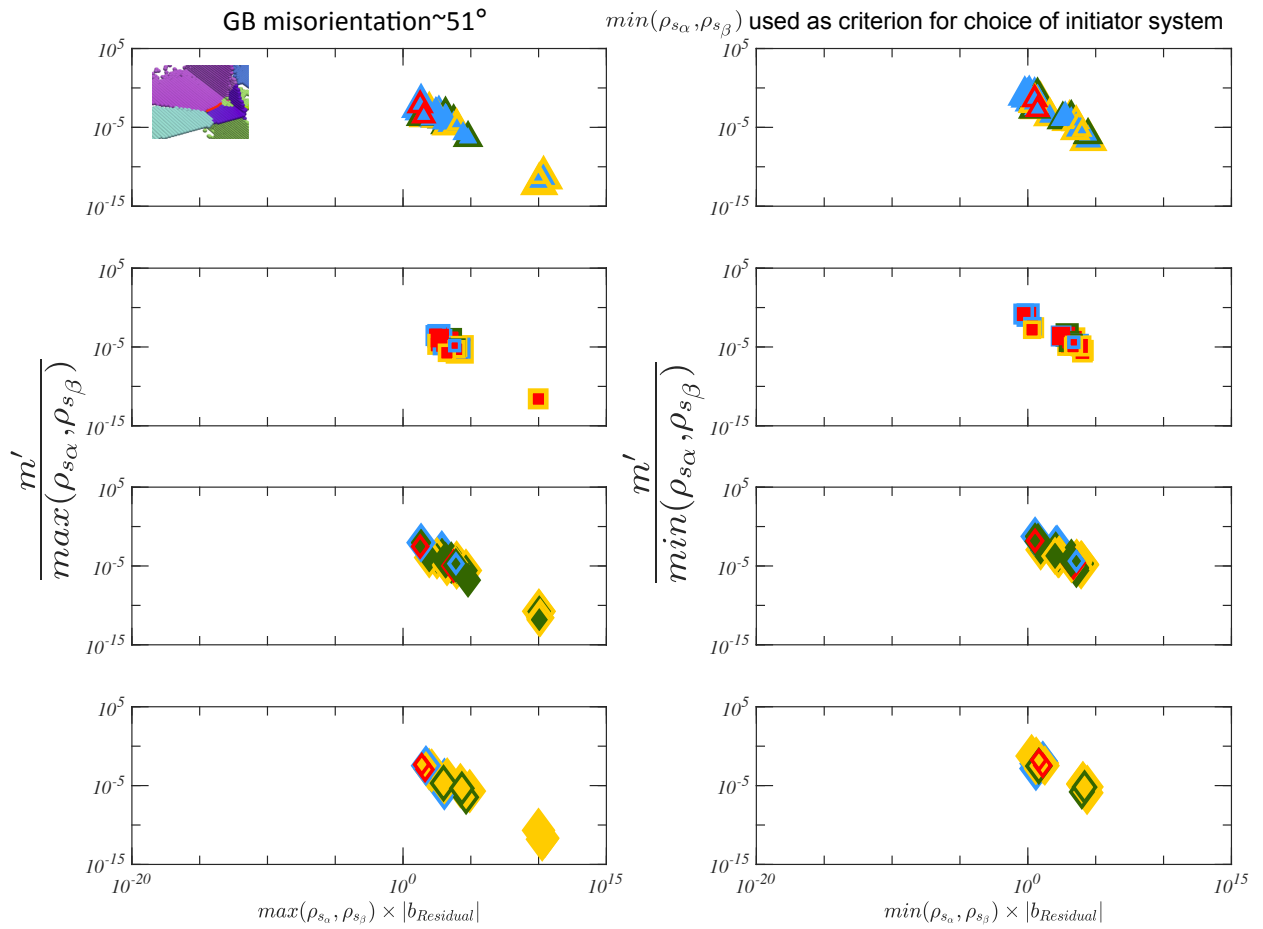


Figure G.3: Bend increment 2: Scaled slip transfer parameter plotted as a function of scaled residual Burgers vector magnitude for the third grain boundary (shown in the inset) constituting the triple junction in region 3 of microstructure described in 7.4.3. The choice of the transmitting slip system is made on the basis of minimum GND density of the voxel pair.

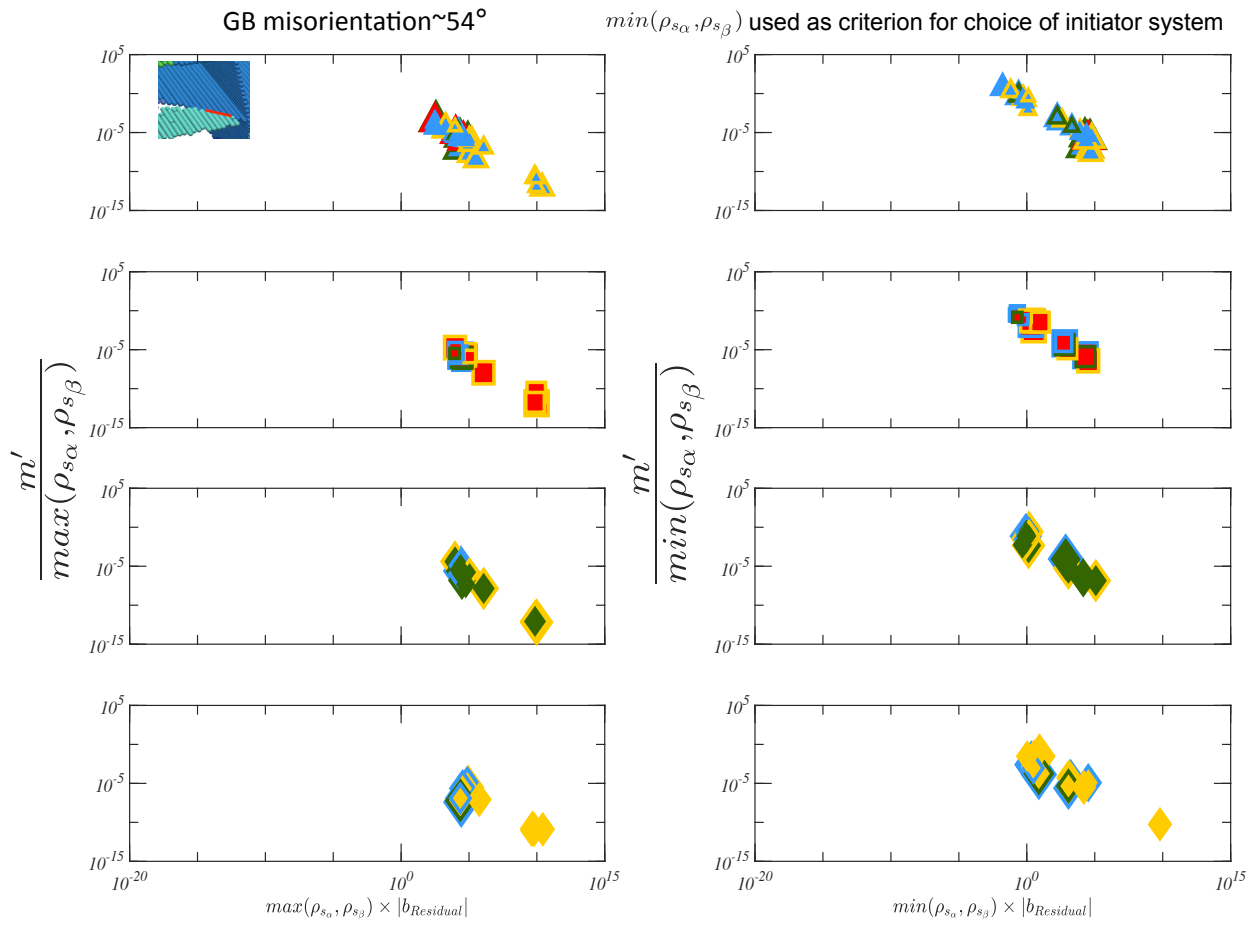


Figure G.4: Bend increment 2: Scaled slip transfer parameter plotted as a function of scaled residual Burgers vector magnitude for the grain boundary in region 4 of microstructure described in 7.4.3.

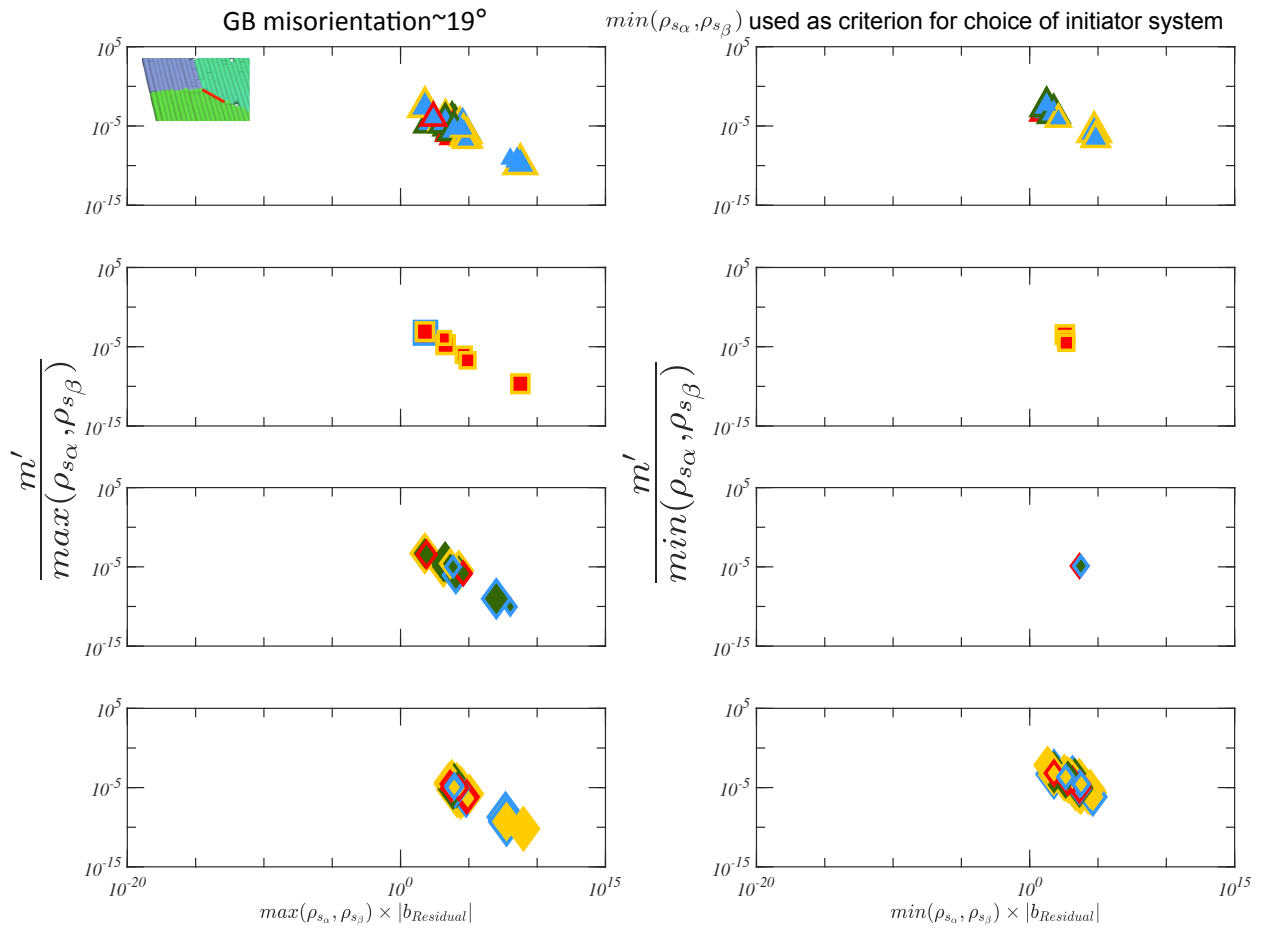


Figure G.5: Bend increment 2: Bend increment 2: Scaled slip transfer parameter plotted as a function of scaled residual Burgers vector magnitude for the first grain boundary constituting the triple junction in region 5 of microstructure described in 7.4.3. Each column of plots correspond to slip system interaction at a grain boundary (inset).

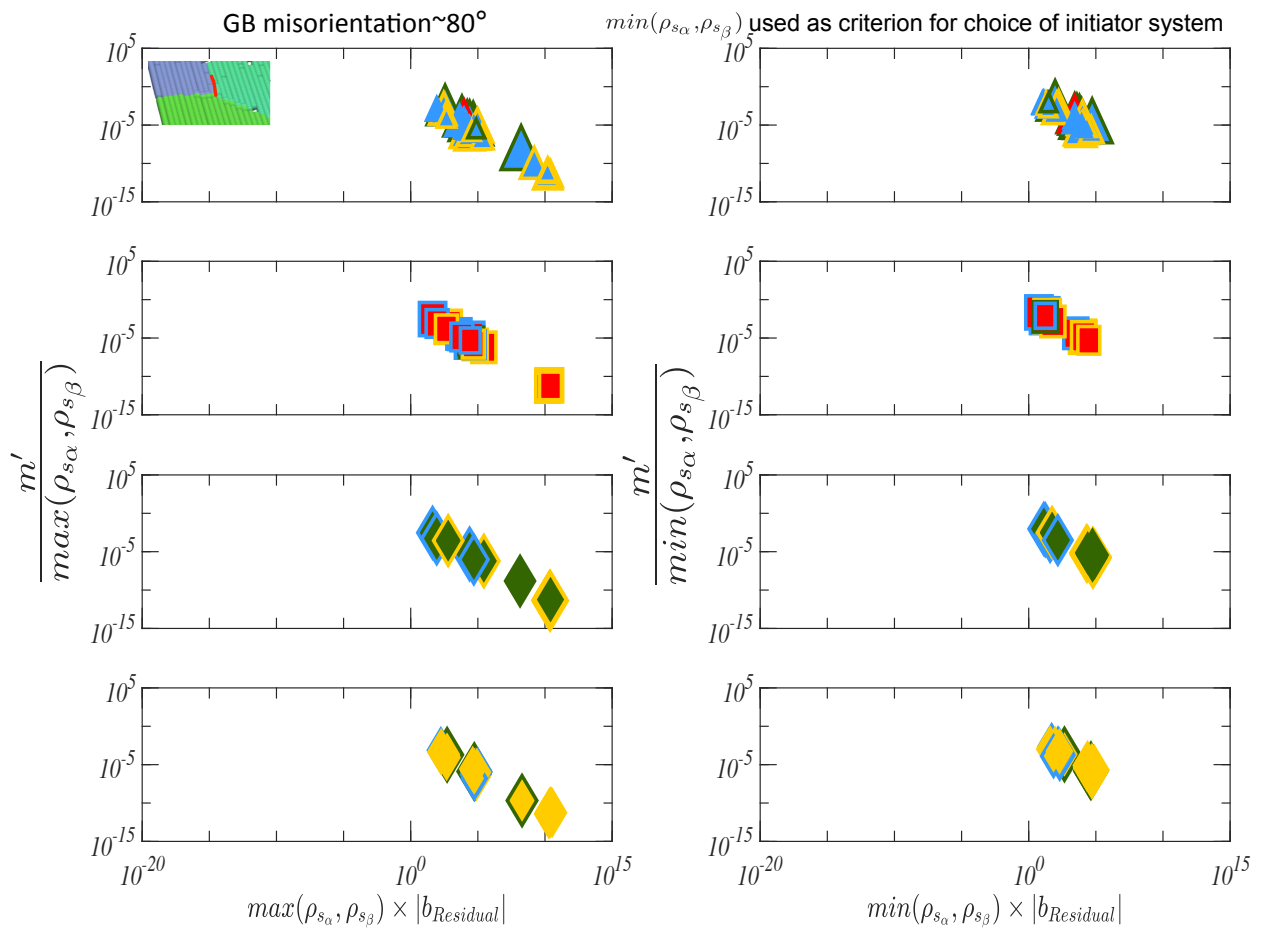


Figure G.6: Bend increment 2: Bend increment 2: Scaled slip transfer parameter plotted as a function of scaled residual Burgers vector magnitude for the second grain boundary constituting the triple junction in region 5 of microstructure described in 7.4.3. Each column of plots correspond to slip system interaction at a grain boundary (inset).

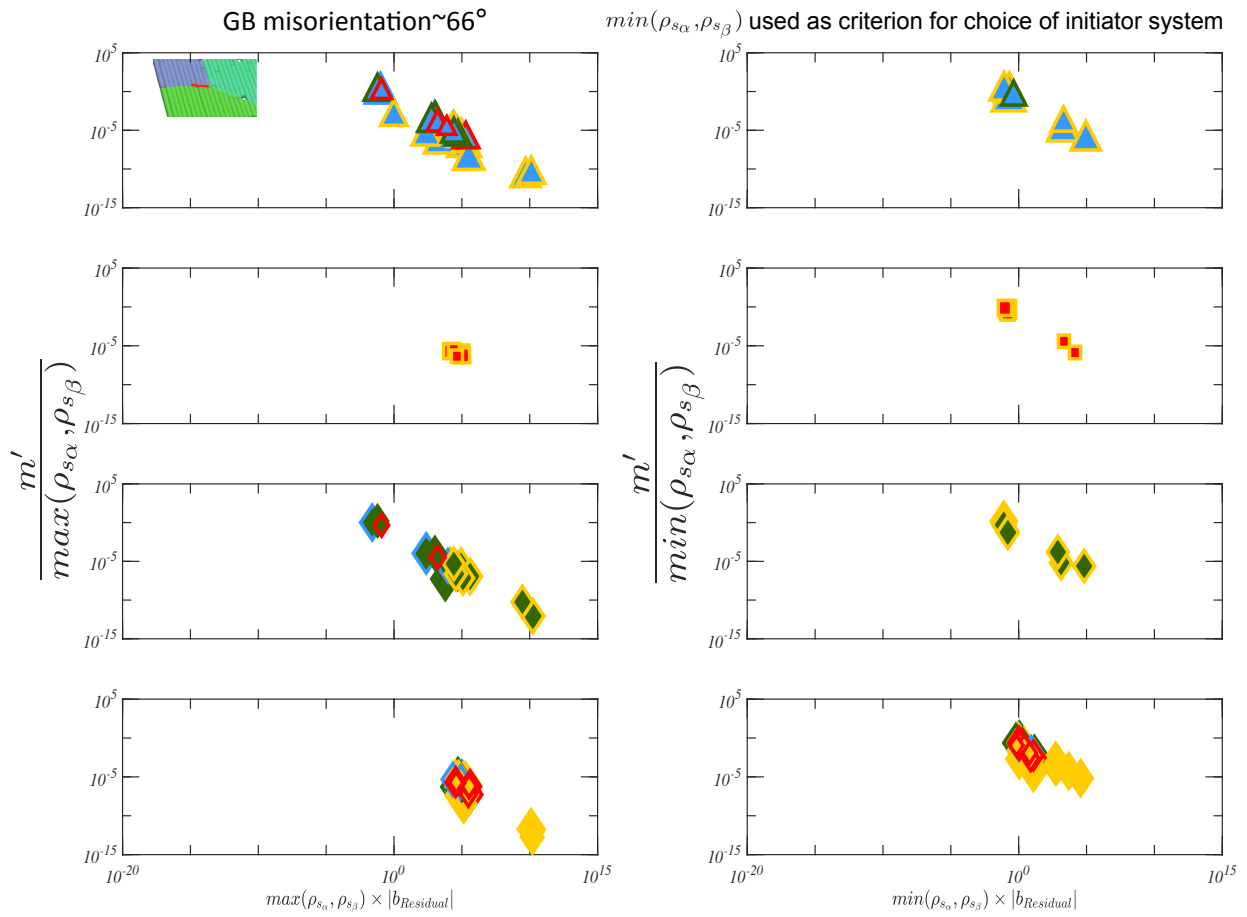


Figure G.7: Bend increment 2: Bend increment 2: Scaled slip transfer parameter plotted as a function of scaled residual Burgers vector magnitude for the third grain boundary constituting the triple junction in region 5 of microstructure described in 7.4.3. Each column of plots correspond to slip system interaction at a grain boundary (inset).

APPENDIX H

COORDINATE TRANSFORMATIONS

The following sections show the steps necessary for transformation to TSL-OIM coordinate system from APS beamlines 1 and 34 ID-E respectively. It is important to note here that the final TSL coordinate system for both transformations has X pointing upwards, Y to the left and Z coming out of the page.

H.1 34 ID-E beamline coordinate system to TSL (OIM) coordinate system

Figure H.1 shows the steps required to calculate the rotation matrix for coordinate transformation from APS beamline 34 ID-E to TSL (OIM) system. The two coordinate systems have a common X axis (Normal to the plane of the page). The direction of the incoming beam is coincident with the beamline Z axis. The APS system can be brought into coincidence with the TSL system by a clockwise rotation of 135° about the X axis. The transformation matrix to accomplish this rotation (g_{TSL}^{34IDE}) is calculated from the the direction cosines between the two coordinate systems.

H.2 ID-1 beamline coordinate system to TSL (OIM) coordinate system

The transformation from the ID1 coordinate system to the TSL system is shown in figure H.2. The direction of the beam is anti-parallel to the ID1 X axis. In order to bring the ID1 system into coincidence with the TSL coordinate system, a counter clockwise rotation of 90° about the common X axis is required. The corresponding transformation matrix g_{TSL}^{ID1} is also shown in figure H.2.

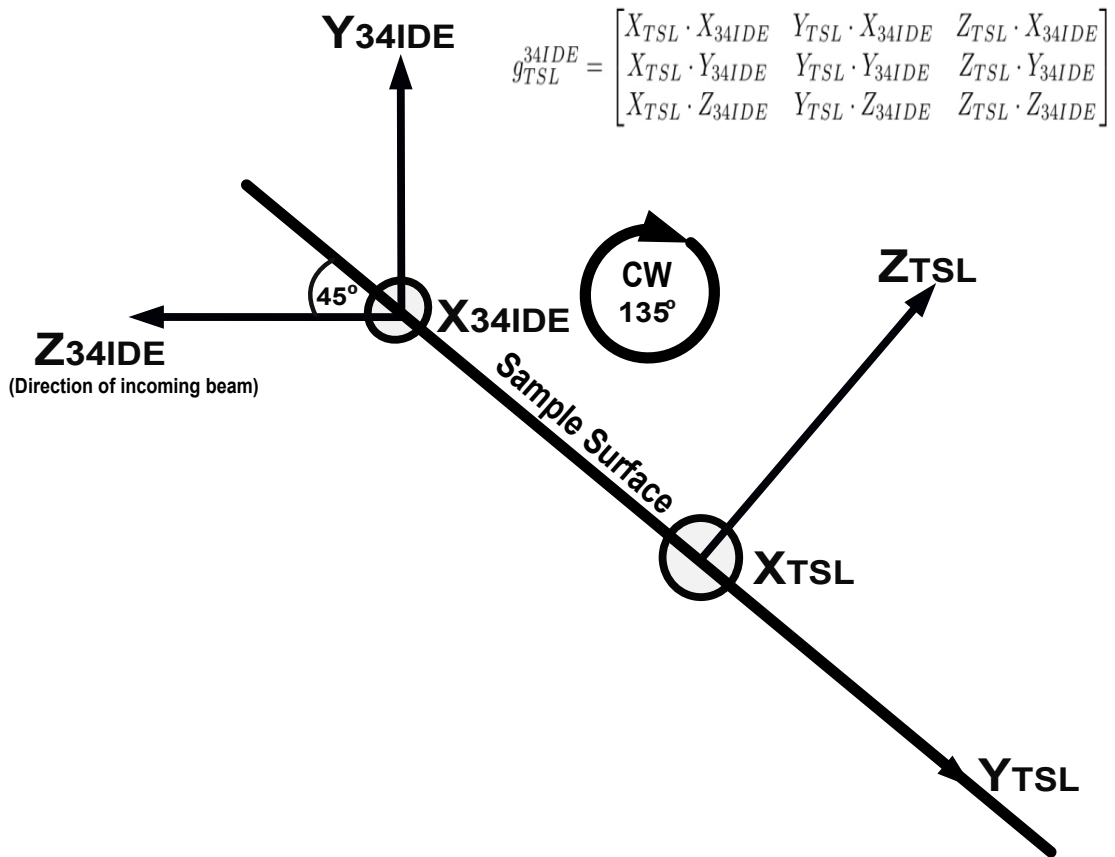


Figure H.1: Schematic showing the transformation from the APS Beamline 34 Coordinate system to TSL-OIM coordinate system. The two systems can be brought into coincidence by rotating the APS system clockwise about the X axis by 135°. The transformation matrix (g_{TSL}^{34IDE}) is calculated from the direction cosines between the two coordinate systems.

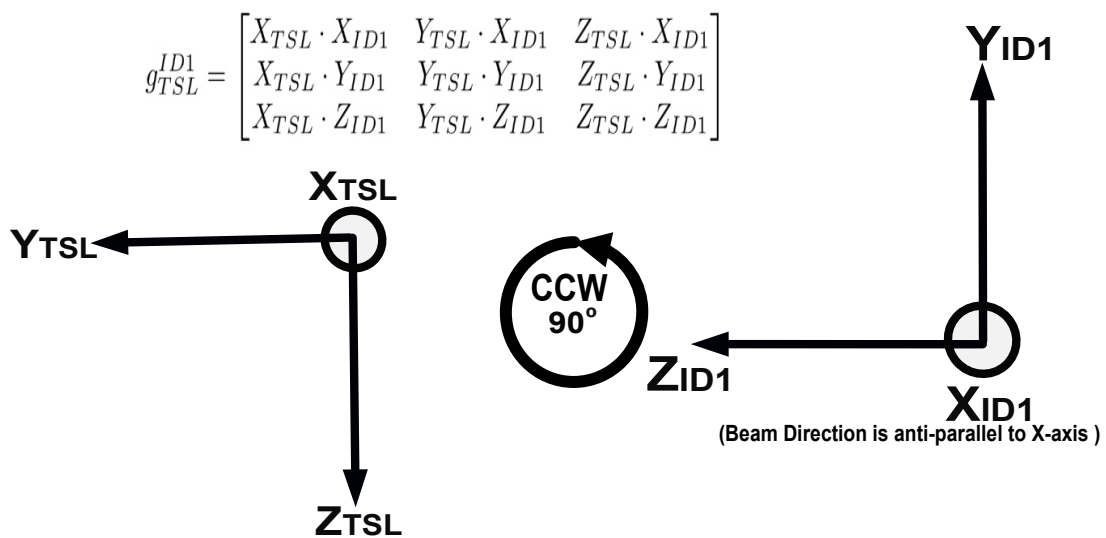


Figure H.2: Schematic showing the transformation from the APS Beamline 1 Coordinate system to TSL-OIM coordinate system. The two systems can be brought into coincidence by rotating the APS system counter clockwise about the X axis by 90°. The transformation matrix (g_{TSL}^{ID1}) is calculated from the direction cosines between the two coordinate systems.

APPENDIX I

LIST OF PYTHON AND MATLAB SCRIPTS USED FOR DATA ANALYSIS

```
#Suite of functions for analyzing Data containing Spatial and
Crystallographic Orientation Information

import damask

import numpy as np

from numba import njit

from scipy import spatial

import math

from scipy import linalg as La

def COMCoords(XYZ):
    """Find the geometric mean COM from a list of coordinates"""
    Xmean=XYZ[:,0].mean()
    Ymean=XYZ[:,1].mean()
    Zmean=XYZ[:,2].mean()
    return np.array([Xmean,Ymean,Zmean])

def AxisRotMat(RotString,Angle):
    """Function to generate rotation matrix: given
    rotation angle in degrees (+ve for CCW, -ve for CW),
    string specifying rotation axis"""
    Ang=np.radians(Angle)
    sA=np.sin(Ang)
    cA=np.cos(Ang)
    if RotString=='X' or RotString=='x':
```

```

    R=np.array([[1.,0.,0.],[0.,cA,-sA],[0.,sA,cA]])
elif RotString=='Y' or RotString=='y':
    R=np.array([[cA,0.,sA],[0.,1.,0.],[-sA,0.,cA]])
else:
    R=np.array([[cA,-sA,0.],[sA,cA,0.],[0.,0.,1.]])
return R

```

```

def AvgOrientation(EulerList,unit='radians'):
    """Function to determine average orientation given list of
    Bunge Euler angles (nx3 numpy array)
    in radians (default).The orientations input must be reduced to
    fundamental zone apriori.
    Based on Cho,Rollett and Oh,
    Metallurgical and Materials Transactions A,
    Volume 36A,3427-3438,December 2005 """
    if unit=='radians':
        eulerList=EulerList
    else:
        eulerList=EulerList*np.pi/180.
    QuatList=damask.Rotation.from_Euler_angles(eulerList).as_quaternion()
    QuatAvg=np.array([np.sum(QuatList[:,0]),np.sum(QuatList[:,1]),\
                    np.sum(QuatList[:,2]),np.sum(QuatList[:,3])])
    QuatAvg/=La.norm(QuatAvg)
    return QuatAvg

```

@njit

```

def OrMat(Euler):
    """Function to calculate orientation matrix
    given Bunge Euler Angles in degrees"""
    sphi1=np.sin(np.deg2rad(Euler[0]))
    sphi=np.sin(np.deg2rad(Euler[1]))
    sphi2=np.sin(np.deg2rad(Euler[2]))
    cphi1=np.cos(np.deg2rad(Euler[0])),
    cphi=np.cos(np.deg2rad(Euler[1]))
    cphi2=np.cos(np.deg2rad(Euler[2]))
    gphi1=np.array([[cphi1,sphi1,0.],[-sphi1,cphi1,0.],[0.,0.,1.]])
    gphi=np.array([[1.,0.,0.],[0.,cphi,sphi],[0.,-sphi,cphi]])
    gphi2=np.array([[cphi2,sphi2,0.],[-sphi2,cphi2,0.],[0.,0.,1.]])
    g=np.dot(gphi,gphi1)
    g=np.dot(gphi2,g)
    return g

```

@njit

```

def HexSymm(g):
    """Function to generate hexagonal symmetry operators
    given orientation matrix"""
    # 12 Symmetry Operation Matrices for hcp systems:
    #Adapted from Hagege et al. 1980
    S01=np.array([[1.,0.,0.],[0.,1.,0.],[0.,0.,1.]])
    S02=np.array([[0.5,0.866,0.],[-0.866,0.5,0.],[0.,0.,1.]])
    S03=np.array([[-0.5,0.866,0.],[-0.866,-0.5,0.],[0.,0.,1.]])
    S04=np.array([[-1.,0.,0.],[0.,-1.,0.],[0.,0.,1.]])
    S05=np.array([[-0.5,-0.866,0.],[0.866,-0.5,0.],[0.,0.,1.]])

```

```

S06=np.array([[0.5,-0.866,0.],[0.866,0.5,0.],[0.,0.,1.]])
S07=np.array([[1.,0.,0.],[0.,-1.,0.],[0.,0.,-1.]])
S08=np.array([[0.5,0.866,0.],[0.866,-0.5,0.],[0.,0.,-1.]])
S09=np.array([[-0.5,0.866,0.],[0.866,0.5,0.],[0.,0.,-1.]])
S10=np.array([[-1.,0.,0.],[0.,1.,0.],[0.,0.,-1.]])
S11=np.array([[-0.5,-0.866,0.],[-0.866,0.5,0.],[0.,0.,-1.]])
S12=np.array([[0.5,-0.866,0.],[-0.866,-0.5,0.],[0.,0.,-1.]])
GMat=np.zeros((12,3,3))

GMat[0,:,:]=np.dot(S01,g)
GMat[1,:,:]=np.dot(S02,g)
GMat[2,:,:]=np.dot(S03,g)
GMat[3,:,:]=np.dot(S04,g)
GMat[4,:,:]=np.dot(S05,g)
GMat[5,:,:]=np.dot(S06,g)
GMat[6,:,:]=np.dot(S07,g)
GMat[7,:,:]=np.dot(S08,g)
GMat[8,:,:]=np.dot(S09,g)
GMat[9,:,:]=np.dot(S10,g)
GMat[10,:,:]=np.dot(S11,g)
GMat[11,:,:]=np.dot(S12,g)

return GMat

```

```
@njit
```

```
def HexMisor(Euler1,Euler2):
```

```
    """Function to calculate misorientation between two hcp
```

```

orientations; given
their Bunge Euler Angles in degrees""""
g1=OrMat(Euler1)
g2=OrMat(Euler2)
g=np.dot(g1,g2.T)
GM=HexSymm(g)
Ang=np.zeros((12,)) # Initialization of Angle Array
# Rounding to 2 Decimal places is done in
#order to ensure
#that values stay within [-1,1] interval!
Ang[0]=(GM[0,0,0]+GM[0,1,1]+GM[0,2,2]-1.)*0.5
Ang[1]=(GM[1,0,0]+GM[1,1,1]+GM[1,2,2]-1.)*0.5
Ang[2]=(GM[2,0,0]+GM[2,1,1]+GM[2,2,2]-1.)*0.5
Ang[3]=(GM[3,0,0]+GM[3,1,1]+GM[3,2,2]-1.)*0.5
Ang[4]=(GM[4,0,0]+GM[4,1,1]+GM[4,2,2]-1.)*0.5
Ang[5]=(GM[5,0,0]+GM[5,1,1]+GM[5,2,2]-1.)*0.5
Ang[6]=(GM[6,0,0]+GM[6,1,1]+GM[6,2,2]-1.)*0.5
Ang[7]=(GM[7,0,0]+GM[7,1,1]+GM[7,2,2]-1.)*0.5
Ang[8]=(GM[8,0,0]+GM[8,1,1]+GM[8,2,2]-1.)*0.5
Ang[9]=(GM[9,0,0]+GM[9,1,1]+GM[9,2,2]-1.)*0.5
Ang[10]=(GM[10,0,0]+GM[10,1,1]+GM[10,2,2]-1.)*0.5
Ang[11]=(GM[11,0,0]+GM[11,1,1]+GM[11,2,2]-1.)*0.5

for i in range(len(Ang)):
    if Ang[i]>1:
        Ang[i]=0.9999999999999999
    elif Ang[i]<-1:

```

```
Ang[i]=round(Ang[i],2)
```

```
return min(np.arccos(Ang)*180./np.pi)
```

```
@jit
```

```
def Euclidean(Coord1,Coord2,Dim3D=True):
```

```
    """Function to return Euclidean distance  
    between two points given coords in 2D or 3D"""
```

```
    if Dim3D:
```

```
        Euc=(Coord1[0]-Coord2[0])**2+(Coord1[1]-Coord2[1])**2+\  
            (Coord1[2]-Coord2[2])**2
```

```
    else:
```

```
        Euc=(Coord1[0]-Coord2[0])**2+(Coord1[1]-Coord2[1])**2
```

```
    return np.sqrt(Euc)
```

```
@jit
```

```
def MisOrList(Euler,EulerList,XYZ,XYZList):
```

```
    MisOr=np.empty((EulerList.shape[0],))
```

```
    EucDist=np.empty((XYZList.shape[0],))
```

```
    for i,j in enumerate(EulerList):
```

```
        MisOr[i]=HexMisor(Euler,j)
```

```
        EucDist[i]=Euclidean(XYZ,XYZList[i,:])
```

```
    return MisOr,EucDist
```

```

@njit
def MisOrIndexList(VoxelNum,CoordList,EulerList,Dim=False):
    """Calculates misorientation of a list of voxels w.r.t
        a given voxel and
        returns a nx3 array:
        (0th col: VoxelNumber, 1st col: misorientation,
        2nd col: Euclidean distance)"""
    EulerRef=EulerList[VoxelNum,:]
    CoordRef=CoordList[VoxelNum,:]
    MisOrList=np.empty((EulerList.shape[0],3))
    for i,j in enumerate(EulerList):
        MisOrList[i,0]=i
        MisOrList[i,1]=HexMisor(EulerRef,j)
        MisOrList[i,2]=Euclidean(CoordRef,CoordList[i,:],Dim3D=Dim)
    return MisOrList

```

```

@njit
def MisOr(Ang,AngList,Tol=5):
    """Returns array of misorientations given an Euler angle
    in degrees and list of EulerAngles below tolerance"""
    Misor=np.empty((AngList.shape[0],))
    for i,j in enumerate(AngList):
        Misor[i]=HexMisor(j,Ang)
    I=np.where(Misor<=Tol)[0]
    return I

```

```

def ReduceOr(OrList,degrees=True,lattice='hP'):

```

```

"""Function to reduce list of orientations to fundamental zone.
Returns list of orientations
in terms of Bunge Euler angles in degrees"""
if degrees==True:
    Angs=OrList
else:
    Angs=np.degrees(OrList)
#Convert Euler angles to orientation matrices
gMat=np.empty((Angs.shape[0],3,3))
for i in range(Angs.shape[0]):
    gMat[i,:,:]=OrMat(Angs[i,:])
#Change orientation matrices to quaternion
Quat=damask.Rotation.from_matrix(gMat).
                                as_quaternion()
AvgOr=damask.Orientation(Quat,lattice=lattice)
Arr=np.array(AvgOr.reduced) #Reduce orientations to fundamental zone
Angs=damask.Rotation.from_quaternion(Arr).
                                as_Euler_angles(degrees=True)

return Angs

```

```

def AverageOr(OrList,degrees=True,lattice='hP'):
    """Function to calculate average orientation (Bunge Euler angles),
    given list of Euler angles (numpy array)"""
    if degrees==True:
        Angs=OrList
    else:

```

```

    Angs=np.degrees(OrList)
#Convert Euler angles to orientation matrices
gMat=np.empty((Angs.shape[0],3,3))
for i in range(Angs.shape[0]):
    gMat[i,:,:]=OrMat(Angs[i,:])
#Change orientation matrices to quaternion
Quat=damask.Rotation.from_matrix(gMat).
        as_quaternion()
AvgOr=damask.Orientation(Quat,lattice=lattice) #
Arr=np.array(AvgOr.reduced) #Reduce orientations to fundamental zone
Q=damask.Rotation.from_quaternion(Arr).average()
return Q.as_Euler_angles(degrees=True)

```

```
@njit
```

```

def gMatList(OrList,degrees=True):
    """Function to calculate equivalent rotation
    matrices given list of orientations"""
    if degrees==True:
        EulerList=OrList
    else:
        EulerList=np.degrees(OrList)
    gMat=np.empty((EulerList.shape[0],3,3))
    for i in range(EulerList.shape[0]):
        gMat[i,:,:]=OrMat(EulerList[i,:])
    return gMat

```

```
def Euclid(p,Lp):
```

```

"""Method to calculate Euclidean distance between a given point and
a list of neighboring points in 3dimensions."""

```

```

Euc=[math.sqrt((p[0]-i[0])**2+(p[1]-i[1])**2+\
              (p[2]-i[2])**2) for i in Lp]

```

```

return Euc

```

```

def KDTreeNN(Coords,VoxelNum,r=2,Print=False):

```

```

"""Function to perform nearest neighbor search for
a chosen voxel and output
the voxel numbers coordinates for streak analysis
Print option included for output arguments <False>"""

```

```

L=Coords.shape[0]

```

```

tree=spatial.cKDTree(Coords)

```

```

idx = tree.query_ball_point(Coords[VoxelNum,:],r)

```

```

E=Euclid(Coords[VoxelNum:],Coords[idx,:])

```

```

E=np.asarray(E)

```

```

E=E.reshape(len(E),1)

```

```

idx=np.asarray(idx)

```

```

idx=idx.reshape(len(idx),1)

```

```

C=np.hstack((idx,E))

```

```

C = C[C[:,1].argsort()] #Sorting by Euclidean Distance

```

```

IdxSorted=C[:,0].astype(int)

#Optional print arguments
if Print:
    print("Total number of Voxels in this file\n")
    print(L)
    print("Coords[IdxSorted]\n")
    print (Coords[IdxSorted])
    print("idx\n")
    print(idx)
    print("VoxelIndex  Euclidean Dist\n")
    print(C)
    print("IdxSorted\n")
    print (IdxSorted)

    return IdxSorted

#####
#Code to reduce NF HEDM Data to Centroids:
#This is pre-processing step prior to
#comparison with FF HEDM Data

import damask
import numpy as np
import pyvista as pv
from scipy import spatial
import math

```

```

from scipy import linalg as La
#Load NF HEDM Orientation and spatial data
Arr=np.loadtxt('NFAffine25CWXDownData.txt')
print(Arr.shape)
CoordsAll=Arr[:, :3]
EulerAngsAll=Arr[:, 3:6]
print(EulerAngsAll.shape)
#####
#-----
#Specify ball radius
Radius=160
#Immutable list of all voxels
AllIndices=np.arange(CoordsAll.shape[0]).
                astype(int)
#Mutable list (Starts same as AllIndices)
IndexList=np.arange(CoordsAll.shape[0]).
                astype(int)

#1st iteration
#-----
Coords=CoordsAll[IndexList,:]
EulerList=EulerAngsAll[IndexList,:]
VoxelNum=IndexList[0]
IdxSorted= KDTreeNN(Coords,VoxelNum,r=Radius,Print=True)
#Further pruning the NN list on the basis of
#given misorientation tolerance
AngList=EulerList[IdxSorted,:]

```

```

MO=MisOr(AngList[0, :], AngList, Tol=5)
print(MO)
print(MO.shape)
Ids=IdxSorted[MO]
print(Ids)
#####
CC=Coords[Ids, :]
print(CC.shape[0])
#####
KK=np.isin(Coords.sum(axis=1), CC.sum(axis=1))
print(KK.shape)
Inds=np.where(KK==False)[0]
print(Inds.shape)

#####
#Lists to store average centers of mass,
#grain size (number of voxels) and avg orientation information!
COMList=[]
EulerMeanList=[]
NumVoxList=[]
COMList.append(COMCoords(CC)) #Avg Center-of-Mass
EulerMeanList.append(AverageOr(AngList[MO, :])) #Avg orientation
NumVoxList.append(CC.shape[0]) #Number of voxels per grain
#-----
#Ready for next iteration
Coords=Coords[Inds, :]
print(Coords.shape)

```

```

EulerList=EulerAngsAll[Inds,:]
print(EulerList.shape)
#-----
count=1
while np.size(Coords)>0:
    IndexList=np.arange(Coords.shape[0]).astype(int)
    print(IndexList.shape[0])
    VoxelNum=IndexList.min()
    IdxSorted= KDTreeNN(Coords,VoxelNum,r=Radius,Print=True)
    print(IdxSorted)
    print(IndexList[IdxSorted])
    #Further pruning the NN list on the basis of
    #given misorientation tolerance
    AngList=EulerList[IdxSorted,:]
    MO=MisOr(AngList[0,:],AngList,Tol=5)
    print(MO)
    print(MO.shape)
    Ids=IdxSorted[MO]
    print(Ids)
    CC=Coords[Ids,:]
    KK=np.isin(Coords.sum(axis=1),CC.sum(axis=1))
    print(KK.shape)
    Inds=np.where(KK==False)[0]
    print(Inds.shape)
    Coords=Coords[Inds,:] #Ready for next iteration
    print(Coords.shape)
    EulerList=EulerList[Inds,:]

```

```

print(EulerList.shape)
COMList.append(COMCoords(CC))
EulerMeanList.append(AverageOr(AngList[M0,:])) #Avg orientation
NumVoxList.append(CC.shape[0]) #Number of voxels per grain
count+=1
print(count)
KK=AngList[M0,:]
print('Count {}, Misor {}'.\
      format(count-1,HexMisor\ (EulerMeanList[count-1],KK[-1])))

print(count)
#####
#Class to Perform Comparison analysis between kinematic and
#local stress descriptions in FF HEDM dataset (Chapter 6)
import os
import plotly.express as px
import damask
import pandas as pd
import numpy as np
from scipy import linalg as La

class FFHEDMQuality:

    def __init__(self,RSSArr,n,LoadStep,EulerArr):
        self.RSSArr=RSSArr
        self.n=n

```

```

self.LoadStep=LoadStep
self.EulerArr=EulerArr

def VecToTens(self,STensVec):
    """Method to convert 6 component stress
    vector into 3x3 symmetric tensor"""
    self.STensVec=STensVec
    Tens=np.zeros((3,3))
    Tens[0,0],Tens[1,1],Tens[2,2]=STensVec[0],STensVec[1],STensVec[2]
    Tens[1,0],Tens[0,2],Tens[2,1]=STensVec[5],STensVec[4],STensVec[3]
    Tens[0,1],Tens[2,0],Tens[1,2]=Tens[1,0],Tens[0,2],Tens[2,1]
    return Tens

def BlendAxes(self,maxangle,a,b,DirArr,Nmix=10,degrees=True):
    self.maxangle=maxangle
    self.a=a
    self.b=b
    self.DirArr=DirArr
    self.Nmix=Nmix
    self.degrees=degrees
    if degrees==True:
        maxang=np.radians(5)
    else:
        maxang=maxangle
    Stereomixaxes = np.zeros((Nmix,2))
    mixaxes = np.zeros((Nmix,3))
    blend = np.linspace(0,maxang,Nmix)

```

```

blendRev=np.zeros((blend.shape[0],))
blendFrac=np.zeros((blend.shape[0],))
for i in range(Nmix):
    Stereomixaxes[i] = damask.util.project_stereographic((
        damask.Rotation.from_axis_angle\
        (list(self.DirArr[self.a])+\
        [blend[i]],normalize=True) *
        damask.Rotation.from_axis_angle\
        (list(self.DirArr[self.b])+\
        [blend[Nmix-i-1]],normalize=True)).\
        as_axis_angle(pair=True)[0])
    mixaxes[i]=(damask.Rotation.from_axis_angle\
    (list(self.DirArr[self.a])+[blend[i]],normalize=True) *
        damask.Rotation.from_axis_angle\
        (list(self.DirArr[self.b])+\
        [blend[Nmix-i-1]],normalize=True)
    ).as_axis_angle(pair=True)[0]
    blendRev[i]=blend[Nmix-i-1]
    blendFrac[i]=blend[i]/(blend[i]+blendRev[i])
return mixaxes,Stereomixaxes,blendFrac

```

```

def SlipDirPlane(self,SlipSysNum,lattice='hP',c=1.58):
    self.SlipSysNum=SlipSysNum
    c=damask.Crystal(lattice='hP',c=1.58)
    k = c.kinematics('slip')
    b=k['direction'][self.SlipSysNum]
    n=k['plane'][self.SlipSysNum]

```

```

return b,n

def SchmidFactor(self,STens,n,b):
    """Method to calculate Schmid factor given
    3x3 symmetric tensor, slip plane normal (n)
    and slip direction"""
    self.STens=STens
    self.n=n
    self.b=b
    STensN=self.STens/La.norm(self.STens)
    nNorm=self.n/La.norm(self.n)
    bNorm=self.b/La.norm(self.b)
    #Tensordot can be used to obtain same result
    SF = np.einsum('ij,i,j',\
        STensN,bNorm,nNorm)
    return SF

def ColorString(self,RGBArr,print=False):
    """Method to generate plotly compatible color string,
    given list of colors as an nx3 array of RGB values"""
    self.RGBArr=RGBArr
    self.print=print
    CL=[]
    for i in self.RGBArr:
        rgb=tuple(int(x) for x in i[0:3])
        rgba='rgb'+str(rgb)
        CL.append(rgba)

```

```

    if self.print==True:
        print(CL)
    return CL

def StereoSlipAxes(self,systemNum,nSlip,SFList):
    """Function to generate 3D Axis and 2D
    stereographic coordinates for a given
    category of slip systems for hcp
    system: category of slip system
    (0: basal, 1: prism<a>, 2: 2nd order prism, 3: pyramidal<a>,
    4:pyramidal<c+a>)
    nSlip: number of slip systems in given category
    SF:Schmid factor
    (sgn(SF)is multiplied to bxn to obtain slip
    system reorientation axis)"""
    self.systemNum=systemNum
    self.nSlip=nSlip
    self.SFList=SFList
    c=damask.Crystal(lattice='hP',c=1.58)
    k = c.kinematics('slip')
    LineDir=np.zeros((self.nSlip,3))
    axes = np.zeros((len(k['direction'])[self.systemNum]),2))
    for i,(m,n) in enumerate(zip(k['direction']\
    [self.systemNum],k['plane'][self.systemNum])):
        axes[i] = damask.util.project_stereographic\
        (np.sign(self.SFList[i])*np.cross\
        (c.to_frame(uvw=m),c.to_frame(hkl=n)))

```

```

        LineDir[i,:]=np.sign(self.SFList[i])*\
        np.cross(c.to_frame(uvw=m),c.to_frame(hkl=n))
        LineDir[i,:]=LineDir[i,:]/La.norm(LineDir[i,:])

    return LineDir,axes

def CollectSlipSys(self,nBasal,nPrism,nPyrca,mBasal,mPrism,mPyrca):
    """Accumulates the slip plane normals
    and slip directions for basal,prism<a>
    and pyramidal<c+a> in that order"""
    self.nBasal=nBasal
    self.nPrism=nPrism
    self.nPyrca=nPyrca
    self.mBasal=mBasal
    self.mPrism=mPrism
    self.mPyrca=mPyrca
    nAll=np.vstack((self.nBasal,self.nPrism,self.nPyrca))
    mAll=np.vstack((self.mBasal,self.mPrism,self.mPyrca))
    return nAll,mAll

def CollectSlipAxes(self,LineDirBasal,\
StereoBasal,LineDirPrism,StereoPrism,LineDirPyrca,StereoPyrca):
    """Accumulates the line directions for
    basal,prism<a> and pyramidal<c+a> in that order"""
    self.LineDirBasal=LineDirBasal
    self.LineDirPrism=LineDirPrism
    self.LineDirPyrca=LineDirPyrca

```

```

self.StereoBasal=StereoBasal
self.StereoPrism=StereoPrism
self.StereoPyrca=StereoPyrca
StereoAll=np.vstack((self.StereoBasal,\
self.StereoPrism,self.StereoPyrca))
LineDirAll=np.vstack((self.LineDirBasal,\
self.LineDirPrism,self.LineDirPyrca))
return LineDirAll,StereoAll

```

```

def StereoAxis(self,OrList,n):
    self.OrList=OrList
    self.n=n
    N=self.OrList.shape[0]
    Axis=np.zeros((N,3))
    AxisStereo=np.zeros((N,2))
    for i in range(n,N-n):
        Axis[i,:]=damask.Orientation.from_Euler_angles\
(phi=self.OrList[i-self.n,:],
                                degrees=True,family='hexagonal')\
        .misorientation\
        (damask.Orientation.\
        from_Euler_angles\
        (phi=self.OrList[i+n,:],degrees=True,family='hexagonal'))\
        .as_axis_angle(pair=True)[0]

    AxisStereo[i,:]=damask.util.project_stereographic(Axis[i,:])

```

```

return Axis[self.n:N-n,:],AxisStereo[self.n:N-n,:]

def TopTwoRSSMag(self,RSSArr,LoadStep):
    """Return the indices of the two highest stressed slip systems"""
    self.RSSArr=RSSArr
    self.LoadStep=LoadStep
    AbsRSSA=np.abs(self.RSSArr)
    q=2
    idx = np.argpartition(AbsRSSA[self.LoadStep], -q)[-q:]
    indices = idx[np.argsort((-AbsRSSA[self.LoadStep])[idx])]
    return indices

def MaxRSS(self,RSSArr,LoadStep,print=False):
    """Given a load step and the full RSS array, finds the Slip system
    numbers with the highest magnitude for that loadstep"""
    self.RSSArr=RSSArr
    self.LoadStep=LoadStep
    self.print=print
    Basal=np.abs(self.RSSArr[self.LoadStep,:3])
    Prism=np.abs(self.RSSArr[self.LoadStep,3:6])
    Pyrca=np.abs(self.RSSArr[self.LoadStep,6:])
    MaxBasal=np.where(Basal==Basal.max())[0][0]
    MaxPrism=np.where(Prism==Prism.max())[0][0]
    MaxPyrca=np.where(Pyrca==Pyrca.max())[0][0]
    if self.print==True:

```

```

    print('MaxPrism={}'.format(MaxPrism))
    print('MaxBasal={}'.format(MaxBasal))
    print('MaxPyrca={}'.format(MaxPyrca))
return MaxBasal,MaxPrism,MaxPyrca

```

```

def VecBlender(self,a,b,LineDirA,LineDirB,misor=5,Nmix=10):
    self.misor=misor
    self.Nmix=Nmix
    maxangle = np.radians(self.misor)
    self.a=a
    self.b=b
    self.LineDirA=LineDirA
    self.LineDirB=LineDirB
    mixaxes = np.zeros((self.Nmix,2))
    mixVec=np.zeros((self.Nmix,3))
    blend = np.linspace(0,maxangle,Nmix)
    N=blend.shape[0]
    for i in range(self.Nmix):
        mixVec[i]=(damask.Rotation.from_axis_angle\
        (list(self.LineDirA[self.a])+[blend[1]],normalize=True) *
        damask.Rotation.\
        from_axis_angle(list(self.LineDirB[self.b])+
        [blend[1]],normalize=True)
        ).as_axis_angle(pair=True)[0]
        mixaxes[i] = damask.util.project_stereographic((
        damask.Rotation.\

```

```

        from_axis_angle(list(self.LineDirA[self.a])\
+[blend[1]],normalize=True) *
        damask.Rotation.\
        from_axis_angle(list(self.LineDirB[self.b])\
+[blend[1]],normalize=True)
    ).as_axis_angle(pair=True)[0])
return mixVec,mixaxes

```

```

def StereoPlotter(self,rPrism,rBasal,rPyrca,\
    axesPyrca,axesP,axesB,mixaxes,CL,AxisStereo,AnnStr):
    self.rPrism=rPrism
    self.rBasal=rBasal
    self.axesPyrca=axesPyrca
    self.axesP=axesP
    self.axesB=axesB
    self.mixaxes=mixaxes
    self.CL=CL
    self.AxisStereo=AxisStereo
    N=self.AxisStereo.shape[0]

    df=pd.DataFrame(dict(x=self.axesPyrca[:,0],
        y=self.axesPyrca[:,1],
        size=15*rPyrca/rPyrca.max(),
        level=self.CL))

    df1=pd.DataFrame(dict(x=self.AxisStereo[:,0],

```

```

        y=self.AxisStereo[:,1],
        S=10,
        level=range(self.AxisStereo.shape[0]))))

cir=np.linspace(0,2*np.pi,1000)

L=list(range(N))
#Pyramidal <c+a> slip
p=px.scatter(df,
             x='x',
             y='y',
             color='level',
             size='size',
             color_discrete_map='identity',
             range_x=[-1.2,1.2],
             range_y=[-1.2,1.2],
             width=400,
             height=370)
#title=AnnStr)

#Prism <a> slip (red markers)
p.add_scatter(x=axesP[:,0],
             y=self.axesP[:,1],
             marker=dict(size=15*rPrism/rPrism.max(),\
             color="rgb(255,0,0)"),

```

```

        mode='markers')
#Basal <a> slip (sky blue markers)
p.add_scatter(x=self.axesB[:,0],
             y=axesB[:,1],
             marker=dict(size=15*rBasal/rBasal.max(),\
                        color="rgb(135,206,235)"),
             mode='markers')

p.add_scatter(x=self.mixaxes[[0,-1],0],
             y=self.mixaxes[[0,-1],1],
             marker=dict(size=4,color="rgb(0,0,255)"),
             mode='lines')

#p.update_traces(marker={'size': 10})

p.add_scatter(x=self.AxisStereo[:,0],
             y=self.AxisStereo[:,1],
             marker=dict(size=10, color=L,colorscale='greys'),
             mode='markers')

```

```

p.add_scatter(x=np.cos(cir),
              y=np.sin(cir),
              marker=dict(size=1,color="rgb(0,0,0)"),
              mode='markers')

```

```

p.update(layout_showlegend=False)
p.show()
return p

```

```
#####
```

```

#Script for matching FF data with NF data based on
#Orientation threshold and Euclidean ball radius specified
#Reverse algorithm

```

```
import os
```

```
import numpy as np
```

```
import damask
```

```
#NFEulerAngs=np.loadtxt('NFReducedEulerAngs.txt')
```

```
NFCoords=np.loadtxt('NFReducedCoords.txt')
```

```
FFDataPath='/Users/harshaphukan/Desktop/Dissertation/NFFFMatching/'
```

```
FFDataFileName='FFReducedRotated.txt'
```

```
FFData=np.loadtxt(os.path.join(FFDataPath,FFDataFileName))
```

```
FFCoords=FFData[:, :3]
```

```
FFEulerAngs=FFData[:, 3:6]
```

```
NFEulerAngsRot=np.loadtxt('NFEulerAngsRot.txt')
```

```

FFIndexList=range(FFCoords.shape[0])

MisOrTol=5
EucTol=1500
#Immutable list of all voxels (Near Field dataset)
AllIndicesNF=np.arange(NFCoords.shape[0]).astype(int)
# mutable number of voxels in Near Field
#Dataset (starts same as AllIndicesNF)
NFIndexList=np.arange(NFCoords.shape[0]).astype(int)

#Initialize list of Near field coordinates and Euler angles
NFCoordList=NFCoords
NFAngList=NFEulerAngsRot

MatchList=[]
NFMatchCoords=[]

for ii in FFIndexList:
    TempCoords=np.vstack((FFCoords[ii,:],NFCoordList))
    IdSorted,EucDist=KDTreeNN(TempCoords,0,r=EucTol,Print=True)
    Ids=IdSorted[1:]-1
    print(IdS)
    MisOrient=np.empty((Ids.shape[0],))
    for i,j in enumerate(IdS):
        MisOrient[i]=HexMisor(FFEulerAngs[ii,:],NFAngList[j,:])
    print(MisOrient)

```

```

I=np.where(MisOrient<=MisOrTol)
print(I[0])
L=len(I[0])
print(np.size(I[0]))
print(Ids[I[0]])
print(EucDist[I[0]+1])
print(MisOrient[I[0]])

if np.size(I[0])>0:
    HArr=np.hstack((Ids[I[0]].reshape(L,1),EucDist[I[0]+1]\
        .reshape(L,1),MisOrient[I[0]].reshape(L,1)))
    print(HArr)

    H=HArr[0,:]
    H=np.hstack((ii,H))
    MinIndex=H[1].astype(int)
    print(MinIndex)
    CC=NFCoordList[MinIndex,:]
    print(CC)
    #Remove voxel from NF datalist
    KK=np.isin(NFCoordList.sum(axis=1),CC.sum())
    print(KK.shape)
    Inds=np.where(KK==False)[0]
    print(Inds.shape)
    NFCoordList=NFCoordList[Inds,:]
    NFAngList=NFAngList[Inds,:]

```

```

MatchList.append(H)
NFMatchCoords.append(CC)

print("Voxel {},Coords {} FF: Coords {} NF".\
      format(ii,FFCoords[ii,:],CC))

MatchList=np.array(MatchList)
Euc=np.array(MatchList[:,-2])
print(MatchList)
#####

%{
MatLab Function to output grain positions, crystallographic
orientations and averaged stress tensors of indexed grains
from FF HEDM data: Takes the .log and g vector files as input
%}

% Note that the Euler angles are corrected by adding 30-degrees to phi2 in
% the Result

function [GrainArray]=LoadDataSameDir(FilePath,LogFile)
%Routine to extract strain/stress tensors and positional data of grains
%from .gve and .log file. Developed by Beaudoin and Wang: Uses least
%squaresapproach proposed by Marguiles et al. [2002]

fPrefixGVE=FilePath;%input('Type in path for .gve file:', 's');
fPrefixLOG=FilePath;%input('Type in path for .log file:', 's');

```

```

file_nameLog=LogFile;%input('Enter log filename, e.g xyz.log:', 's');
log_data=loadGrainSpotterLog(file_nameLog, fPrefixLOG);

S1=strsplit(file_nameLog, '_');
file_nameGVE=strcat(S1{1}, '_', S1{2}, '_', S1{3}, '.gve');...
        %input('Enter GVE filename, e.g xyz.gve:', 's');

fPostfix = '';
[name, ext]=fileparts(file_nameLog);
logStem=strtok(ext, '_');
fLogStem=strcat(logStem, '_', '00');

fGVEstem=fLogStem;

[nameG, extG]=fileparts(file_nameGVE);

[a, fPostfixGVE]=strtok(extG, 't');
fPostfixGVE=strcat('_', fPostfixGVE);

[b, fPostfixLOG]=strtok(ext, 't');
fPostfixLOG=strcat('_', fPostfixLOG);

N_grain=length(log_data);

```

```

%% This part extracts the Image Number from the .log filename
if length(ext)==22
    Image_string=strcat(ext(9),ext(10),ext(11));
elseif length(ext)==21
    Image_string=strcat(ext(8),ext(9),ext(10));
else
    print('Please rename your .log and .gve files to ...
    fit the compatible format.\n')
end
if Image_string(1)=='0'
    ImageString=strcat(Image_string(2),Image_string(3));
else
    ImageString=Image_string;
end

Image_number=str2num(ImageString);

scanNo = Image_number*ones(N_grain,1);

grainNo = 1:N_grain;

strain=zeros(3,3);

[g0Cry, g_idl] = g0hcp(2.95, 4.683); % New parameter

```

```

g_ideal = g_idl;
EulerAng=zeros(length(scanNo),3);
GrainArray=zeros(length(scanNo),12);

for scan = 1 : length(scanNo)

    filelog = parseGrainSpotterLog([fPrefixLOG fLogStem num2str...
        (scanNo(scan)) fPostfixLOG '.log']); % fPostfix '.log'];

    % Read the corresponding Fable g-vector file

    peaks_gve_dat = loadGVE([fPrefixGVE fGVEstem ...
        num2str(scanNo(scan)) fPostfixGVE '.gve']);

    % find g-vectors for grains in the log file,
    %using indices to the g-vector file

    clear strn stddevs

    igrain = 0;

    for ig=grainNo(scan):grainNo(scan)

        igrain = igrain + 1;

```

```

clear gve gveID A B hkl2_
% Find the number of g-vectors in the log file
Ngvec = length(filelog(ig).refl...
              (:,1));

cnt = 0;
for i=1:Ngvec
    % Only include if below some threshold internal angle
    if filelog(ig).refl(i,22)...
        < 2.0
        cnt = cnt+1;
        gveID(cnt) = find(peaks_gve_dat(:,9)==...
                        filelog(ig).refl(i,3));

% The measured 2-theta, omega and eta for this g-vector
        toe(cnt,:) = filelog(ig).refl(i,[13 16 19]);

        hklS(cnt, :) = filelog(ig).refl(i,4:6);

    end
end
Ngvec = cnt;

% Load in the g-vector and it's norm (or 1/d-spacing)
gve = peaks_gve_dat(gveID,[1:3 6]);

% The following was a check, to make certain that we did not have

```

```

% Friedel pairs
% close(1)
%figure(1)
%plot(gve(:,2),gve(:,3),'+')
%hold on
%plot(-gve(:,2),-gve(:,3),'o');

FriedelPairs = zeros(Ngvec,1);

for i=1:Ngvec
    for j=1:Ngvec
        if i ~= j

                if isequal(hkls(i,1:3), -hkls(j,1:3))

%
                mag = (dot(a,b)/(norm(a).^2));
%
                if mag>0.998 && mag<1.001

                        FriedelPairs(i) = 1;
                        FriedelPairs(j) = 1;

                end

        end

    end

end

% FIX-UP DISTANCE
% gve = 0.999*gve;

```

```

%     idx = find(FriedelPairs==1);
%
%     [Ngvec length(idx)]
%
%     Ngvec = length(idx);
%     gve = gve(idx,:);

OutSide = zeros(Ngvec,1);
for i=1:Ngvec
    OutSide(i) = (norm(gve(i,1:3)) > 0.92)...
                & (norm(gve(i,1:3)) < 0.95) ; % 0.795;
end

idx = find(OutSide ~= 1);

[Ngvec length(idx)];

Ngvec = length(idx);
gve = gve(idx,:);

% Now, the least squares problem
%  $A \cdot X = B$ , or  $X = A \setminus B$ 

```

```

B = zeros(Ngvec,1);

for i=1:Ngvec

    % The delta spacing will be a minimum with
    %corresponding ideal hkl
    gs = norm(gve(i,1:3))-g_ideal;
    [val,midx] = min(abs(gs));
% B is the measured elastic strain for
%each reflection (i.e. g vector)
    B(i,1) = -gs(midx)/...
            g_ideal(midx);
end

for i=1:Ngvec

    % lmn is the g vector in sample coordinate system
    lmn = gve(i,1:3)/norm(gve(i,1:3));

    % new parameter
    dx_term = -( cosd(toe(i,2)) +(sind(toe(i,2))...
    *sind(toe(i,3)))/tand(toe(i,1)/1.0) )/999654.8;
    % new parameter from Ti_1516.par
    dy_term = -( sind(toe(i,2)) +(cosd(toe(i,2))...
    *sind(toe(i,3)))/...

```

```

tand(toe(i,1)/1.0) )/999654.8;

A(i,:) = [lmn(1)^2 lmn(2)^2 lmn(3)^2 2*lmn(1)*...
          lmn(2) 2*lmn(1)*lmn(3) 2*lmn(2)*...
          lmn(3) -dx_term -dy_term];

end

X =A\B; % matlab solve least square problem in one command!
%figure(4)
%plot(B-A*X);
fit_error = B - A*X;

strn(:,igrain) = A\B;
stddevs(igrain) = std(B-A*X);

% Filter results from the fit, here.
% mark's 0.8e-3)
idx = find(abs(fit_error)<0.004);...
      % .0018); % 0.8e-3);

B1 = B(idx);
A1 = A(idx,:);

```

```

    strn(:,igrain) = A1\B1;
    %figure(5)
    %plot(B1-A1*strn(:,igrain))

    stddevs(igrain) = std(B1-A1*strn(:,igrain));

    %pause
end

Rowstrn(scan,:)=strn'; % display strain and position for all grains
%Strain tensor calculation
strain(1,1)=strn(1);
strain(2,2)=strn(2);
strain(3,3)=strn(3);
strain(1,2)=strn(4);
strain(2,1)=strn(4);strain(1,3)=strn(5);
strain(3,1)=strn(5);strain(2,3)=strn(6);strain(3,2)=strn(6);

% 90 deg rotation
filelog(ig).U=filelog(ig).U*[0 -1 0;1 0 0;0 0 1];
% strain tensor in crystal coordinate,
%filelog(ig).U is the R matrix of the grain
strain_c(:,:)=filelog(ig).U'*...
        strain(:,:,igrain)*filelog(ig).U;
% stiffness tensor of Ti
C=[162.4e3,  92e3,  69e3,  0.0,  0.0,  0.0;
   92e3, 162.2e3,  69e3,  0.0,  0.0,  0.0;

```

```

69e3, 69e3, 181.6e3, 0.0, 0.0, 0.0;
0.0, 0.0, 0.0, 47.2e3, 0.0, 0.0;
0.0, 0.0, 0.0, 0.0, 47.2e3, 0.0;
0.0, 0.0, 0.0,
0.0, 0.0, 35.2e3];
strain_c_vec=[strain_c(1,1), strain_c(2,2),...
              strain_c(3,3),strain_c(2,3)*2...
              ,strain_c(3,1)*2,strain_c(1,2)*2]';
% Stress in the crystal coordinate system using General Hooke's Law
stress_c_vec=C*...
              strain_c_vec;
stress_crystal(scan,:)=stress_c_vec';
stress_c=[stress_c_vec(1),stress_c_vec(6),stress_c_vec(5);
          stress_c_vec(6),stress_c_vec(2),stress_c_vec(4);
          stress_c_vec(5),stress_c_vec(4),stress_c_vec(3)];

% stress in the sample coordinate system
stress=filelog(ig).U*stress_c*...
          filelog(ig).U';
% stress in the sample coordinate system in vector form
stress_vec(scan,:)= [stress(1,1),stress(2,2),...
                    stress(3,3),stress(1,2),...
                    stress(1,3),...
                    stress(2,3)]';

```

```
EulerAng(scan,1)=log_data(scan).euler(1);  
EulerAng(scan,2)=log_data(scan).euler(2);  
EulerAng(scan,3)=log_data(scan).euler(3)+30;
```

```
GrainArray(scan,1)=scan;  
GrainArray(scan,2:3)=Rowstrn(scan,7:8);  
GrainArray(scan,4:9)=stress_vec(scan,:);  
GrainArray(scan,10:12)=EulerAng(scan,:);
```

```
end
```

```
end
```

BIBLIOGRAPHY

BIBLIOGRAPHY

- Abdolvand, H., Majkut, M., Oddershede, J., Wright, J. P., and Daymond, M. R. (2015a). Study of 3-d stress development in parent and twin pairs of a hexagonal close-packed polycrystal: Part i – in-situ three-dimensional synchrotron x-ray diffraction measurement. *Acta Materialia*, 93:246–255.
- Abdolvand, H., Majkut, M., Oddershede, J., Wright, J. P., and Daymond, M. R. (2015b). Study of 3-d stress development in parent and twin pairs of a hexagonal close-packed polycrystal: Part ii – crystal plasticity finite element modeling. *Acta Materialia*, 93:235–245.
- Akhtar, A. and Teghtsoonian, E. (1975). Prismatic slip in α -titanium single crystals. *Metallurgical and Materials Transactions A*.
- Ardeljan, M., McCabe, R. J., Beyerlein, I. J., and Knezevic, M. (2015). Explicit incorporation of deformation twins into crystal plasticity finite element models. *Computer Methods in Applied Mechanics and Engineering*, 295:396–413.
- Arsenlis, A. and Parks, D. M. (1999). Crystallographic aspects of geometrically-necessary and statistically-stored dislocation density. *Acta Materialia*, 47(5):1597–1611.
- Arul Kumar, M., Kanjarla, A. K., Niezgoda, S. R., Lebensohn, R. A., and Tomé, C. N. (2015). Numerical study of the stress state of a deformation twin in magnesium. *Acta Materialia*, 84:349–358.
- Ashby, M. F. (1970). The deformation of plastically non-homogeneous materials. *Philosophical Magazine*, 21(170):399–424.
- Aydiner, C., Bernier, J., Clausen, B., Lienert, U., Tomé, C., and Brown, D. (2009). Evolution of stress in individual grains and twins in a magnesium alloy aggregate. *Physical Review B*, 80(2).
- Beyerlein, I. J. and Tomé, C. N. (2010). A probabilistic twin nucleation model for hcp polycrystalline metals. *Proceedings of the Royal Society A*, 466(2121):2517–2544.
- Bhadeshia, H. (1996). Effect of stress & strain on formation of bainite in steels. *Canadian Institute of Mining, Minerals and Petroleum*.
- Bieler, T. R. (2014). Orientation and rotation matrix toolkit. *Class notes, Michigan State University*.
- Bieler, T. R., Alizadeh, R., Peña-Ortega, M., and Llorca, J. (2019). An analysis of (the lack of) slip transfer between near-cube oriented grains in pure al. *International Journal of Plasticity*, 118(February):269–290.

- Bieler, T. R., Eisenlohr, P., Roters, F., Kumar, D., Mason, D. E., Crimp, M. A., and Raabe, D. (2009). The role of heterogeneous deformation on damage nucleation at grain boundaries in single phase metals. *International Journal of Plasticity*, 25(9):1655–1683.
- Bieler, T. R., Wang, L., Beaudoin, A. J., Kenesei, P., and Lienert, U. (2014). In situ characterization of twin nucleation in pure ti using 3d-xrd. *Metallurgical and Materials Transactions A*, 45(1):109–122.
- Bilby, B. A. and Crocker, A. G. (1965). The theory of the crystallography of deformation twinning. *Proceedings of the Royal Society of London. Series A, Mathematical and Physical Sciences*, 288(1413):240–255.
- Britton, T. B., Dunne, F. P. E., and Wilkinson, A. J. (2015). On the mechanistic basis of deformation at the microscale in hexagonal close-packed metals. *Proceedings of the Royal Society A: Mathematical, Physical and Engineering Science*, 471(2178):20140881.
- Capolungo, L., Beyerlein, I. J., and Tomé, C. N. (2009). Slip-assisted twin growth in hexagonal close-packed metals. *Scripta Materialia*, 60(1):32–35.
- Cass, T. R. (1970). Slip modes and dislocation substructures in titanium and titanium and aluminum single crystals. In Jaffee, R. and Promisel, N., editors, *The Science, Technology and Application of Titanium*, pages 459 – 477. Pergamon.
- Cheng, J. and Ghosh, S. (2017). Crystal plasticity finite element modeling of discrete twin evolution in polycrystalline magnesium. *Journal of the Mechanics and Physics of Solids*, 99:512–538.
- Chichili, D. R., Ramesh, K. T., and Hemker, K. J. (1999). *The influence of deformation twinning on the mechanical response of alpha-titanium*. Advances in Twinning.
- Cho, J. H., Rollett, A. D., and Oh, K. H. (2005). Determination of a mean orientation in electron backscatter diffraction measurements. *Metallurgical and Materials Transactions A*, 36:3427–3438.
- Christian, J. W. and Mahajan, S. (1995). Deformation twinning. *Progress in Materials Science*, 39(1-2):1–157.
- Das, S., Hofmann, F., and Tarleton, E. (2018). Consistent determination of geometrically necessary dislocation density from simulations and experiments. *International Journal of Plasticity*, 109(April):18–42.
- Di Gioacchino, F., Edwards, T. E., Wells, G. N., and Clegg, W. J. (2020). A new mechanism of strain transfer in polycrystals. *Nature: Scientific Reports*, 10(1):1–15.
- Dieter, G. E. (2011). *Mechanical Metallurgy*. McGraw Hill.

- Eisenlohr, P., Diehl, M., Lebensohn, R., and Roters, F. (2013). A spectral method solution to crystal elasto-viscoplasticity at finite strains. *International Journal of Plasticity*, 46:37 – 53. Microstructure-based Models of Plastic Deformation.
- Eisenlohr, P., Shanthraj, P., Vande Kieft, B. R., Bieler, T. R., Liu, W., and Xu, R. (2017). Subsurface grain morphology reconstruction by differential aperture x-ray microscopy. *JOM*, 69(6):1100–1105.
- Fleck, N. A., Muller, G. M., Ashby, M. F., and Hutchinson, J. W. (1994). Strain gradient plasticity: Theory and experiment. *Acta Metallurgica Et Materialia*.
- Guan, X. X., Lu, L., Luo, S. N., and Fan, D. (2021). In situ observations of detwinning and strain localization in pure titanium. *Materials Science and Engineering A*, 813(January):1–7.
- Guo, Y., Abdolvand, H., Britton, T. B., and Wilkinson, A. J. (2017). Growth of 112-2 twins in titanium: A combined experimental and modelling investigation of the local state of deformation. *Acta Materialia*, 126:221–235.
- Guo, Y., Britton, T. B., and Wilkinson, A. J. (2014). Slip band-grain boundary interactions in commercial-purity titanium. *Acta Materialia*, 76:1–12.
- Guo, Y., Collins, D. M., Tarleton, E., Hofmann, F., Wilkinson, A. J., and Britton, T. B. (2020). Dislocation density distribution at slip band-grain boundary intersections. *Acta Materialia*.
- Han, S. and Crimp, M. A. (2020). Ecci analysis of shear accommodations at grain boundaries in commercially pure alpha titanium. *International Journal of Plasticity*, 131(March):102731.
- Hémery, S., Nizou, P., and Villechaise, P. (2018). In situ sem investigation of slip transfer in ti-6al-4v: Effect of applied stress. *Materials Science and Engineering A*, 709(October 2017):277–284.
- Huang, Z. W., Jin, S. B., Zhou, H., Li, Y. S., Cao, Y., and Zhu, Y. T. (2019). Evolution of twinning systems and variants during sequential twinning in cryo-rolled titanium. *International Journal of Plasticity*, 112(August 2018):52–67.
- Hull, D. and Bacon, D. J. (2011). *Introduction to Dislocations*. Butterworth-Heinemann.
- Ice, G. E. and Pang, J. W. L. (2009). Tutorial review: Tutorial on x-ray microprobe diffraction. *Materials Characterization*, 60(11):1191–1201.
- Joseph, S., Bantounas, I., Lindley, T. C., and Dye, D. (2018). Slip transfer and deformation structures resulting from the low cycle fatigue of near-alpha titanium alloy ti-6242si. *International Journal of Plasticity*, 100:90–103.
- Kacher, J., Eftink, B. P., Cui, B., and Robertson, I. M. (2014). Dislocation interactions with grain boundaries. *Current Opinion in Solid State and Materials Science*, 18(4):227–243.

- Kalidindi, S. R. (1998). Incorporation of deformation twinning in crystal plasticity models. *Journal of the Mechanics and Physics of Solids*, 46(2):267–271.
- Kishida, K., Kim, J. G., Nagae, T., and Inui, H. (2020). Experimental evaluation of critical resolved shear stress for the first-order pyramidal $\langle c+a \rangle$ slip in commercially pure ti by micropillar compression method. *Acta Materialia*, 196:168–174.
- Kochmann, D. M. and Le, K. C. (2009). A continuum model for initiation and evolution of deformation twinning. *Journal of the Mechanics and Physics of Solids*, 57(6):987–1002.
- Konijnenberg, P. J., Zaefferer, S., and Raabe, D. (2015). Assessment of geometrically necessary dislocation levels derived by 3d ebsd. *Acta Materialia*, 99:402–414.
- Larson, B. C., Tischler, J. Z., El-Azab, A., and Liu, W. (2008). Dislocation density tensor characterization of deformation using 3d x-ray microscopy. *J. Eng. Mater. Technol.*, 130(2):021024/1–021024/10.
- Larson, B. C., Yang, W., Ice, G. E., Budai, J. D., and Tischler, J. Z. (2002). Three-dimensional x-ray structural microscopy with submicrometer resolution. *Nature*, 415(6874):887–890.
- Lee, T. C., Robertson, I. M., and Birnbaum, H. K. (1989). Prediction of slip transfer mechanisms across grain boundaries. *Scripta Metallurgica*, 23(5):799–803.
- Levine, E. D. (1966). Deformation mechanisms in titanium at low temperatures. *AIME MET SOC TRANS*, 236(11):1558–1565.
- Li, S. F. and Suter, R. M. (2013). Adaptive reconstruction method for three-dimensional orientation imaging. *Journal of Applied Crystallography*, 46(2):512–524.
- Littlewood, P. D., Britton, T. B., and Wilkinson, A. J. (2011). Geometrically necessary dislocation density distributions in ti–6al–4v deformed in tension. *Acta Materialia*, 59(16):6489–6500.
- Livingston, J. D. and Chalmers, B. (1957). Multiple slip in bicrystal deformation. *Acta Metallurgica*, 5(6):322–327.
- Louca, K. and Abdolvand, H. (2021). Accurate determination of grain properties using three-dimensional synchrotron x-ray diffraction: A comparison with ebsd. *Materials Characterization*, 171(June 2020):110753.
- Louca, K., Abdolvand, H., Mareau, C., Majkut, M., and Wright, J. (2021). Formation and annihilation of stressed deformation twins in magnesium. *Communications Materials*, 2(1):1–11.
- Luster, J. and Morris, J. M. (1995). Compatibility of deformation in two-phase ti-al alloys: Dependence on microstructure and orientation relationships. *Metallurgical and Materials Transactions*

- A, 26(7):1745–1756.
- Lütjering, G. and Williams, J. C. (2007). *Titanium*, pages 15–52. Springer Berlin Heidelberg, Berlin, Heidelberg.
- Ma, A. and Roters, F. (2004). A constitutive model for fcc single crystals based on dislocation densities and its application to uniaxial compression of aluminium single crystals. *Acta Materialia*.
- Margulies, L., Lorentzen, T., Poulsen, H. F., and Leffers, T. (2002). Strain tensor development in a single grain in the bulk of a polycrystal under loading. *Acta Materialia*, 50(7):1771–1799.
- Menasche, D. B., Shade, P. A., and Suter, R. M. (2020). Accuracy and precision of near-field high-energy diffraction microscopy forward-model-based microstructure reconstructions accuracy and precision of hedm reconstructions. *Journal of Applied Crystallography*, 53:107–116.
- Nemat-Nasser, S., Guo, W. G., and Cheng, J. Y. (1999). Mechanical properties and deformation mechanisms of a commercially pure titanium. *Acta Materialia*.
- Nervo, L., King, A., Fitzner, A., Ludwig, W., and Preuss, M. (2016). A study of deformation twinning in a titanium alloy by x-ray diffraction contrast tomography. *Acta Materialia*, 105:417–428.
- Nye, J. (1953). Some geometrical relations in dislocated crystals. *Acta Metallurgica*, 1(2):153–162.
- Park, J. S., Zhang, X., Kenesei, P., Wong, S. L., Li, M., and Almer, J. (2017). Far-field high-energy diffraction microscopy: A non-destructive tool for characterizing the microstructure and micromechanical state of polycrystalline materials. *Microscopy Today*, 25(5):36–45.
- Park, J. S., Zhang, X., Sharma, H., Kenesei, P., Hoelzer, D., Li, M., and Almer, J. (2015). High-energy synchrotron x-ray techniques for studying irradiated materials. *Journal of Materials Research*.
- Paton, N. E. and Backofen, W. A. (1970). Plastic deformation of titanium at elevated temperatures. *Metallurgical Transactions*, 1(10):2839–2847.
- Paton, N. E., Williams, J. C., and Rauscher, G. P. (1973). The deformation of alpha-phase titanium. *Proceedings of the World Conference on Titanium*, 2(3):1049–1069.
- Petch, N., J. (1953). The cleavage strength of polycrystals. *Journal of the Iron and Steel Institute, UK*, 174:25–28.
- Poulsen, H. F. (2012). An introduction to three-dimensional X-ray diffraction microscopy. *Journal of Applied Crystallography*, 45(6):1084–1097.

- Poulsen, H. F., Garbe, S., Lorentzen, T., Jensen, D. J., Poulsen, F. W., Andersen, N. H., Frello, T., Feidenhans'l, R., and Graafsma, H. (1997). Applications of high-energy synchrotron radiation for structural studies of polycrystalline materials. *Journal of Synchrotron Radiation*.
- Read, W. T. (1953). *Dislocations in crystals*. McGraw Hill, New York.
- Rice, J. R. (1971). Inelastic constitutive relations for solids: An internal-variable theory and its application to metal plasticity. *Journal of the Mechanics and Physics of Solids*.
- Richeton, T., Schuman, C., Lecomte, J. S., Bao, L., and Fressengeas, C. (2012). Relations between twin and slip in parent lattice due to kinematic compatibility at interfaces. *International Journal of Solids and Structures*, 49(11-12):1355–1364.
- Roters, F., Eisenlohr, P., Hantcherli, L., Tjahjanto, D. D., Bieler, T. R., and Raabe, D. (2010). Overview of constitutive laws, kinematics, homogenization and multiscale methods in crystal plasticity finite-element modeling: Theory, experiments, applications. *Acta Materialia*, 58(4):1152–1211.
- Ruggles, T. J. and Fullwood, D. T. (2013). Estimations of bulk geometrically necessary dislocation density using high resolution ebsd. *Ultramicroscopy*, 133:8–15.
- Sachs, G. (1928). Zur ableitung einer fließbedingung. *Zeitschrift des Vereines deutscher Ingenieure*, pages 732–736.
- Schmidt, S. (2014). Grainspotter: A fast and robust polycrystalline indexing algorithm. *Journal of Applied Crystallography*, 47(1):276–284.
- Schuman, C., Bao, L., Lecomte, J. S., Zhang, Y., Raulot, J. M., Philippe, M. J., and Esling, C. (2012). A new variant selection criterion for twin variants in titanium alloys (part 2). *Advanced Engineering Materials*.
- Schuman, C., Bao, L., Sébastien Lecomte, J., Zhang, Y., Marc Raulot, J., Jeanne Philippe, M., and Esling, C. (2011). A new variant selection criterion for twin variants in titanium alloys (part 1). *Advanced Engineering Materials*, 13(12):1114–1121.
- Schuren, J. C., Shade, P. A., Bernier, J. V., Li, S. F., Blank, B., Lind, J., Kenesei, P., Lienert, U., Suter, R. M., Turner, T. J., Dimiduk, D. M., and Almer, J. (2015). New opportunities for quantitative tracking of polycrystal responses in three dimensions. *Current Opinion in Solid State and Materials Science*, 19(4):235–244.
- Seal, J. R., Crimp, M. A., Bieler, T. R., and Boehlert, C. J. (2012). Analysis of slip transfer and deformation behavior across the α/β interface in ti-5al-2.5sn (wt.%) with an equiaxed microstructure. *Materials Science and Engineering A*, 552:61–68.
- Sharma, H., Huizenga, R. M., and Offerman, S. E. (2012a). A fast methodology to determine the

- characteristics of thousands of grains using three-dimensional x-ray diffraction. i. overlapping diffraction peaks and parameters of the experimental setup. *Journal of Applied Crystallography*.
- Sharma, H., Huizenga, R. M., and Offerman, S. E. (2012b). A fast methodology to determine the characteristics of thousands of grains using three-dimensional x-ray diffraction. ii. volume, centre-of-mass position, crystallographic orientation and strain state of grains. *Journal of Applied Crystallography*.
- Shastri, S. D., Almer, J., Ribbing, C., and Cederström, B. (2007). High-energy x-ray optics with silicon saw-tooth refractive lenses. *Journal of Synchrotron Radiation*, 14(2):204–211.
- Simons, H., King, A., Ludwig, W., Detlefs, C., Pantleon, W., Schmidt, S., Stöhr, F., Snigireva, I., Snigirev, A., and Poulsen, H. F. (2015). Dark-field x-ray microscopy for multiscale structural characterization. *Nature Communications*, 6:1–6.
- Soare, Stefan, C. (2014). Plasticity and non-schmid effects. *Proceedings: Mathematical, Physical and Engineering Sciences*, 470(2161):1–18.
- Taddei, M. (2015). *Fundamentals and applications of x-ray diffraction with emphasis on powder x-ray diffraction*. Paul Scherrer Institute, ETH Zürich.
- Taylor, G. I. (1938). Plastic strain in metals. *Institute of Metals*, pages 307–324.
- Turner, T. J., Shade, P. A., Bernier, J. V., Li, S. F., Schuren, J. C., Lind, J., Lienert, U., Kenesei, P., Suter, R. M., Blank, B., and Almer, J. (2016). Combined near- and far-field high-energy diffraction microscopy dataset for ti-7al tensile specimen elastically loaded in situ. *Integrating Materials and Manufacturing Innovation*, 5(1):94–102.
- Wang, J., Hoagland, R. G., Hirth, J. P., Capolungo, L., Beyerlein, I. J., and Tomé, C. N. (2009a). Nucleation of a (10-12) twin in hexagonal close-packed crystals. *Scripta Materialia*, 61(9):903–906.
- Wang, L. (2011). *Evolution of deformation twins and dislocations near grain boundaries in commercial purity titanium*. PhD thesis, Michigan State University. Copyright - Database copyright ProQuest LLC.
- Wang, L., Eisenlohr, P., Yang, Y., Bieler, T. R., and Crimp, M. A. (2010a). Nucleation of paired twins at grain boundaries in titanium. *Scripta Materialia*, 63:827–830.
- Wang, L., Lind, J., Phukan, H., Kenesei, P., Park, J.-S., Suter, R. M., Beaudoin, A. J., and Bieler, T. R. (2014). Mechanical twinning and detwinning in pure ti during loading and unloading – an in situ high-energy x-ray diffraction microscopy study. *Scripta Materialia*, 92:35–38.
- Wang, L., Yang, Y., Eisenlohr, P., Bieler, T. R., Crimp, M. A., and Mason, D. E. (2009b). Twin nucleation by slip transfer across grain boundaries in commercial purity titanium. *Metallurgical*

- and Materials Transactions A*, 41(2):421.
- Wang, L., Yang, Y., Eisenlohr, P., Bieler, T. R., Crimp, M. A., and Mason, D. E. (2010b). Twin nucleation by slip transfer across grain boundaries in commercial purity titanium. *Metallurgical and Materials Transactions A*, 41(2):421–430.
- Wang, L., Zheng, Z., Phukan, H., Kenesei, P., Park, J.-S., Lind, J., Suter, R. M., and Bieler, T. R. (2017). Direct measurement of critical resolved shear stress of prismatic and basal slip in polycrystalline ti using high energy x-ray diffraction microscopy. *Acta Materialia*, 132:598–610.
- Wozniak, J. M., Sharma, H., Armstrong, T. G., Wilde, M., Almer, J. D., and Foster, I. (2015). Big data staging with mpi-io for interactive x-ray science. *Proceedings - 2014 International Symposium on Big Data Computing, BDC 2014*, pages 26–34.
- Wronski, M., Arul Kumar, M., Capolungo, L., McCabe, R. J., Wierzbanski, K., and Tomé, C. N. (2018). Deformation behavior of cp-titanium: Experiment and crystal plasticity modeling. *Materials Science and Engineering A*, 724(March):289–297.
- Xu, S., Gong, M., Jiang, Y., Schuman, C., Lecomte, J. S., and Wang, J. (2018). Secondary twin variant selection in four types of double twins in titanium. *Acta Materialia*, 152:58–76.
- Yang, W., Larson, B. C., Tischler, J. Z., Ice, G. E., Budai, J. D., and Liu, W. (2004). Differential-aperture x-ray structural microscopy: A submicron-resolution three-dimensional probe of local microstructure and strain. In *Micron*.
- Yang, Y., Wang, L., Bieler, T. R., Eisenlohr, P., and Crimp, M. A. (2011). Quantitative atomic force microscopy characterization and crystal plasticity finite element modeling of heterogeneous deformation in commercial purity titanium. *Metallurgical and Materials Transactions A: Physical Metallurgy and Materials Science*, 42(3):636–644.
- Yu, Q., Sun, J., Morris, J. W., and Minor, A. M. (2013). Source mechanism of non-basal <c+a> slip in ti alloy. *Scripta Materialia*, 69(1):57–60.
- Zaefferer, S., Kuo, J. C., Zhao, Z., Winning, M., and Raabe, D. (2003). On the influence of the grain boundary misorientation on the plastic deformation of aluminum bicrystals. *Acta Materialia*.
- Zhang, C., Bieler, T. R., and Eisenlohr, P. (2018). Scripta materialia exploring the accuracy limits of lattice strain quantification with synthetic diffraction data. *Scripta Materialia*, 154:127–130.
- Zhang, C., Li, H., Eisenlohr, P., Liu, W. J., Boehlert, C. J., Crimp, M. A., and Bieler, T. R. (2015). Effect of realistic 3d microstructure in crystal plasticity finite element analysis of polycrystalline ti-5al-2.5sn. *International Journal of Plasticity*, 69:21–35.